LOW DENSITY NUCLEAR MATTER IN HEAVY ION COLLISIONS

A Dissertation

by

LIJUN QIN

Submitted to the Office of Graduate Studies of
Texas A&M University
in partial fulfillment of the requirements for the degree of

DOCTOR OF PHILOSOPHY

December 2008

Major Subject: Physics

LOW DENSITY NUCLEAR MATTER IN HEAVY ION COLLISIONS

A Dissertation

by

LIJUN QIN

Submitted to the Office of Graduate Studies of
Texas A&M University
in partial fulfillment of the requirements for the degree of

DOCTOR OF PHILOSOPHY

Approved by:

Co-Chairs of Committee,	Robert Tribble
	Joseph Natowitz
Committee Members,	John Hardy
	Che-Ming Ko
Head of Department,	Edward Fry

December 2008

Major Subject: Physics

ABSTRACT

Low Density Nuclear Matter in Heavy Ion Collisions. (December 2008)

Lijun Qin, B.S., Xi'An Jiaotong University, China;
M.S., Institute of Modern Physics, Chinese Academy of Sciences
Co–Chairs of Advisory Committee: Dr. Joseph Natowitz
Dr. Robert Tribble

The symmetry energy is the energy difference between symmetric nuclear matter and pure neutron matter at a given density. Around normal nuclear density, i.e. $\rho/\rho_0 = 1$, and temperature, i.e. T = 0, the symmetry energy is approximately 23.5 MeV/nucleon for finite nuclear matter and 30 MeV/nucleon for infinite nuclear matter, but at other densities, the symmetry energies are very poorly understood. Since the symmetry energy is very important in understanding many aspects of heavy ion reactions, structure, and nuclear astrophysics, many different models have been developed and some predications of the density dependence of symmetry energy have been made. Intermediate energy heavy ion collisions provide a unique tool to probe the nuclear equation of state. The initial compression and the thermal shock in Fermi-Energy heavy ion collisions lead naturally to the production of nucleonic matter at varying temperatures and densities which are interesting in this context. Since the light particle emission during this stage witnesses each stage of the reaction, it carries essential information on the early dynamics and on the degree of equilibration at each stage of the reaction. The kinematic features and yields of emitted light particles and clusters in the invairant velocity frame have been exploited to probe the nature of the intermediate system and information on the Equation Of State (EOS) with emphasis on the properties of the low density participant matter produced in such collisions. In order to pursue this effort and broaden the density range over which the symmetry energies are experimentally determined we have now carried out a series of experiments in which the reactions of ^{112}Sn and ^{124}Sn with projectiles, ranging from ^{4}He,^{10}B, ^{20}Ne, ^{40}Ar to ^{64}Zn, all at the same energy per nucleon, 47 Mev/u, were performed.

In this series of experiments different collision systems should lead to different average densities. By careful comparisons of the yields, spectra and angular distributions observed for particle emission from these different systems we attempted to cleanly separate early emission resulting from nucleon-nucleon collisions from that resulting from evaporation from the thermalized system and obtain a much cleaner picture of the dynamic evolution of the hotter systems. The Albergo Model has been used to calculate the density and temperature, symmetry free energies with the isoscaling technique for systems with different N/Z ratios. Those are compared with Roepke Model results. Also other models like VEOS, Lattimer, and Shen-Toki have been added to calculate the alpha mass fraction in order to understand the properties of low density matter further.

To My mother Kailan Zhu, my father Kui Qin, and my wife Li Zhang

ACKNOWLEDGMENTS

It was my great pleasure to carry out my doctoral studies at the Cyclotron Institute at Texas A&M University with such a wonderful, friendly and supportive staff team, very knowledgable faculty members, and amazingly collaborative graduate students. First and foremost I want to express my tremendous appreciation to my advisor, Dr. Joe Natowitz, the best mentor I have ever had, for all his advice, support and brainstorming. I have been incredibly lucky to work under his guidance for several years, which will impact many aspects of my life in the future. In his group I was able to see all aspects of research including: concept, setup, testing, acquisition, analysis, simulations, programming, computer management, and problem solving which is fundamentally important to the development of my career after graduation. I also want to greatly thank Roy Wada, Kris Hagel, and Thomas Keutgen, with whom I have worked through the years, for their advice and support. I also want to thank my co-advisor, Dr. Robert Tribble for financial aid and his administration of the Cyclotron Institute in delivering the best quality research service. I am also grateful to my committee members, Dr. Ko and Dr. Hardy, for all their suggestions, guidance, and support. Last but not least, I want to thank my family for their encouragment and tolerance which made completion of my dissertation project possible.

TABLE OF CONTENTS

LIST OF TABLES

LIST OF FIGURES

FIGURE Page

FIGURE Page

FIGURE Page

FIGURE Page

CHAPTER I

INTRODUCTION

A. General Picture of Heavy Ion Collisons

Extensive studies have been conducted to investigate the dynamical and thermodynamical evolution of the interaction region in near fermi energy heavy ion collisions and to understand the extent to which equilibration of various degrees of freedom, thermal, chemical, N/Z ratio, etc is realized. The importance of both nucleon-nucleon collision and mean-field effects leads to a high complexity of the reaction process. A widely accepted picture of the reaction process is that, at the early stage of the collision, a compressional and thermal shock creates a hot composite nucleus that may expand to low densities and form clusters. Such clusters might reflect both equilibrium and non-equilibrium production mechanisms. Extensive experimental efforts have been carried out and a number of theoretical models have been constructed to address this issue [1, 2, 3, 4, 5, 6, 7, 8, 9, 10, 11]. In recent years, investigations of the dynamics in a large series of heavy ion reaction experiments indicate that much of the early particle emission may be attributed to nucleon-nucleon collisions occurring during the thermalization stage of the reaction [12, 13, 14, 15]. Figure 1 shows a cartoon showing the reaction process. In nuclear collisions the nuclei are at normal nuclear density before the interaction happens, the density may become higher in the early stage of the interaction, and later on will decrease. At this lower density, clusteration can occur and the fragments are formed. In general the heavier fragments still carry excitation energy and undergo secondary decay. The lower density region can be probed by observing the ejectiles and the heavier fragments which are formed. The

---

The journal model is *Physical Review C.*

high density region can be probed using early emission particles or gamma rays, neutron and proton differential flow, or more complex observables such as pion emission ratios and kaon emission ratios [16, 17].

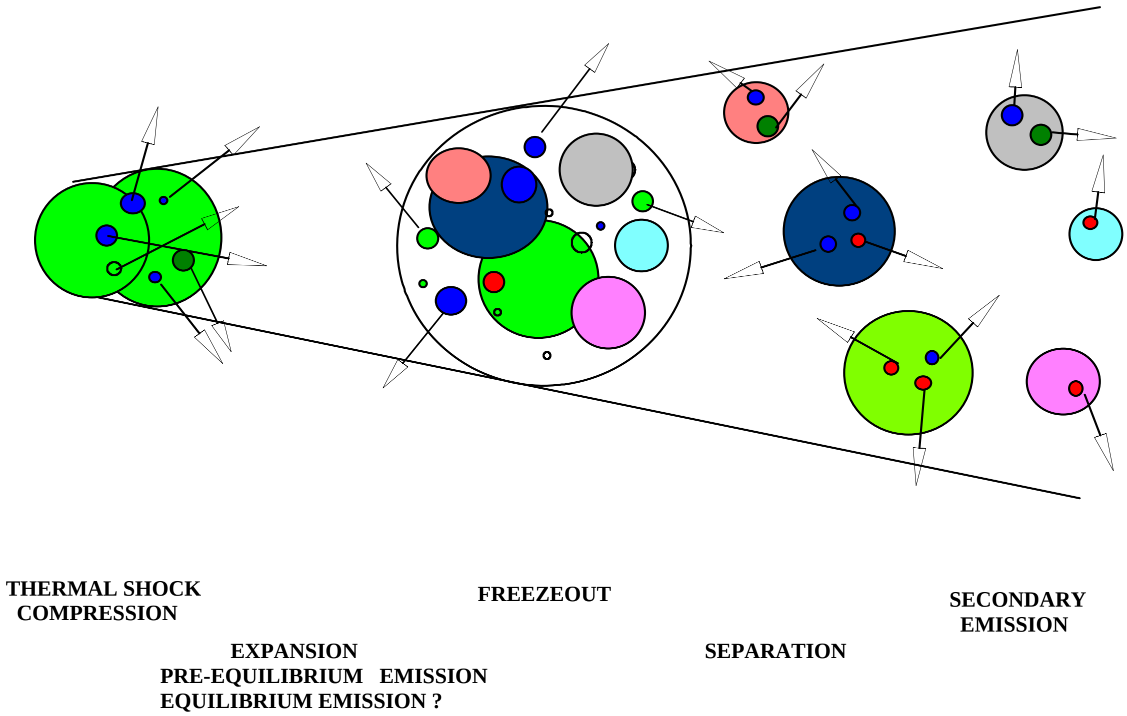

Fig. 1. General picture of a heavy ion collison in the Fermi energy domain.

B. Transport Models to Simulate Heavy Ion Collisions

A heavy ion collision (HIC) may be a very complicated process, especially in the Fermi Energy region because both mean-field and nucleon-nucleon collision effects contribute. Many transport theories based on a molecular dynamics model have been proposed to model these collisions. The most widely used are classical molecular dynamics (CMD), quantum molecular dynamics (QMD), and antisymmetrized molecular dynamics(AMD) approaches [14, 15]. CMD treats nucleons as point particles and their movement is governed by a classical equation of motion in a given mean field. The nucleon-nucleon interaction is like a classical hard sphere scattering. In QMD, each single nucleon of the two colliding nuclei is described by a Gaussian in momentum and coordinate space. At the beginning, the nuclei move along Coulomb trajectories. Once the distance between the two nuclei is less than 2 fm, the nuclear interaction occurs and the centroids of the Gaussians are propagated under the influence of the mutual two-body or three-body interactions. Normally the interaction is chosen as a local Skyrme-type interaction which is commonly used in time-dependent Hartree-Fock (TDHF) calculations and has been proven to reproduce the static properties of nuclei. Often, two parameterizations which are called "hard" and "soft" are chosen to yield different compressibilities of nuclear matter, supplemented by the Yukawa interaction and Coulomb interaction. To study the momentum dependence of the nuclear interaction and make comparison of experimental observables with calculated results, the momentum-dependent interaction is an option in the model calculation. During the time evolution of the wave packets the Pauli principle is respected only by the Liouville theorem of classical mechanics. In the model NN collisions are allowed and the Pauli blocking is treated in an approximate manner. During the propagation of the wave packets, however, the time evolution based on the classical equation of motion eventually leads the initial state into a Pauli forbidden zone and the occupation number of nucleons in phase space often significantly exceeds $1/\mathrm{h}^3$.

Currently many people use the antisymmetrized molecular dynamics (AMD) model as the main theoretical model to guide in understanding the reaction process [14, 15]. In AMD, the total wave function of the system is anti-symmetrized and described by a Slater determinant of Gaussian wave packets. The time evolution of the centroid of the wave packets is treated in a classical manner. So far, in AMD

(AMD-V) the Pauli blocking in stochastic NN collisions is treated in an unambiguous manner and the probabilistic nature of the wave packet is considered as a diffusion process during its propagation. For the AMD-V calculations, the effective interaction and in-medium NN cross section are the two important ingredients. The Gogny interaction has been used successfully in many analyses [14]. This interaction gives a soft EOS with an incompressibility value K of 228 MeV for infinite nuclear matter and has a momentum-dependent mean field.

Many papers employ the Li-Machleidt's cross section formula 1.1 to model the N-N cross section modification in medium [18, 19, 20].

$$\begin{aligned}\sigma_{pn} &= \left[31.5 + 0.092 \times \left|20.2 - E^{0.53}\right|^{2.9}\right] \frac{1.0 + 0.0034E^{1.51}\rho^2}{1.0 + 21.55\rho^{1.34}}, \\ \sigma_{pn} &= \left[23.5 + 0.00256 \times \left|18.2 - E^{0.5}\right|^{4.0}\right] \frac{1.0 + 0.1667E^{1.05}\rho^2}{1.0 + 9.704\rho^{1.2}}. \end{aligned} \tag{1.1}$$

The fragments generated in AMD-V are generally in an excited state at time about 300fm/c. An unavailable amount of CPU time would be needed if the AMD Model were followed with all fragments de-excited to their ground states. In fact most calculations normally use a statistical decay code (GEMINI) to follow the cooling process and generate the final results [14].

C. Nuclear Binding Energy

The binding energy equation is shown in equation 1.2, where BE is the binding energy in MeV, Z is the number of protons, M_p is the mass of hydrogen atom, N is the neutron number, M_n is the mass of the neutron and M_{nucl} is the mass of the nuclide. The factor 931.5 is a constant to convert mass to energy in MeV.

$$BE = 931.5(ZM_p + NM_n - M_{nucl}) \tag{1.2}$$

Figure 2 shows a plot of binding energy per nucleon as a function of mass number for the most bound nuclide at each mass [21]. There is a peak in the binding energy per nucleon around iron with ^{56}Fe the most tightly bound nucleus. This peak divides the nuclides into two groups, with those having lower masses able to provide energy from fusion, and the higher masses able to provide energy from fission.

For nuclides in the ground state at normal nuclear density with given masses, their binding energy can be calculated using Weizsackers phenomenological formula developed in 1935 [22, 23]:

$$BE(A,Z) = a_b A - a_s A^{2/3} - a_a \frac{(A-2Z)^2}{4A} - a_c \frac{Z(Z-1)}{A^{1/3}} + B \tag{1.3}$$

The binding energy (BE) for a given nuclide (A, Z) is determined using five terms, four of which depend on the mass (A) and/or charge (Z). The first term is called the bulk term, and the asymmetry term is the third term. The other three terms arise from the finite size of the nucleus. The second term, or surface term, corrects for the nuclear surface. The fourth term is Coulomb term which adjusts the repulsion of the protons. The last term is pairing term which corrects for the neutron and proton pairing. A systematic study of nuclear masses shows that nuclei are more stable when they have an even number of protons and/or neutrons. In fact, the exact constants for each of the terms are determined by fitting experimental data and depend on the mass range: a_b = 15.67 MeV/c^2, a_s = 17.23 MeV/c^2, a_c = 0.714 MeV/c^2, a_a = 93.15 MeV/c^2, and the pairing term, B, is 0 MeV/c^2 for odd-even or even-odd nuclei, -11.2 MeV/c^2 for even-even nuclei and +11.2 MeV/c^2 for odd-odd nuclei [24, 25, 26, 27, 28]. A classical result is shown in the Fig. 2.

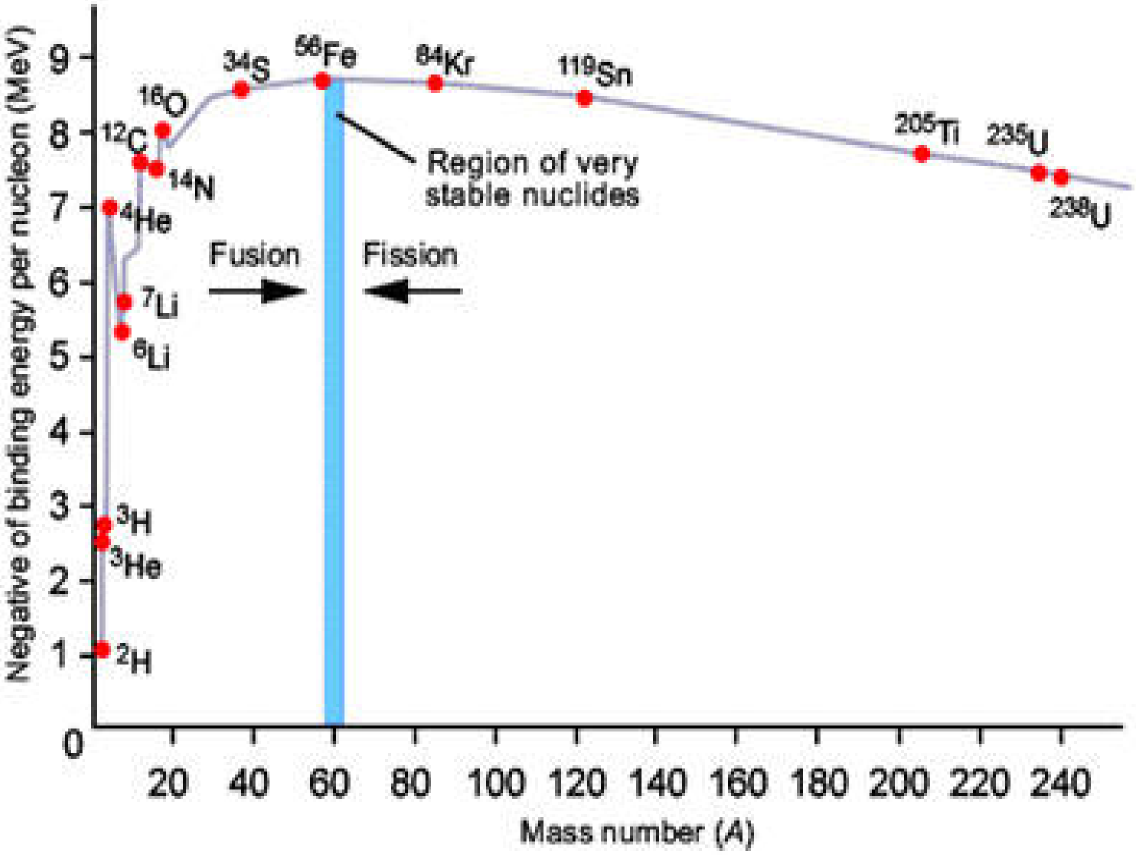

Fig. 2. Binding energy per nucleon with mass number [21].

D. Symmetry Energy and EOS

The symmetry energy is the energy difference between symmetric nuclear matter and pure neutron matter at a given density. Around normal nuclear density, i.e. $\rho/\rho_0 = 1$, and temperature, i.e. T = 0, the symmetry energy is approximately 23.5 MeV/nucleon for finite nuclear matter and 30 MeV/nucleon for infinite nuclear matter, but at other densities, the symmetry energies are very poorly understood. The nuclear EOS shown in equation 1.4, relates the density (ρ), temperature (T), and asymmetry (δ) with the binding energy [29, 30]. The asymmetry is given by equation 1.5, where N is the neutron number and Z is the proton number. When Z is equal to 0 (for the case of pure neutron matter) $\delta = 1$, while if Z is equal to N (for the case of symmetric nuclear matter) $\delta = 0$, and if N is equal to 0 (for the case of pure proton matter) δ = -1. The total binding energy is an inherent property of nuclei and to first order there is a linear dependence with mass number. To compare the binding energies of different nuclei, the binding energy is divided by the mass number to get the binding energy per nucleon (MeV/nucleon). The dependence of latter on the nuclear density is called the equation of state (EOS).

There are two parts to the nuclear EOS, the symmetric part and the asymmetric part, which both depend on the density and temperature.

$$BE_{asym}(\rho, T, \delta) = BE_{sym}(\rho, T) + C_{sym}(\rho, T)\delta^2 \tag{1.4}$$

$$\delta = (N - Z)/(N + Z) \tag{1.5}$$

Since the symmetry energy is of importance in the understanding many aspects of heavy ion reactions and the structure of radioactive nuclei as well as issues in nuclear astrophysics such as the properties of neutron stars, many different models have been developed and some predications of the density dependence of symmetry energy have been made. Figure 3 shows the symmetry energy calculations reported by B.A. Li et al. [31] in which different interaction potentials are used.

Recent studies of excited, i.e. low density and high temperature, nuclear matter have shown a decrease in the symmetry energy with increasing excitation energy down to approximately 15 MeV [30] .

Understanding the nuclear matter equation of state over a wide range of temperature and density is important in both the nuclear and astrophysical context [32, 33, 34, 35, 36]. In the latter, knowledge of specific heats and the density dependence of the symmetry energy are crucial to understanding collapse of supernovae

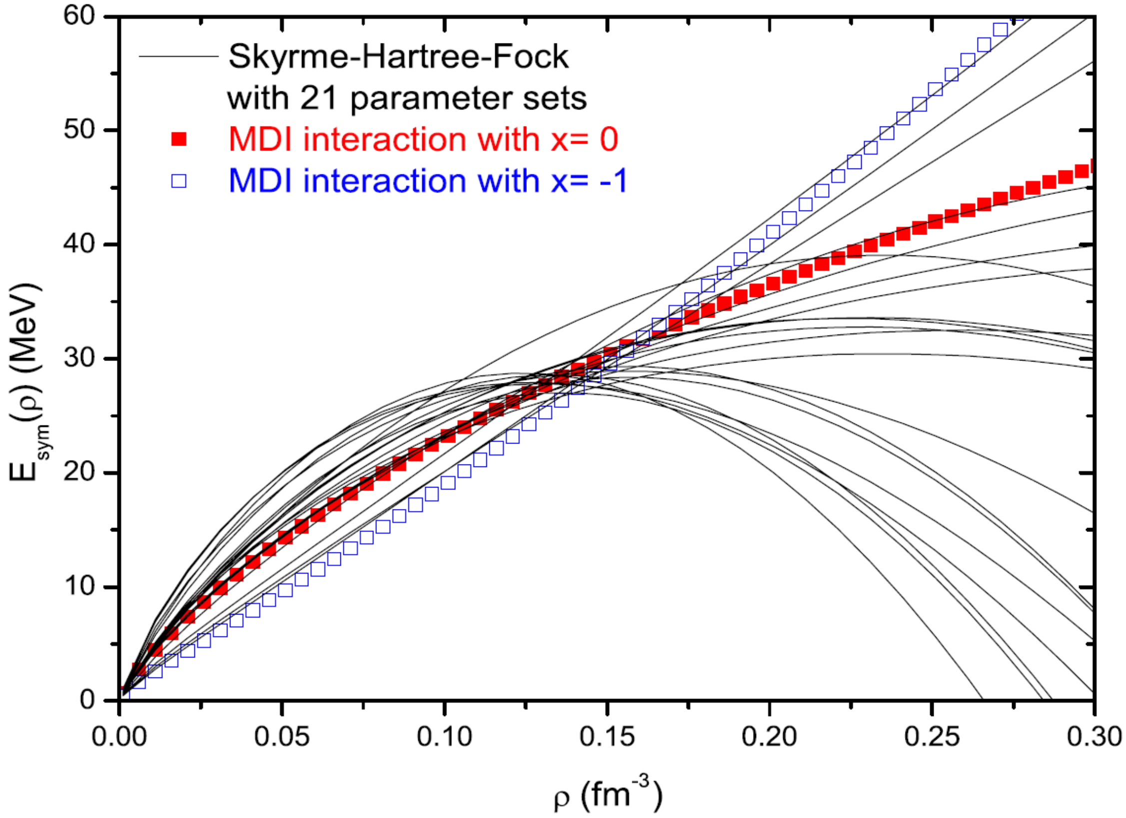

Fig. 3. Density dependence of the symmetry energy predicated by various interactions.

and the properties of neutron stars resulting from supernova collapse [37, 38, 39, 40].

A great effort has been made to explore the symmetry energy in different ways in many different works [41, 42, 43, 44, 45]. The strength of the density dependence of the symmetry energy affects neutron star masses and radii. Neutron stars are very dense forms of nuclear material and could contain exotic phases of matter such as hyperons and the quark gluon plasma (QGP). A stiffer dependence of the symmetry energy on the density allows for the creation of massive neutron stars with large radii [46, 47].

To employ intermediate energy heavy ion collisions as a tool to probe the nuclear equation of state, a detailed understanding of the reaction dynamics in well characterized collisions is essential. The initial compression and the thermal shock in Fermi-Energy heavy ion collisions lead naturally to the production of nucleonic matter at varying temperatures and densities which are interesting in this context. To illustrate this, we present in Figure 4, results of Antisymmetrized Molecular Dynamics (AMD) model calculations [15] for the systems $^{10}B + ^{124}Sn$ and $^{64}Zn + ^{124}Sn$, both at 47 MeV/u.

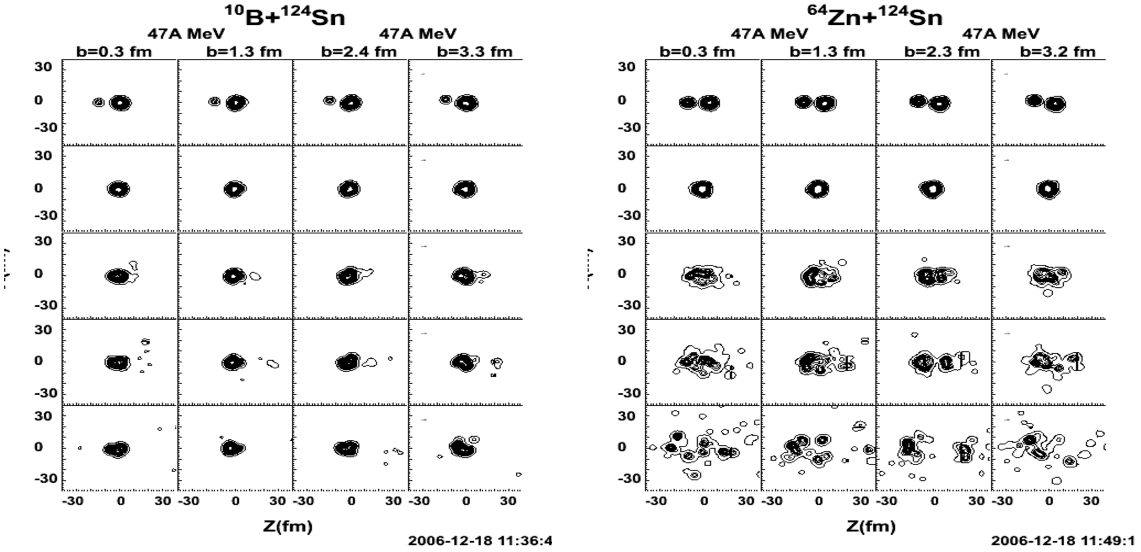

Fig. 4. Density profiles from Antisymmetrized Molecular Dynamics calculations for collisions of 47A MeV ^{10}B and ^{64}Zn with ^{124}Sn targets. Results are shown for times ranging from initial collision to 300 fm/c and for impact parameters ranging from 0.3 to 3.3 fm.

In an ideal situation this disassembly would be that of a thermally and chemically equilibrated nucleus. In practice this ideal state may not be reached and the final product distribution may include fragments and particles originating from non-equilibrium processes and reflecting correlations already present in the separated projectile and target nuclei. Distinguishing between these different production mechanisms of light particle and fragment production is difficult but essential to our understanding of near-Fermi energy collisions.

Since the light particle emission, which occurs during the collisions, witnesses each stage of the reaction, it carries essential information on the early dynamics and on the degree of equilibration at each stage of the reaction. Recently our group has emphasized investigations of nucleon and light cluster emission to obtain a more detailed experimental picture of the pre-equilibrium, thermalization and disassembly phases of such reactions [13, 14, 48, 49, 50]. The kinematic features and yields of emitted light particles and clusters have been exploited to probe the nature of the intermediate system and information on the EOS can be extracted. Much of our previous work utilizes coalescence model based techniques to follow the time evolution of the reaction [51, 52, 53, 54, 55] and references therein. As the nucleus expands and the density decreases the possibility of clusters condensing from the nuclear liquid is expected to increase. Already at relatively low energies there may be some evidence of clusterization in low density nuclear matter. For example, Alexander and co-workers have reported significant emission barrier lowerings for light particles emitted from moderately excited nuclei [56, 57]. The observed barriers appear to decrease with increasing excitation energy but attempts to introduce these lower barriers into statistical model calculations lead to great overestimates of the particle emission rates. The concept of a nuclear stratosphere, an extended low density region from which such particles might arise, was suggested and supported by some theoretical calculations. Experiments in which systems expected to have very different deformations produce identical spectra, even though the emission times are expected to be fast relative to the shape relaxation times, provide further support for this concept [58].

At low densities and high temperatures strong alpha clustering of nuclear matter is predicted by many theoretical models [15, 39, 59, 60, 61, 62]. such clusterization can be expected in low density nuclear matter, whether it be the low density surface of a neutron star, an expanded high temperature nucleus or a rarified region produced in the early stages of a nuclear collision. A reliable understanding of the nuclear EOS over a range of densities remains a very important requirement in nuclear astrophysics. Several extensive calculations and existing tabulations, based on varying nucleon-nucleon interactions, serve as standards for a wide variety of astrophysical simulations [59, 60].

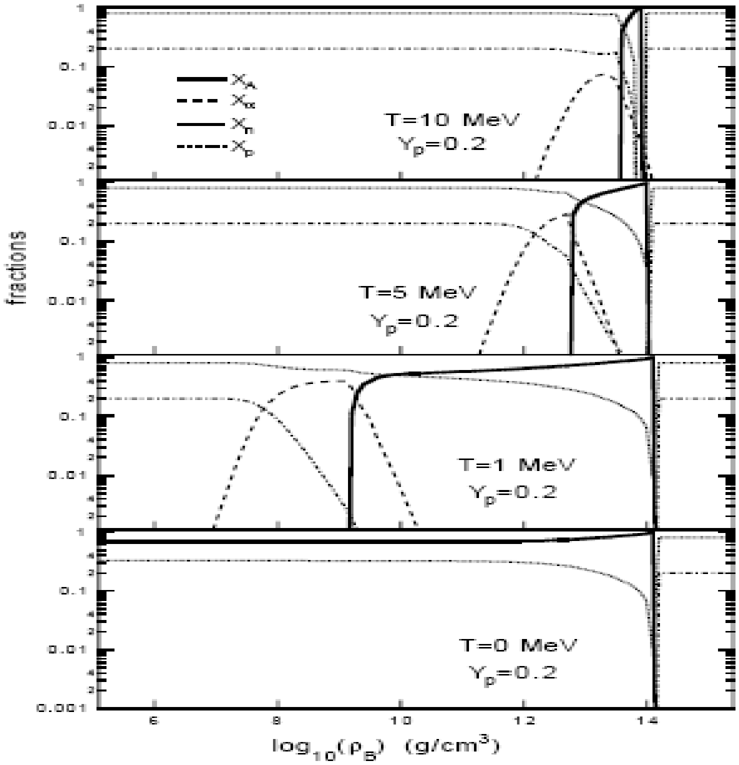

Fig. 5. Calculated mass fractions as a function of temperature and density in nuclear matter with a proton fraction of 0.2. Normal density is $\sim 10^{13}$ grams/cm^3.

Fig.5, from reference [60], presents calculated mass fractions for protons, neutrons, alpha particles and heavier nuclei predicted for nuclear matter at various temperatures and densities. While this is a calculation for a proton fraction of 0.2, similar results are observed for other proton fractions.

In a recent theoretical paper, Horowitz and Schwenk have reported the development of a Virial Equation of State (VEOS) for low density nuclear matter [39]. This equation of state, derived from experimental observables should be "model-independent, and therefore it sets a benchmark for all nuclear equations of state at low densities." Its importance in both nuclear physics and in the physics of the neutrinosphere in supernovae is emphasized in the VEOS paper [39]. An important feature of the VEOS is the natural inclusion of clustering which leads to large symmetry energies at low baryon density. These results are compared to those of other calculations in Figure 6.

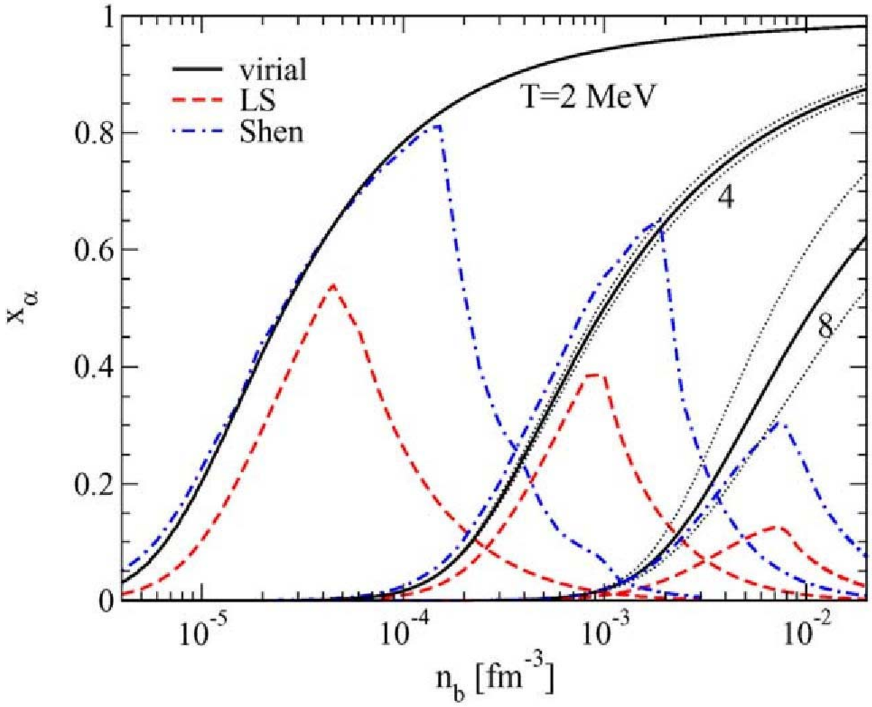

Fig. 6. Virial equation of state results (solid lines) at T = 2, 4 and 8 MeV are compared to those of two other theoretical models [39]. The present Virial model does not include heavier nuclei and is not expected to be adequate above the point where the Shen Calculation peaks [59].

We recently adapted our investigations of the nucleon and light cluster emission that occurs in near Fermi energy heavy ion collisions to probe the properties of the low density participant matter produced in such collisions [43]. The reactions of 35 MeV/nucleon ^{64}Zn projectiles with ^{92}Mo and ^{197}Au target nuclei were studied. The data provide experimental evidence for a large degree of alpha clustering resulting from nucleon coalescence in this low density matter. For nuclear gases with average proton fraction, Yp $\sim$ 0.44, and densities at and below 0.05 times normal nuclear density and varying temperatures, experimental symmetry energy coefficients have been derived using the isoscaling method [41, 42]. In order to pursue this effort and broaden the density range over which the symmetry energies are experimentally determined we have now carried out a series of experiments in which the reactions of ^{112}Sn and ^{124}Sn with projectiles, ranging from ^{4}He to ^{64}Zn, all at the same energy per nucleon, 47Mev/u. The systems chosen for this study were :

$$\begin{aligned}
&{}^4He +^{112} Sn, \quad {}^4He +^{124} Sn,\\
&{}^{10}B +^{112} Sn, \quad {}^{10}B +^{124} Sn,\\
&{}^{20}Ne +^{112} Sn, \quad {}^{20}Ne +^{124} Sn,\\
&{}^{40}Ar +^{112} Sn, \quad {}^{40}Ar +^{124} Sn,\\
&{}^{64}Zn +^{112} Sn, \quad {}^{64}Zn +^{124} Sn.
\end{aligned} \tag{1.6}$$

In this series of experiments different collision systems should lead to different average densities [14]. By careful comparisons of the yields, spectra and angular distributions observed for particle emission from these different systems we attempt to cleanly separate early emission resulting from nucleon-nucleon collisions from that resulting from evaporation from the thermalized system and obtain a much cleaner picture of the dynamic evolution of the hotter systems. Information on the symmetry potential included in the mean field can then be extracted using empirical techniques such as isoscaling for systems with different N/Z ratios or from comparison of the data with results of the dynamic transport model calculations (and statistical afterburners) [15]. In this dissertation we concentrate on the former.

CHAPTER II

EXPERIMENTAL SETUP AND RAW SPECTRA

In this chapter, the details of the NIMROD detector and typical raw spectra are introduced. The first section discusses the beams and targets. The NIMROD detector system and detection modules are then described. This is followed by a presentation of raw spectra generated by the fast and slow signals from CsI Detectors and two Si detector combinations.

A. Targets and Beams

The experiments were conducted at the Cyclotron Institute of Texas A&M University. A series of ion beams was delivered by the K500 Superconducting Cyclotron whose layout is indicated in Fig.7.

Table I lists the projectile species, energies, charge states and neutron to proton ratios, N/Z. Beam current intensities were in the range of 30 and 60 particle nanoamperes. To aid transmission to the target, a 0.25 millimeter thick aluminum foil which stripped almost all electrons from the projectiles was placed in the beam near the exit of the cyclotron. The two targets were ^{112}Sn and ^{124}Sn. The thicknesses of the targets ^{112}Sn and ^{124}Sn were 1.30 mg/cm^2 and 1.15 mg/cm^2 respectively. The run number sequence is listed in Table II.

Table I. List of beam species Z, N, N/Z, energies.

Beam	Z	N	N/Z	Energy	$(N-Z)/A$
P	1	0	0	47 Mev/A	-1
d	1	1	1	47 Mev/A	0
^{4}He	2	2	1	47 Mev/A	0
^{10}B	5	5	1	47 Mev/A	0
^{20}Ne	10	10	1	47 Mev/A	0
^{40}Ar	18	22	1.22	47 Mev/A	0.010
^{64}Zn	30	34	1.133	47 Mev/A	0.063

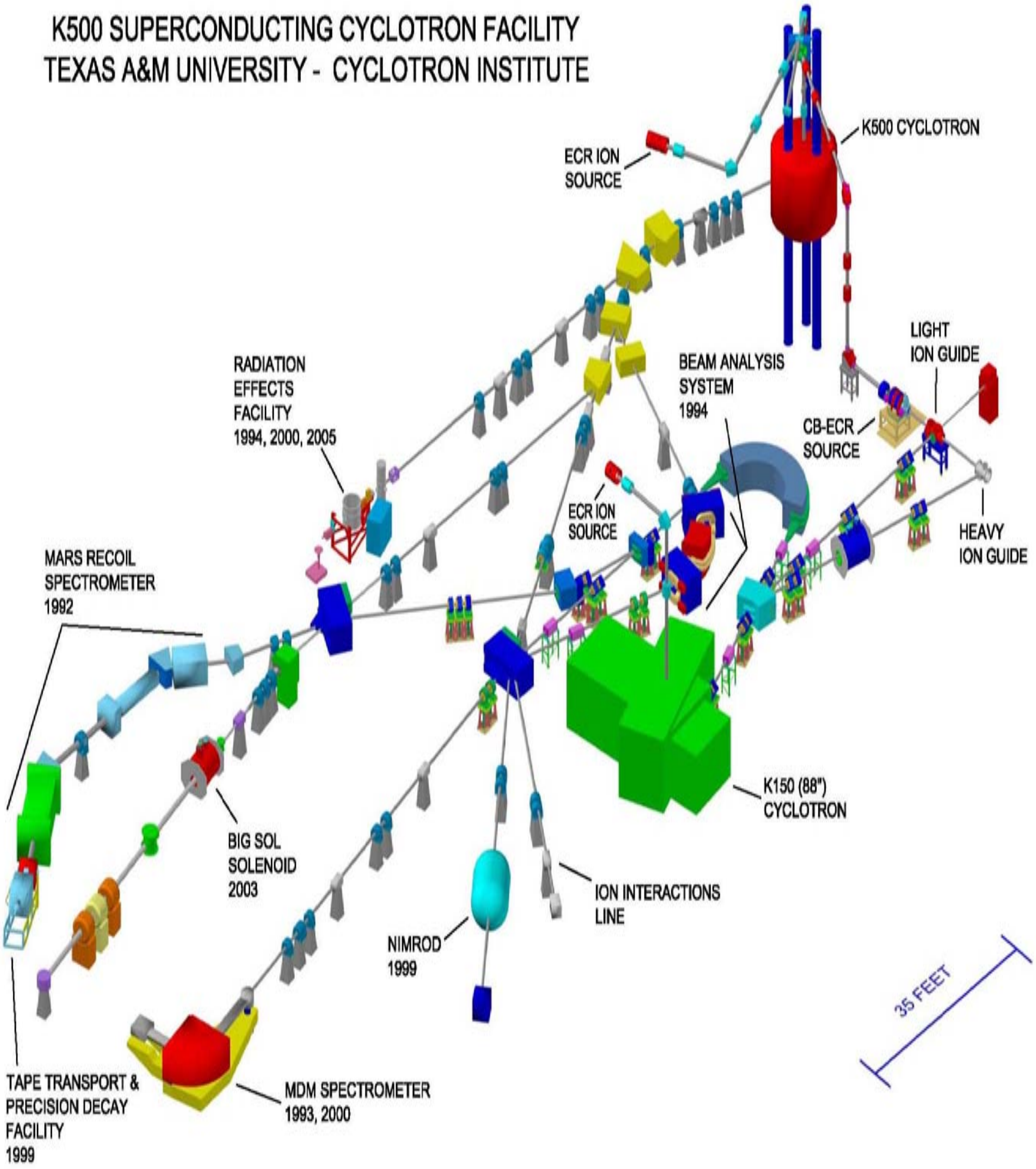

Fig. 7. Cyclotron layout at Texas A&M University

Table II. List of reaction systems and run numbers in chronologic order.

Chronologic Sequence Number	Projectile	Target	Run Number
1	^{40}Ar	$^{112}_{50}Sn_{62}$	$11, 12, 13, 14, 15$
2	^{40}Ar	$^{124}_{50}Sn_{74}$	$16, 17, 18, 19, 20$
3	^{4}He	$^{112}_{50}Sn_{62}$	$25, 26, 27$
4	^{4}He	$^{124}_{50}Sn_{74}$	$30, 31$
5	d	$^{112}_{50}Sn_{62}$	$32, 33, 34$
6	d	$^{124}_{50}Sn_{74}$	35
7	p	$^{112}_{50}Sn_{62}$	36
8	p	$^{124}_{50}Sn_{74}$	37
9	^{10}B	$^{112}_{50}Sn_{62}$	40
10	^{10}B	$^{124}_{50}Sn_{74}$	41
11	^{20}Ne	$^{112}_{50}Sn_{62}$	$43, 44, 45$
12	^{20}Ne	$^{124}_{50}Sn_{74}$	46
13	^{64}Zn	$^{112}_{50}Sn_{62}$	$48, 49, 50, 51$
14	^{64}Zn	$^{124}_{50}Sn_{74}$	52

B. Neutron Ball

The experiments were performed with the 4π multi-detector systems NIMROD [63] (Neutron Ion Multi-detector for Reaction Oriented Dynamics) which is composed of a Neutron Ball (NBL) and Detection Arrays consisting of Si-CsI telescopes arranged in 12 rings. The purpose of the NBL is to measure neutron multiplicity distribution to provide a means to better understand excitation energy deposition for heavy ion reaction systems [64]. It is specifically designed in a cylindrical shape (The designation as a ball reflects an earlier geometry of the system.) filled with about 1700 liters of

Gadolinium (Gd) doped (0.3% wt) pseudocumene liquid scintillator. The NBL has a central cylindrical section and two hemispherical endcaps. Each hemisphere has four photomultiplier tubes evenly distributed as shown in Fig. 8. The center ring is segmented into four removable modules, each of which has three photomultiplier tubes as shown in Fig. 9.

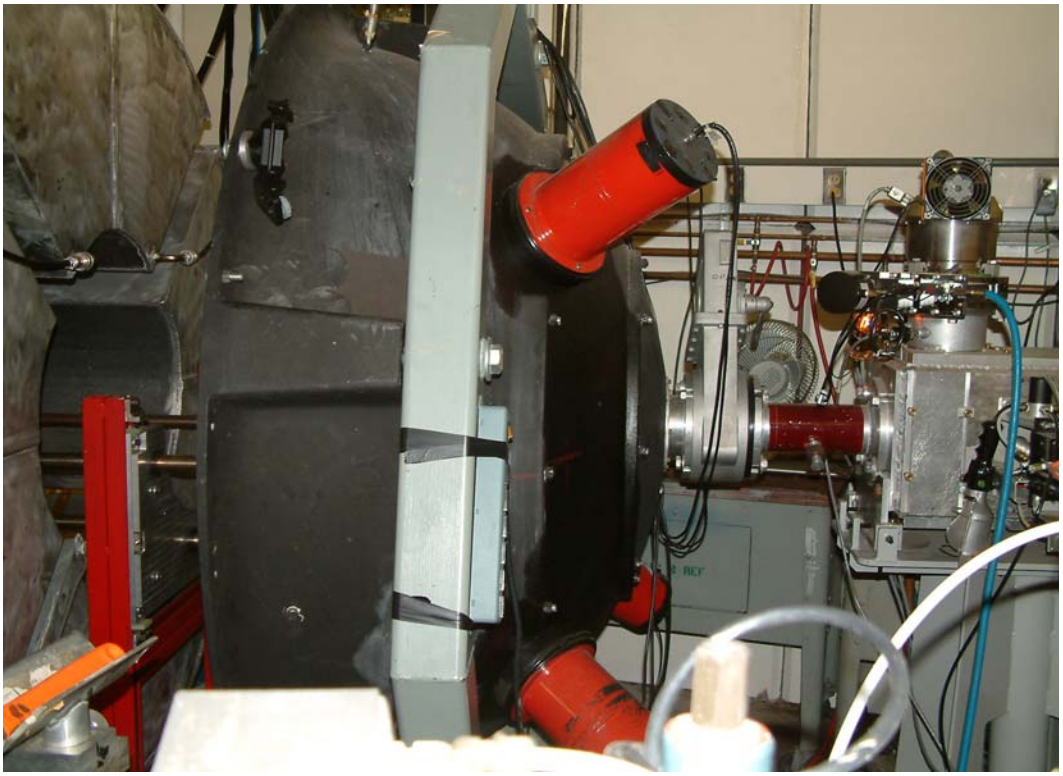

Fig. 8. End hemisphere of neutron ball.

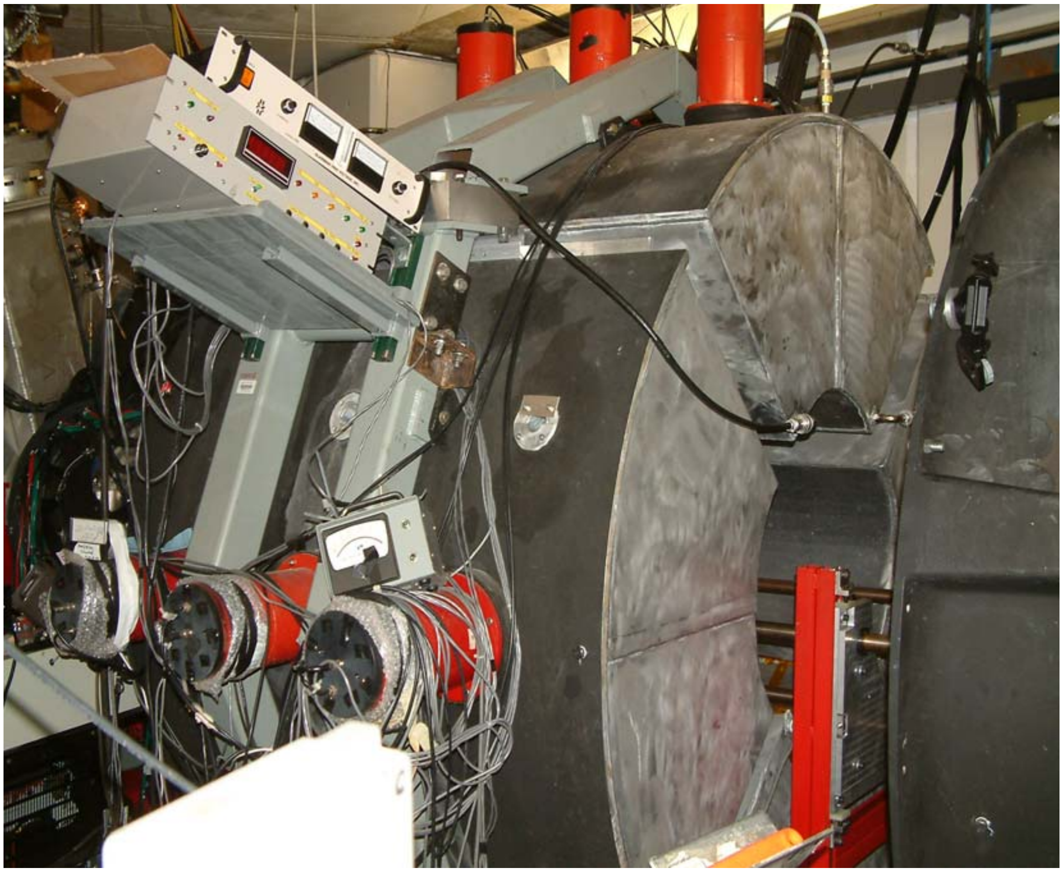

Fig. 9. The center ring of neutron ball.

When a nuclear reaction occurs inside the Neutron Ball, gamma rays are produced during the neutron and proton collisions and seen by the photomultiplier. This generates a "fast flash" signal which carries information about the total kinetic energy of all neutrons emitted and the energies of the gamma rays emitted from the event. It is proportional primarily to the neutron kinetic energy loss. Following that, the majority of the neutrons are thermalized, and captured by Gd nuclei, which happens over a period of about 100 microseconds. The excited Gd nucleus de-excites with emission of an average of three gamma rays. This produces a series of delayed signals representing the capture of individual neutrons. With correction for detection efficiency, those signals allow determination of the number of neutrons emitted in the event. The range of thermalization times allows reaction rates of the order of 500 events per second. Neutron detection time can be reduced from the scale of microseconds to the scale of nanoseconds by triggering on the gamma fast flash energy. However determination of neutron multiplicity then requires knowledge of the neutron kinetic energies and the contributions of gamma rays to the fast flash signal.

C. Charged Particle Detection Array

NIMROD is composed of a 166 segment charged-particle array surrounded by the Neutron Ball. The charged-particle detection array is arranged in 12 concentric rings around the beam axis. The configuration and geometrical dimensions of the forward eight rings are similar to the multidetector system INDRA at GANIL but NIMROD has less granularity. Figure 10 shows a typical ring including CsI detectors, Si detectors, and ionization chambers(ICs).

In those rings, the individual segments are fronted by ionization chambers (ICs) as Fig.11 filled with 30 Torr of CF4 gas. The front and back windows of the ICs are covered by 2.0 μm aluminized Mylar foil. In each of those eight rings, two of the segments have two Si detectors (150 and 500 μm thick) between the IC and CsI scintillation detectors which are called super telescopes in Fig.12, and four have only one Si detector as Fig.13 (300 μm thick). The CsI detectors shown in Fig.14 are made of 10 cm thick Tl-doped crystals glued to Hamamatsu photomultiplier tubes using BC-610 epoxy. For those scintillation detectors, light charged particles are identified using a pulse-shape discrimination method so that isotopes with Z=1 or 2 are clearly separated. For the super telescopes as Fig.15, the 2 Si detectors in the modules allow isotope identification capability for $Z \leq 11$. Using this 4π NIMROD detection system [63], we can measure the yields, spectra and angular distributions of light charged species which are emitted from these different systems over a range of angles between 3 and 170 degrees whose schematic map of angular coverage is shown in Fig.16. During the experiments, depending on the reaction systems studied, two different trigger modes are typically employed to take data. One is a minimum-bias trigger in which at least one of the CsI detectors detects a particle. The other is a high-multiplicity trigger requiring that three to five particles are detected in CsI detectors. A complete list of nuclear electronic modules and CAMAC crates can be found in Elizabeth Bell's dissertation [65] which lists every single module's specification and its source.

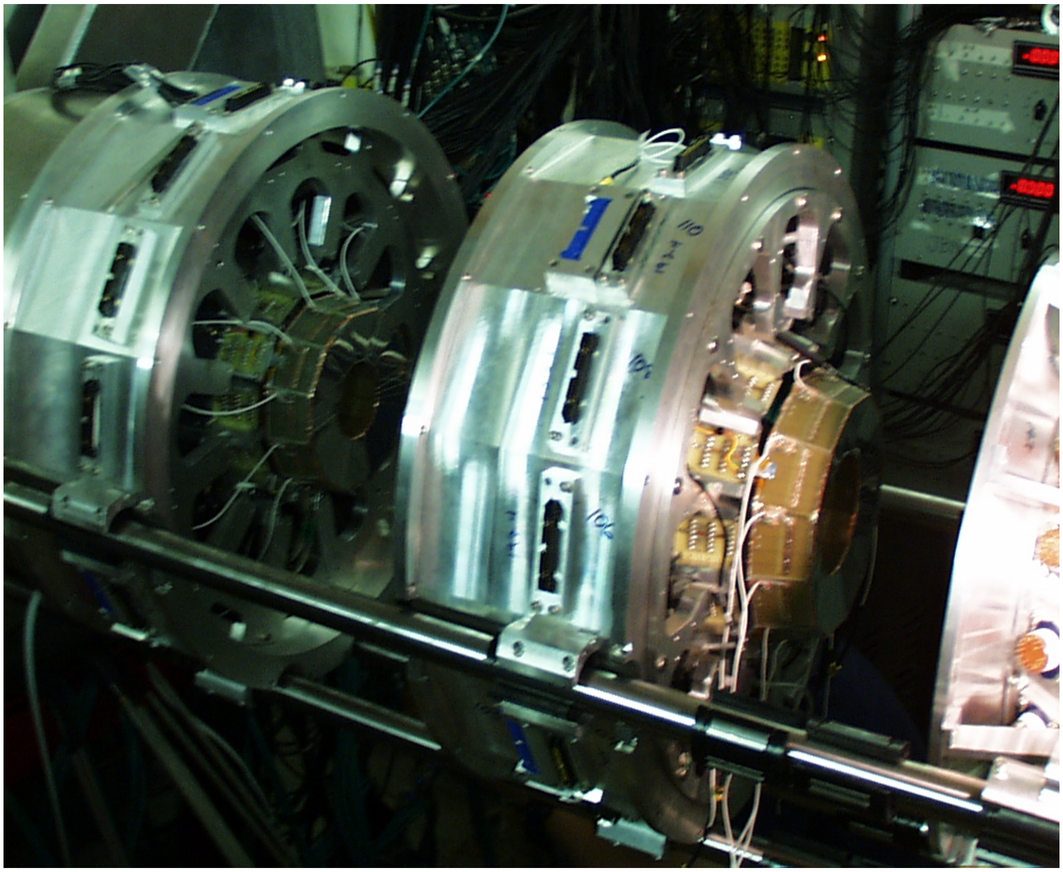

Fig. 10. A typical ring of NIMROD.

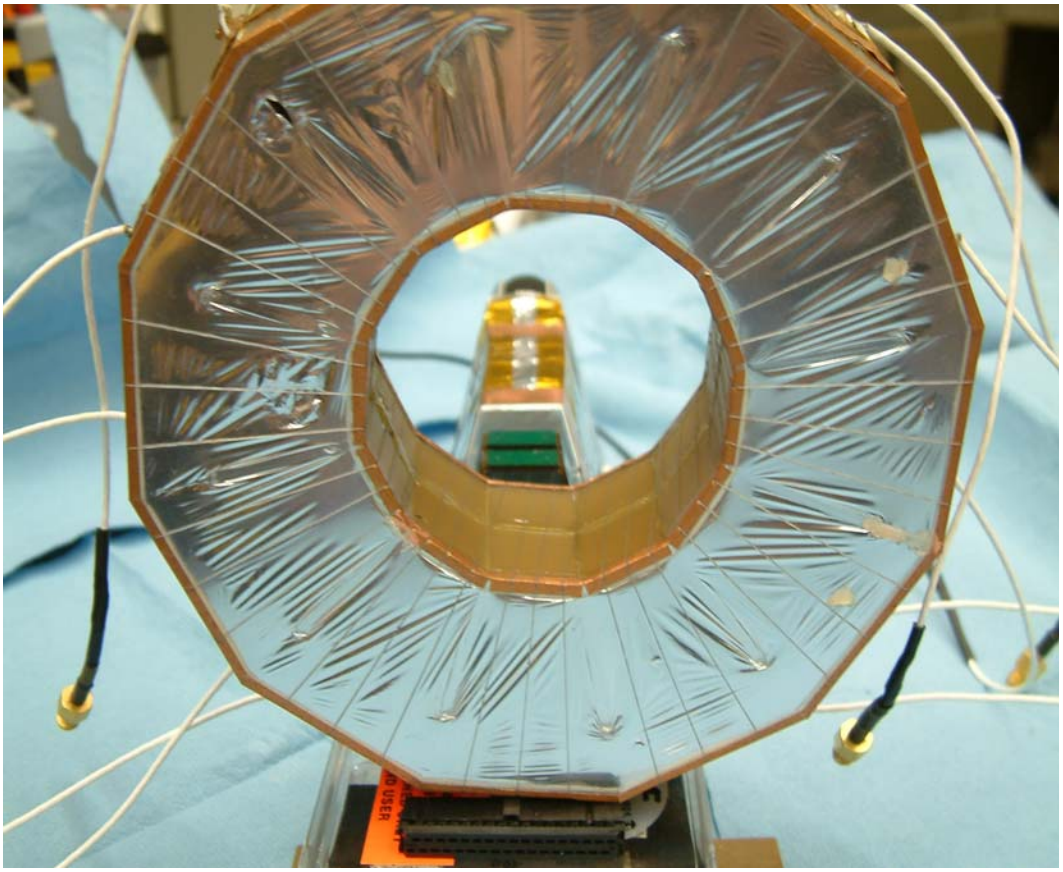

Fig. 11. IC chamber of NIMROD

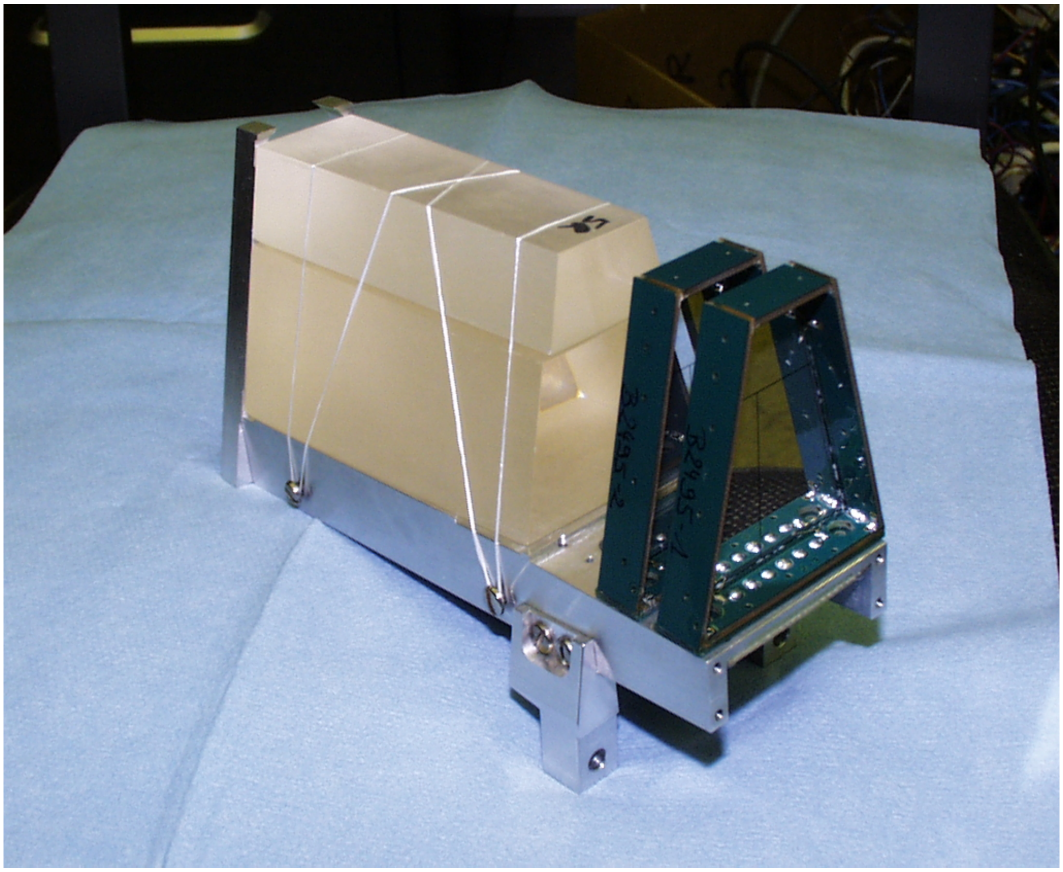

Fig. 12. NIMROD dection module composed of one CsI detector and two Si detectors.

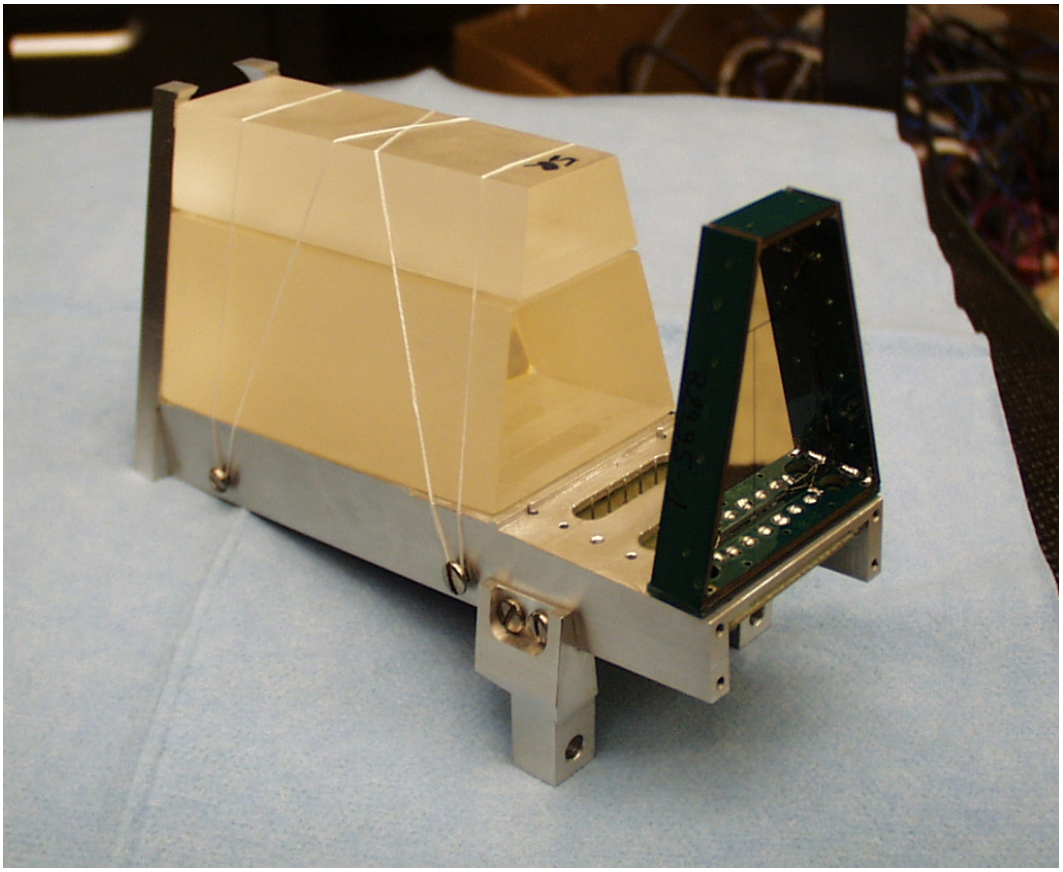

Fig. 13. NIMROD detection module composed of one CsI detector and one Si detector.

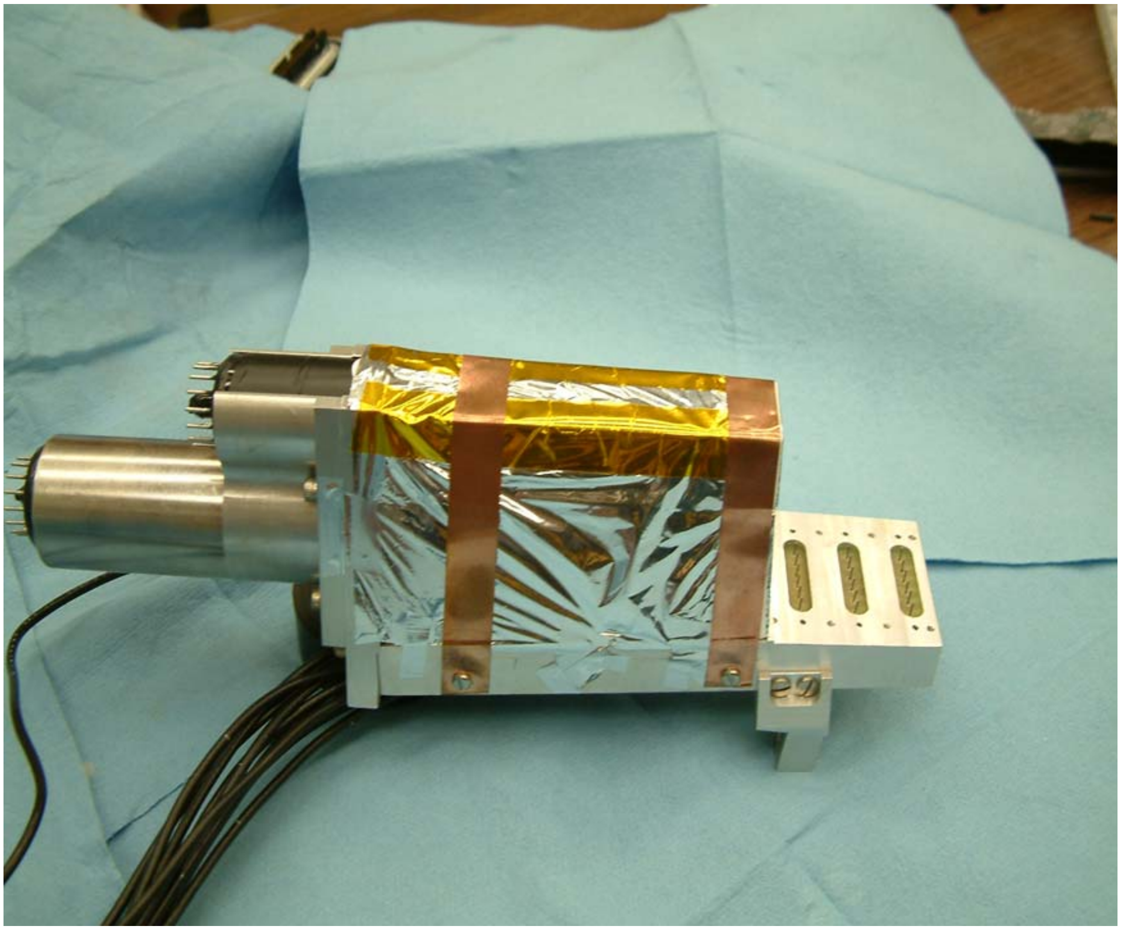

Fig. 14. NIMROD detection module of CsI detector.

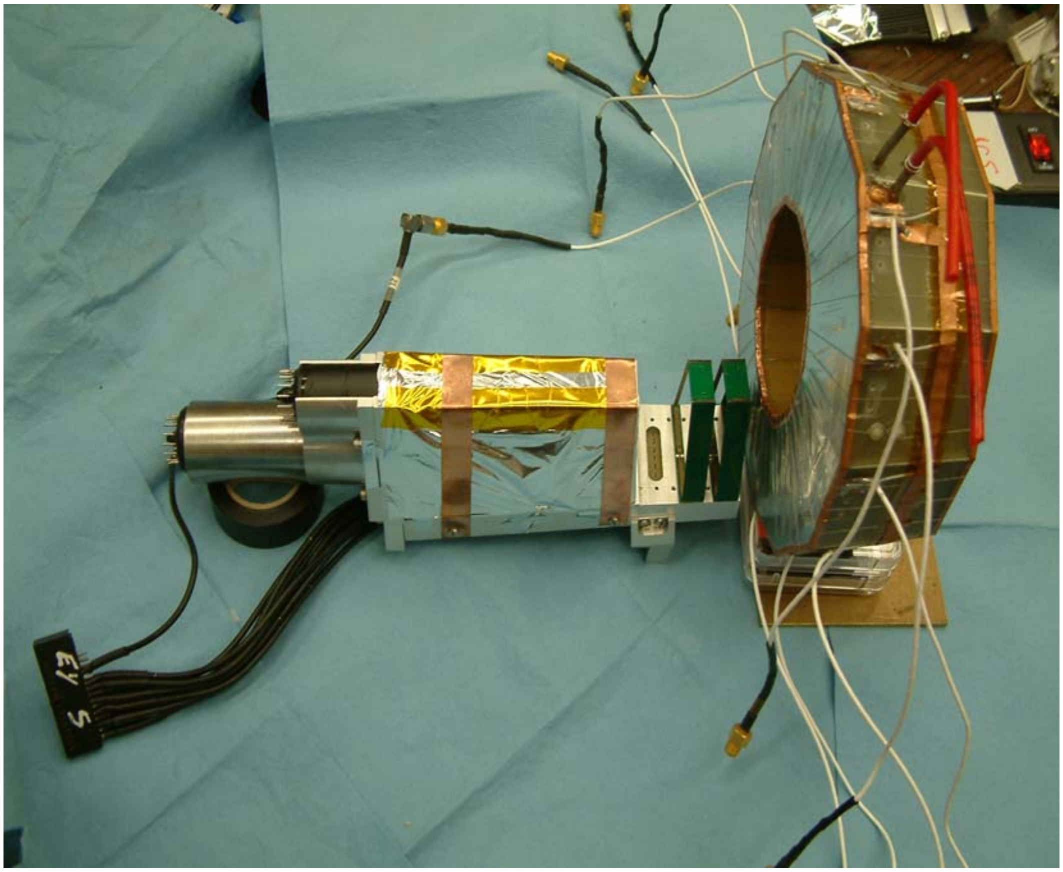

Fig. 15. NIMROD dection module composed of CsI, two Si, and an IC.

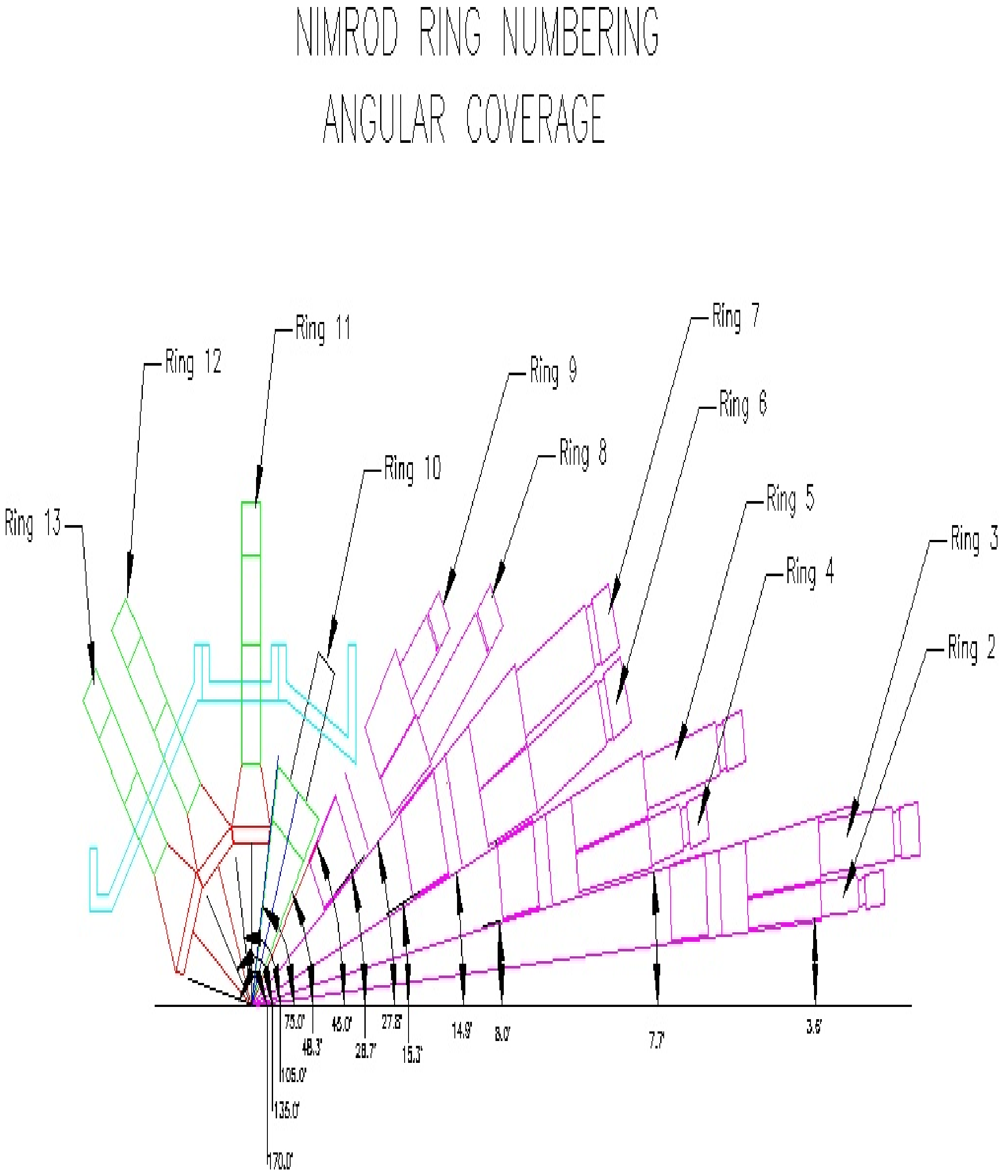

Fig. 16. Angular coverage of NIMROD.

D. Some Typical Raw Spectra from the Detection Modules

For the light charged particles, isotopes with Z=1 or 2 can be clearly identified using a pulse-shape discrimination method. Fig.17 shows the Particle Identification in which different groups of lines correspond to different atomic numbers.

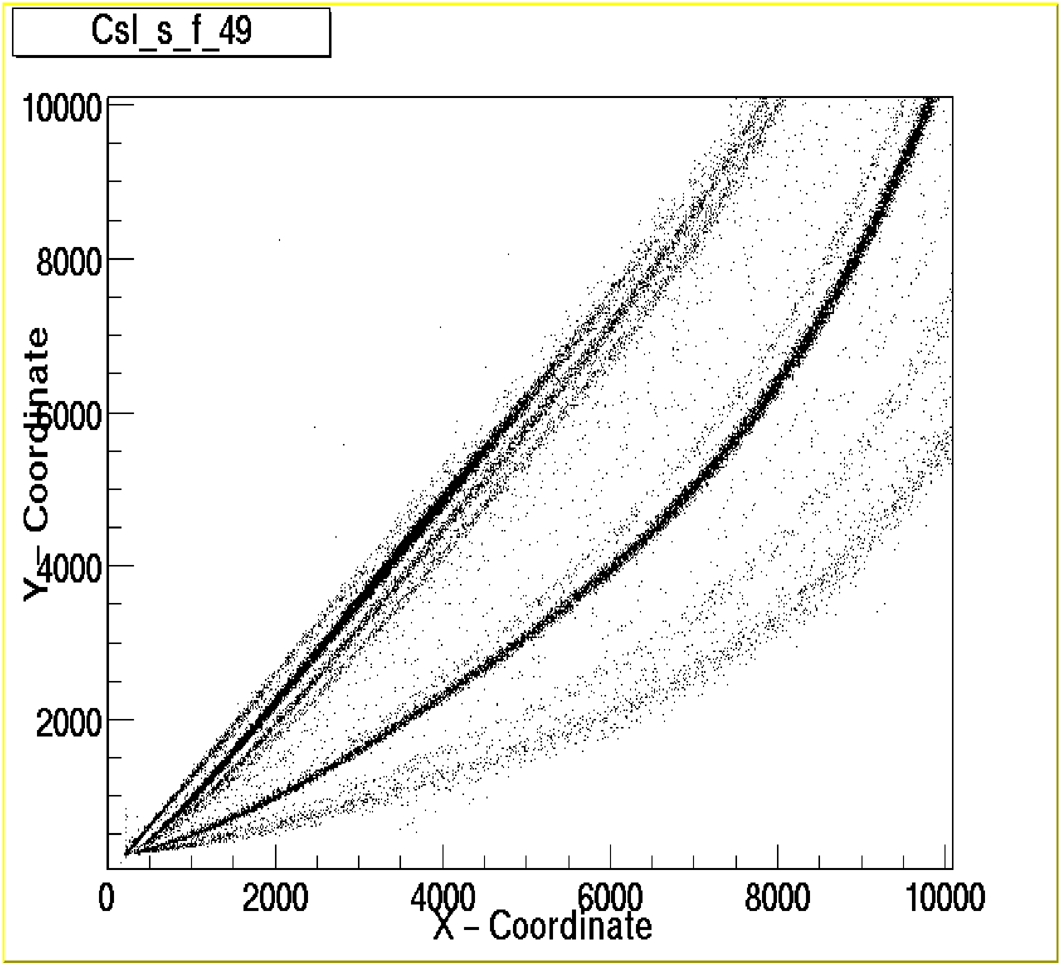

Fig. 17. Two dimensional plot of fast vs slow components of charge integrated light output from a CsI detector. Different lines correspond to different isotopes. X-Coordinate is the fast component of energy loss in channel unit. Y-Coordinate is the slow component of energy loss in channel units.

In this series of reaction systems, a variety of particle species are expected to be emitted. In order to allow the high Z identification capability, the super telescopes are normally employed, as shown in Fig.12. Here a typical of spectrum shown in Fig.18 shows the iostope identification for Z $\leq$ 6.

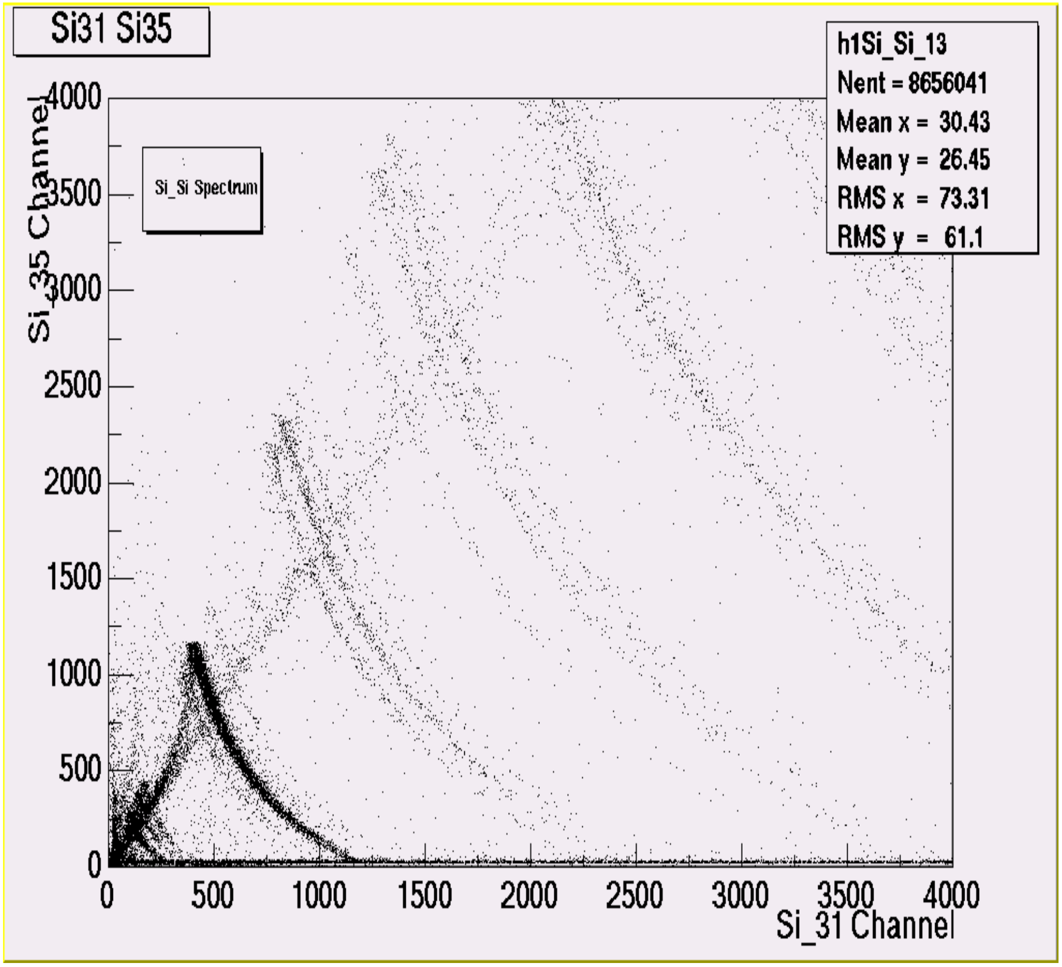

Fig. 18. Representative two dimensional plot of energy loss in Si1 E1 vs energy loss in Si2 E2. Different groups correspond to different elements. Within these groups individual lines correspond to different isotopes.

CHAPTER III

DETECTOR CALIBRATION AND SPECTRUM NORMALIZATION

This chapter first discusses the calibration of the Si and CsI detectors. In the second section the normalization of spectra from different detectors in the same ring is discussed.

A. Si Detector Calibration

During data acquisition, the gains of the Silicon detectors were very stable. The basic procedure to make the Si calibration employed isotope punch through points in the Silicon1 versus Silicon2 spectra from the super telescope in each ring. Using the known thicknesses of the Si detectors, the punch-through energy in MeV for each isotope was calculated using the SRIM range energy code to convert observed channels to energies [66]. The thickness of Si detectors are 500μm, 300μm, and 150μm. Table III shows punch-through energies (in MeV) for different detected species.

A C++ fitting routine in the ROOT [67] software was used to obtain the best three parameters describing the Silicon energy as a function of channel. The formula employed was

$$E_n(L) = \begin{cases} AL + B & : \quad L > F \\ EL^2 + DL + C & : \quad L < F \end{cases} \tag{3.1}$$

with $D = A - 2EF$ and $C = (A - D)F + B - EF^2$.

At the first step, the Cut-off Channel number F was selected. Above that limit, the relationship between channel number and Energy (MeV) is linear, otherwise it is nonlinear. Here L is the particle's energy loss in Si in channel units. E$_n$ is the

Table III. Particle punch-through energies in different Si detectors.

	Si thickness in microns		
particle	500μm	300μm	150μm
p	8.08	6.01	4.02
d	10.83	8.02	5.29
t	12.76	9.41	6.14
^{3}He	28.54	21.14	14.1
^{4}He	32.13	23.86	15.8
^{6}Li	60.71	44.93	29.69
^{7}Li	64.79	47.91	31.58
^{8}Li	68.31	50.5	33.17
^{7}Be	89.88	66.64	44.06
^{9}Be	99.78	73.77	48.29
^{10}Be	104.17	76.84	50.43
^{10}B	134.38	99.45	65.23
^{11}B	139.95	103.33	67.64
^{12}B	144.8	106.96	69.8

particle's energy deposited in Si in MeV units.

The ROOT solver functions automatically minimize the sums of the squares of the differences between the SRIM punch-through energy values and values calculated using the above equation. The minimization is achieved by varying an initial set of calibration parameters, A, B and E. In the low energy region below the cut-off channel, the nonlinear relation is meant to address a possible nonlinear response of the Silicon detector. Normally the non-linearity present in the Si calibration is negligible as most fits of the punch through energies versus the corresponding channels have small Chi square values, which implies a high degree of linearity. Fig.19 shows a typical Si calibration curve.

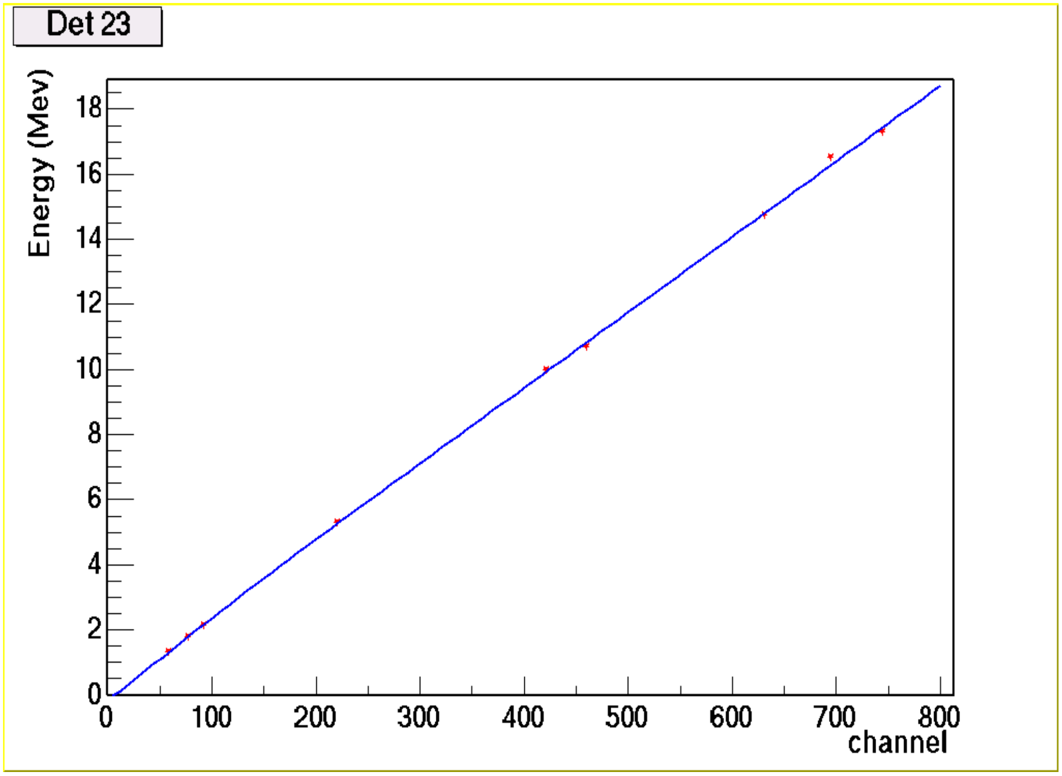

Fig. 19. Si calibration using punch-through point energies. X axis is the channel number of light particles. Y axis is energy in MeV.

B. CsI Detector Calibration

The relationship of CsI light output with a particle(Z,A) of energy E stopped inside CsI detector is called CsI calibration.

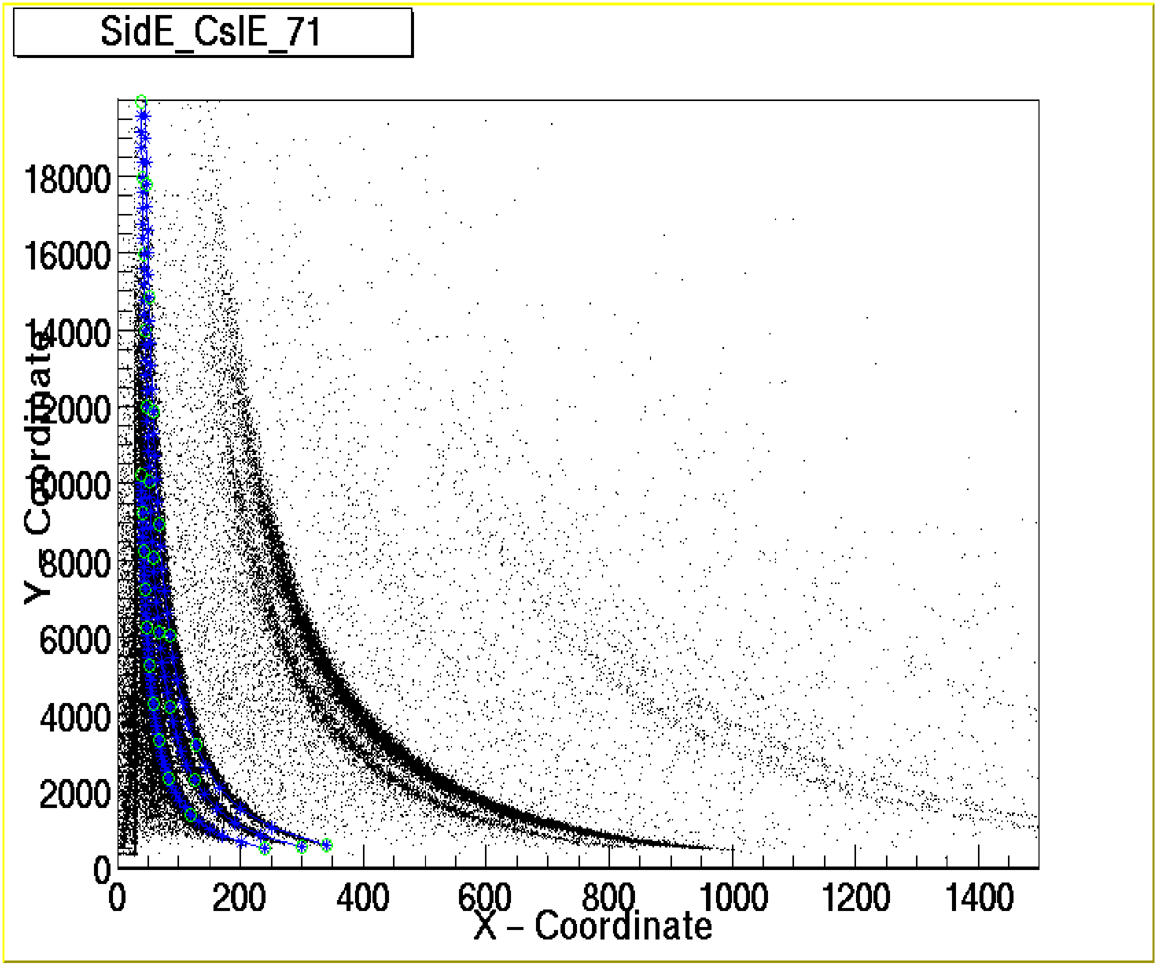

Fig. 20. CsI calibration using CsI verus Si spectrum. X axis is the channel number of Si response. Y axis is the channel number of CsI response.

$$L = a_0 \left\{ E \left[1 - \frac{a_1 A Z^2}{E} \ln \left(1 + \frac{E}{a_1 A Z^2} \right) \right] + c_1 a_1 A Z^2 \ln \left(\frac{E + a_1 Z^2}{a_2 + a_1 A Z^2} \right) \right\} + M \quad (3.2)$$

with

$$\begin{aligned} c_1 &= \frac{a_3}{1+\exp[-(E-a_2)/a_4]}, \\ c_2 &= \frac{a_3}{1+\exp(a_2/a_4)}, \\ M &= -a_0 c_2 a_1 \ln\left(\frac{a_1 A Z^2}{a_1 A Z^2 + a_2}\right). \end{aligned} \tag{3.3}$$

$$\begin{aligned} T_1 &= 1 + \frac{E}{a_1 A Z^2}, \\ T_2 &= \frac{E + a_1 A Z^2}{a_2 + a_1 A Z^2}. \end{aligned} \tag{3.4}$$

when $T_1 > 0$ and $T_2 > 0$,

otherwise $L = 0$.

Here the a0, a1, a2, a3 a4 are parameters to be searched. A is the particle mass number, Z is the particle atomic number. L is the lightout of CsI in channel units and the E is the energy in MeV units. This formula includes a variety of nonlinear response of CsI detectors [14, 34].

ROOT C++ Program [67] routines were used to pick off various channels from isotope lines in raw spectra of the slow component CsI(Tl) versus Silicon signals. The Silicon calibration parameters obtained in the first step were applied to convert the Silicon channels into energy in MeV units. Then, the SRIM energy loss code was used to match the energy loss in the Silicon detector with the energy dumped in the CsI(Tl) detector, which provided the set of channel and energy pairs for the CsI(Tl) as Fig.20 shows two-dimensional correlations of the channels in the Si and CsI detectors in the super telescope modules and the blue points are those selected to make the calibration ,and Fig.21 shows one of typical calibration curve.

The minimization technique in TMinits C++ with ROOT was used again to find the best parameters for the above equations which represent the light output from a CsI(Tl) detector as a function of the energy (E) of the particle. The CsI(Tl) energy spectra produced using those energy calibration procedures were checked with the elastic scattering peaks observed in the p + ^{124}Sn, d + ^{124}Sn, and ^{4}He + ^{124}Sn experiments as a verification of accuracy.

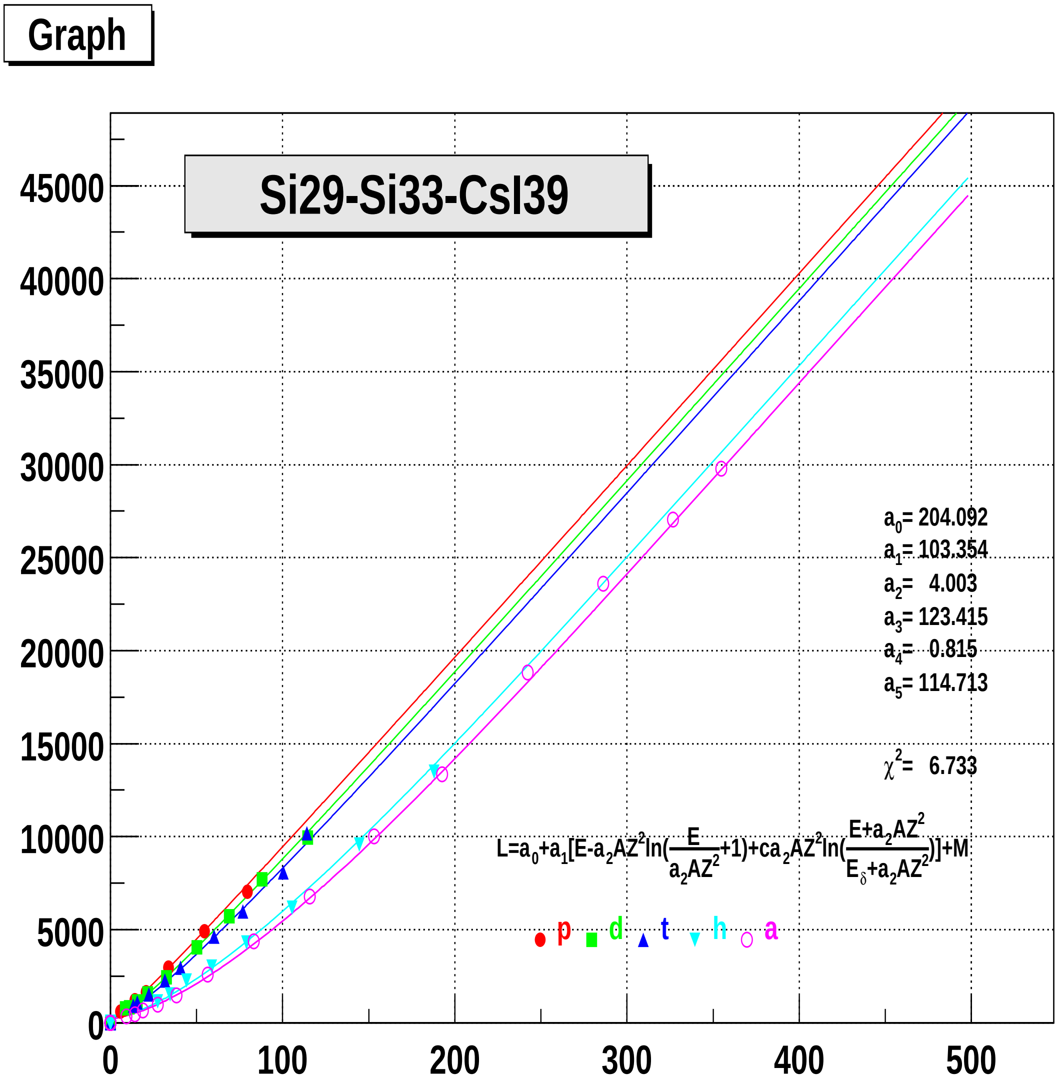

Fig. 21. CsI calibration curve. X axis is energy in MeV. Y axis is the channel number of CsI light output.

C. First Step Energy Spectrum Normalization

In the data analysis procedure, the raw spectra of light particles are generated in the channel units. The gains and thresholds for all of the CsI Detectors in the same ring are slightly different from each other, which makes the raw spectra look different. Assuming cylindrical symmetry, the energy spectra for all of the CsI Detectors in the same ring should be the same. In each ring, the CsI detector in the calibrated super telescope is selected as the standard and reference CsI Detector and the raw spectrum in each CsI Detector was normalized to the reference detector using the following formula:

$$\mathrm{Chan}_{\mathrm{new}} = P_0 + \mathrm{Chan}_{\mathrm{raw}} \times P_1, \tag{3.5}$$

with P_0 is offset, and P_1 is gain.

As a typical result, the raw p, d, t, ^{3}He ,^{4}He spectra of 12 CsI Detectors in Ring3 from reaction system ^{64}Zn +^{112}Sn are plotted in Fig.22-26

The energy spectra with number 2 in red color are reference spectra in reference detectors in Ring3. It is very clear that the spectra look different from each other because of different gain and offset of different CsI detectors. After first normalization of raw spectra in channel units, the new proton spectra of these 12 CsI detectors are shown in from figure 27. It is very clear that all of proton spectra look in the same shape. The same proton normalization factors were then applied to other particles d, t, ^{3}He, and ^{4}He. It is shown that after the proton normalization factors were applied to the other particles, the difference in the given particle spectra became much less , which are indicated in from figure 28 to 31.

D. Second Step Energy Spectrum Normalization

After normalization, the energy spectra in MeV for p, d, t, ^{3}He, and ^{4}He were generated with the first step calibration parameters. The spectrum of the calibrated super telescope in each ring was again chosen to be the standard reference detectors and others were normalized with respect to them using the following formalism

$$E_{\text{new}} = E_0 + E_{\text{raw}} \times P_1 \tag{3.6}$$

with E_0 is an offset, and P_1 is the gain.

The final energy spectra in MeV units show the typical results in Ring3 after the second normalization in MeV units for the reaction system ^{64}Zn $+^{112}$Sn, which will reduce the spectra difference caused by nonlinear responses. The Second normlization table is listed in Table IV, in which p_0, p_1 , d_0 , d_g , t_0 , t_g , h_0 , h_g , a_0 , a_g are offsets and gains of p, d, t, ^{3}He, and ^{4}He respectively. The Fig.32 shows the typical spectra of p after the second normlization, all of which look very simlar. Spectra of d, t, ^{3}He, and ^{4}He after second normlization are attached in Appendix A.

Now each of the light particles in the Ring3 has same shape and we will average all of those spectra to increase statistics to get final angular spectra in MeV.

Table IV. Second normalization factors for Ring3 of reaction system ^{64}Zn + ^{112}Sn.

CsI	p_0	p_1	d_0	d_g	t_0	t_g	h_0	h_g	a_0	a_g
2	0.0	1.0	0.0	1.0	0.0	1.0	0.0	1.0	0.0	1.0
4	0.0	1.0	0.0	1.02	0.0	1.0	-1.0	0.85	0.0	0.98
6	0.0	1.0	-5.0	1.04	0.0	1.0	-12.0	1.0	-3.0	0.985
8	0.0	1.0	4.0	0.90	0.0	0.97	0.0	0.8	-2.5	0.9
10	0.0	1.0	0.0	0.99	3.0	1.0	0.0	1.03	-10.0	1.06
12	0.0	1.0	0.0	1.0	0.0	1.0	-1.0	0.98	0.0	0.96
14	5.0	0.94	-2.0	0.94	-3.0	0.94	-9.0	1.05	0.0	0.95
16	-1.0	1.04	-5.0	1.05	0.0	1.0	-10.0	0.98	0.0	0.99
18	0.0	1.0	-2.0	1.05	0.0	1.0	0.0	0.98	0.0	1.05
20	0.0	1.0	-7.0	1.06	0.0	1.0	0.0	1.0	-3.0	1.06
22	0.0	1.0	3.0	1.01	0.0	1.05	-1.0	0.95	-11.0	1.03
24	0.0	1.0	0.0	0.98	-1.0	0.99	0.0	0.90	0.0	0.93

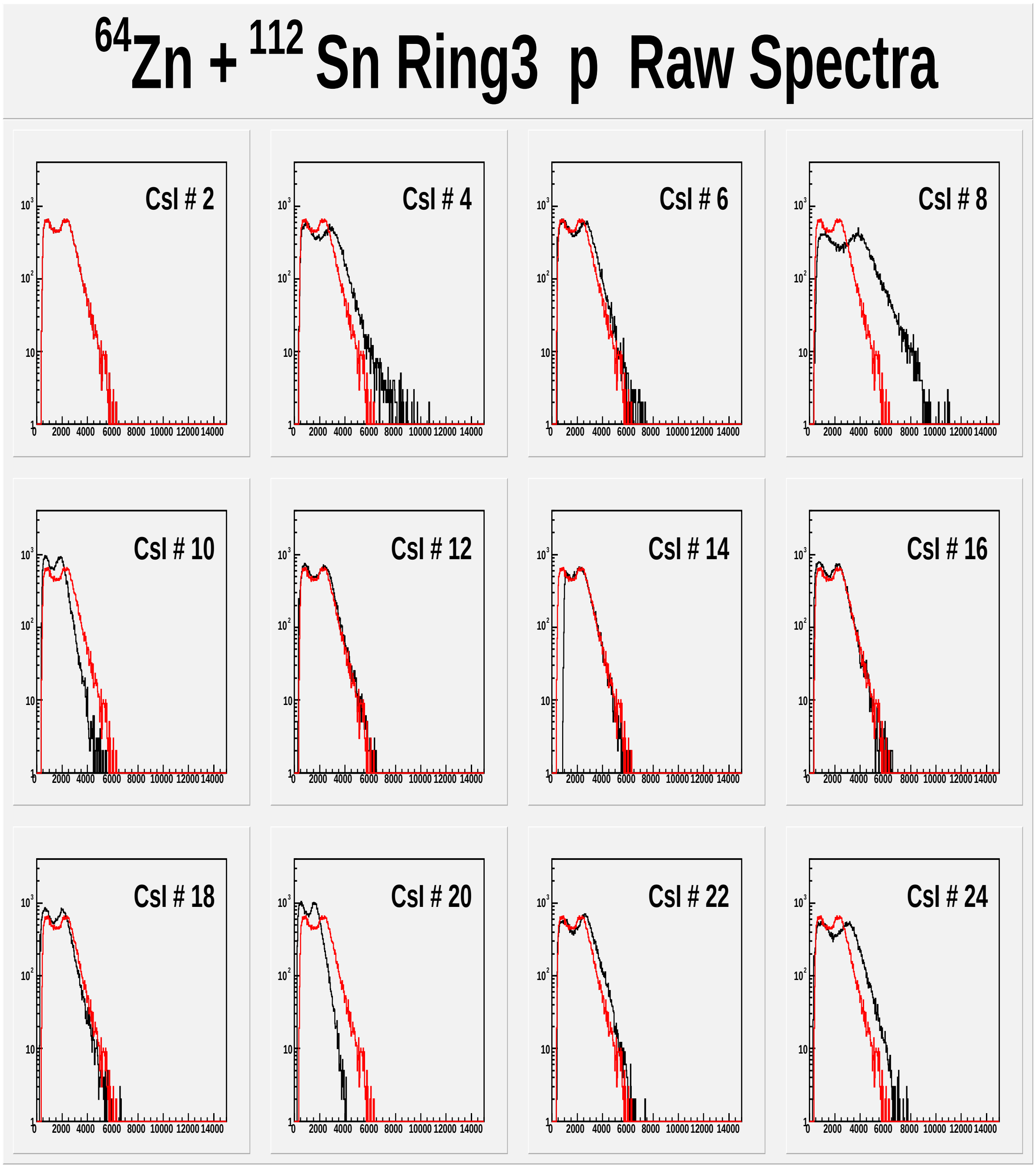

Fig. 22. X axis is energy in channel units. Y axis is the counts in log scale.

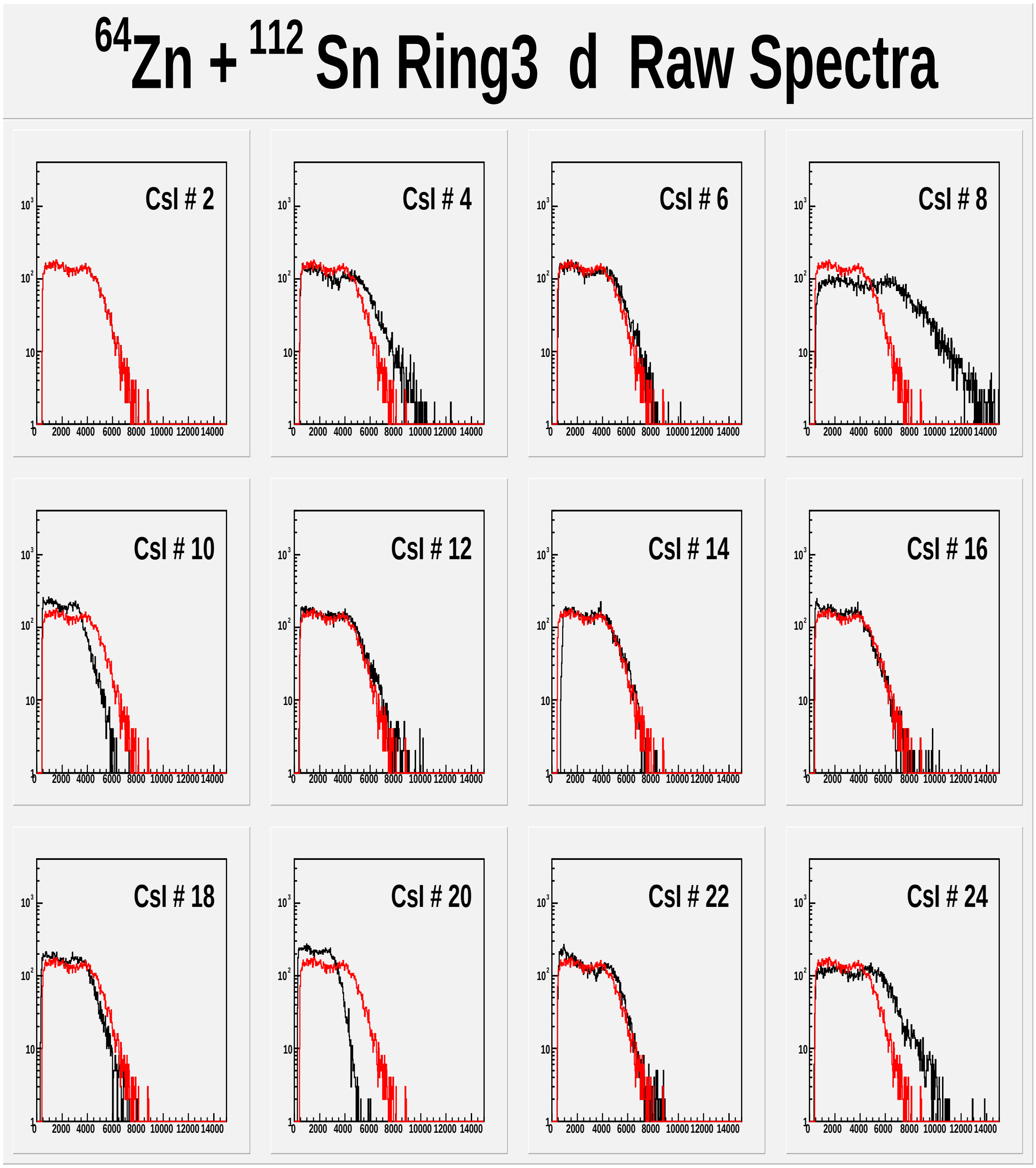

Fig. 23. X axis is energy in channel units. Y axis is the counts in log scale.

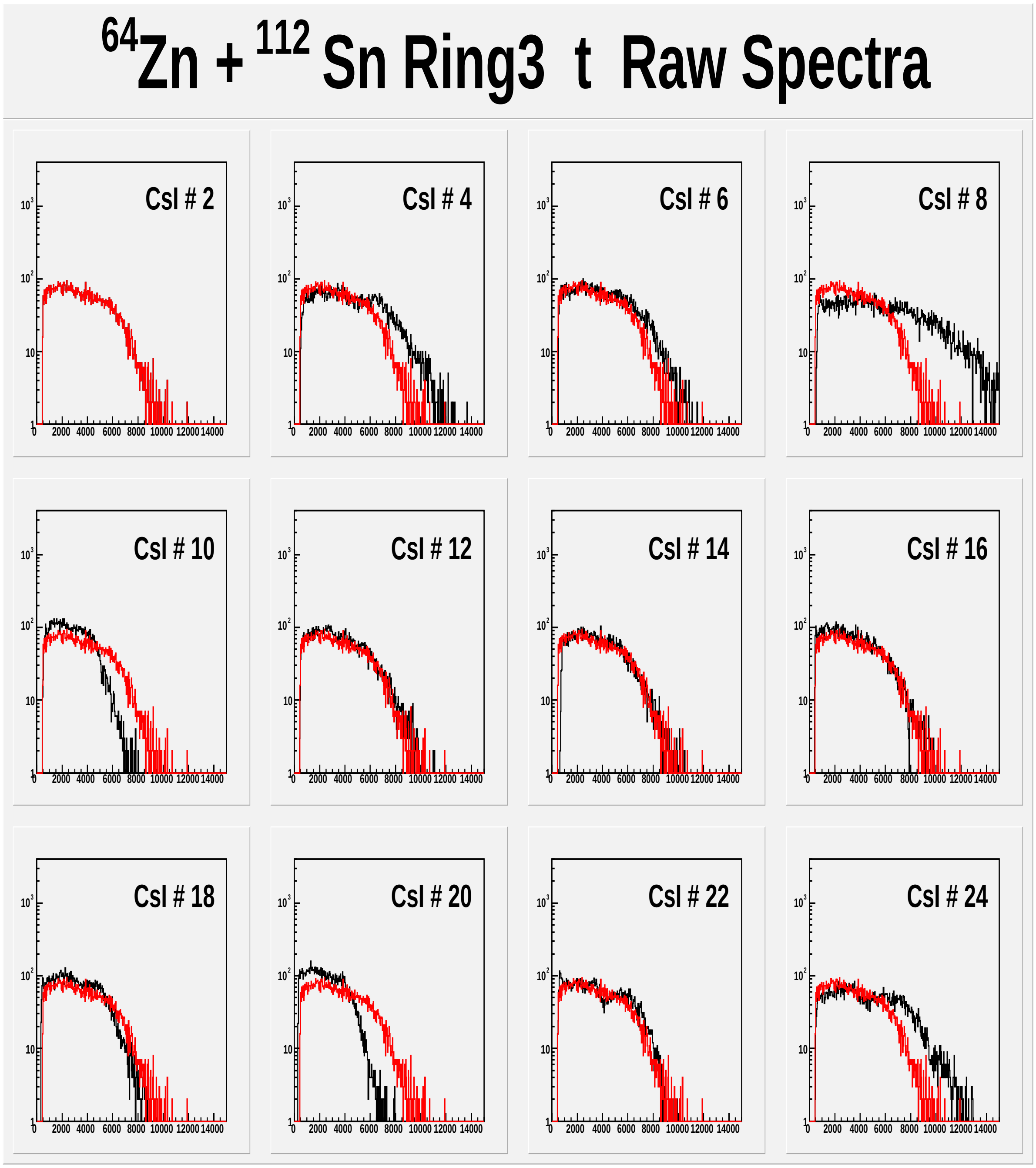

Fig. 24. X axis is energy in channel units. Y axis is the counts in log scale.

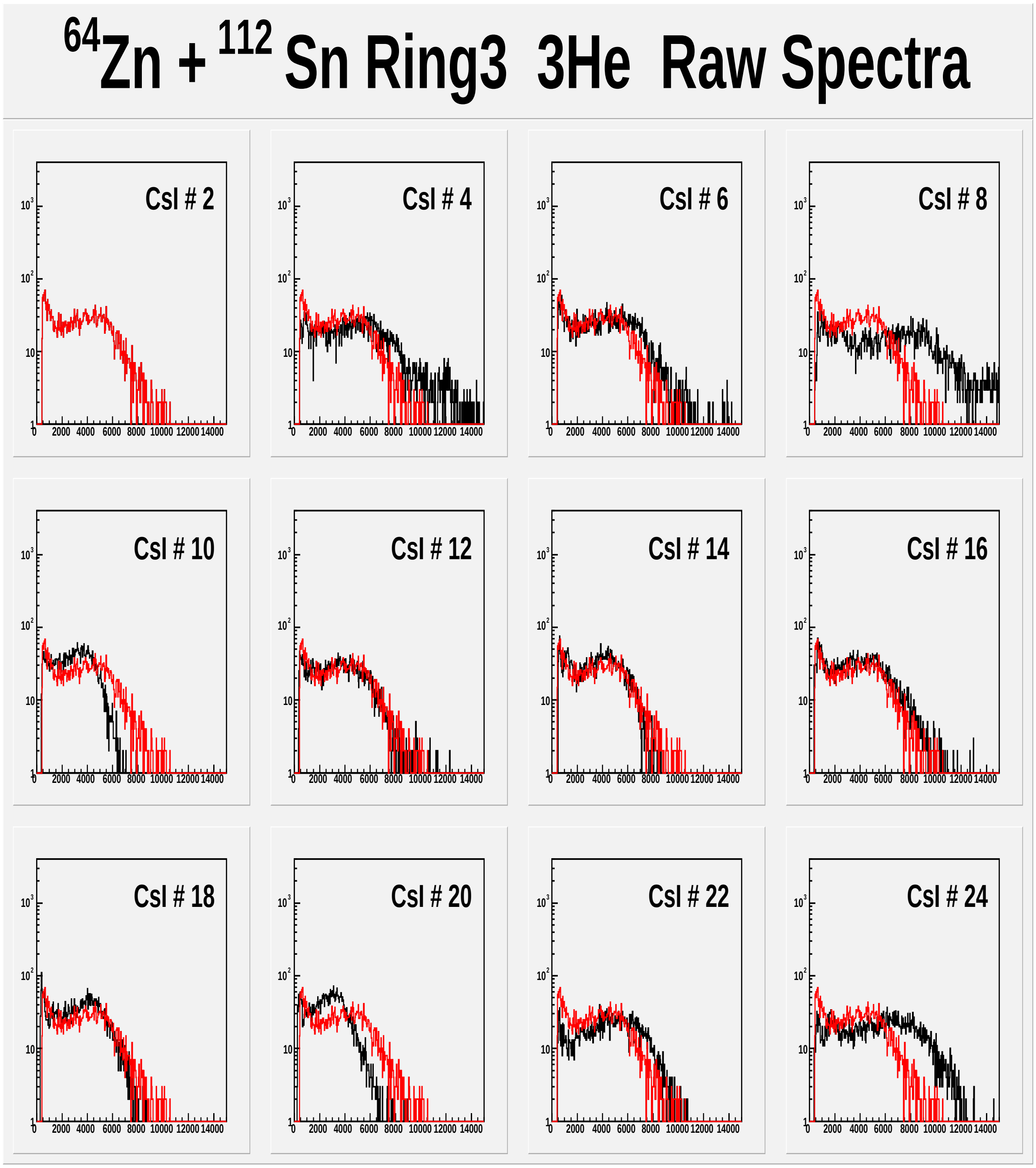

Fig. 25. X axis is energy in channel units. Y axis is the counts in log scale.

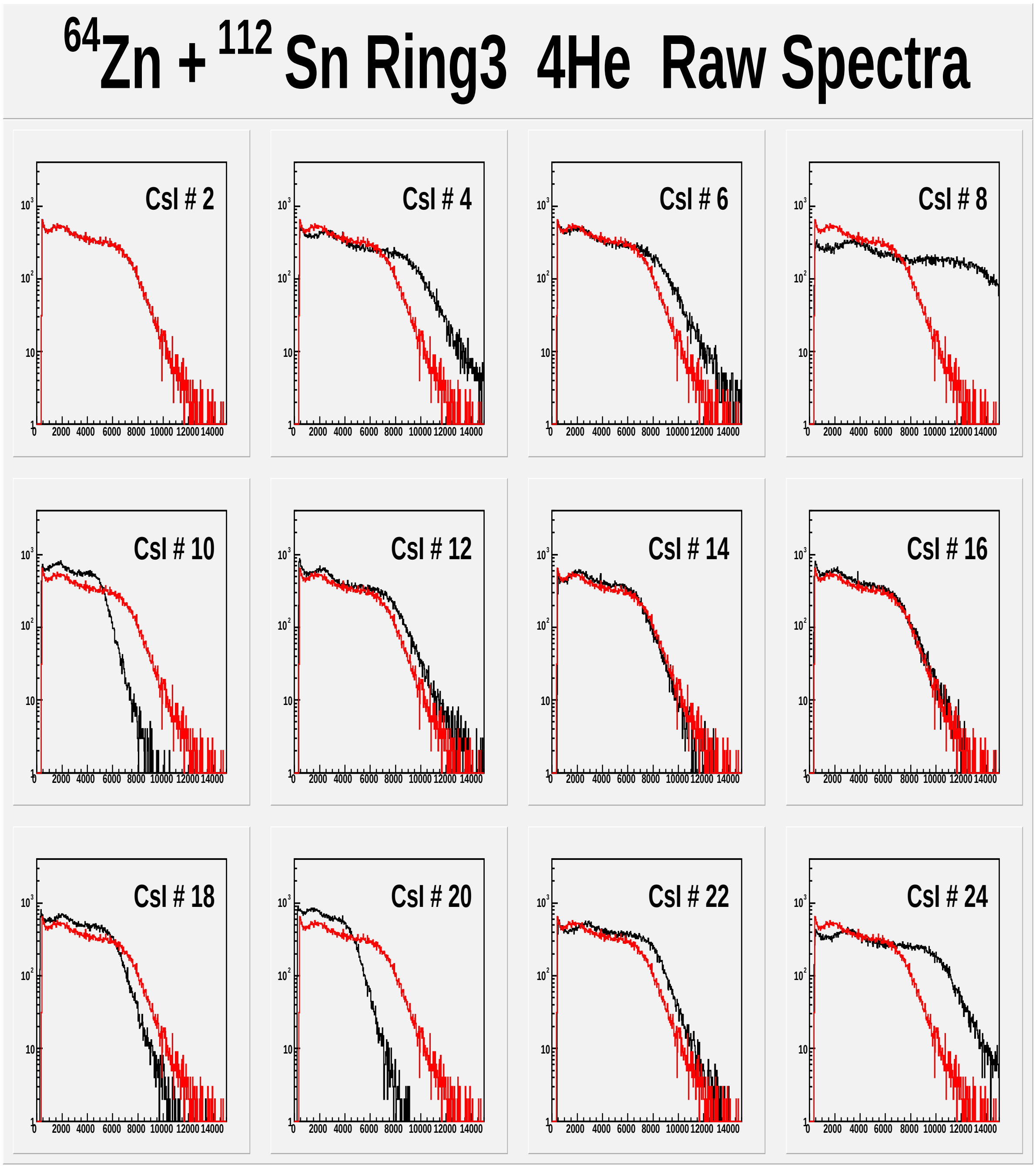

Fig. 26. X axis is energy in channel units. Y axis is the counts in log scale.

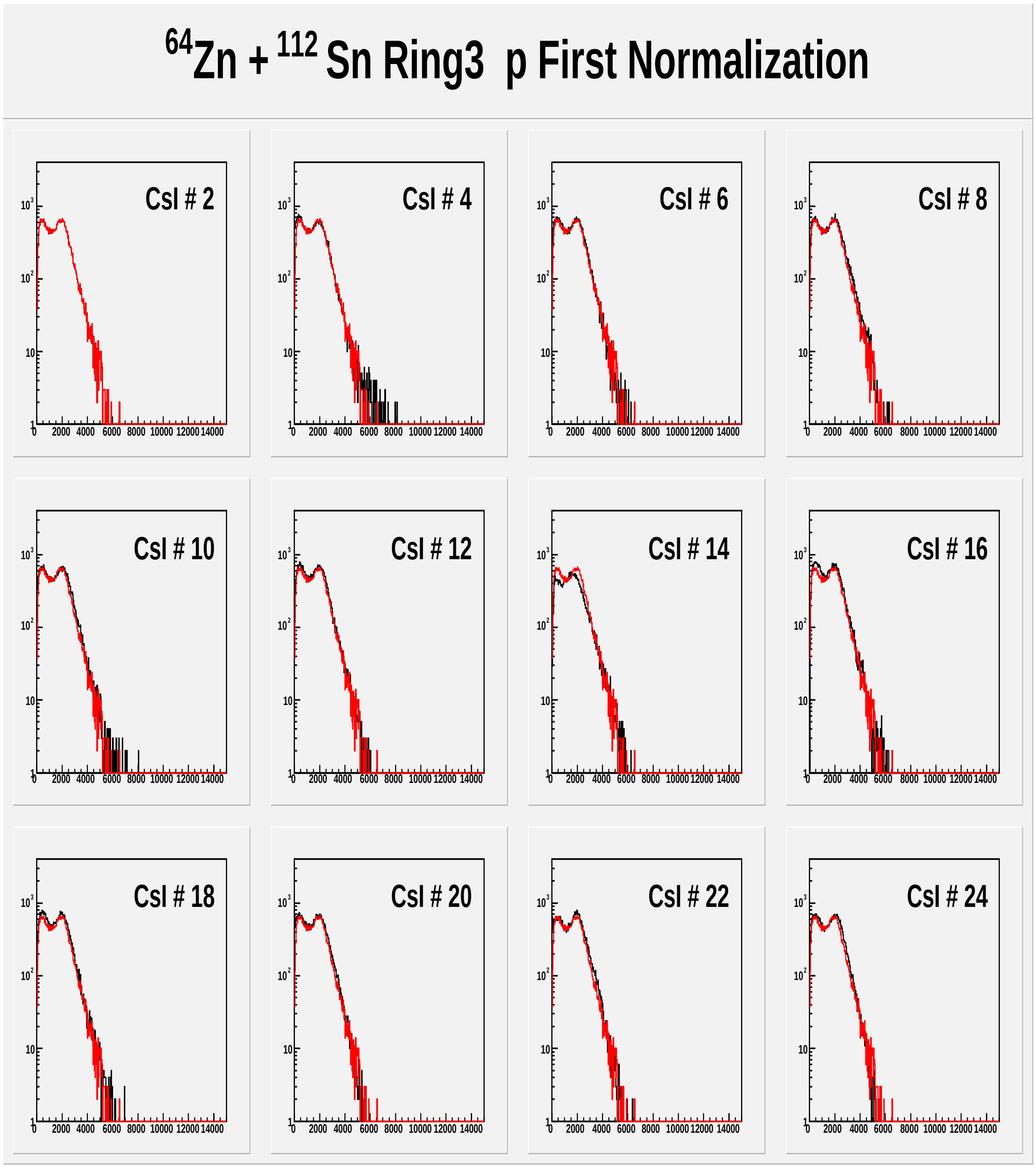

Fig. 27. X axis is energy in channel units. Y axis is the counts in log scale.

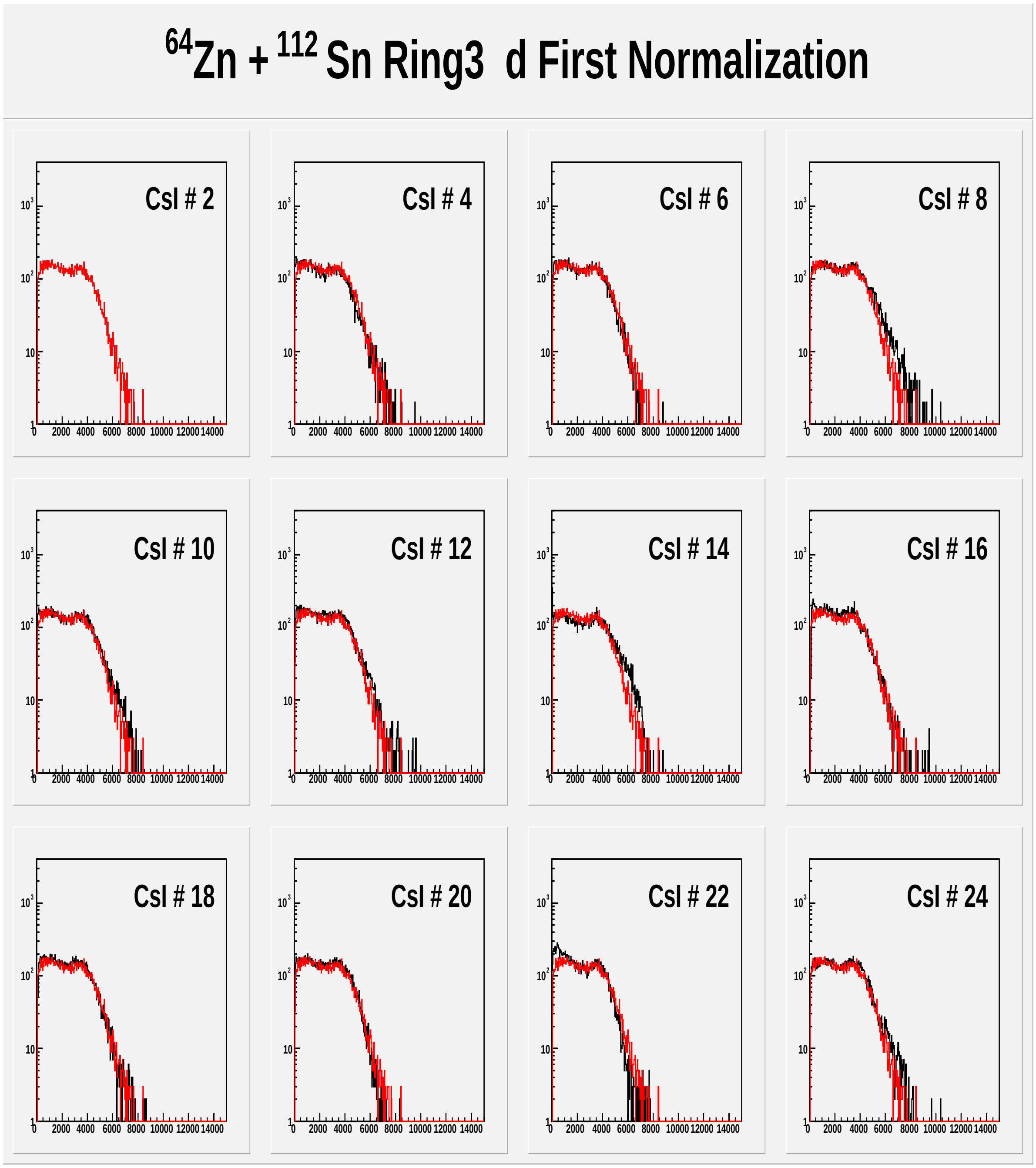

Fig. 28. X axis is energy in channel units. Y axis is the counts in log scale.

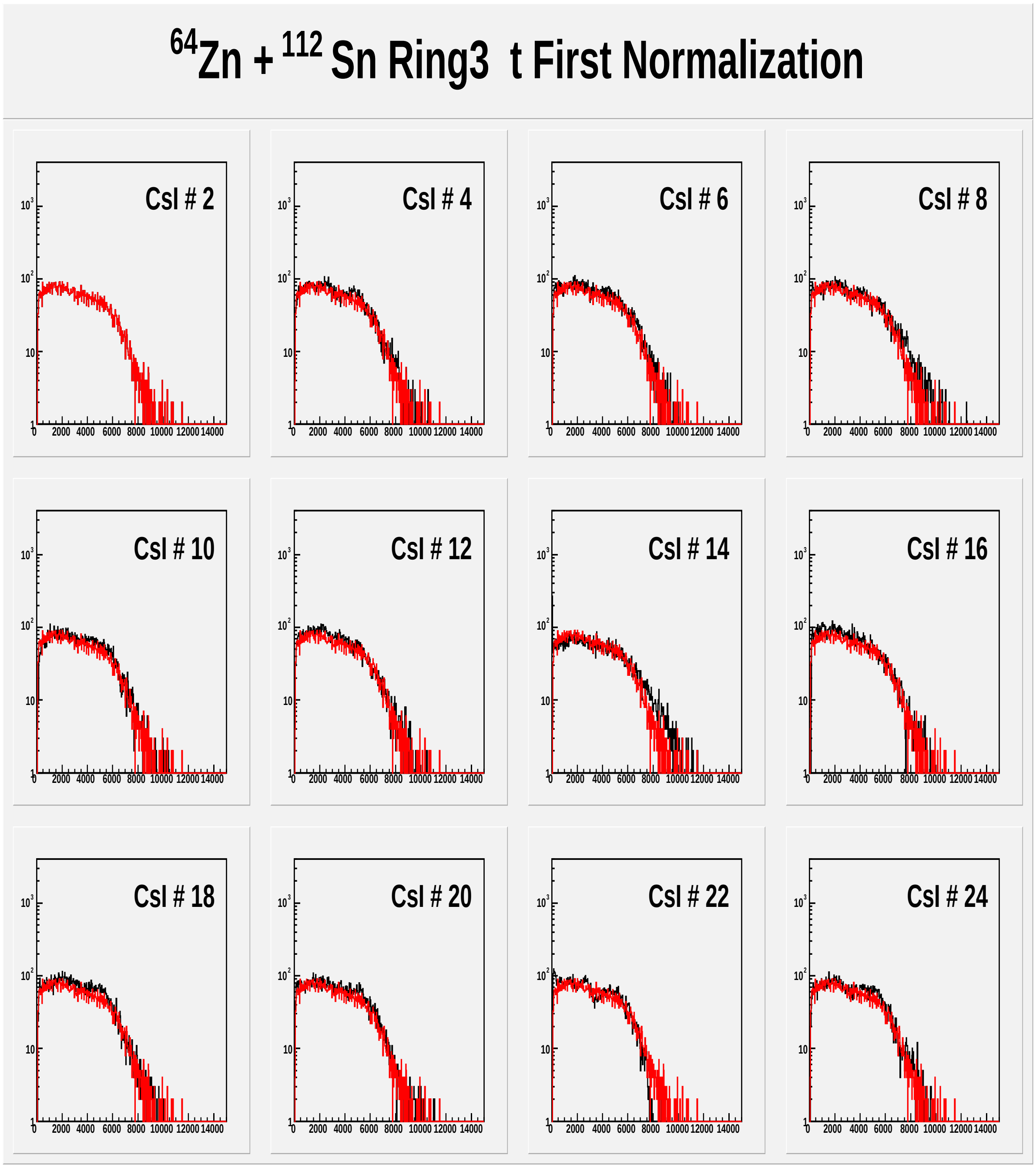

Fig. 29. X axis is energy in channel units. Y axis is the counts in log scale.

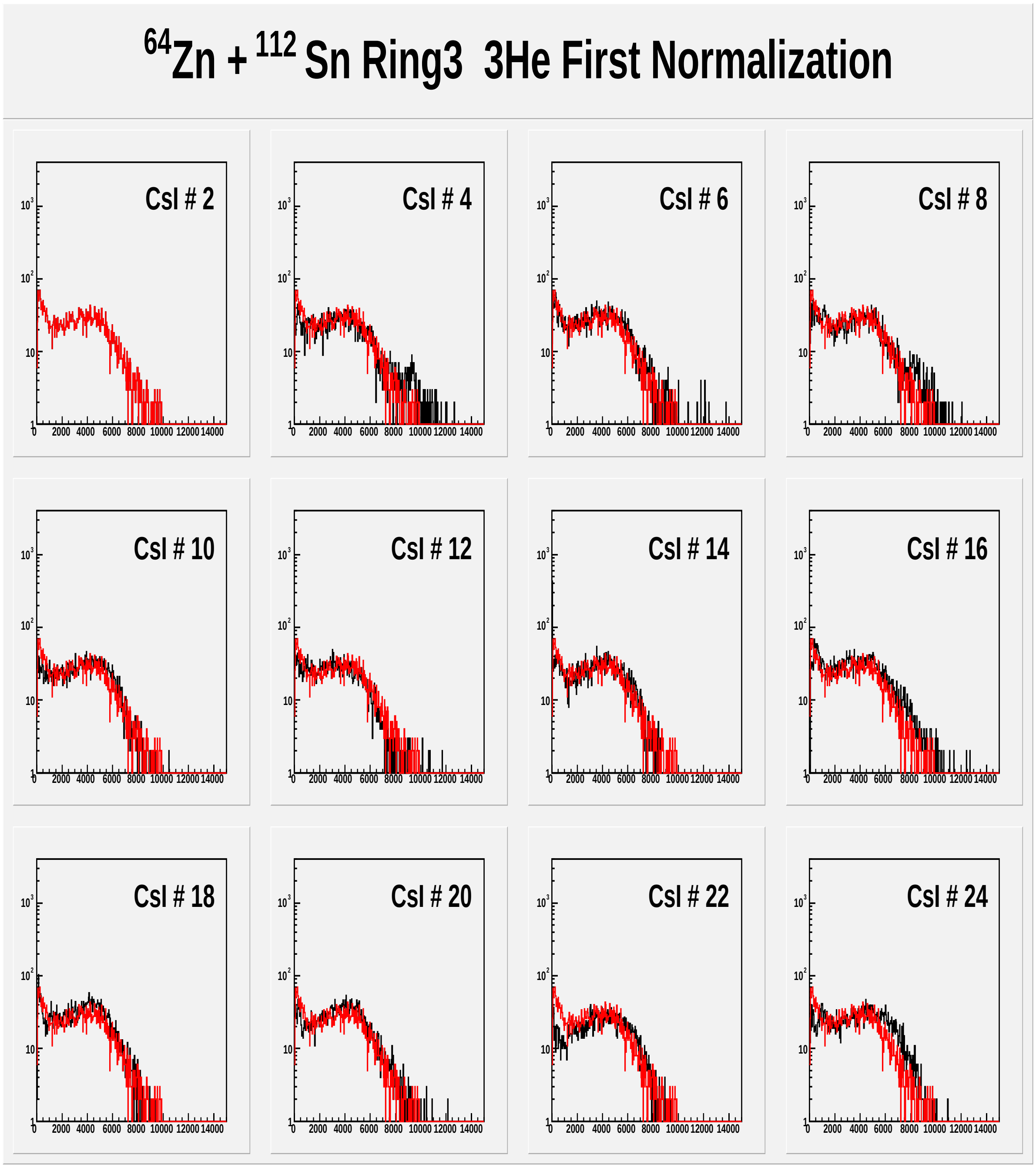

Fig. 30. X axis is energy in channel units. Y axis is the counts in log scale.

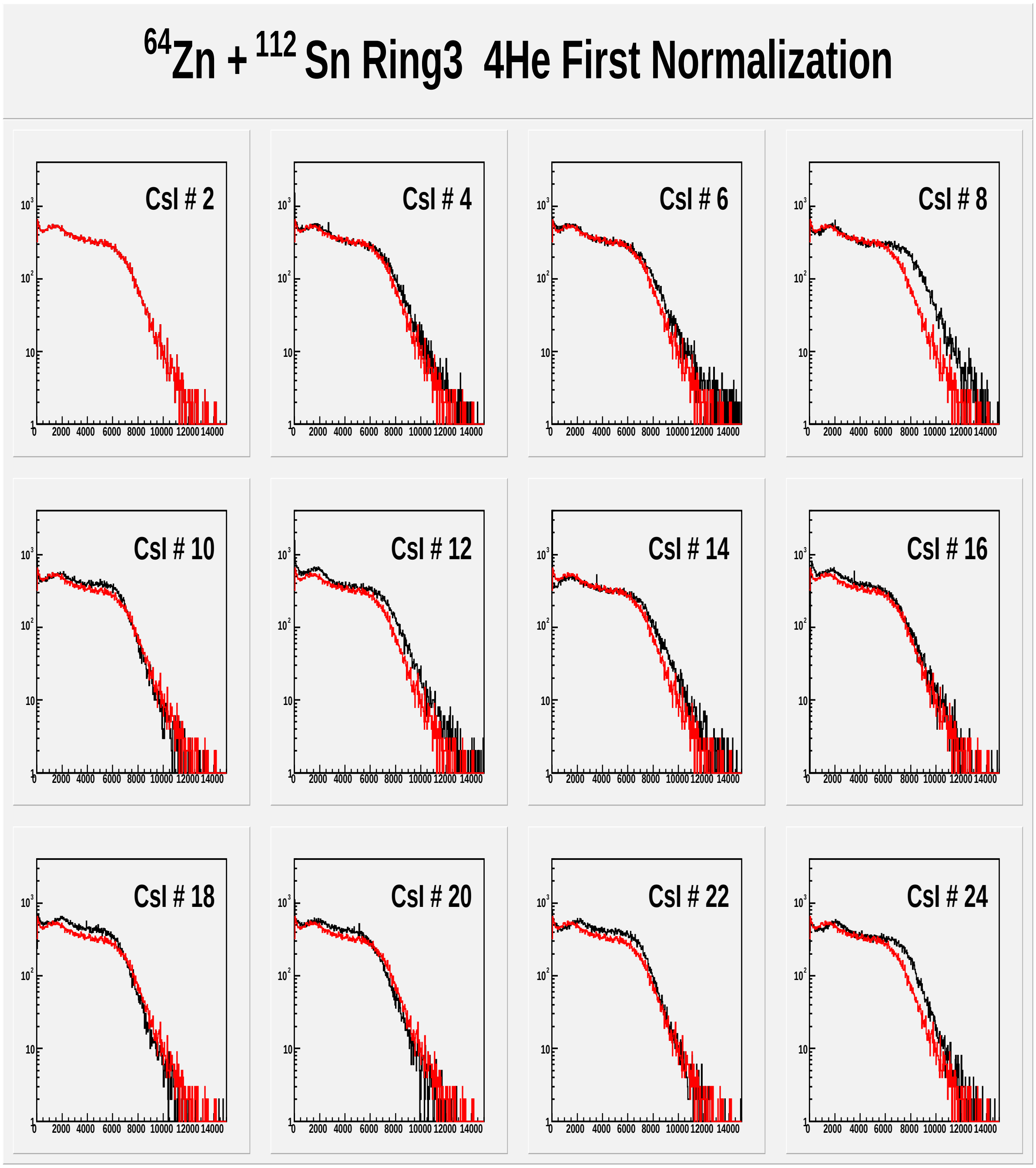

Fig. 31. X axis is energy in channel units. Y axis is the counts in log scale.

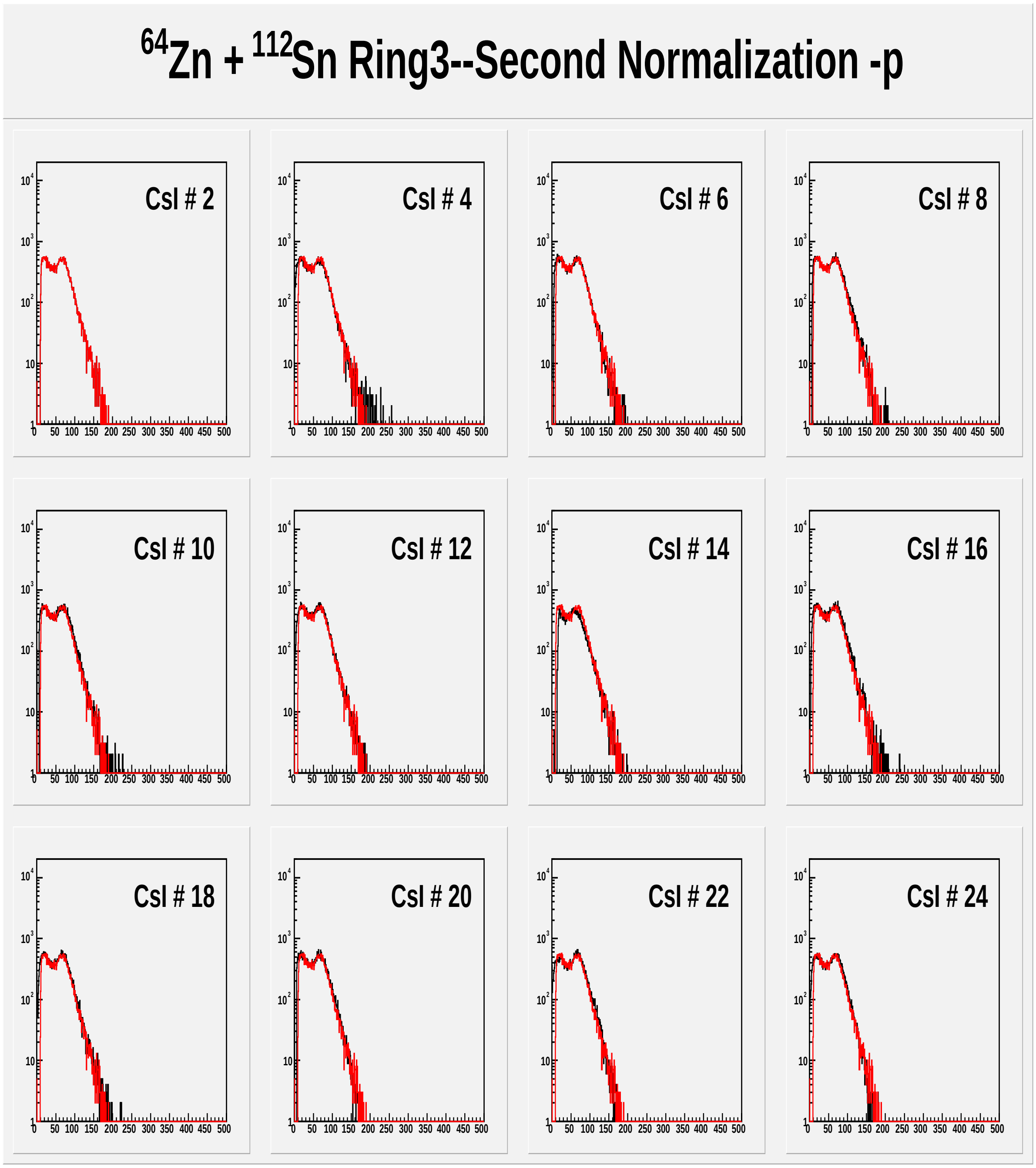

Fig. 32. X axis is energy in MeV. Y axis is the counts in log scale.

CHAPTER IV

EVENT SELECTION

A. Observables to Characterize the Collision Violence

In this dissertation project, the primary analysis efforts have been focused on the most violent collisions which are generally associated with the lowest impact parameters. In previous data analyses, a large number of authors have discussed the merits of different observables to determine collision violence and several physical observables which are sensitive to the collision violence have been proposed for various types of reaction systems [14]. Some studies indicate that determination of violence with two or more observables are more accurate than those relying on a single observable [14]. However, various factors, such as conservation laws of mass, charge and energy can introduce autocorrelations which can distort a sample of events. Therefore special consideration must be taken when choosing more than one observable in order to avoid autocorrelations among those observables.

This chapter first introduces the critera used for event selection in this work. Two dimensional plots of charged particle multiplicity versus neutron multiplicty are generated and discussed. In the last section, a table of multiplicity ranges associated with the collision violence is presented.

In the previous reports on heavy ion reaction systems studied with the NIMROD Detector, two different approaches were chosen with different selection criteria for collision violence. One employs light charged particle multiplicity and transverse energy of light charged particles and the other one uses the multiplicities of light charged particle and neutrons [13]. In the present data analysis, the combined charged particle and neutron multiplicities are used. Extensive studies have indicated that these multiplicities are correlated to both collision violence and impact parameter. In this work, the multiplicity of charged particles is the total number of detected and identified charged particles per event. It includes both the light charged particles with Z $\leq$ 3 and the Intermediate Mass Fragments (IMF) with Z $>$ 3. The per event detected neutron multiplicity is that recorded by the neutron ball in NIMROD.

The two dimensional correlation of charged particle multiplicity vs neutron multiplicity are presented in contour plots of Fig.33 for each system studied. As the mass of the projectile increases from 4 (bottom row of the figure) to 64 (top row of the figure), the energy available in the center of mass and the possible excitation energy deposition increase significantly. This is reflected in progressive increases in both the neutron and charged particle multiplicities.

Typically, increasing charged-particle multiplicity is associated with increasing neutron multiplicity. Although there are significant fluctuations, reflecting both the competition between different decay modes and the neutron detection efficiencies, this correlation provides a reasonable criterion to determine the violence of the collisions. In the low multiplicity region which corresponds to low excitation energies (and generally more peripheral collisions), the charged particle multiplicity changes much more slowly than the neutron multiplicity, presumably because the Coulomb barrier reduces the charged particle emission probabilities at low excitation energies.

While at higher excitations, the Coulomb barrier does not supress the charged particle yields as much. Thus charged particle emission competes more effectively with neutron emission.

The general pattern of neutron and charged particle multiplicities observed in charged particle multiplicity versus neutron multiplicity plots is consistent with the results of calculations using QMD and AMD transport codes[13].

B. Two Dimensional Plots of Charged Particle Multiplicity versus Neutron Multiplicity

The detected particles include p , d ,t, ^{3}He, and ^{4}He and Intermediate Mass Fragments. In our case, event selection will be based upon the sum of neutron and light charged particle multiplicities. We select the most violent events by choosing the 30% of the minimum bias events having the highest total detected ejectile multiplicity. In Fig.34 we show the observed distributions of the total charged particle plus neutron multiplicity distribution from each reaction system studied.

C. Observable Tables to Characterize the Collision Violence

This section list the multiplicity ranges which are actually choosen in our data analysis. The group of events in Bin4 are the most interesting to us on which our data analysis are based . The detail range numbers are listed in Table V.

Table V. Multiplicity ranges of the four bins of collision violence for each reaction system.

Reaction System	Bin4	Bin3	Bin2	Bin1
^{4}He + ^{112}Sn	$M \geq 6$	$4 \leq M < 6$	$2 \leq M < 4$	$0 < M < 2$
^{4}He + ^{124}Sn	$M \geq 7$	$4 \leq M < 7$	$2 \leq M < 4$	$0 < M < 2$
^{10}B + ^{112}Sn	$M \geq 11$	$6 \leq M < 11$	$3 \leq M < 6$	$0 < M < 3$
^{10}B + ^{124}Sn	$M \geq 12$	$6 \leq M < 12$	$2 \leq M < 6$	$0 < M < 2$
^{20}Ne + ^{112}Sn	$M \geq 15$	$8 \leq M < 15$	$3 \leq M < 8$	$0 < M < 3$
^{20}Ne + ^{124}Sn	$M \geq 16$	$7 \leq M < 16$	$3 \leq M < 7$	$0 < M < 3$
^{40}Ar + ^{112}Sn	$M \geq 23$	$19 \leq M < 23$	$14 \leq M < 19$	$0 < M < 14$
^{40}Ar + ^{124}Sn	$M \geq 26$	$21 \leq M < 26$	$16 \leq M < 21$	$0 < M < 16$
^{64}Zn + ^{112}Sn	$M \geq 26$	$17 \leq M < 26$	$3 \leq M < 17$	$0 < M < 3$
^{64}Zn + ^{124}Sn	$M \geq 24$	$10 \leq M < 24$	$3 \leq M < 10$	$0 < M < 3$

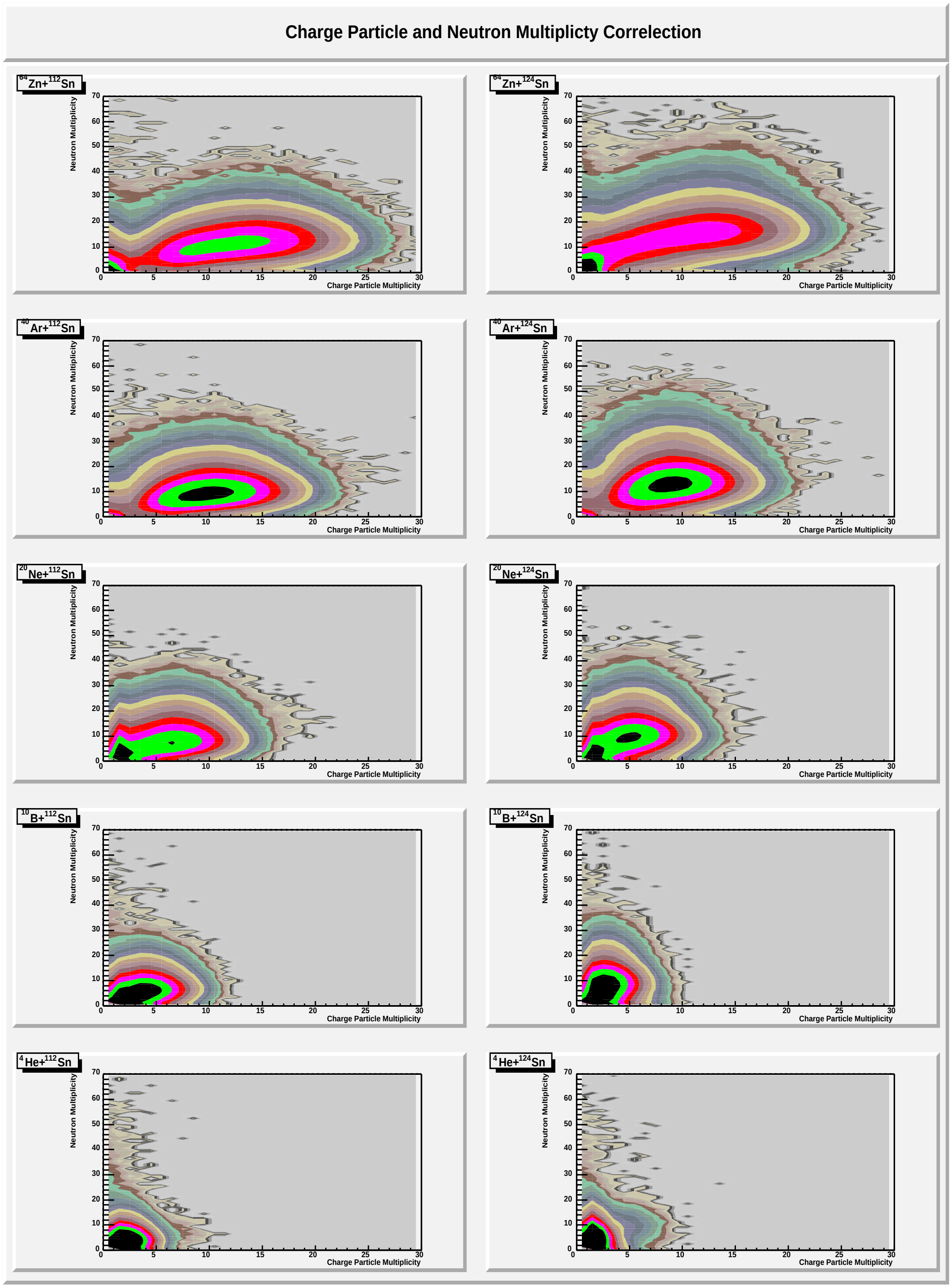

Fig. 33. X axis represents the multiplicity of charged particles(M_{cp}). Y axis represents the multiplicity of Neutron(M_n).

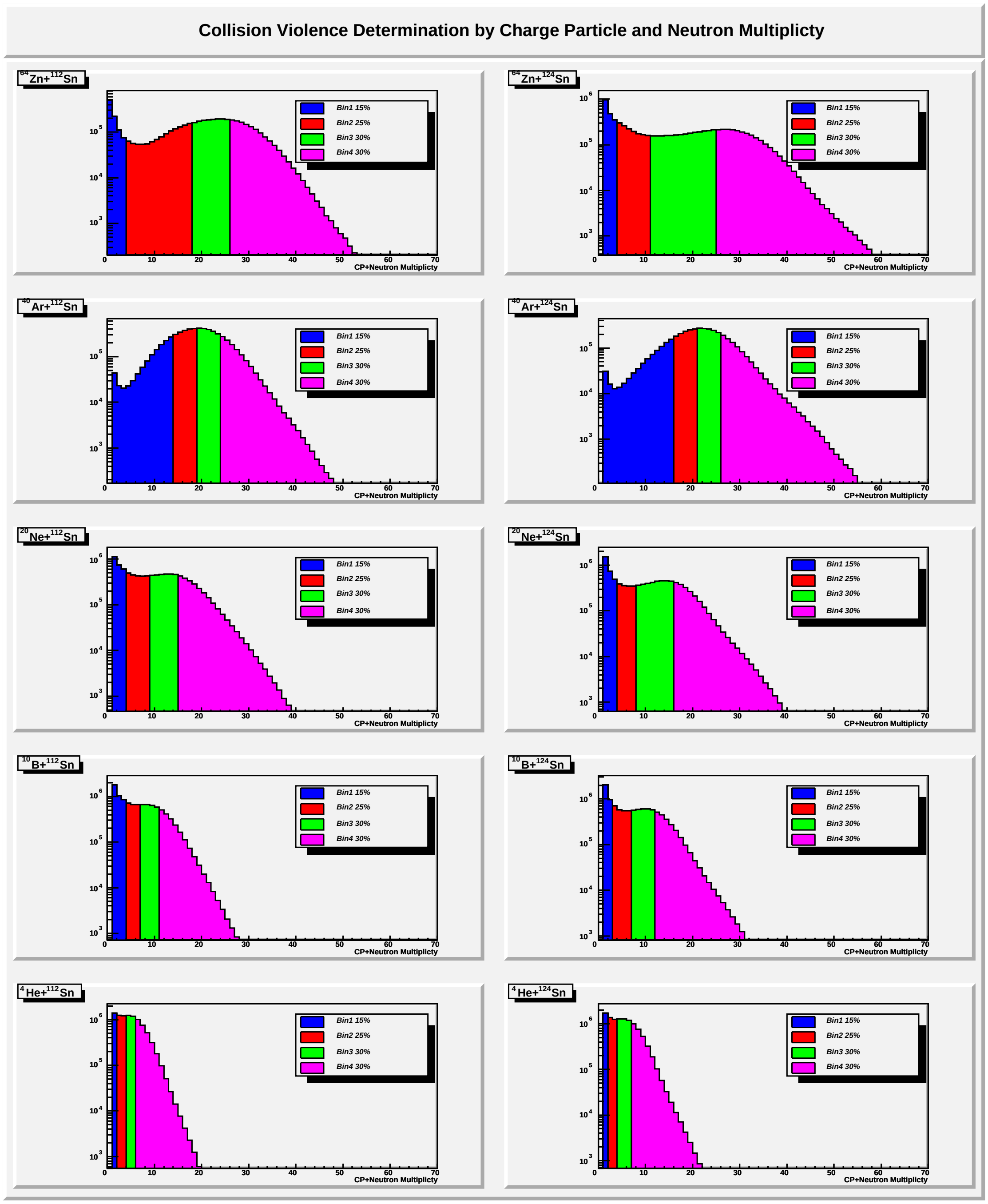

Fig. 34. Sum of neutron and charged particle multiplicty distribution of each reaction system. Bin4 corresponds to the most violent collision events, Bin3 corresponds to the semiviolent events, Bin2 corresponds to the semiperipheral events, and Bin1 corresponds to the peripheral events.

CHAPTER V

ENERGY SPECTRA AND THREE SOURCE FITTING

A. LCP Energy Spectra and Angular Distribution

In this dissertation project, the light charged particle (LCP) emission is the primary probe to follow the dynamic and thermal evolution of the system [13, 14]. We first present angular distributions of the observed particle energy spectra for the five systems studied. The angles and solid angles determined by the sizes and geometrical arrangement of NIMROD's rings are presented in tables VI and VII.

The differential angular distributions of the particle multiplicity, $dM^2/dEd\Omega$, are generated in order of decreasing collision violence, from the most violent (Bin4) to the least violent (Bin1).

The peaks in the Alpha particle spectra in Bin4 from the ^{4}He + ^{124}Sn as Fig.35 is generated by the elastic scattering of alpha projectiles at forward angles. The bumps in the Alpha partilce spectra in Bin4 from ^{10}B+^{124}Sn in Fig.36, and ^{20}Ne+^{124}Sn in Fig.37 reflect the alpha cluster structure of projectiles which were reported in many papers. Fig.38 and Fig.39 represent the light particle spectra of systems ^{40}Ar+^{124}Sn and ^{64}Zn+^{124}Sn respectively. The proton spectra in the backward angle (Ring 11, Ring 12, Ring 13) in Bin4 from all of the reaction systems have cut off because those CsI detectors are thinner and proton particles punch through at energies around 50 MeV.

For the full list of all spectra in window Bin4, Bin3, Bin2, Bin1, they are attached in Appendix B, C, D, E, respectively.

From Ring2 to Ring13, the multiplicities of all the light particles progressively decrease except for the ^{4}He+^{124}Sn and ^{4}He+^{112}Sn because the electronics of the forward

Table VI. Angle parameters in very forward NIMROD rings.

RingId	2	3	4	5	6	7
θ	4.3	6.41	9.43	12.93	18.15	24.45
$d\Omega$	9.56×10^{-4}	2.67×10^{-3}	4.26×10^{-3}	7.99×10^{-3}	1.61×10^{-2}	1.27×10^{-2}

Table VII. Angle parameters in forward and backward NIMROD rings.

RingId	8	9	10	11	12	13
θ	32.08	40.39	61.17	90.0	120.0	152.5
dΩ	3.36×10^{-2}	2.76×10^{-2}	1.54×10^{-1}	2.07×10^{-1}	3.78×10^{-1}	2.41×10^{-1}

rings had some problems during the experimental runs.

For the most violent collision events, the light particle emssion increases as the projectile mass increases. This increase is consistent with the results of the transport code calculations.

Even though the mass numbers, charge numbers and deposited excitation energies differ significantly among these reaction systems similar spectral patterns are observed, particularly for the higher energy particles. This strongly suggests a similar mechanism of emission for those particles, presumably indicating the similar source contribution of light particle emission.

B. Global Three Source Fitting

A widely used technique to characterize light particle emission in this energy range has been to fit the observed spectra assuming contributions from three emitting sources, a projectile-like fragment (PLF) source, an intermediate velocity (NN) source, and a target like fragment (TLF) source [13, 14]. We follow the same procedure in our initial analyses. However, given the continuous dynamic evolution of the system, source fits should be considered as providing a rough schematic picture of the emission process [13].

We will try to use them to estimate the multiplicities and energy emission at each stage of the reaction. In this analysis the source velocities, emission barriers, temperatures, and particle multiplicities for the three different sources are searched for [12]. The individual formulas for the source fitting are

$$\textbf{TLF}: \quad \frac{d^2N}{dE_{lab}d\Omega_{lab}} = \frac{M_{source}N_{tag}}{4\pi T_{source}^2}E''\sqrt{E_{lab}/E'}e^{-E''/T_{source}} \tag{5.1}$$

with

$$\begin{aligned} E' &= E_{lab} - 2\sqrt{E_{lab}\frac{1}{2}m_{LCP}v_{source}^2}\cos(\theta) + \frac{1}{2}m_{LCP}v_{source}^2 \\ E'' &= E' - V_{source} \end{aligned}$$

Here $\mathrm{N_{tag}}$ is the number of observed LCPs, $\mathrm{M_{source}}$ is the multiplicity associated to the source, $\mathrm{T_{source}}$ is the temperature and $\mathrm{V_{source}}$ is the Coulomb barriers. $\mathrm{v_{source}}$ is the magnitude of the source velocity in the direction of the beam. θ is the angle from the source direction to the detected LCP [12].

$$\mathbf{NN}: \quad \frac{d^2N}{dE_{lab}d\Omega_{lab}} = \frac{M_{source}N_{tag}}{2(\pi T_{source})^{3/2}}\sqrt{E'}e^{-E''/T_{source}} \tag{5.2}$$

$$\mathbf{PLF}: \quad \frac{d^2N}{dE_{lab}d\Omega_{lab}} = \frac{M_{source}N_{tag}}{4\pi T_{source}^2}\sqrt{E'E''}e^{-E''/T_{source}} \tag{5.3}$$

with

$$\begin{aligned} E' &= E_{lab} - V_{source} \\ E'' &= E' - 2\sqrt{E'\frac{1}{2}m_{LCP}v_{source}^2}\cos(\theta) + \frac{1}{2}m_{LCP}v_{source}^2. \end{aligned} \tag{5.4}$$

Certainly, to depict the time evolution of the system in more detail a more sophisticated analysis of the particle emission is necessary. As an example, the Fig.40 - 44 indicate the p, d, t,^{3}He, ^{4}He energy spectra from the reaction system ^{40}Ar+^{112}Sn. All of the values of fitted parameters are indicated in the spectra.

In the fitting process, which assumes isotopic emission and a Maxwellian spectral shape in the particular source frame considered, accounting for forward emitted particles with projectile like velocities, requires a PLF source. For the violent collisions, we consider these particles to be of pre-equilibrium emission origin and not evaporated from a fragment.

Even though the system evolves in a continuous fashion, such source fits provide a useful schematic picture of the emission process. From the fits, we obtained parameters describing the ejectile spectra and multiplicities that can be associated to the three different sources. As in the earlier works, the NN source is found to have a source velocity very close to half of that of the projectile reflecting the initial decoupling of the momentum sphere of the participant matter from that of the remaining nucleons. This important feature of the dynamically evolving system manifests itself as kinematic differences between the early emitted light (gas) ejectiles and the remaining (liquid) matter (TLF). As the system relaxes toward equilibrium the two momentum spheres become more and more similar. Eventually the distinction is lost. The source fitting has been done for the four different windows on violence of the collision. The full list of source fitting spectra from different systems are listed in Appendix F, G, H, I, and J, in which all of source parameteres, i.e. multiplicity (M), temperature (T MeV), Coulomb barrier (E_L MeV) and source velocity (V_S cm/ns), are indicated in the spectra. One typical set of result of the extracted parameters are listed in Table VIII. We emphasize that for the later analysis the primary event selection is on the most violent and presumably more central collisions.

Table VIII. Typical results of multiplicity (M) temperature (T MeV) Coulomb barrier (E_L MeV) and source velocity (V_S cm/ns).

System	Particle	Parameter	Bin4		
			TLF	NN	PLF
^{64}Zn + ^{112}Sn	p	M	0.691	4.398	0.6040
		T	3.97	13.8440	4.0000
		E_L	3.997	1.0010	2.0010
		V_S	0.398	5.4130	9.8860
	d	M	0.3640	2.0750	0.3406
		T	4.2520	18.1390	5.3920
		E_L	0.001	5.0021	12.0000
		V_S	0.001	4.6330	8.8600
	t	M	0.1001	1.0620	0.2738
		T	5.0930	19.5100	7.7540
		E_L	3.2050	2.3800	12.0000
		V_S	0.6360	4.4400	8.3170
	^{3}He	M	0.0725	0.3957	0.2606
		T	4.4080	25.0000	10.8400
		E_L	3.4950	2.3260	12.0000
		V_S	2.0010	3.9190	8.7400
	^{4}He	M	2.7050	2.0090	1.3980
		T	7.4560	12.9510	7.9460
		E_L	0.0010	11.00	4.00
		V_S	1.5120	4.7150	8.1930

Table VIII Continued

System	Particle	Parameter	Bin4		
			NN	PLF	TLF
^{64}Zn + ^{124}Sn	p	M	0.6074	2.9020	0.5102
		T	5.00	12.87	4.00
		E_L	1.430	4.5	2.0
		V_S	0.001	5.594	9.73
	d	M	0.4159	1.783	0.3473
		T	4.839	18.846	5.646
		E_L	0.001	3.998	11.557
		V_S	0.035	4.627	8.756
	t	M	0.1980	1.137	0.2676
		T	5.610	19.165	7.586
		E_L	3.027	2.238	0.001
		V_S	0.675	4.589	8.881
	^{3}He	M	0.05173	0.2797	0.1890
		T	3.481	23.383	9.863
		E_L	2.831	2.002	12.00
		V_S	1.856	4.610	8.783
	^{4}He	M	2.129	1.632	1.495
		T	7.110	13.158	8.857
		E_L	0.001	11.00	4.001
		V_S	1.396	4.351	8.042

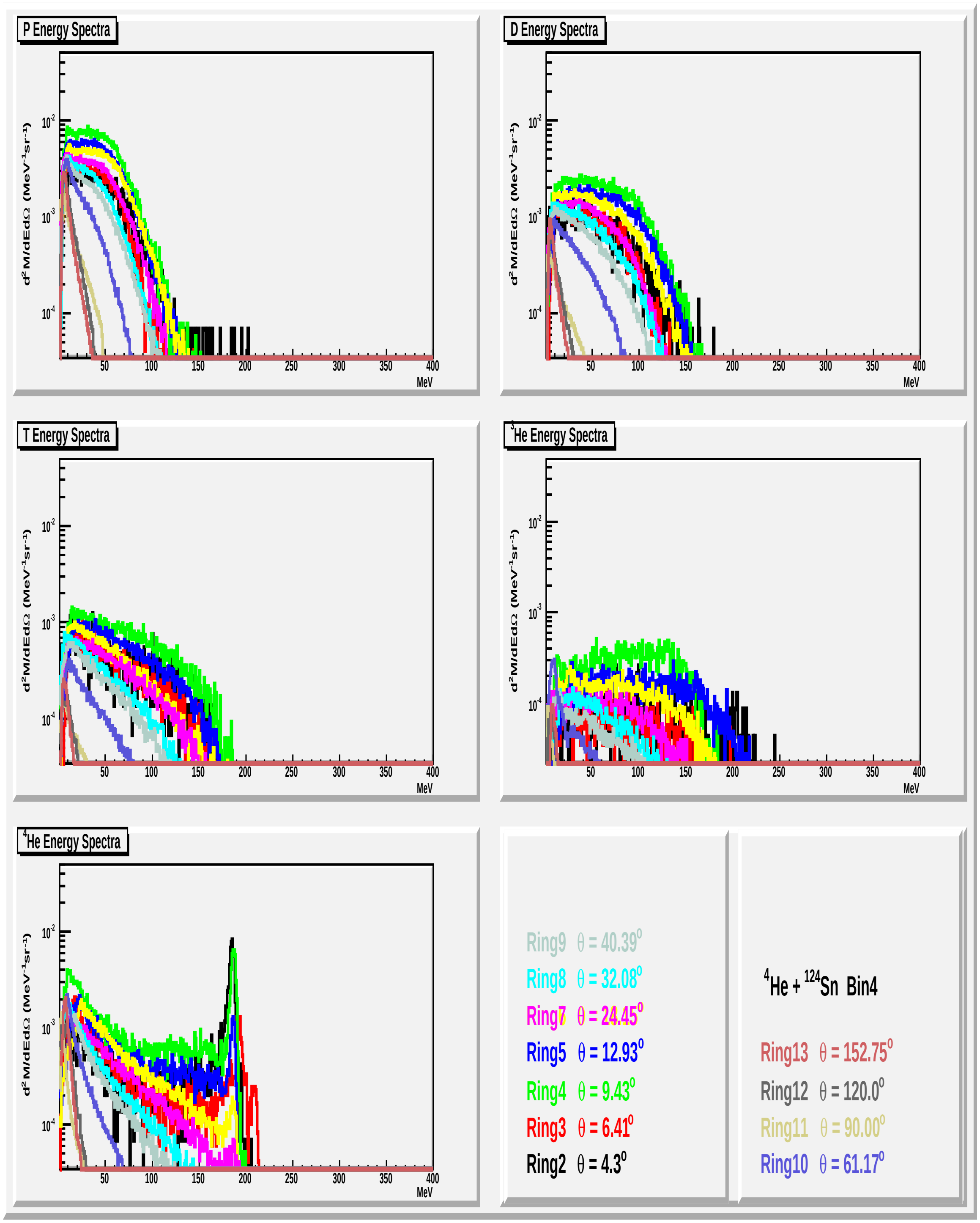

Fig. 35. X axis is energy in MeV. Y axis is the multiplicity distribution

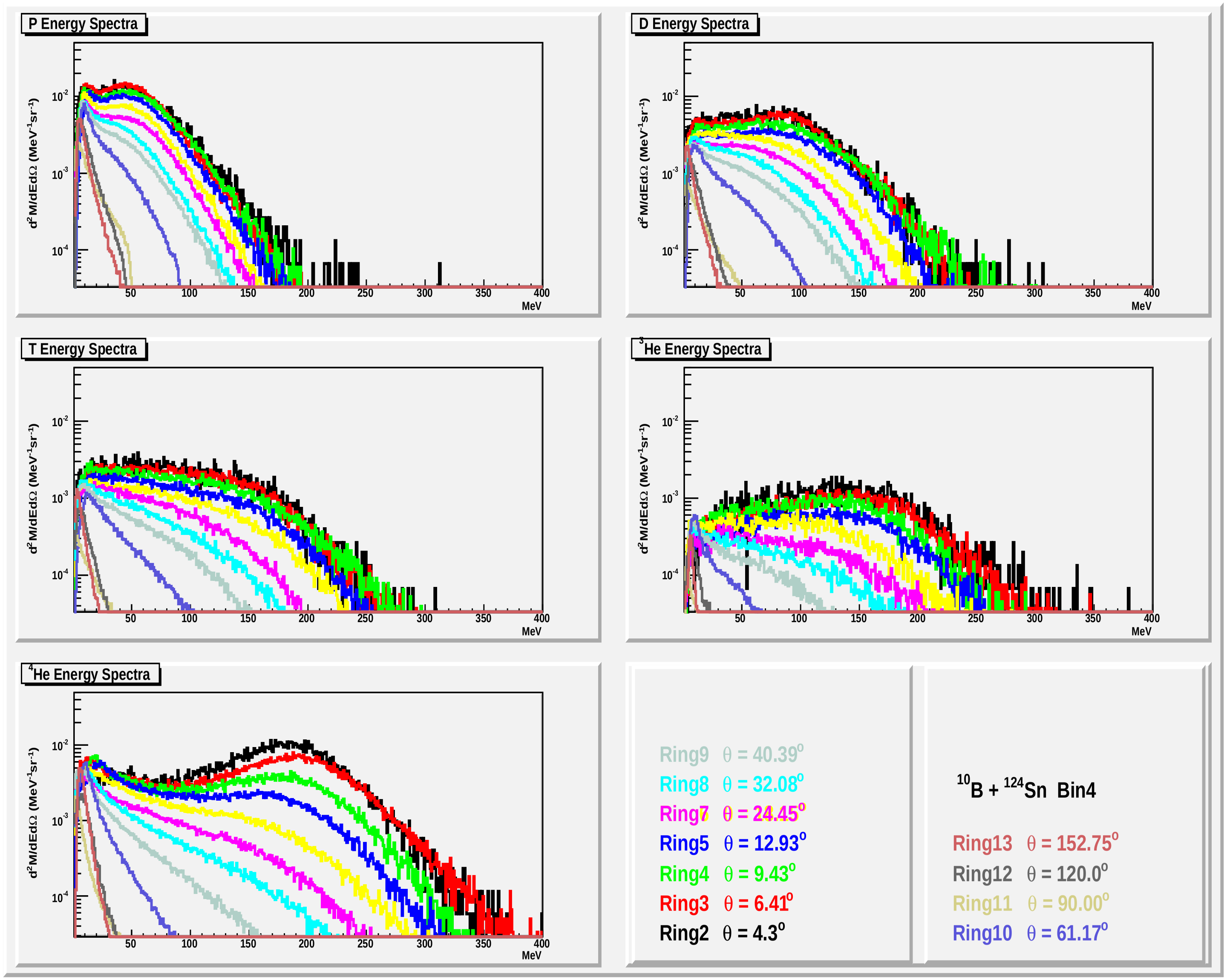

Fig. 36. X axis is energy in MeV. Y axis is multiplicity distribution

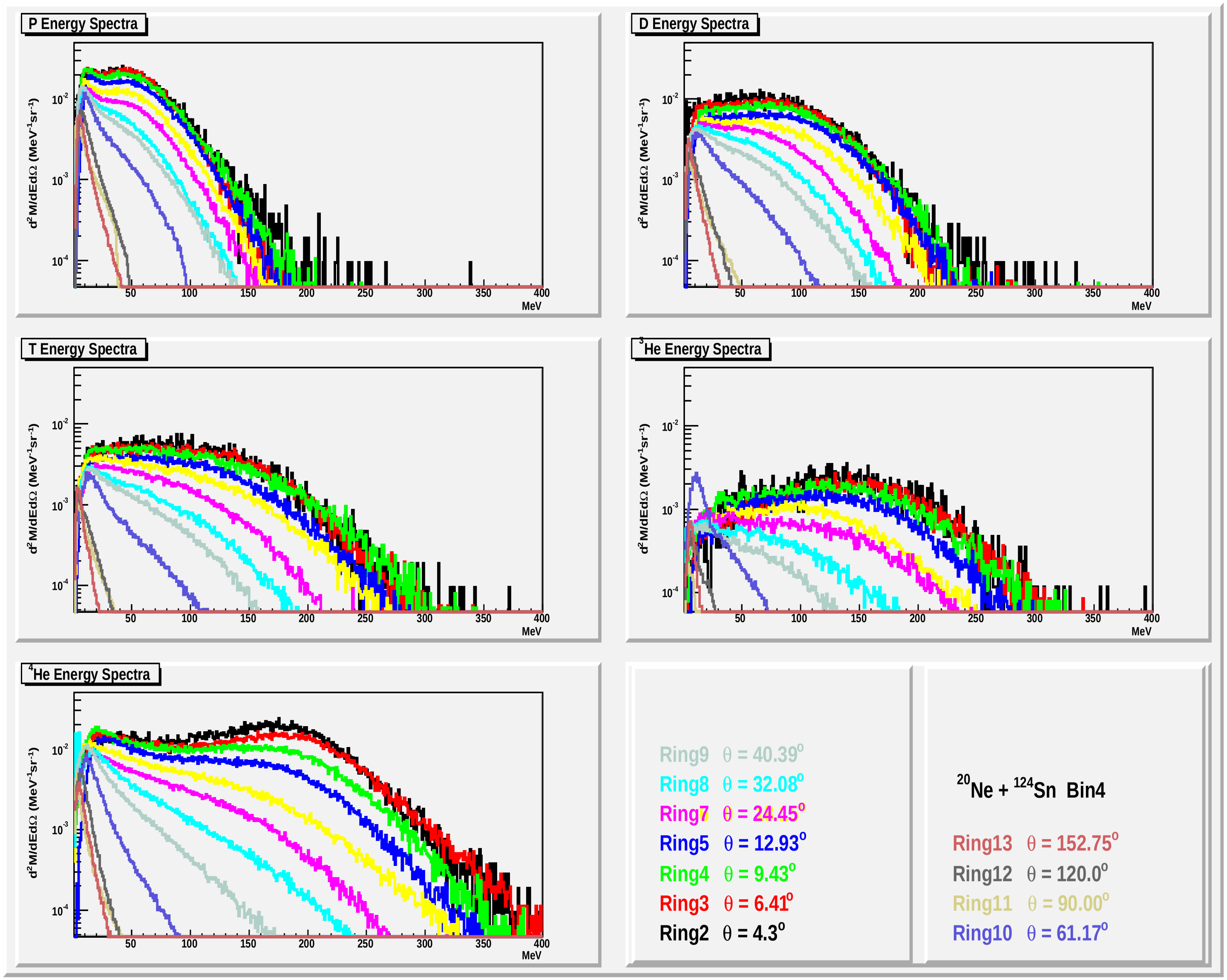

Fig. 37. X axis is energy in MeV. Y axis is multiplicity distribution

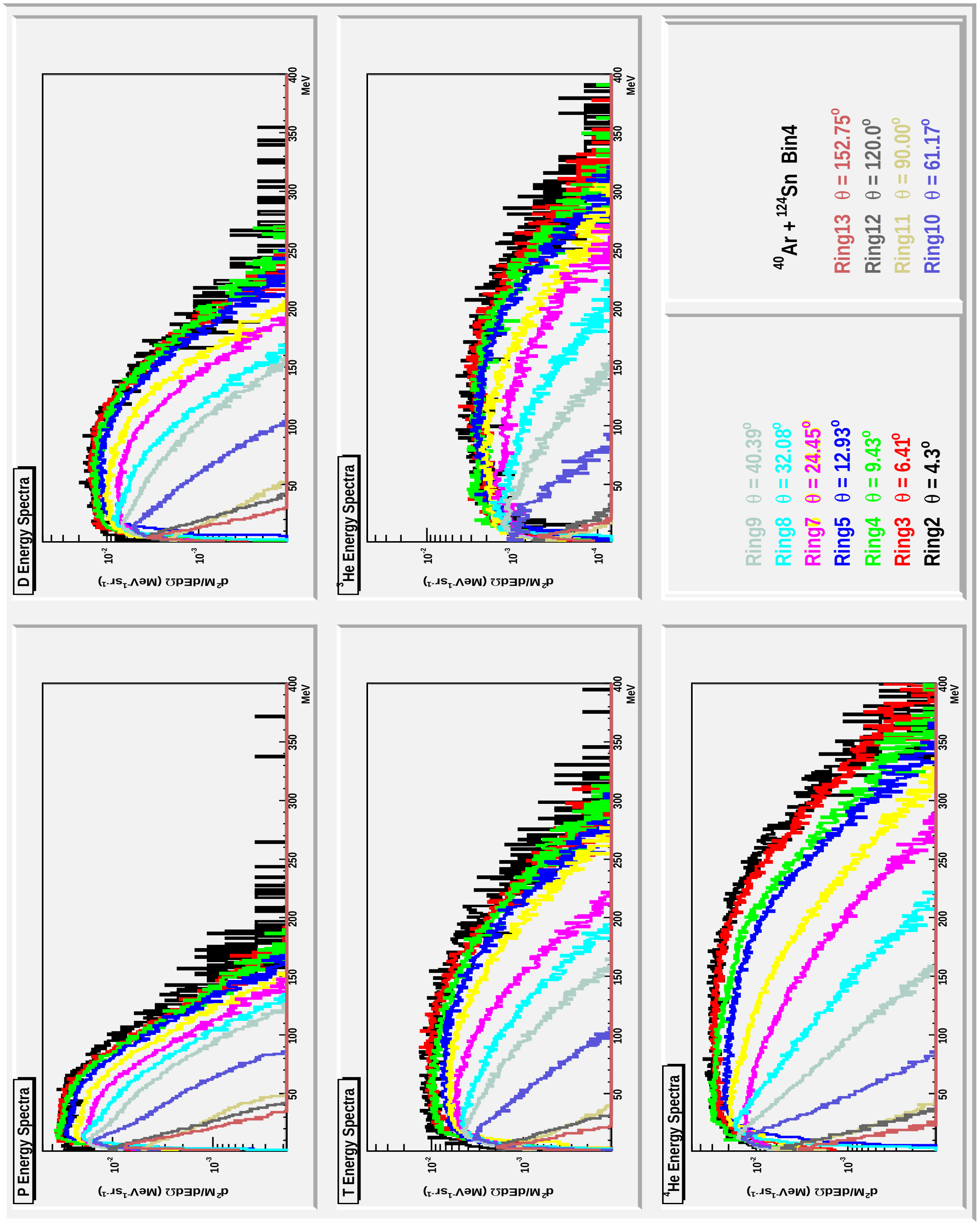

Fig. 38. X axis is energy in MeV. Y axis is multiplicity distribution

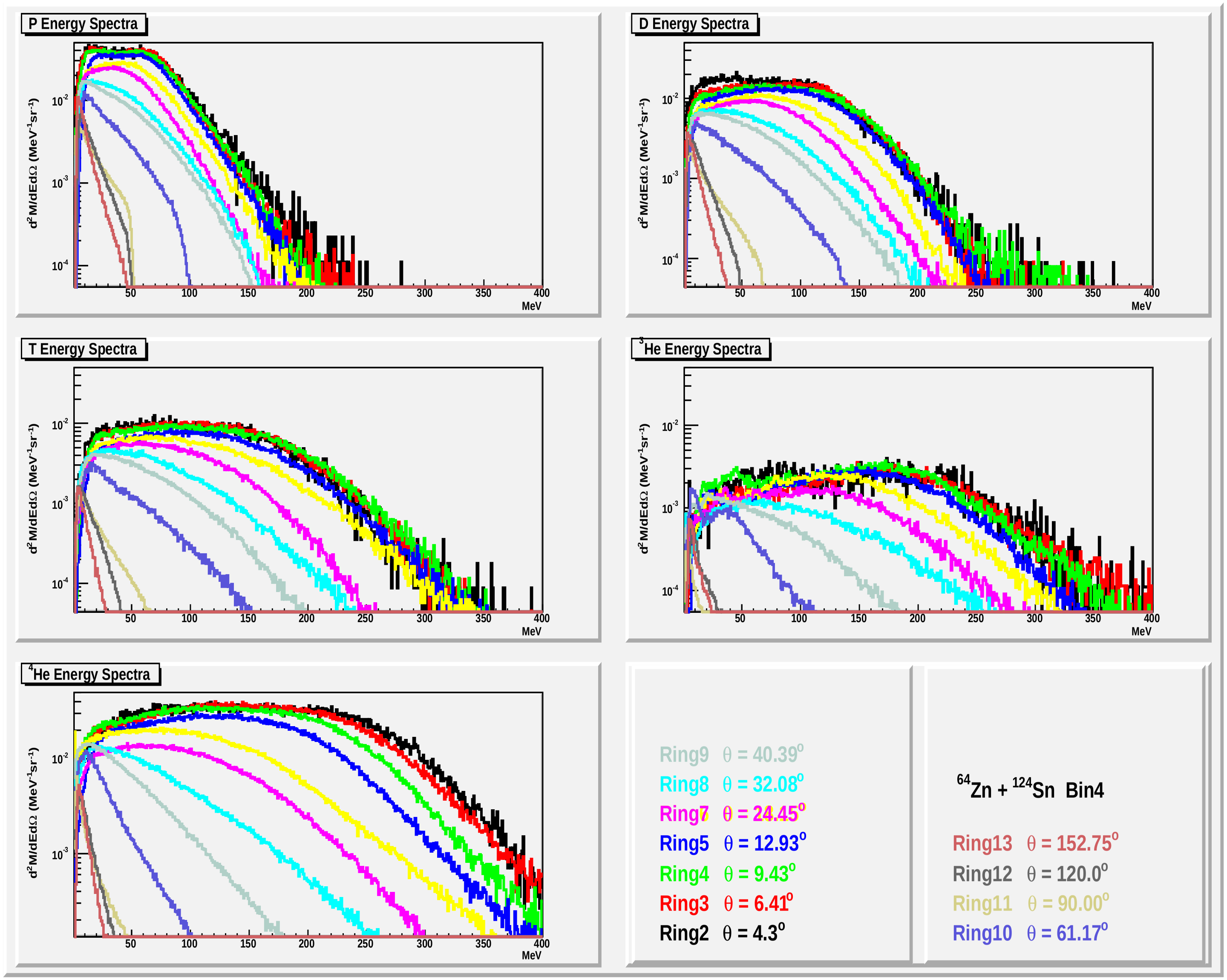

Fig. 39. X axis is energy in MeV. Y axis is multiplicity distribution

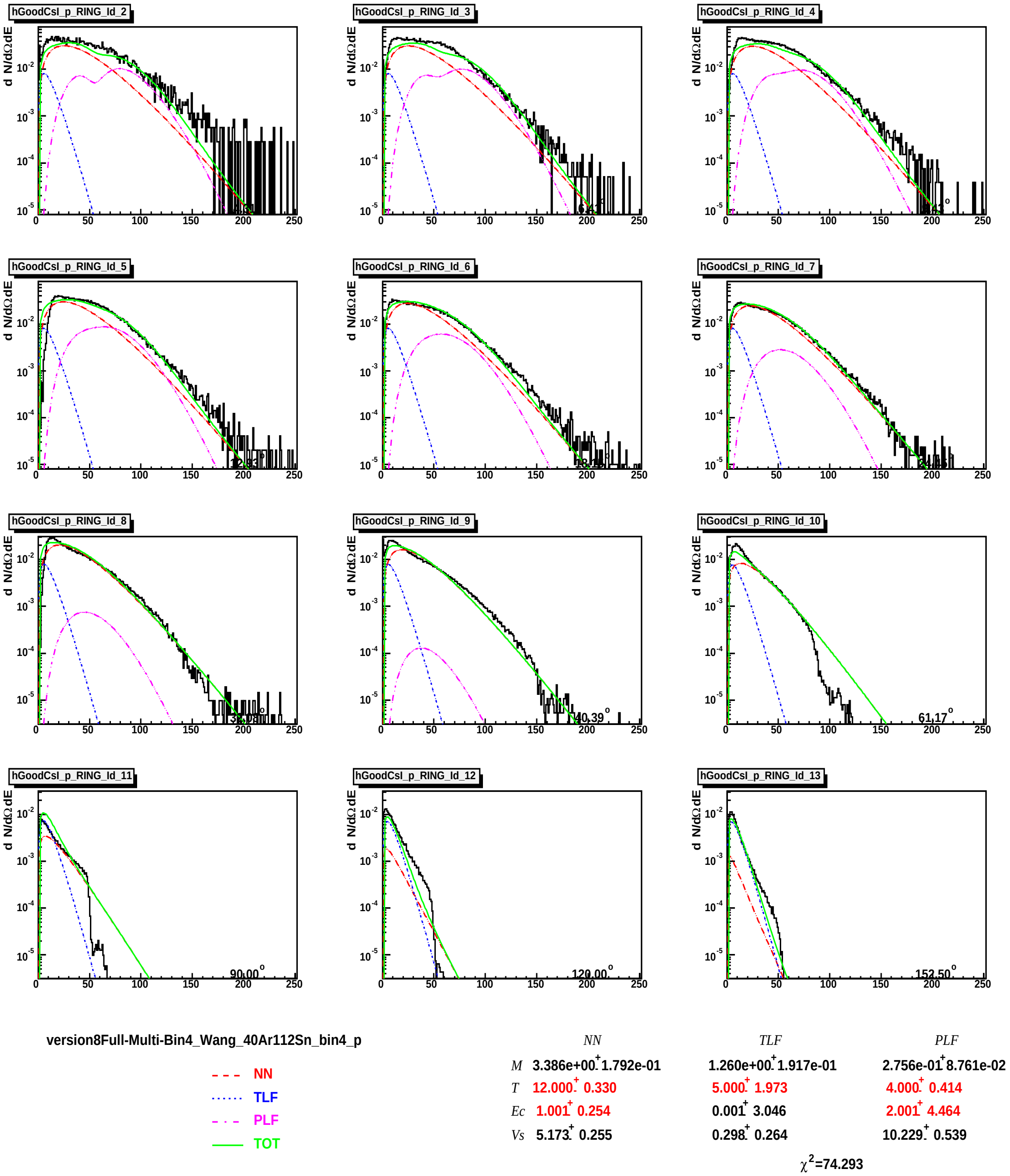

Fig. 40. X axis is energy in MeV. Y axis is multiplicity distribution.

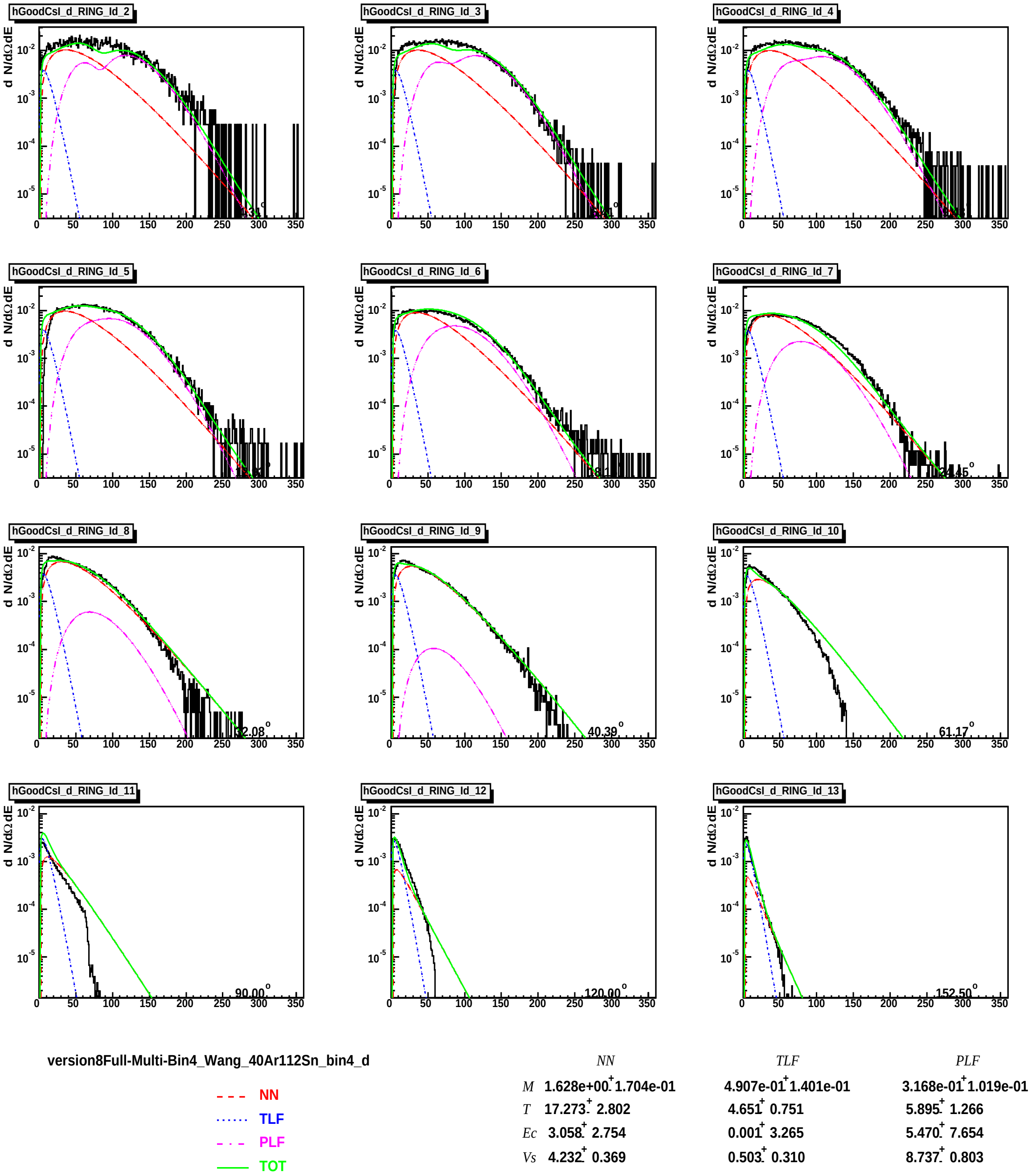

	NN	TLF	PLF
M	1.628e+00 $\pm$ 1.704e-01	4.907e-01 $\pm$ 1.401e-01	3.168e-01 $\pm$ 1.019e-01
T	17.273 $\pm$ 2.802	4.651 $\pm$ 0.751	5.895 $\pm$ 1.266
Ec	3.058 $\pm$ 2.754	0.001 $\pm$ 3.265	5.470 $\pm$ 7.654
Vs	4.232 $\pm$ 0.369	0.503 $\pm$ 0.310	8.737 $\pm$ 0.803

χ^2=29.700

Fig. 41. X axis is energy in MeV. Y axis is multiplicity distribution.

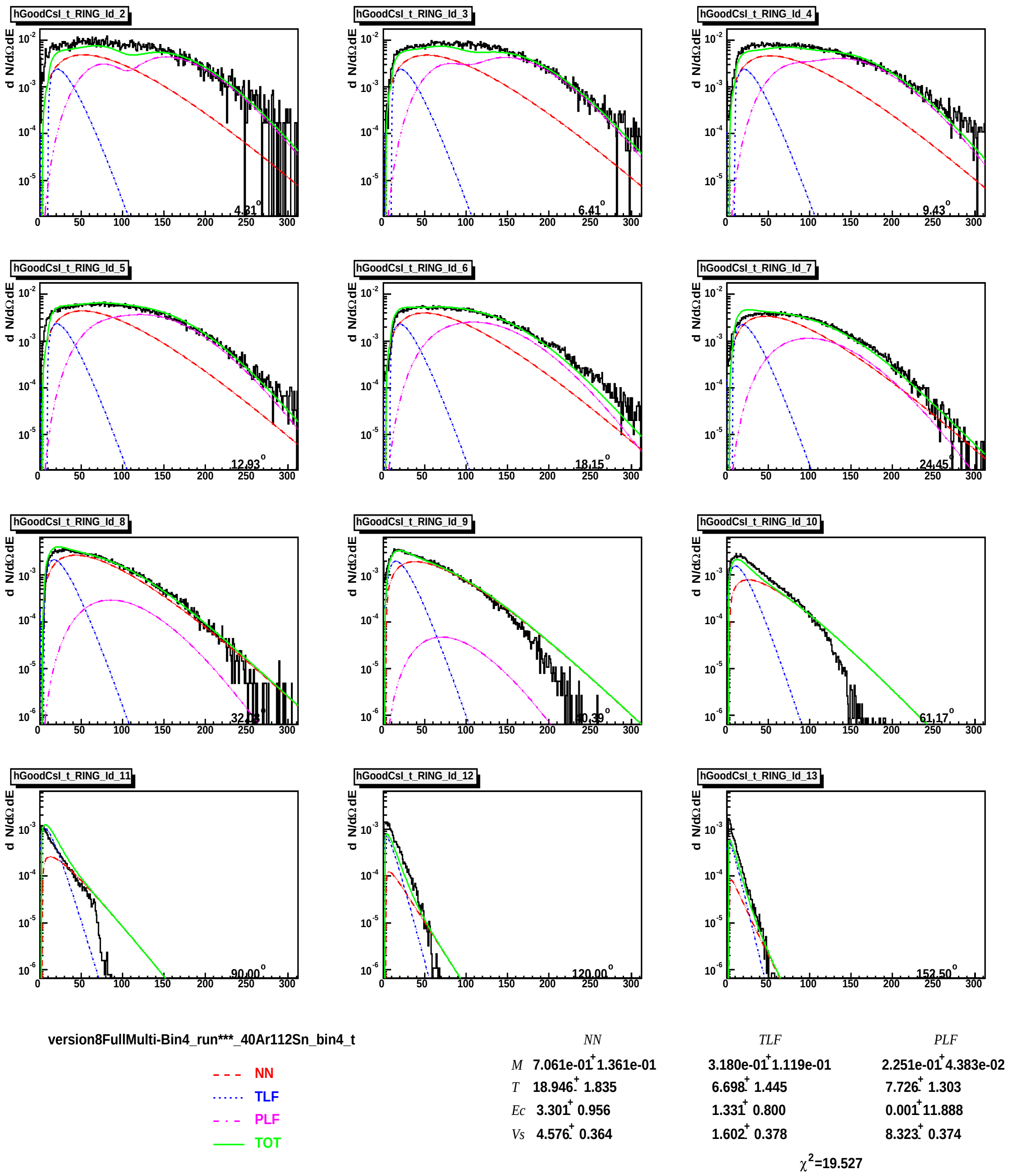

	NN	TLF	PLF
M	7.061e-01 ± 1.361e-01	3.180e-01 ± 1.119e-01	2.251e-01 ± 4.383e-02
T	18.946 ± 1.835	6.698 ± 1.445	7.726 ± 1.303
Ec	3.301 ± 0.956	1.331 ± 0.800	0.001 ± 11.888
Vs	4.576 ± 0.364	1.602 ± 0.378	8.323 ± 0.374

χ^2=19.527

Fig. 42. X axis is energy in MeV. Y axis is multiplicity distribution.

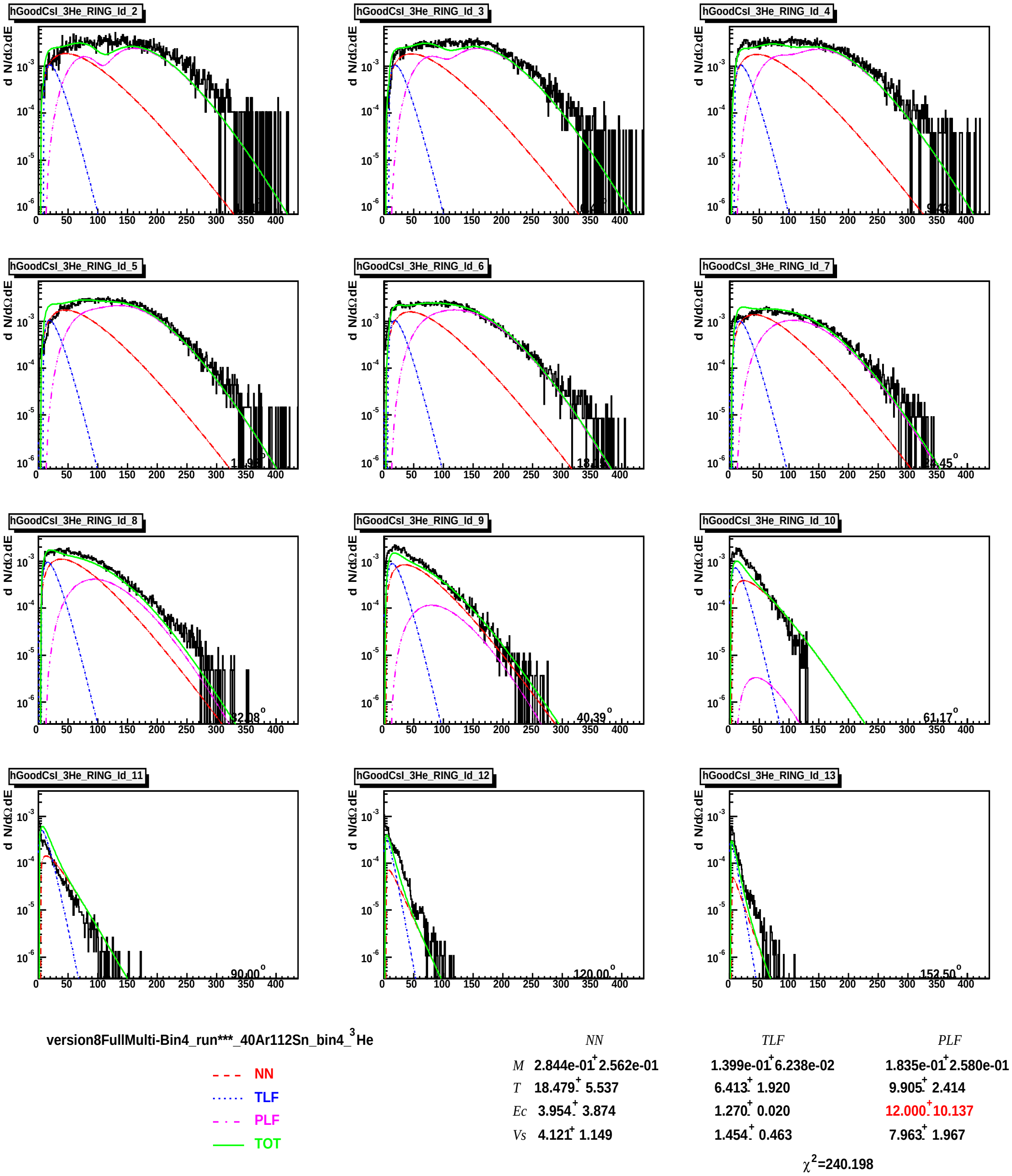

	NN	TLF	PLF
M	2.844e-01 ± 2.562e-01	1.399e-01 ± 6.238e-02	1.835e-01 ± 2.580e-01
T	18.479 ± 5.537	6.413 ± 1.920	9.905 ± 2.414
Ec	3.954 ± 3.874	1.270 ± 0.020	12.000 ± 10.137
Vs	4.121 ± 1.149	1.454 ± 0.463	7.963 ± 1.967

χ^2=240.198

Fig. 43. X axis is energy in MeV. Y axis is multiplicity distribution

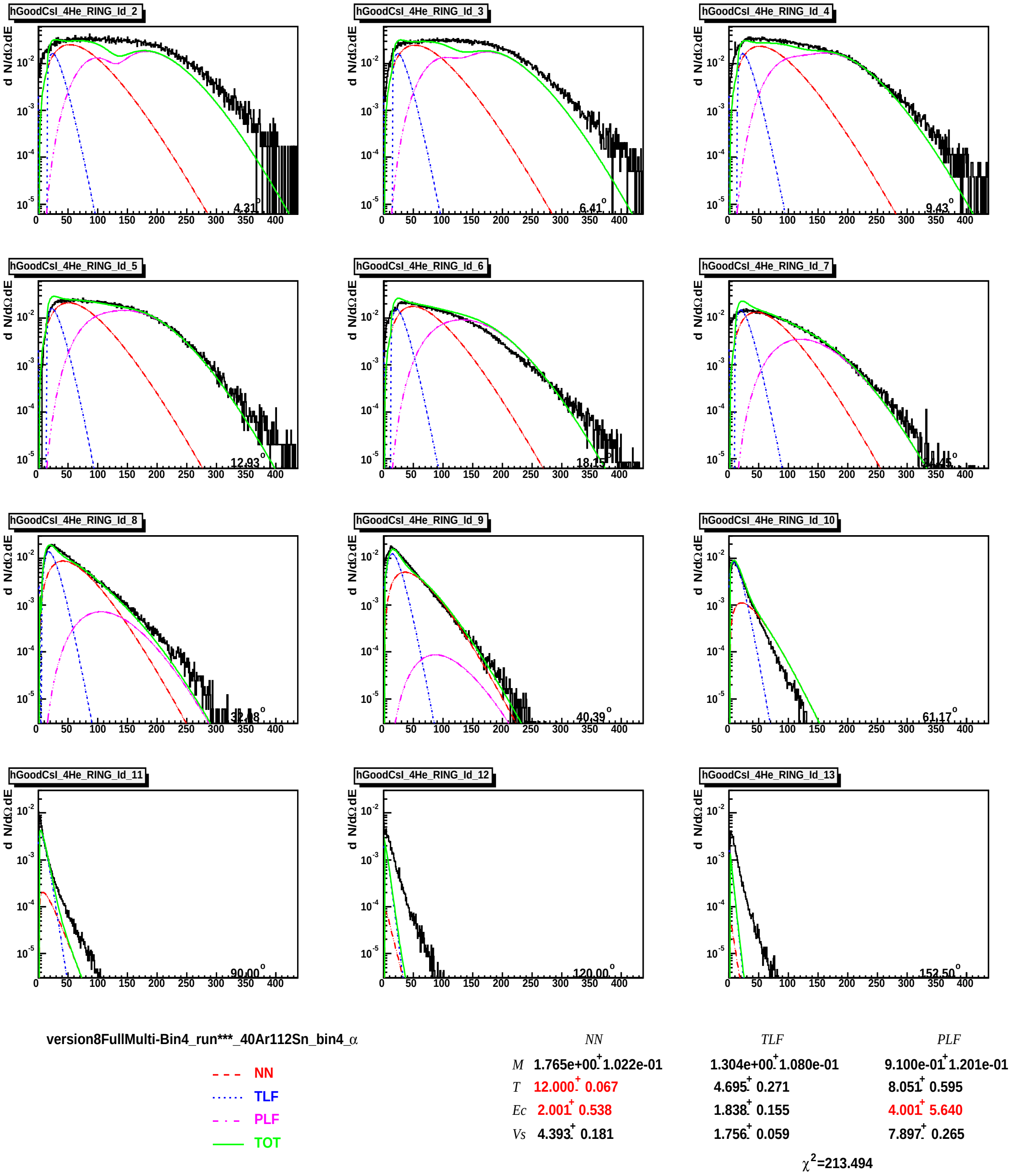

	NN	TLF	PLF
M	1.765e+00 ± 1.022e-01	1.304e+00 ± 1.080e-01	9.100e-01 ± 1.201e-01
T	12.000 ± 0.067	4.695 ± 0.271	8.051 ± 0.595
Ec	2.001 ± 0.538	1.838 ± 0.155	4.001 ± 5.640
Vs	4.393 ± 0.181	1.756 ± 0.059	7.897 ± 0.265

χ^2=213.494

Fig. 44. X axis is energy in MeV. Y axis is multiplicity distribution.

CHAPTER VI

DATA ANALYSIS

The light particles which are emitted carry essential information on the evolution of the collision. This chapter begins with an overview of the experimental results for light particle emission selected for 4 different windows of collision violence as indicated by the combined neutron and charged particle multiplicities. This is qualitatively explored assuming that the observed light charged particle emission can be attributed to three primary sources moving in the laboratory frame [13, 14]. The emission is assumed to have a Maxwellian distribution in the source frame and each of the sources is described by a source velocity, temperature, Coulomb barrier and particle multiplicity.

We derive information on the early thermalization stage of the reaction [13, 53, 54] by focusing on the properties of early emitted mid-rapidity particles identified with the NN source frame. Such a selection minimizes contributions from the other sources. In addition, yields assigned to the TLF source are subtracted from the experimental yields. Thus, the yields of higher energy particles are relatively uncontaminated by later emission processes. AMD-V calculations reported previously [14, 48] indicate that the velocities of early emitted light particles decrease rapidly with increasing average emission time. We have exploited this correlation by determining various parameters characterizing the ejectile yields, i.e., temperature and isoscaling parameters, as a function of ejectile velocity. The velocity employed is the “surface velocity”, V_{surf}, of the emitted particles, defined as the velocity of an emitted species at the nuclear surface, prior to acceleration in the Coulomb field [13]. The energy prior to Coulomb acceleration is obtained in our analysis by subtraction of the Coulomb barrier energy derived from the source fits. In earlier studies we have employed the calculated correlation from AMD-V calculations to calibrate the time-scale associated with our data [13, 48, 49, 54].

The focus of the data analysis is then shifted to the events with the highest collision violence. A variety of observables are explored employing invariant velocity plots. Simulated plots of the same observables are also generated using the fitting parameters derived from the source fits. For later analysis, in the spirit of thermal coalescence models [52], the Coulomb contributions to the energy spectra are subtracted and new velocity plots, referred to as V_{surf} plots, are generated.

In order to further isolate the low density nuclear matter which results from early emission, the source fits (also in V_{surf}) are later employed to remove the TLF component to minimize the contamination from LCP emitted in the later stages of reaction evolution.

Finally we derive temperatures and densities from the yield data and carry out an isoscaling analysis of the selected data and derive Symmetry Free Energies.

A. Reaction Tomography of the Most Violent Collision Events

A more general view of the particle emission patterns can be obtained using Gallilean invariant velocity plots. For the reactions studied, typical light cluster results are shown in figures 47 and 48, which contain plots of the intensities of the light charged particles plotted as a function of their parallel and transverse velocities in the laboratory frame. Those plots are for the most violent collision events, whose full list can be found in Appendix K. To construct this plot, the histogrammed data from the discrete detector rings were smoothed by assignment of the position for a particle detected in a given detector according to the angular distribution function generated with the parameters derived from the three source fitting. For the most violent collisions these plots for p,d, t, ^{3}He, and ^{4}He reveal very strong similarities for the different systems.

For the most peripheral events, the plots of proton and alpha velocity for all of the systems are presented in figures 45 and 46. The contour level patterns of the particle intensity distributions in the velocity frame show emission dominated by PLF sources with velocity close to that of projectile and TLF sources with source velocities with low velocities near to zero. Those velocity patterns show that the reaction mechanism is similar even for the least violent collision events.

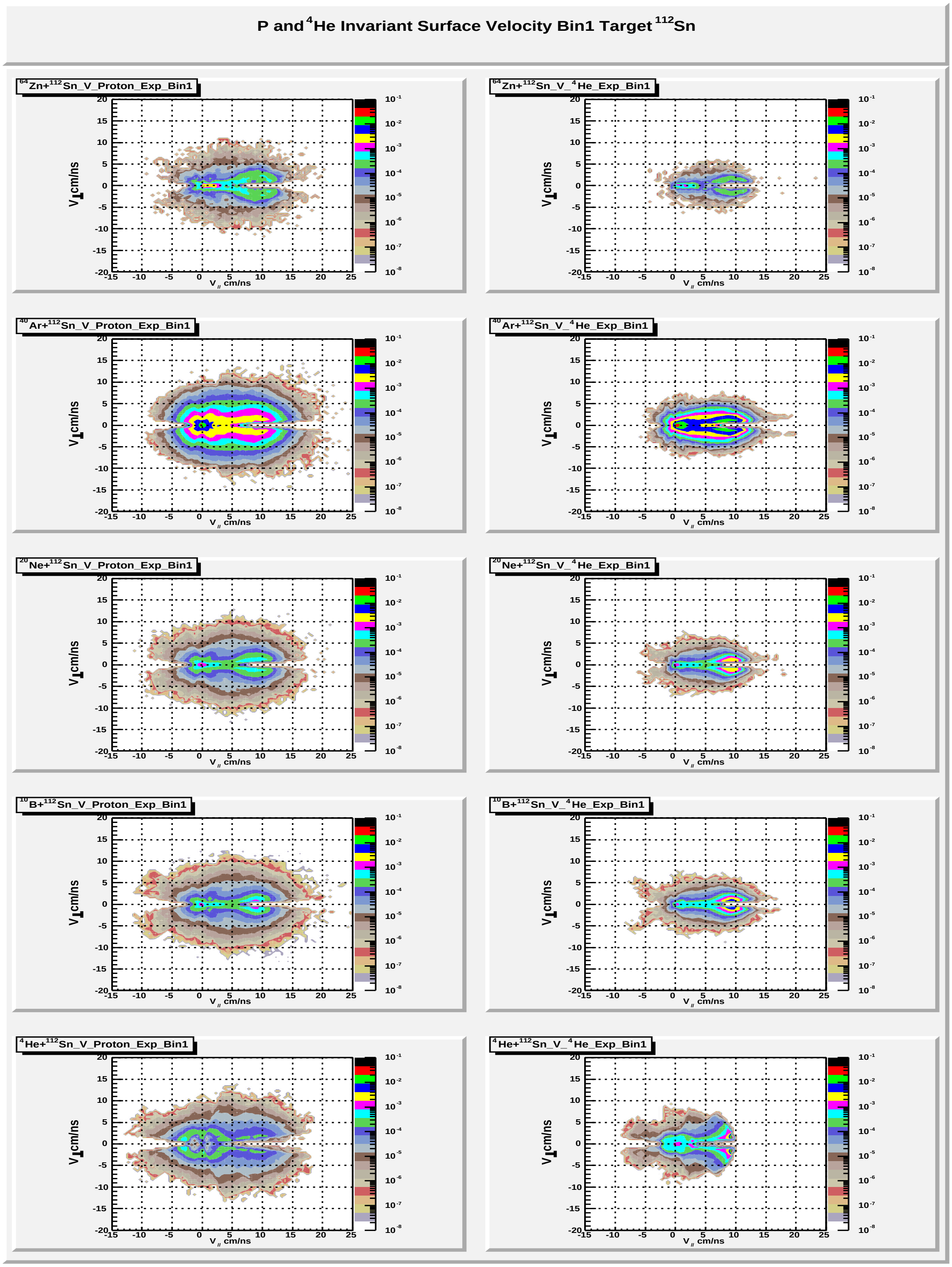

Fig. 45. Particle surface velocity plot of for Bin1 ^{112}Sn.

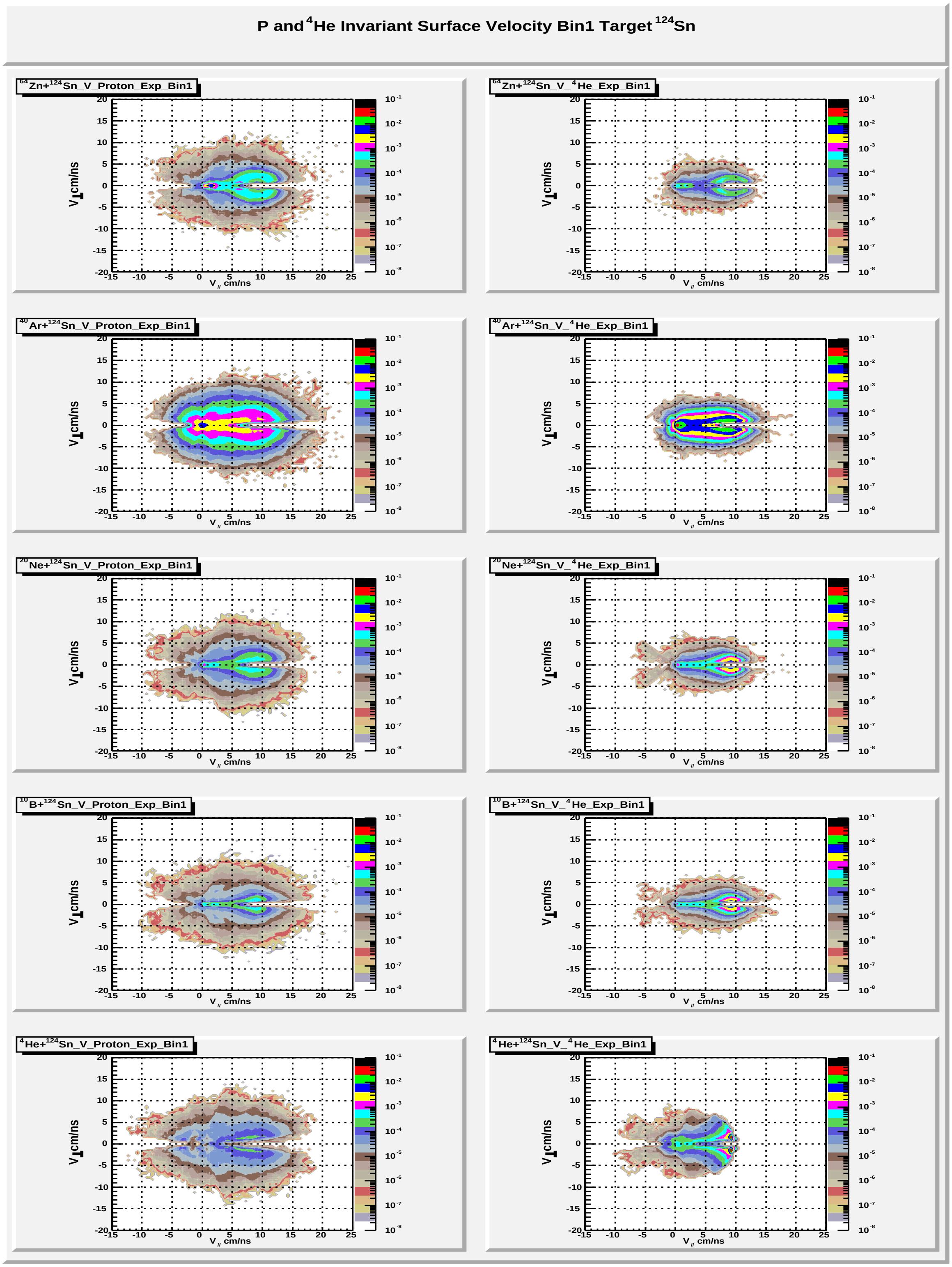

Fig. 46. Particle surface velocity plot of for Bin1 ^{124}Sn.

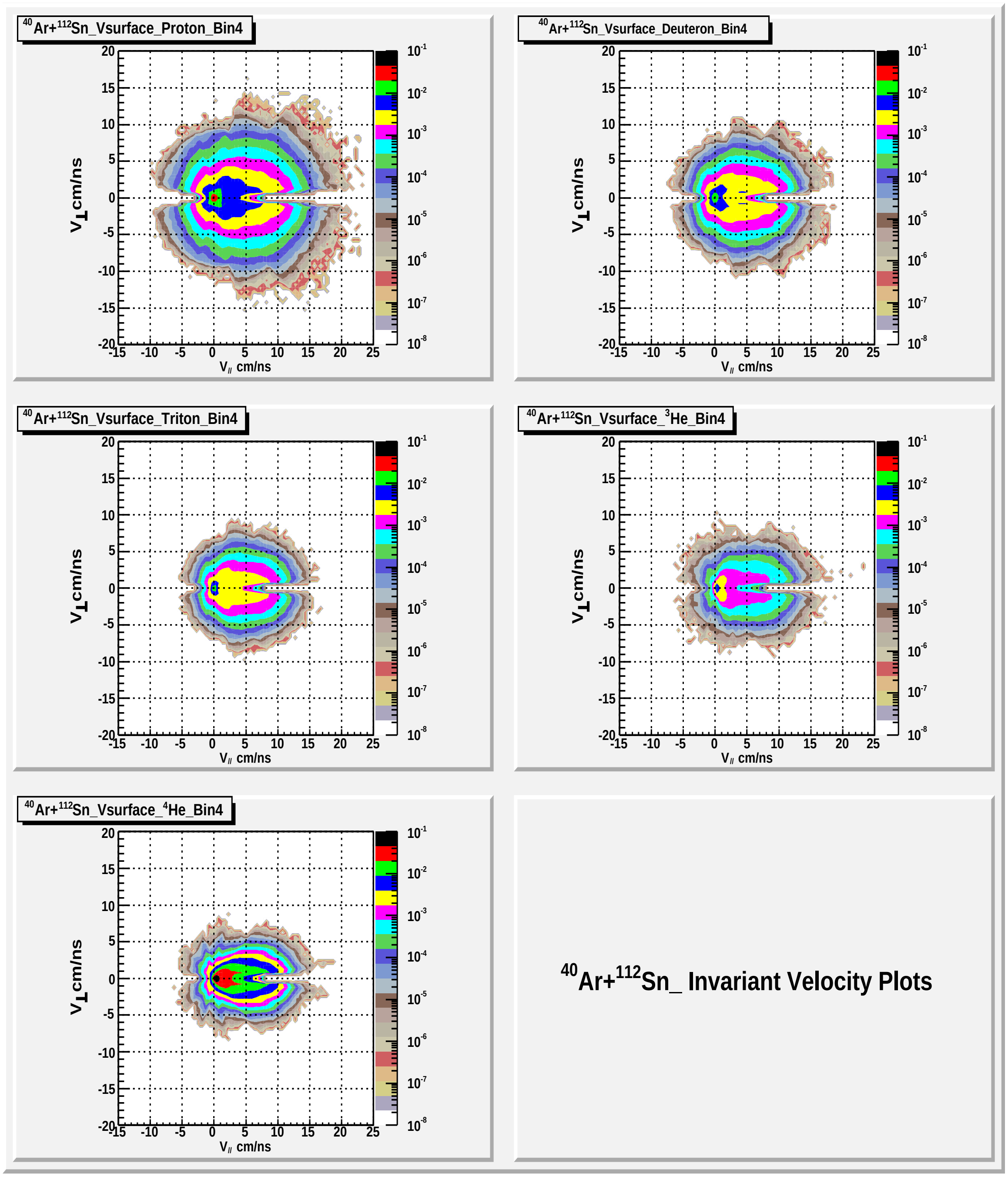

Fig. 47. Particle surface velocity plot of ^{40}Ar+ ^{112}Sn.

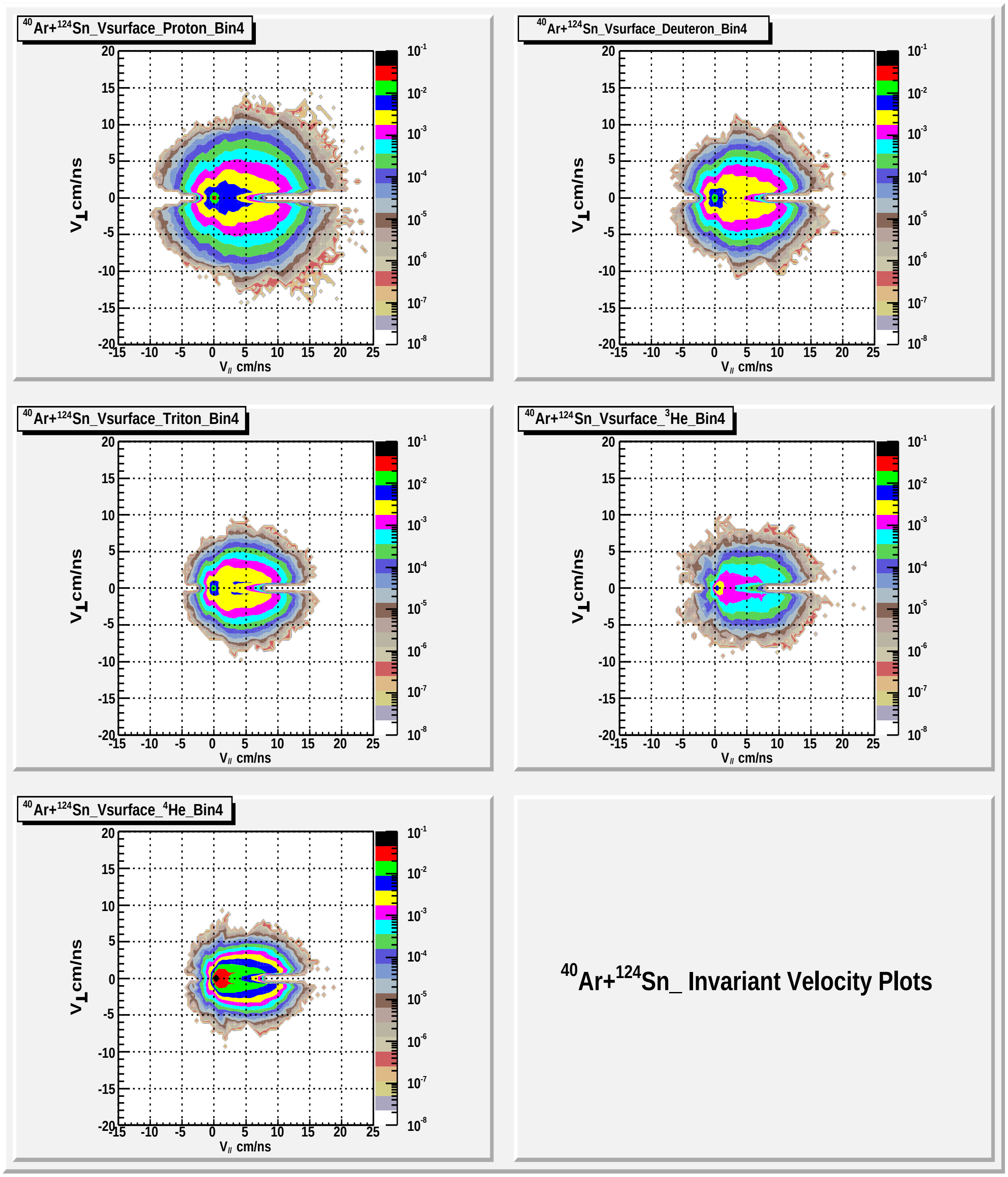

Fig. 48. Particle surface velocity plot of ^{40}Ar+ ^{124}Sn.

We also took the source fitting parameters to simulate the individual source to generate the velocity plot to remove the particluar components that we need. We can use the simulated TLF source velocity plot to remove the late emission part.

One of typical pictures is shown in Fig.49 which demonstrates the PLF + NN + TLF simulated spectra of proton agree very well the experimental spectra.

B. Experimental Determination of Temperature and Density

Coalescence and thermodynamic equilibration models are widely used in interpretations of light cluster emission. For the most violent collision events, the temperature and density of the emitting systems were first calculated using the Albergo model [68]. The Albergo model evaluates the temperatures and free nucleon densities based on a dilute-nuclear-matter chemical equilibrium assumption which makes use of the known data for ^{2}H, ^{3}H , ^{3}He, ^{4}He cluster emission. The Albergo model assumes that the first stage of a heavy-ion collison creates a hot interaction region. During the second stage, this hot system will cool and expand leading to lower densities and temperatures. Eventually the reacting system reaches the chemical freeze-out stage. At that point it is assumed that the particles do not interact further except by the Coulomb repulsion and are emitted from the system and identified by the experimental detection system. Based on those assumptions, the emitted clusters carry the essential information on the freeze-out stage temperature, density, N/Z composition, etc.

While spectral “temperatures” may be extracted from fitting exponential slopes of the measured particle spectra, those observed spectra slopes are not necessarily appropriate estimates of the temperatures because they reflect dynamic effects in the evolving systems. For early emitted particles, for example, the spectral slopes are generally consistent with those calculated with transport models. They are characterized by high apparent temperatures but the observed spectra are convolutions of the spectra at different emission times and include high energy particles which are emitted before the thermal equilibrium is reached. For this reason, in this work we employ chemical temperatures derived from relative yields of the emitted species. In order to probe the temperature evolution of the systems we determine these temperatures as a function of V_{surf}. This is based upon a large body of previous experimental work and comparisons with transport model calculations which indicate that there is a strong correlation between energy and emission time for the early emitted particles [68]. Of course, for the concept of temperature to make sense, statistical equilibrium is required, at least on a local basis. We have addressed the question of evidence for equilibration in a number of previous papers on similar collisions [68] and will provide further evidence that this assumption seems justified in the following chapter.

The Albergo Model assumes that a thermal equilibrium is established between free nucleons and composite fragments contained within a certain interaction volume V at a temperature T. The density of P(A,Z) of a particle (A,Z) with Z bound protons and (A-Z) bound neutrons can be written as Equation 6.2.

As pointed out by Albergo et al [68], knowledge of the temperature allows the extraction of the free proton densities from the yield ratios of ejectiles which differ by one proton, e.g., the yield ratio of ^{4}He to ^{3}He. Specifically,

$$\rho_p = 0.62 \times 10^{36} T^{3/2} \mathrm{e}^{-19.8/T} [Y(^4\mathrm{He})/Y(^3\mathrm{H})]. \tag{6.1}$$

Here T is the temperature in MeV, Y refers to the yield of the species under consideration, and ρ_p has units of nucleons/cm^3. Correspondingly, the free neutron densities may be extracted from the yield ratios of ejectiles which differ by one neutron, e.g., the yield ratio of ^{3}H to ^{2}H . For this work we have first derived the free nucleon densities and then determined densities of the Z = 1 and Z = 2 clusters from their yield ratios relative to the free protons.

$$\rho(A,Z) = \frac{\mathcal{N}(A,Z)}{V} = \frac{A^{3/2}\omega(A,Z)}{\lambda^3_{T\mathcal{N}}} F_{MB}\left[\frac{\mu(A,Z)}{T}\right], \tag{6.2}$$

where $\mathcal{N}(A,Z)$ is the number of particles (A,Z) within the volume V; $\lambda^3_{T\mathcal{N}} = h/(2\pi m_0 T)^{1/2}$ is the thermal nucleon wave-length, where m_0 is the mass of a nucleon $\mathcal{N}$. T is the temperature expressed in MeV; $\mu(A,Z)$ is the chemical potential of the particle (A,Z);

$$\omega(A,Z) = \sum_j \{[2s_j(A,Z)+1]\mathrm{exp}[-E_j(A,Z)/T]\} \tag{6.3}$$

is the internal partition function of the particle (A,Z), where $s_j(A,Z)$ are ground- and excited-state spins and $E_j(A,Z)$ are energies of these states and $F_{MB}[\mu(A,Z)/T] = \mathrm{exp}[\mu(A,Z)/T]$.

Here the Maxwell-Boltzmann statistics is chosen for temperature more than some MeV and $\rho < \rho_0$ /2.0. Also Albergo Model assumes the system is in chemical equilibrium which satisfies the equation:

$$\mu(A,Z) = Z\mu_{pF} + (A-Z)\mu_{nF} + B(A,Z), \tag{6.4}$$

where B(A,Z) is the binding energy of cluster (A,Z). μ_{pF} and μ_{nF} are the chemical potentials of free proton P_f and of free neutrons N_f, respectively.

From the above equations, Albergo derives the formula:

$$\rho(A,Z) = \frac{\mathcal{N}(A,Z)}{V} = \frac{A^{3/2}\lambda_{T\mathcal{N}}^{3(A-1)}\omega(A,Z)}{(2s_{pF}+1)^Z(2s_{nF}+1)^{A-Z}}\rho_{pF}^Z\rho_{nF}^{A-Z}\mathrm{exp}\left[\frac{B(A,Z)}{T}\right], \tag{6.5}$$

ρ(A,Z), ρ_{pF} and ρ_{nF} being the densities of the composite fragment (A,Z), of free protons and of free neutrons, respectively, contained in the same interaction volumes V at the temperature T. Based on the above analysis, Albergo also derived the ratio of experimental yields of two clusters as the equation 6.6:

$$\begin{aligned}\frac{Y(A,Z)}{Y(A',Z')} = \frac{\rho(A,Z)}{\rho(A',Z')} &= \left(\frac{A}{A'}\right)^{3/2} \left(\frac{\lambda^3_{T\mathcal{N}}}{2}\right)^{A-A'} \frac{\omega(A,Z)}{\omega(A',Z')} \rho_{pF}^{Z-Z'} \rho^{(A-Z)-(A'-Z')} \\ &\times \exp\left[\frac{B(A,Z) - B(A'-Z')}{T}\right]. \qquad (6.6)\end{aligned}$$

By calculation of experimental yield ratios between the two fragments differing only a proton, such as (A,Z) and (A+1, Z+1), Albergo showed the free-proton density (nucleons/cm^3) of the emitting source during the system disassembly.

$$\begin{aligned}\rho_{pF} &= \left\{\left(\frac{A}{A+1}\right)^{3/2} \frac{10^{36}}{2.1} \frac{2s(A,Z)+1}{2s(A+1,Z+1)+1} T^{3/2} \right. \\ &\left. \times \exp\left[\frac{B(A,Z) - B(A+1,Z+1)}{T}\right]\right\} \frac{Y(A+1,Z+1)}{Y(A,Z)}. \qquad (6.7)\end{aligned}$$

Similarily, using the yield ratio of the two fragments differing only for a neutron, such as (A,Z) and (A+1,Z), Albergo derived the free-neutron density:

$$\begin{aligned}\rho_{nF} &= \left\{\left(\frac{A}{A+1}\right)^{3/2} \frac{10^{36}}{2.1} \frac{2s(A,Z)+1}{2s(A+1,Z)+1} T^{3/2} \right. \\ &\left. \times \exp\left[\frac{B(A,Z) - B(A+1,Z)}{T}\right]\right\} \frac{Y(A+1,Z)}{Y(A,Z)}. \qquad (6.8)\end{aligned}$$

Given the experimental yields of ^{2}H , ^{3}H , ^{3}He and ^{4}He, Albergo derived the free proton and neutron density (nucleons/cm^3) formula:

$$\rho_{pF} = [0.39 \cdot 10^{36} T^{3/2} \exp(-5.5/T)] \frac{Y(^3\mathrm{He})}{Y(^2\mathrm{H})}$$

$$= \quad [0.62 \cdot 10^{36} T^{3/2} \exp(-19.8/T)] \frac{Y(^4\mathrm{He})}{Y(^3\mathrm{H})}, \tag{6.9}$$

$$\begin{aligned} \rho_{nF} &= [0.39 \cdot 10^{36} T^{3/2} \exp(-6.3/T)] \frac{Y(^3\mathrm{H})}{Y(^2\mathrm{H})} \\ &= [0.62 \cdot 10^{36} T^{3/2} \exp(-20.6/T)] \frac{Y(^4\mathrm{He})}{Y(^3\mathrm{He})}, \end{aligned} \tag{6.10}$$

Albergo deduced a very simple formula to calculate the temperature using the double ratios of light clusters which can be measured with experimental detection systems. For our case, using the light charged particles,

$$T = \frac{14.3}{\ln\left[\sqrt{9/8}(1.59) R_{V_{surf}}\right]}. \tag{6.11}$$

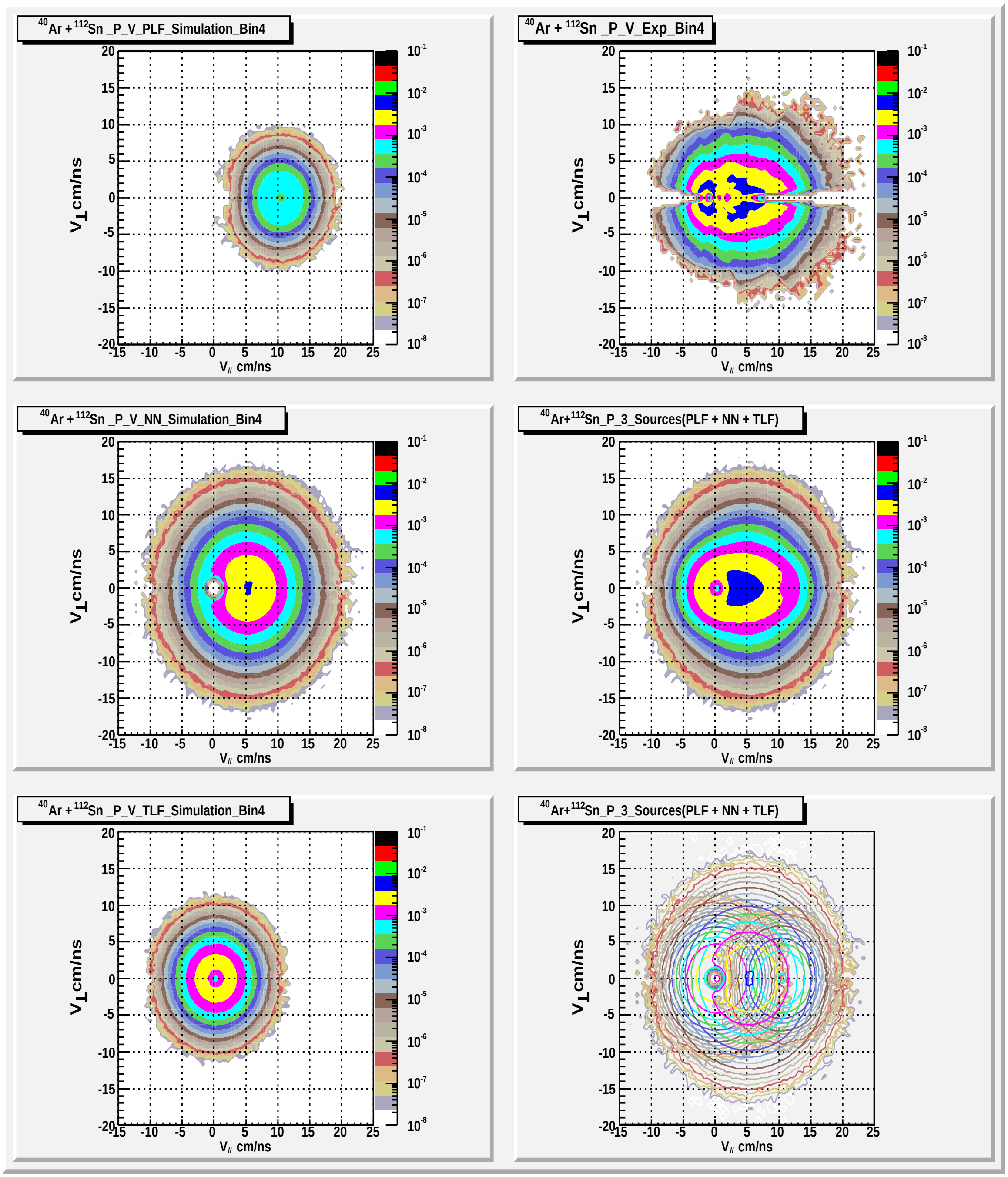

Fig. 49. Proton particle velocity simulated plot of ^{40}Ar+ ^{112}Sn.

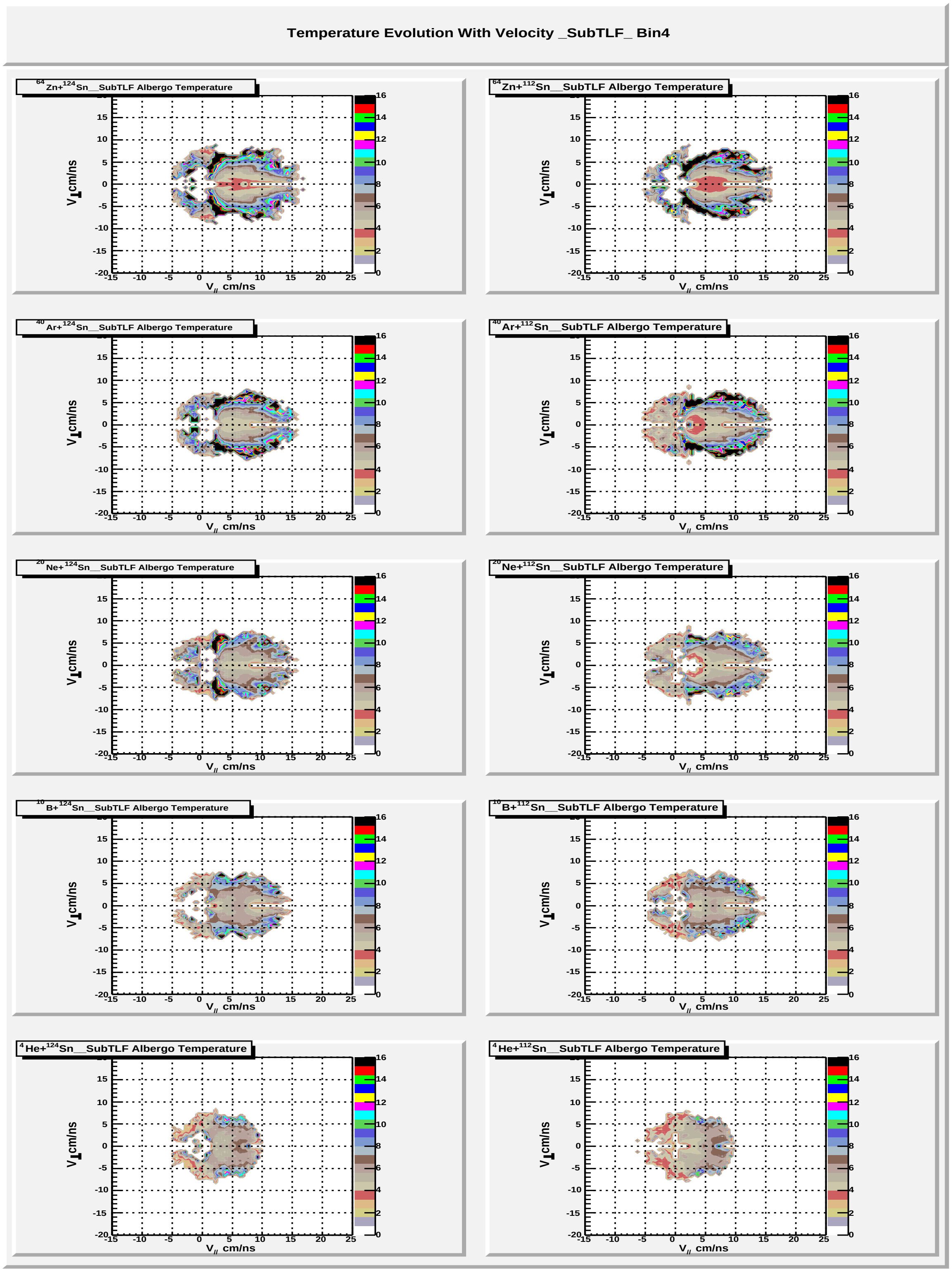

Fig. 50. Temperature evolution in velocity frame

In the case of strong system evolution the double isotope yield ratio temperatures derived from integrated yields are certainly not accurate because the isotopes can be produced at very different times or by different mechanisms [13]. Selection of yields in a particular energy range, even when the energies are Coulomb corrected, may also lead to errors in temperature determinations if the isotopes are not in fact produced during the same time interval of the system evolution [13, 14].

In this dissertation project, particle velocities are employed to select the particles emitted at particular emission times. This is done for a range of velocities in the NN source frame for which emission from other sources is minimal. If secondary emission contributions are negligible, derivations of double isotope yield ratio temperatures as a function of particle velocity allow us to follow the average temperature evolution of the system. In our data analysis, the relative yields of the light clusters are taken in the invarant velocity frame. We have derived the double isotope yield ratio temperature T_{HHe}, from the yields of d, t, ^{3}He, and ^{4}He particles as a function of parallel and perpendicular velocity. We note that for particles emitted from a single source of temperature T and having a volume Maxwellian spectrum $E^{1/2}\mathrm{e}^{-E/T}$, the HHe double isotope yield ratio evaluated for particles of equal surface velocity is $\sqrt{9/8}$ times the ratio derived from either the integrated particle yields or the yields at a given energy above the barrier. Thus the formula is given as Equation 6.11, where the constants 14.3 and 1.59 reflect binding energy, spin, masses and mass differences of the ejectiles and $R_{V_{surf}} = Y(d)Y(^4He)/Y(t)Y(^3He)$ with cluster yields Y taken at the same surface velocity.

In Fig.50 we present the derived temperatures as a function of V_{surf}. The temperatures increase slightly with projectile mass and decrease with decreasing V_{surf}.

C. Reaction Tomography of Densities

In references [48, 49] we discuss this evolution and present the evidence that chemical equilibrium is achieved, at least on a local basis. Although densities are not easily accessible experimental quantities in collision studies, knowledge of the densities at which the symmetry free energy F_{sym} determinations are being made is critical to an interpretation of the measured values. As pointed out by Albergo et al, knowledge of the temperature allows the extraction of the free proton densities from the yield ratios of ejectiles that differ by one proton. Correspondingly, the free neutron densities may be extracted from the yield ratios of ejectiles which differ by one neutron. Once the free nucleon densities are known, the densities of the other particles may be calculated from the experimentally observed yields. This, again, is done as a function of surface velocity. The results, obtained by summing the densities of particles with A = 1 to 4, for the all reaction systems with the removal of TLF components, are presented in Fig. 51. The values for the two systems with same projectiles, but different targets show quite similar results and low densities. From the light projetciles to heavy ones, ^{4}He, ^{10}B, ^{20}Ne, ^{64}Zn, the density evolution pattern in the velocity frame changes significantly. For a given system, the density changes as velocity evolves. It is worth noting that our measurements of both the temperature and the associated Alpha mass fraction, also provide a means of estimating the densities by comparison with the Schwenk and Horowitz, Shen, Lattimer, or Roepke calculations. Like the Albergo calculation these calculations assume chemical equilibrium and lead to similar low densities. $\rho_{\mathrm{total}} = \rho_p + \rho_n + 2\rho_d + 3\rho_t + 3\rho_{^3\mathrm{He}} + 4\rho_{^4\mathrm{He}}$. The unit of total density ρ_{total} is nucleons/cm^3.

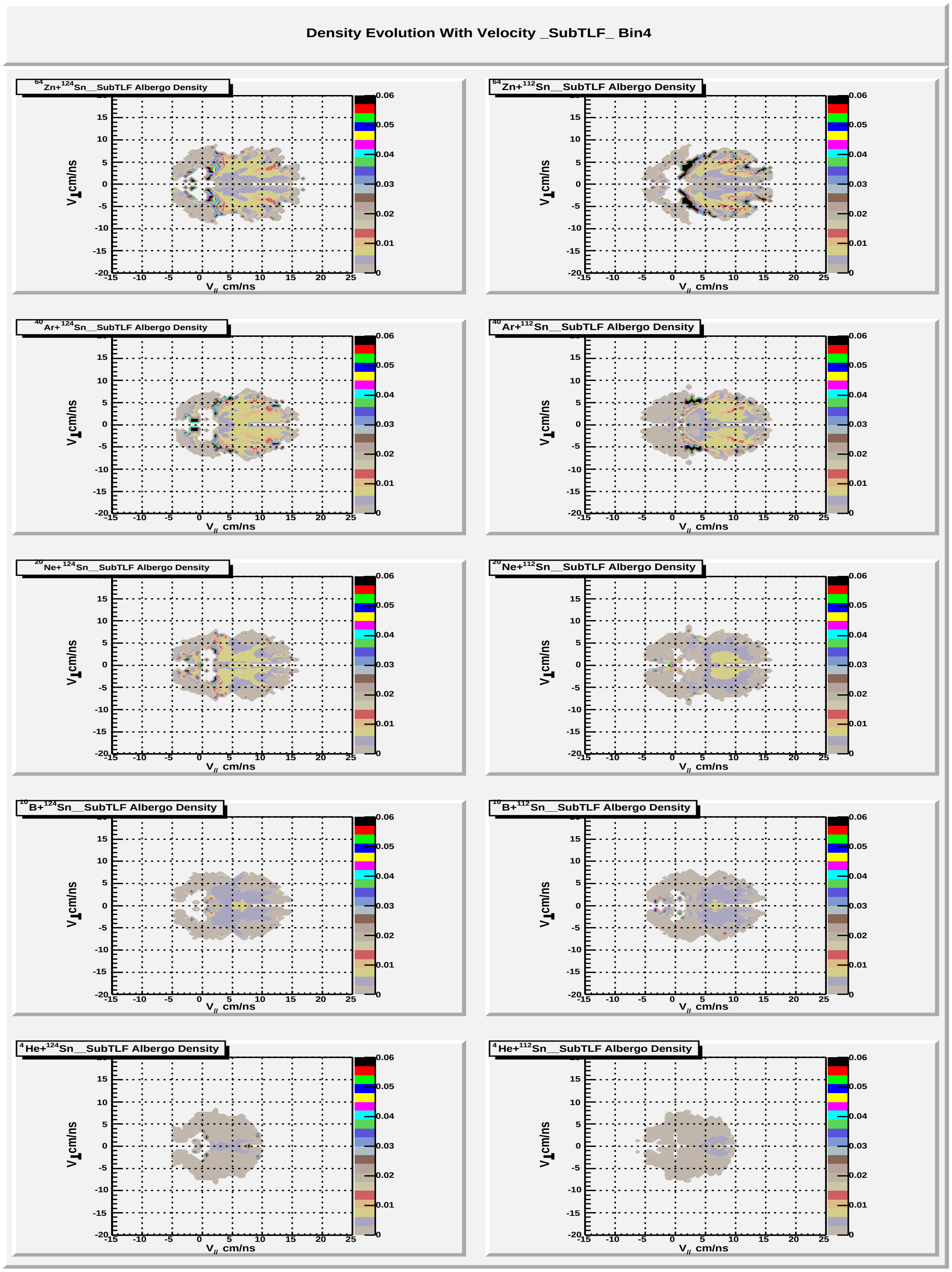

Fig. 51. Total Density Evolution in Velocity Frame

D. Isocaling Parameter Alpha

Horowitz and Schwenk have pointed out that extensive alpha clustering in the low-density gas leads naturally to an increase in the symmetry energy for the clustering system [39]. For comparison to the symmetry energy predictions of the VEOS model we will derive symmetry free energies from the ejectile yield data by employing an isoscaling analysis. Such analyses have been reported in a number of recent articles [43, 41, 42]. In this approach the yields of a particular species Y (N,Z) from two different equilibrated nuclear system 1 and 2 of similar temperature but different neutron to proton ratios, N/Z are expected to be related through the isoscaling relationship

$$\frac{Y_2}{Y_1} = C\mathrm{e}^{\alpha N + \beta Z}, \tag{6.12}$$

where C is a constant, $\alpha = [\mu_2(n) - \mu_1(n)]/T$ and $\beta = [\mu_2(p) - \mu_1(p)]/T$, representing the difference in chemical potential between the two systems, may be extracted from suitable plots of yield ratios. Either parameter may then be related to the symmetry free energy, F_{sym}. With the usual convention that system 2 is richer in neutrons than system 1,

$$\begin{aligned} \alpha &= 4F_{\mathrm{sym}}[(Z_1/A_1)^2 - (Z_2/A_2)^2]/T, \\ \beta &= 4F_{\mathrm{sym}}[(N_1/A_1)^2 - (N_2/A_2)^2]/T, \end{aligned} \tag{6.13}$$

where Z is the atomic number and A is the mass number of the emitter. Thus, F_{sym} may be derived directly from determinations of system temperatures, Z/A ratios, and isoscaling parameters. In this work, the isoscaling parameter Alpha is determined from yield ratioes of p, d, t ^{3}He ^{4}He for the two targets studied.

Figures 52 and 53 present a representation of the isoscaling parameter alpha for reactions with ^{112}Sn and ^{124}Sn in velocity space. In order to focus on the low density matter ejected from the the system, we focus on the mid-velocity region of this plot. The velocity region has $V_{\|}$ from 4.75 to 5.75 cm/ns. For this $V_{\|}$, the $V_{\perp}$ is sampled. To illustrate those values, the fitting line and data points are plotted in Fig.52.

The Y axis in each figure represents the ratio of ejectile yields, yield ratios are displaced to make a clear representation for different $V_{\perp}$. All results shown here have error on Alpha less than 10%. The data are for ^{40}Ar Projectiles. Some typical results of ^{4}He, ^{10}B, ^{20}Ne, ^{64}Zn projectiles are shown in Appendix L.

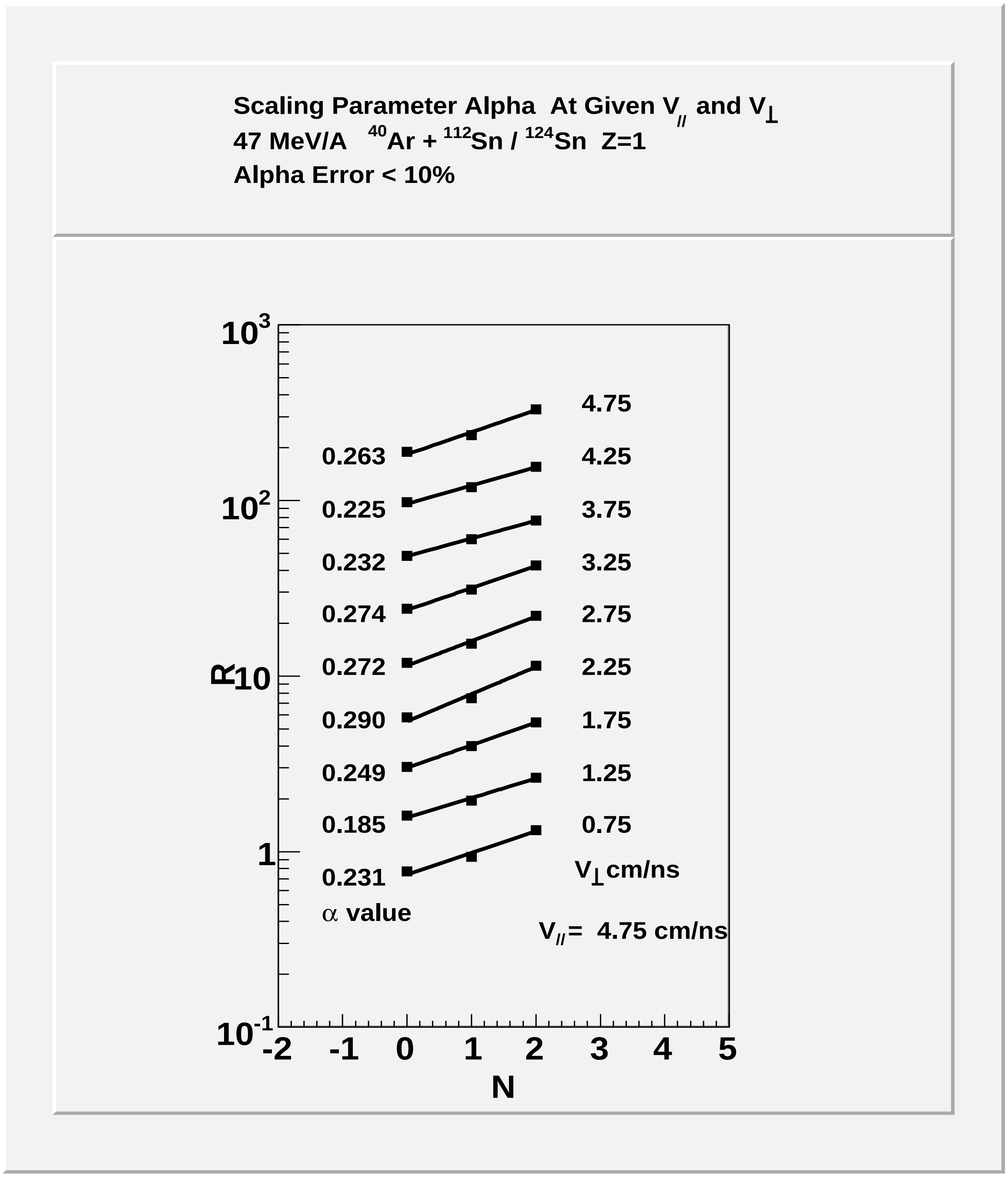

Fig. 52. Scaling parameter Alpha at $V_{\parallel}$ = 4.75 cm/ns and different $V_{\perp}$ ^{40}Ar+^{124}Sn/^{112}Sn.

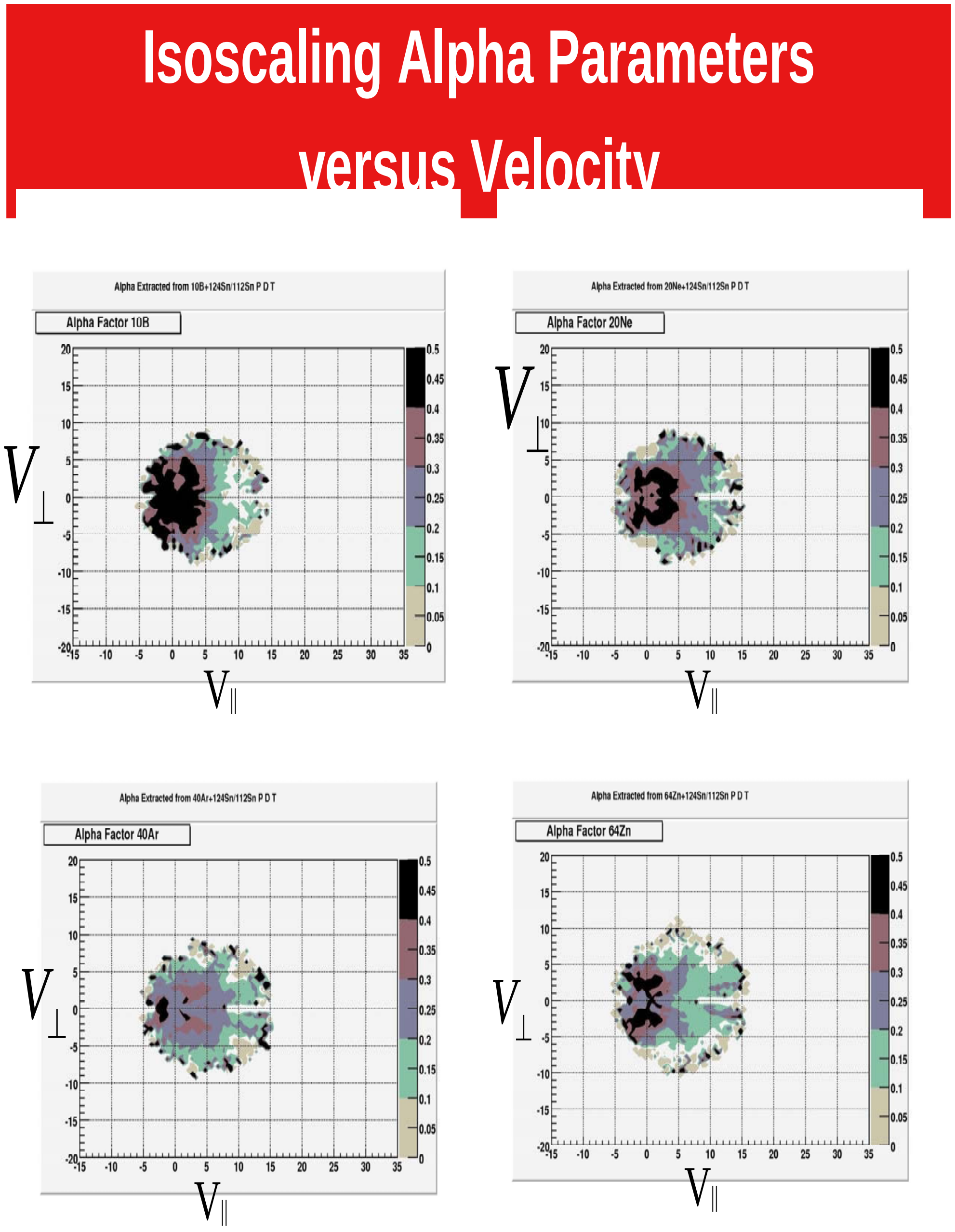

Isoscaling Alpha Parameters versus Velocity

Fig. 53. Isoscaling parameter Alpha in velocity frame.

E. Symmetry Free Energies

Figure 54 shows results in the mid rapidity region, from which one sees relatively low values of the symmetry free energy consistent with those reported in our previous work on low density gases [43]. In the target-like region near 0 cm/ns and the projectile-like region above 10 cm/ns significantly larger values are derived. These values are close to symmetry energy coefficients of Liquid Drop Model mass formulae and of those derived from earlier isoscaling experiments reported in the literature. It is tempting to associate the observed evolution with an evolution in density at emission. However a detailed understanding of the density variations requires very careful evaluation of the secondary evaporative contributions in the PLF and TLF regions as well as a consideration of in-medium effects as addressed at the end of the previous section.

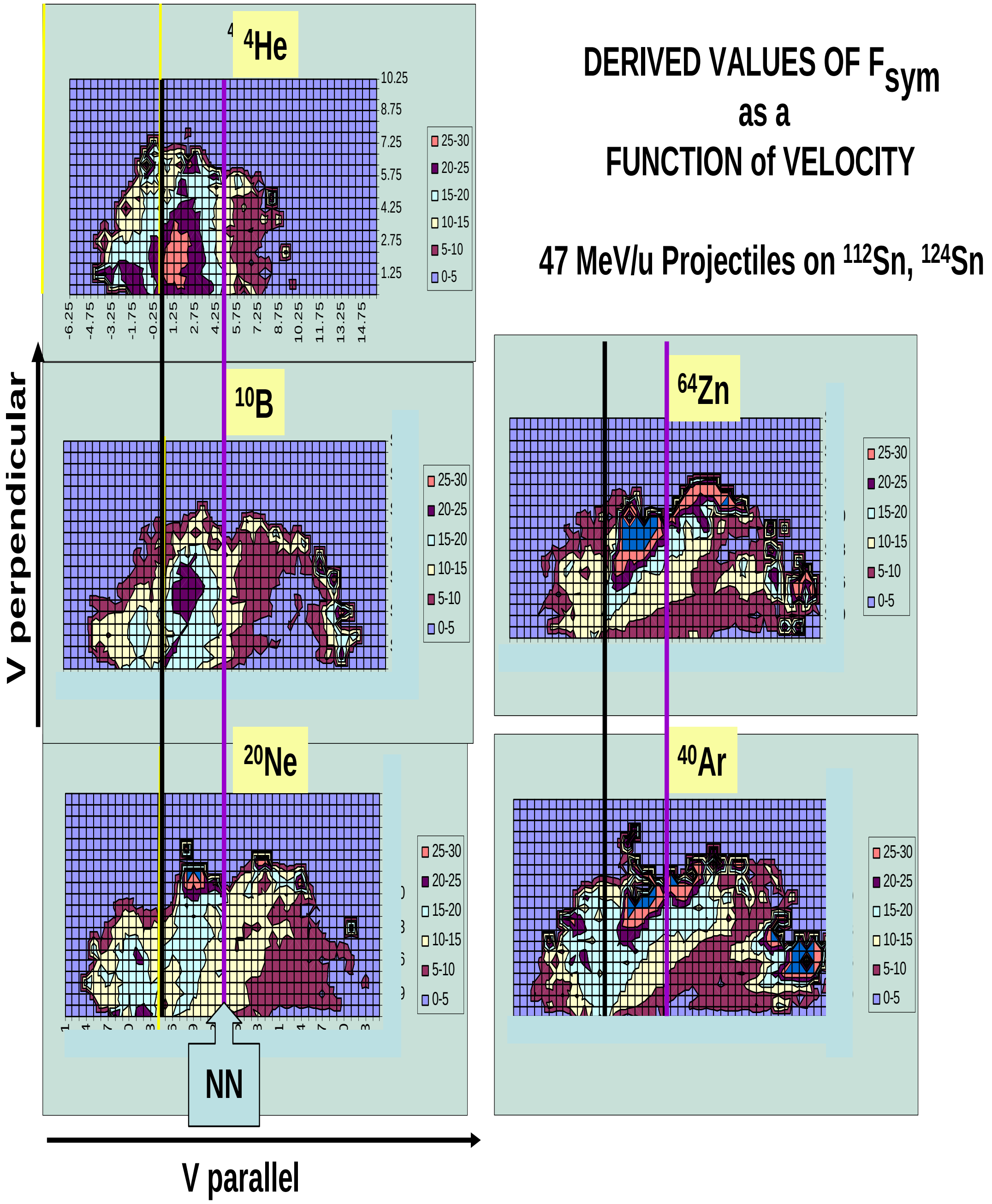

Fig. 54. Derived Values of Fsym as a Function of velocity.

CHAPTER VII

RESULTS AND CONCLUSIONS

The primary focus of this research was to isolate and characterize low density nuclear matter produced in the reactions of various 47A MeV projectiles with ^{112}Sn and ^{124}Sn target nuclei. Our results indicate that a low density nuclear gas consisting of nucleons and light clusters with A $\leq$ 4 is produced in these collisions. The dynamics of the collision process allow us to associate this gas with an assumed nucleon-nucleon or intermediate velocity source required to fit the global emission pattern. This source is most easily sampled at mid-rapidity in the invariant velocity plots where contributions from other sources are minimized. The total mass of this gas increases with projectile mass and is approximately 0.6 times the projectile mass. These gases appear to equilibrate at temperatures near 5 MeV and densities in the range of 0.03 to 0.10 times the normal nuclear density. They manifest a large degree of clusterization as predicted in various theoretical treatments of low density nuclear matter [39]. Table IX contains a summary of some of the parameters which have been derived for the low density matter produced in the five systems studied. For this purpose we have selected Bins in the V_{surf} plot corresponding to equal to 4.5-6.0 cm/ns and $V_{\perp}$ is in the range 0.0-5.0 cm/ns to form on the equilibrated systems. Only those Bins for which the isocaling parameters alpha have errors of less than 10% were included. Listed in the table for each value of $V_{\perp}$ are the values for the Albergo model temperatures and densities, the Roepke Model temperatures and densities, the symmetry free energies derived from the isocaling analysis and the alpha mass fractions. All the quantities are averaged over the 4.5-6.0 cm/ns range in V_{surf}.

In the following sections we discuss some of these results.

Table IX. $V_\perp$ is the particle perpendicular velocity in units of cm/ns, T_{alb} is the Albergo temperature in MeV, ρ_{alb} is the Albergo density in units of nuc/fm^3, F_{salb} is the Albergo symmetry free energy, T_{roe} is Roepke temperature in MeV, ρ_{roe} is Roepke density in nuc/fm^3, F_{sroe} is the Roepke symmetry free energy in MeV, and X_α is the Alpha mass fraction.

Beam	$V_\perp$	T_{alb}	ρ_{alb}	F_{salb}	T_{roe}	ρ_{roe}	F_{sroe}	X_α
^{64}Zn	4.25	7.38	0.00729	15.5	6.8	0.01339	16.9	0.225
	3.75	6.37	0.00652	13.9	5.99	0.01373	14.8	0.316
	3.25	5.67	0.0064	13.7	5.39	0.01613	14.5	0.414
	2.75	4.61	0.00587	9.53	4.48	0.01561	9.79	0.579
	2.25	4.61	0.00527	9.53	4.48	0.01561	9.79	0.579
	1.75	4.23	0.00457	8.52	4.15	0.01325	8.82	0.637
	1.25	3.77	0.0026	6.4	3.75	0.0053	6.54	0.634
	0.75	3.82	0.00272	3.87	3.79	0.00606	4.15	0.593
	0.25	3.75	0.00217	3.44	3.74	0.00388	3.53	0.592
^{40}Ar	4.25	8.05	0.00766	16.7	7.48	0.01259	18.0	0.159
	3.75	6.81	0.0067	13.6	6.42	0.01283	14.3	0.257
	3.25	5.89	0.00617	12.3	5.67	0.01283	12.9	0.361
	2.75	5.25	0.00558	13.0	5.08	0.01374	13.6	0.458
	2.25	5.11	0.00667	12.9	4.8	0.02273	14.2	0.535
	1.75	4.83	0.00662	9.32	4.57	0.02472	10.0	0.59
	1.25	4.45	0.00547	8.67	4.29	0.01929	9.25	0.618
	0.75	4.38	0.00563	8.9	4.24	0.02105	9.52	0.633
	0.25	4.38	0.00507	9.89	4.2	0.01631	10.4	0.616

Table IX Continued

Beam	$V_\perp$	T_{alb}	ρ_{alb}	F_{salb}	T_{roe}	ρ_{roe}	F_{sroe}	X_α
^{20}Ne	4.25	7.14	0.00471	13.8	6.97	0.0069	14.9	0.159
	3.75	6.44	0.00432	13.8	6.18	0.0069	14.7	0.231
	3.25	5.99	0.00474	13.1	5.75	0.00858	13.6	0.302
	2.75	5.49	0.0047	12.7	5.3	0.00952	13.0	0.381
	2.25	5.19	0.00503	14.6	5.02	0.01158	15.1	0.455
	1.75	5.0	0.00554	12.8	4.82	0.01498	13.7	0.525
	1.25	4.79	0.00526	11.9	4.65	0.0146	12.6	0.551
	0.75	4.58	0.00435	12.3	4.48	0.0106	12.5	0.55
	0.25	4.51	0.00464	9.83	4.4	0.01227	9.72	0.562
^{10}B	4.25	7.13	0.00314	12.4	6.9	0.00411	12.8	0.113
	3.75	6.58	0.00322	13.7	6.38	0.00448	14.4	0.167
	3.25	6.08	0.00322	11.8	5.92	0.00475	12.4	0.219
	2.75	5.75	0.00327	12.2	5.6	0.00509	12.7	0.265
	2.25	5.64	0.00386	14.2	5.48	0.00664	14.7	0.319
	1.75	5.3	0.00357	12.1	5.18	0.00625	12.5	0.359
	1.25	5.1	0.00339	11.1	4.99	0.00603	11.5	0.384
	0.75	5.26	0.00406	12.5	5.12	0.00792	13.4	0.379
	0.25	5.28	0.00428	6.28	5.12	0.0087	6.7	0.38
^{4}He	3.25	5.14	0.00152	9.21	5.67	0.00191	8.25	0.142
	2.75	4.71	0.0019	8.67	5.63	0.00235	7.38	0.174
	2.25	5.32	0.00185	7.79	5.21	0.00215	7.94	0.216
	1.75	4.78	0.00243	9.26	5.2	0.00279	8.52	0.249
	1.25	8.06	0.0027	6.68	5.31	0.00328	10.3	0.247
	0.75	5.25	0.00359	10.3	5.77	0.00524	9.42	0.246

A. Alpha Mass Fractions

As indicated in the introduction to this work, at low densities and high temperatures strong alpha clustering of nuclear matter is predicted. Such clusterization can be expected in a gas or the low density surface of an expanded high temperature nucleus. The data presented in the previous chapter provide experimental evidence for a large degree of alpha clustering in low density matter. In Table IX the degree of alpha clustering we observed in the experiments is quantified in terms of alpha mass fraction.

Our first order analysis of the particle yields was based upon the assumption of chemical equilibrium of free nucleons and clusters at low density, i.e., the clusters are assumed to be non interacting and to have their free binding energies. We designate this as the Albergo Model and present the temperatures and densities derived from this model in the previous chapter. In figure 55 we present the temperatures and densities derived from this model for several different temperatures (solid lines). As the temperature increases, the alpha mass fraction at a given density decreases.

In contrast to this simplest model, the Virial Equation of State model of Horowitz and Schwenk [39] takes particle interactions into account through the use of Virial coefficients derived from experimental scattering phase shifts. While the original work on the VEOS did not include A=3 clusters, this has now been remedied [43] and the authors of that work have provided us with calculated results for low density nuclear matter at several different temperatures. Since the VEOS model does not include competition with species heavier than alpha particles its range of applicability is confined to systems for which no additional species are important. In the astrophysical context this VEOS implies relatively low densities. At those low densities this is believed to set a benchmark for all other theoretical nuclear equations of state. The results of the Virial calculation are also presented in Figure 55 (dotted lines). We note that there are some differences from the Albergo Model results, suggesting that at densities above 0.001 nucleons/fm^3 the particle interactions are important.

The VEOS paper [39] employs the alpha mass fraction, X_α, to characterize the degree of alpha clustering at different densities and temperatures. As seen in table IX, we have determined experimental values of X_α as a function of velocity, for mid-rapidity emissions. For this purpose it was assumed that the unmeasured neutron multiplicity at a given velocity was the product of the $t/^3$He yield ratio times the proton yield for that velocity. This is consistent with the results of thermal equilibrium coalescence models [13], and consistent with experimental results [69]. In this way both the total mass yields and the mass fractions could be calculated.

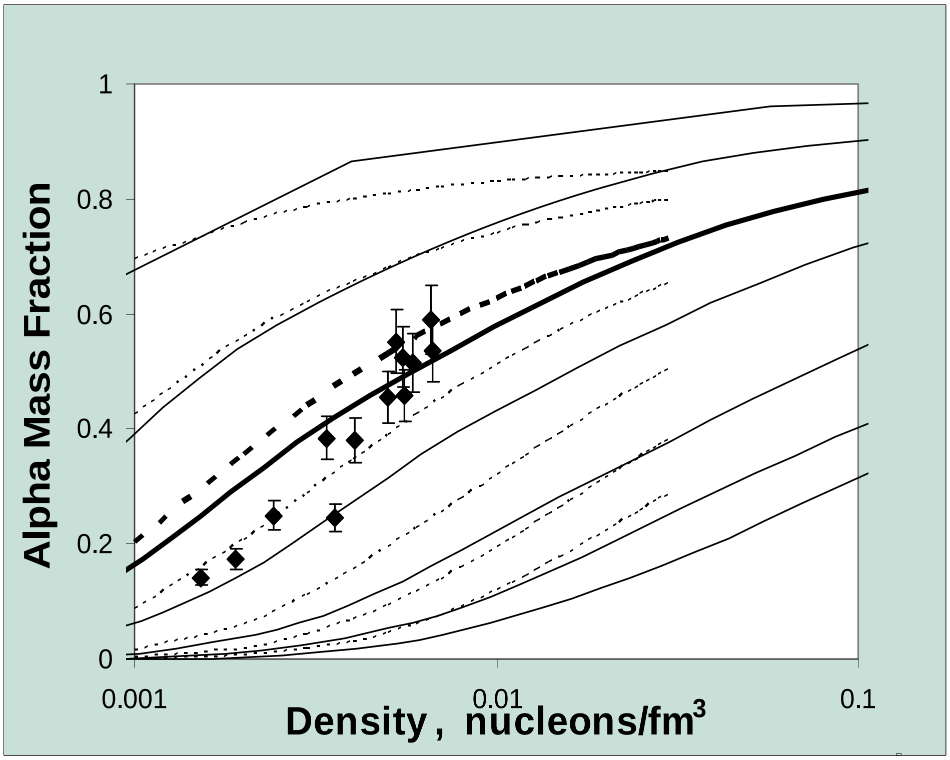

Fig. 55. Alpha mass fraction vs total nuclear density. Solid lines - Albergo Model's results and dotted lines - VEOS Model results. Solid points T = 5 MeV results from the Albergo Model.

From Table IX we have taken all Alpha mass fraction results with T_{albergo} between 4.75 and 5.25 MeV. We refer to these as the T = 5 results and plot them in Figure 55 where they may be compared with the calculated lines for T = 5 MeV. Here we note that the data plotted as a function of the "Albergo Density," are in reasonable agreement with the model calculations at the higher densities sampled but deviate more from the models at lower densities. This appears to be somewhat counter intuitive.

To this point, the analysis has explicitly assumed that at such low densities the chemical equilibrium model of Albergo et al. is applicable. However the differences between the results of the Albergo model calculation and those of the VEOS calculations, together with the data comparison suggest that, even at the densities sampled, particle-particle interactions are important. Thus more sophisticated treatments which are appropriate over a wider range of densities are clearly needed. Such treatments have in fact been attempted both in the astrophysical context and in nuclear matter studies. In the former, chemical equilibrium of free nucleons and light clusters, are in equilibrium with a heavier nucleus which serves as a surrogate for all heavier species. The system includes electrons and is charge neutral. Results of the two models most commonly employed for astrophysical calculations are presented in Figures 56 and 57. These are taken from tabulations provided by the authors [39, 38] and thus are not at exactly the same temperatures as chosen for Figure 55.

The most notable features of these calculations are the general decrease with increasing T and the the rapid decline in alpha mass fraction for a given T seen as heavier species become more competitive. The peaks in the mass fraction have been used by Horowitz and Schwenk to define the upper density limits, of applicability for their current VEOS model.

A more sophisticated treatment of clustering in low density matter is that of G.

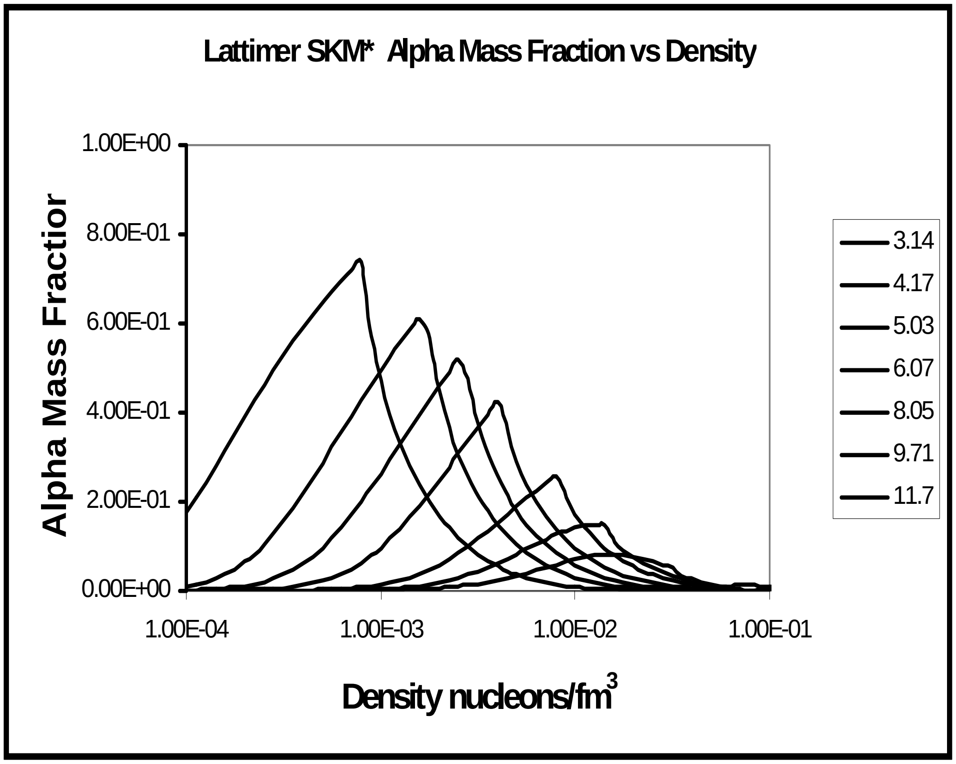

Fig. 56. Alpha mass fractions at different densities and temperatures from the Lattimer-Swesty Model

Roepke and his collaborators who explicitly treat the density-dependent in-medium modification of cluster properties. Nucleon correlations are calculated in a quantum statistical approach starting from a nucleon-nucleon potential and including the effects of the mean field and of Pauli blocking [44, 45]. They find that, the model of an ideal mixture of free nucleons and clusters applies to the low density limit (up to densities of about 0.001 fm^3). At higher baryon density medium effects are important. In Figure 58 values of the in-medium binding energies of A = 2, 3 and 4 clusters derived from this model, are plotted as a function of density [70] for T = 10 MeV. For a temperature of 10 MeV, the binding energies of the clusters decrease from the standard values (at 0 on the density axis) with increasing density and reach 0 at a point known as the Mott density. At this point the cluster is no longer bound relative to the surrounding

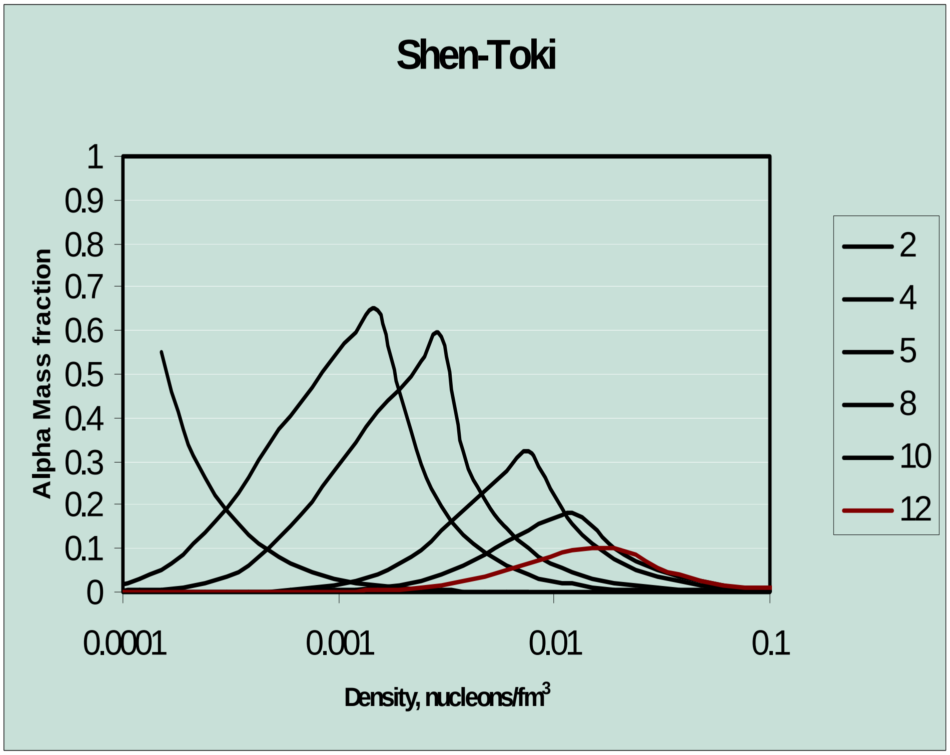

Fig. 57. Alpha mass fractions with different densities and temperatures from Shen–Toki model.

medium. For alpha particles this occurs near 0.1 times the normal density. This disappearance of the cluster binding energy in medium is closely related to the peaks in the calculated alpha mass fractions seen in Figure 56.

The Mott density for a cluster increases with temperature as is seen in Figure 59 where the calculated binding energy variations for deuterons and tritons are presented for both 10 and 20 MeV [70]. In addition to this, any collective motion of a cluster relative to the center of mass of the system in which it resides acts to decrease the rate of binding energy decrease with increasing density and further increase the Mott density. This effect is seen in Figure 59 where the binding energy shifts for tritons are calculated for increasing values of the total momentum relative to the medium [70]. There we see that as these momenta increase the Pauli blocking effect becomes

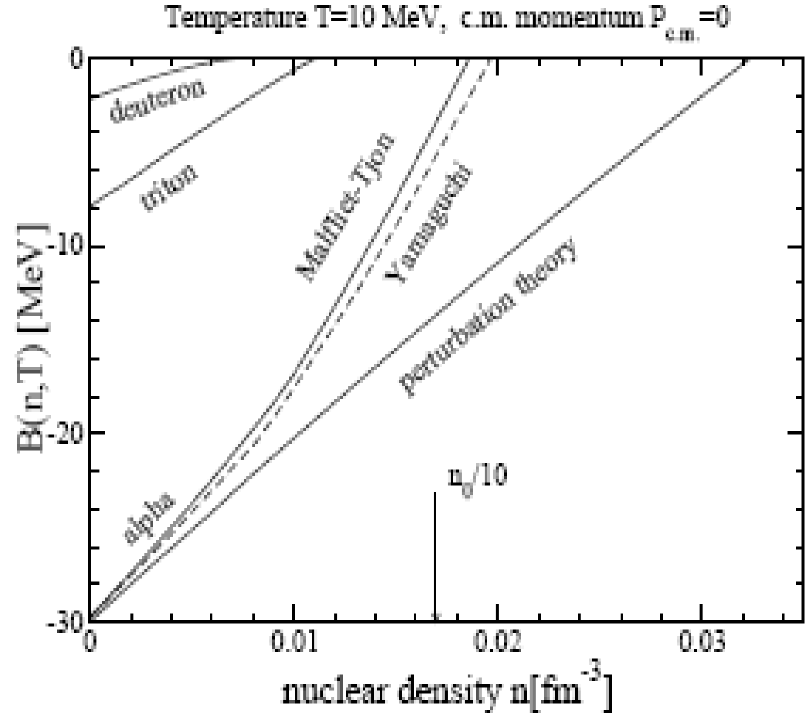

Fig. 58. Calculated in medium binding energies of light clusters at T = 10 MeV [70].

less important and the binding energy at any particular density moves closer to that of the free cluster.

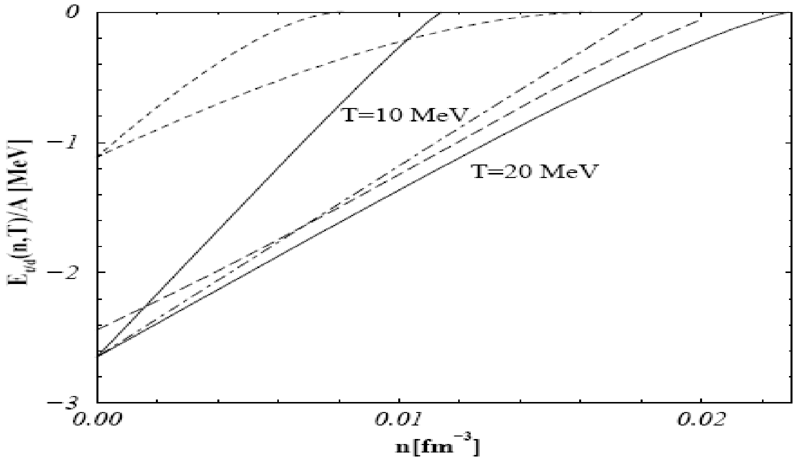

FIG. 3. Triton binding energy per nucleon (solid lines, Yamaguchi potential) as a function of the uncorrelated nuclear density at a given temperature T; long-dashed lines: corresponding pertubation result, dashed-dotted lines: Paris (EST) potential. Dashed lines show the Nd continuum threshold for $T = 10$ MeV (left) and $T = 20$ MeV (right).

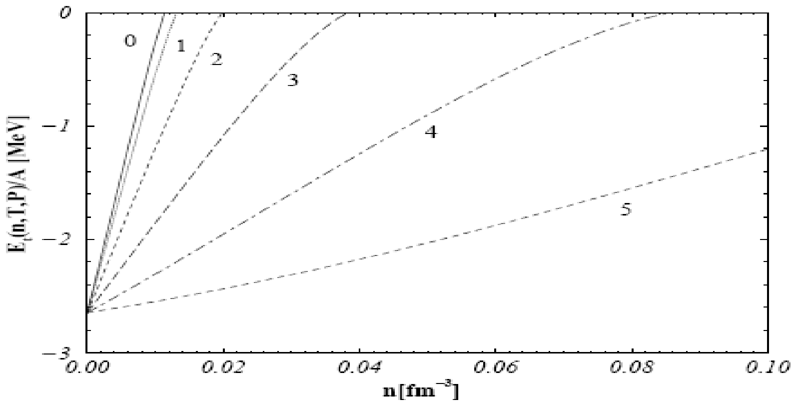

FIG. 4. Triton binding energy as a function of nuclear density at $T = 10$ MeV, and total momentum relative to the medium. From left to right: $P = 0, 1, 2, 3, 4, 5$ fm^{-1}.

Fig. 59. Difference of cluster binding cluster on T (top) and on cluster momentum in medium (bottom) [70].

Using this model, G. Roepke has made calculations of the low density symmetry energy for comparison to our experimental results [43]. That the alpha mass fractions predicted by this calculation differ significantly from those seen in the previous calculations is easily seen by comparison of the relevant figures, such as Figure 60. The major change reflects the calculated variation of the in-medium binding energies.

Clearly, if these binding energies are changing then the temperatures and densities derived from the simpler Albergo model, which assumes free cluster binding energies, are derived from yield ratios and only approximations to the actual temperatures and densities. Thus, to compare our results with the Roepke calculation results requires that we take account of the binding energy shifts. At this point the reader will note that, since both temperature and density are determined from observed yields of the species produced there is a correlation between the model assumed and the results presented. Recognizing this we proceed, arguing only that the ideal gas limit is probably not reached and that more sophisticated approach of Roepke demands these corrections.

G. Roepke has provided us with analytical formulae to calculate the binding energy shifts. The formulae assume no collective motion of the clusters relative to the medium. Any such contribution would reduce the rate of binding energy shift and increase the Mott densities for a given temperature. The formulae are:

$$\begin{aligned}
\Delta E_d^{\text{Pauli}} &= \frac{\rho_p+\rho_n}{T^{3/2}}\left\{\frac{8269.8}{(0.042995+1.1125/T)^{1/2}}\right. \\
&\quad \left. -15301\mathrm{e}^{1.1125/T}\mathrm{Erfc}[(0.042995+1.1125/T)^{1/2}]\right\}, \\
\Delta E_t^{\text{Pauli}} &= \left(\frac{2}{3}\rho_p+\frac{4}{3}\rho_n\right)2939.7(1+0.1114T)^{-3/2}, \\
\Delta E_h^{\text{Pauli}} &= \left(\frac{4}{3}\rho_p+\frac{24}{3}\rho_n\right)3527.9(1+0.14519T)^{-3/2},
\end{aligned}$$

$$\Delta E_{\alpha}^{\text{Pauli}} = (\rho_p + \rho_n)\, 4277.5(1 + 0.08422T)^{-3/2}, \tag{7.1}$$

where ρ_p and ρ_n are the total proton and neutron densities, T is the temperature and Erfc is the associated error funaction.

In order to determine the binding energy shifts required we use the Albergo model temperatures and densities as input and carry out a single step iteration to determine new temperatures and densities. These are the temperatures and densities referred to as Roepke temperatures and Roepke densities in the Table IX. Temperatures change only slightly. The lower densities (Roepke density < 0.005 nucleons/ fm^3) hardly change, reflecting the fact that the binding energy changes are small at low density. At higher densities the Roepke densities are about 2 times the Albergo model densities.

In Figure 60 we present the alpha mass fraction results for T Roepke = 5 ± 0.25 MeV, plotted as a function of the new Roepke density and compare them to the results of the various calculations which we have discussed.

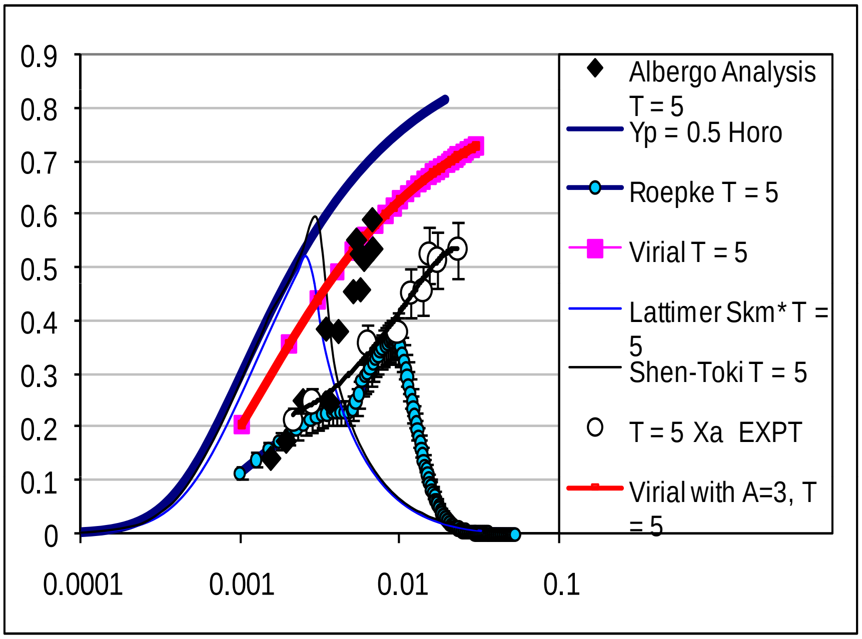

Fig. 60. Alpha mass fraction in low density matter.

At the lower densities, the agreement between the data and the calculation of Roepke is quite good. However, the turnover at the calculated Mott density is not observed. We believe that the reason for this is that the technique that we use, selection of the mid-rapidity particle group which constitutes our low density nuclear gas, isolates a gas of particles of A $\leq$ 4 which, constituted of scattered nucleons and clusters formed from these nucleons, exists in a momentum sphere that is initially detached from that of the surrounding matter and thus has some collective motion relative to the bulk of the medium. In this case the Mott density for T = 5 is shifted to a higher density. Clusters with A>4 associated with this NN source are very rare. A parallel analysis of these systems by C. Bottoso indicates that inclusion the ^{6}Li and ^{7}Li clusters will change the derived alpha mass fractions by only $\sim$ 1% [44, 71]. This result is also supported by recent calculations taking into account the dynamic time limitations to cluster formation [44, 72].

B. Symmetry Free Energies

In their VEOS paper, Horowitz and Schwenk have pointed out that extensive alpha clustering in the low density gas leads naturally to an increase in the symmetry energy and the symmetry free energy for the clustering system [39]. See Figure 61 which presents the VEOS results for unclustered and clustered matter at T = 4 MeV. In the clustered matter the symmetry energy and symmetry free energy at low density are both much larger than in the unclustered matter. It is also noteworthy that in contrast to the unclustered case, the symmetry energy in the clustered system is larger than the symmetry free energy. In this calculation the signs of the symmetry entropy coefficients at low density, are different in the two cases considered.

As discussed in the previous chapter, we have derived symmetry free energies from the ejectile yield data by employing an isoscaling analysis. The resultant symmetry free energy coefficients are presented in Table IX. For Roepke temperature T = 5 MeV, the values are plotted against density in Figure 62. There they are compared to those calculated by Roepke for clustering matter and to the T = 0 values (E_{sym}) which are predicted by the Gogny effective interaction for uniform density nucleonic matter [73]. At low density, the experimentally derived symmetry energies reported in Fig. 62 are far above those obtained in common effective interaction calculations and reflect the cluster formation, primarily of alpha particles, not included in such calculations.

In Kowalski et al. [43] the symmetry entropy coefficients were also derived from the experimental data. In the present work we find that the differences between the entropies of the two systems are small and it is difficult to extract a meaningful symmetry entropy coefficient. Roepke has calculated these values in his model. In Table IX we show the symmetry energies which are derived from our measurements for T = 5 MeV if the symmetry entropy coefficients of the Roepke calculation are assumed to be correct,

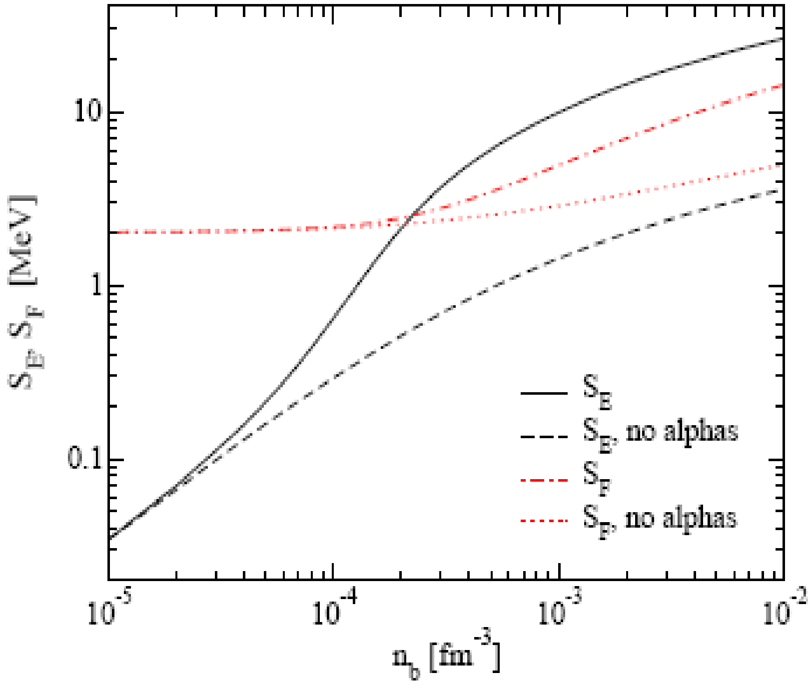

Fig. 61. Calculated densities dependence of symmetry energy and symmetry free energy in unform nuclear matter and clustered matter for T = 4 Mev and Yp = 0.5 by Horowitz.

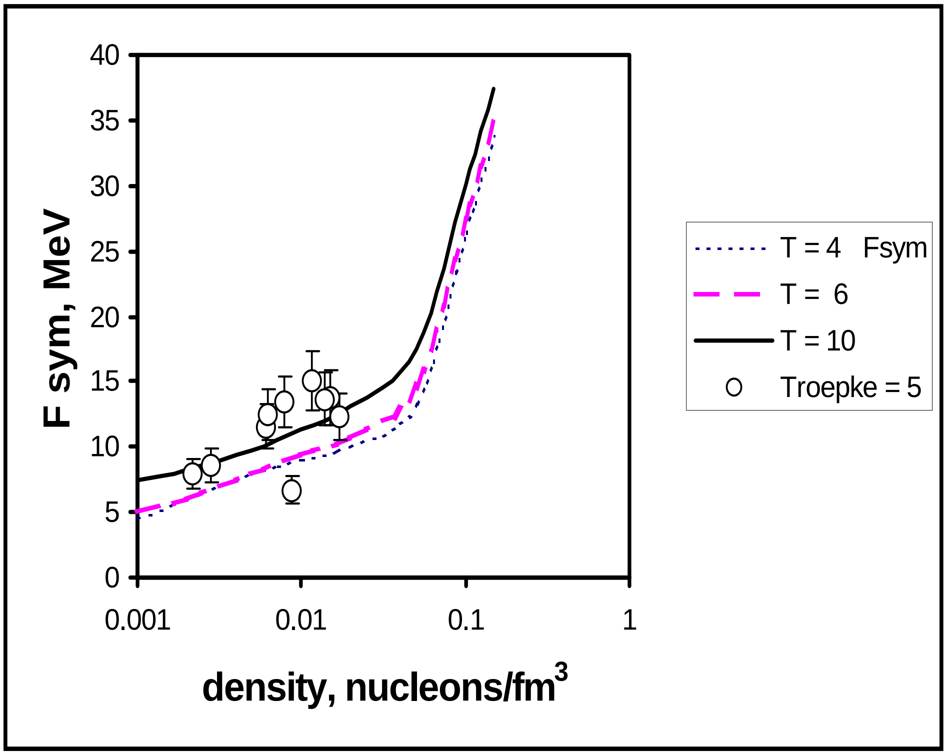

Fig. 62. Symmetry free energy vs density. Lines–Results of Roepke calculation, open points – Experimental Resluts for T = 5 MeV, with both T and density based on Roepke model.

C. Possible Future Directions

We finish with a brief discussion of some futher analyses which might be done with these data and suggestions of future work in this area.

1. Symmetry free energies and symmetry energies at higher densities

Our velocity plots for the symmetry free energy clearly indicate a wide variation of F_{sym} values over different regions of velocity. The most natural explanation of this is a wide range of densities being sampled. In recent times the extraction of symmetry energies at somewhat higher densities has been attempted by a number of groups using various techniques. However, in essentially all of the reaction based symmetry energy determinations previously reported there are significant uncertainties of the actual densities (and temperatures) being sampled. For the low density systems sampled in this work we believe that these are under much better control. However, these techniques are not applicable at much higher densities. Thus, while various observation indicate that the values of F_{sym} in the 20 - 25 MeV range seen in the TLF region of the velocity plots reflect emission from near normal density nuclei and the decrease in symmetry free energy as we move toward the mid-rapidity region reflects a lowering of the density, quantitative extraction of the density is difficult. Our previous work suggests two different approaches to determining the densities in the TLF (liquid) region and both will be tested in the near future. If these methods are successful we believe we should be able to construct an experimental symmetry energy curve valid in the density range $0.03 \leq \rho/\rho_0 \leq 1$.

The present data also constitute an important resource for investigations of other observables which have been predicted to be sensitive to the symmetry energy. Among these are ratios of triton/^{3}He emission and differential neutron and proton flow- as manifested in proton-deuteron flow comparisons [74, 75].

2. Low density matter and Bose Condensates in nuclei

The ability to isolate low density matter in near Fermi Energy collisions and the high degree of alpha clustering which is observed suggest that we search for evidence of Bose Condensates which are predicted to occur in the density and temperature range which we are exploring [44, 75].

The phenomena in quantum many-particle systems about the formation of quantum condensates, particularly, strongly coupled fermion systems where bound states arise is very intersting [44]. In the low-density limit, where even-number fermionic bound states can be considered as bosons, Bose-Einstein condensation may be expected to occur at low temperatures. Condensates can be investigated in systems where the crossover from Bardeen-Cooper-Schrieffer (BCS) pairing to Bose-Einstein condensation (BEC) can be observed. Strong correlations in nuclear matter can be indicated by the formation of bound states which can make changes or even disappear with the density changing. In reference [44], Roepke et al. point that in the low-density region the transition to triplet pairing is not realized, because four-particle correlations are more dominant there. At chemical equilibrium, in the low-density region at low temperatures the dominant part of nuclear matter will be found in Alpha particles which are much more strongly bound than the deuteron. Therefore, the triplet pairing (Bose condensation of deuterons) has to compete with quartetting (Bose condensation of Alpha particles). As an example of the type of results which are obtained theoretically we present Figure 63 from reference [44]. This figure shows the critical temperature of neutron-proton triplet pairing $\mathrm{T_t}$ and quartetting $\mathrm{T_4}$ obtained from the solution of the Gorkov equation as a function of the uncorrelated density $\mathrm{n_1}$. In the low-temperature limit, with increasing chemical potential the transition to quartetting occurs prior to the pairing transition. A simple argument for the behavior of T_4 and T_t as a function of n_1 in the limit of low densities can be given from the law of mass fraction, which is discussed in this article.

This calculation leads to Bose Condensation of both alpha and deuterons at low density. In addition to pursuing this question with the present data the group is currently planning experiments on alpha cluster nuclei which might show a more natural predilection to evolve into a Bose Condensate. The definitive experimental signature of the phase transition to the condensate is yet to be determined but we believe that the cluster formation itself continues to be an interesting area of investigation [76, 77]. We are currently discussing this problem with A. Bonasera, G. Roepke and S. Shlomo, all theorists interested in clustering and quantum phase changes in nuclear matter.

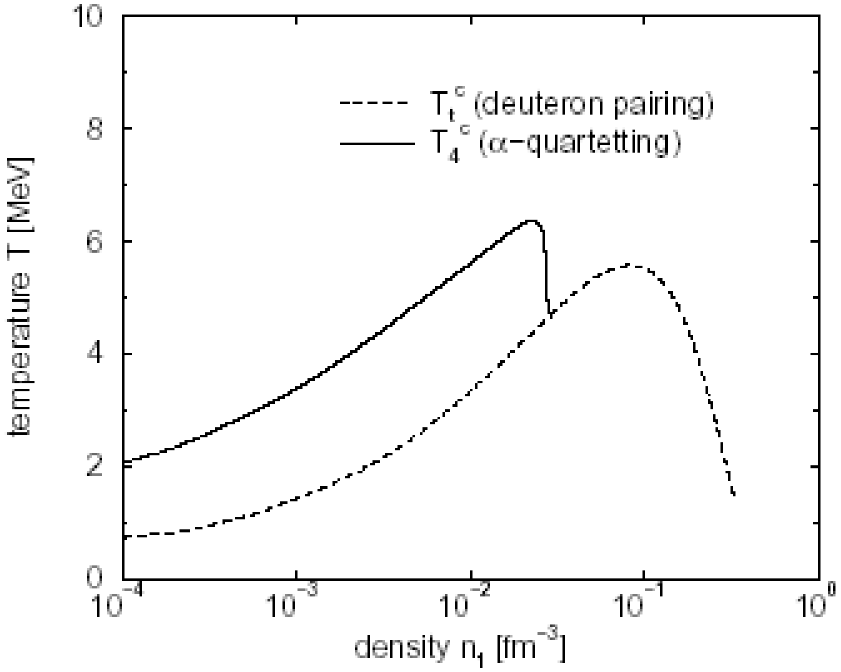

Fig. 63. Alpha and deuteron Bose condensation by Roepke [44].

REFERENCES

[1] J. B. Natowitz, K. Hagel, Y. Ma, M. Murray, L. Qin, S. Shlomo, R. Wada, J. Wang, Phys. Rev. C **66**, 031601 (2002).

[2] E. Suraud *et al.*, Prog. Part. Nucl. Phys. **23**, 357 (1989).

[3] D. H. E Gross Phys. Rep. **279**, 119 (1997).

[4] J. Bondorf *et al.*, Nucl. Phys. **A433**, 321 (1985).

[5] W. A. Friedman, Phys. Rev. C **42**, 667 (1990).

[6] P. B. Gossiaux *et al.*, Phys. Rev. C **56**, 2109 (1997).

[7] J. P. Bondorf *et al.*, Phys. Lett. **B359**, 261(1995).

[8] N. Marie *et al.* Phys. Rev. C **58**, 256 (1998).

[9] L. P. Csernai*et al.*, Phys. Rep. **131**, 223 (1986).

[10] H. Sato *et al.*, Phys. Lett. **B98**, 153 (1981).

[11] T. C. Awes *et al.*, Phys. Rev. C **24**, 89 (1981).

[12] D. Prindle *et al.*, Phys. Rev. C **57**, 1305 (1998).

[13] K. Hagel, R. Wada, J. Cibor, M. Lunardon, N. Marie, R. Alfaro, W. Shen, B. Xiao, Y. Zhao, Z. Majka, J. Li, P. Staszel, B.-A. Li, M. Murray, T. Keutgen, A. Bonasera, and J. B. Natowitz, Phys. Rev. C **62**, 034607 (2000).

[14] R. Wada, T. Keutgen, K. Hagel, Y. G. Ma, J. Wang, M. Murray, L. Qin, P. Smith, J. B. Natowitz, R. Alfarro, J. Cibor, M. Cinausero, Y. El Masri, D. Fabris, E. Fioretto, A. Keksis, M. Lunardon, A. Makeev, N. Marie, E. Martin,

A. Martinez-Davalos, A. Menchaca-Rocha, G. Nebbia, G. Prete, V. Rizzi, A. Ruangma, D. V. Shetty, G. Souliotis, P. Staszel, M. Veselsky, G. Viesti, E. M. Winchester, S. J. Yennello, Z. Majka and A. Ono, Phys. Rev. C, Phys. Rev. C **69**, 044610 (2004).

[15] A. Ono, Phys. Rev. C **59**, 853 (1999).

[16] B. A. Li, Phys. Rev. C **69**, 034614 (2004).

[17] G. Ferini *et al.*, Phys. Rev. Lett. **97**, 202301 (2006).

[18] F. Haddad *et al.*, Phys. Rev. C **53**, 1437 (1996).

[19] W. D. Myers *et al.*, Nucl. Phys. **A601**, 141 (1996).

[20] G. Q. Li *et al.*, Phys. Rev. C **48**, 1702 (1994).

[21] Web Linkage for Figure of Binding Engery per Nucleon of Some Typical Nuclei, http://www4.nau.edu/meteorite/Meteorite/Images/BindingEnergy.jpg, Northern Arizona Meteorite Laboratory, 2008.

[22] C. F. V. Weizsacker, Z. Phys. **96**, 431 (1935).

[23] A. L. Keksis, N/Z Equilibration In Deep Inelastic Collisions and the Fragmentation of the Resulting Quasiprojectiles, Ph.D dissertation, Texas A&M University, College Station, 2007.

[24] K. S. Krane, *Introductory Nuclear Physics* (John Wiley & Sons, USA, 1998).

[25] W. N. Cotting and D. A. Greenwood, *An Introduction to Nuclear Physics* (Cambridge University Press, NY, 2001).

[26] G. Friedlander *et al.*, *Nuclear and Radiochemistry* 3rd Edition (John Wiley &Sons, New York, 1981).

[27] G. Audi *et al.*, Nucl. Phys. **A729**, 337 (2003).

[28] P. Moller *et al.*, Atomic Data and Nuclear Data Tables **59**, 185 (1995).

[29] B. A. Li, C. M. Ko and W. Bauer, Inter. Jour. Mod. Phys. **E7**, 147 (1998).

[30] J. Iglio *et al.*, Phys. Rev. C **74**, 024605 (2006).

[31] B. A. Li *et al.*, J. Phys. G. Nucl. Part. Phys. **35** (2008).

[32] D. J. Nice *et al.* Astrophys. J. **634**, 1242 (2005).

[33] J. M. Lattimer *et al.* Phys. Rep. **333**, 121 (2000).

[34] G. Tabacaru *et al.* NIM **A428**, 379 (1999).

[35] W. H. Lee, Rev. Mex. AA **10**, 176 (2001).

[36] S. Wanajo, Astrophys. J **606**, 1057 (2004).

[37] D. Arnett, *Supernovae and Nucleosynthesis*, Princeton University Press, Princeton, NJ, 1996.

[38] J. M. Lattimer and M. Prakash, Phys. Rep. **333**, 121 (2000).

[39] C. J. Horowitz and A. Schwenk, ArXiv preprint nucl-th/0507033 (2005).

[40] E. O'Connor *et al.*, arXiv:nucl-th/0702044, in press, Phys. Rev. C.

[41] M. B. Tsang, W. A. Friedman, C. K. Gelbke, W. G. Lynch, G. Verde, and H. S. Xu, Phys. Rev. Lett. **86**, 5023-5026 (2001).

[42] M. B. Tsang, W. A. Friedman, C. K. Gelbke, W. G. Lynch, G. Verde, H. S. Xu, Phys. Rev. C **64**, 041603 (2001).

[43] S. Kowalski *et al.*, Phys. Rev. C **75**, 014601 (2007).

[44] G. Roepke, A. Schnell, P. Schuck and P. Nozieres, Phys. Rev. Lett. **80**, 3177 (1998).

[45] G. Roepke, Private Communication.

[46] H-J Schulze *et al.*, Phys. Rev. C **74**, 058801 (2006).

[47] A. W. Steiner and Bao-An Li Phys. Rev. C **72**, 041601R (2005).

[48] J. Wang, R. Wada, T. Keutgen, K. Hagel, Y. G. Ma, M. Murray, L. Qin, A. Botvina, S. Kowalski, T. Materna, J. B. Natowitz, R. Alfarro, J. Cibor, M. Cinausero, Y. El Masri, D. Fabris, E. Fioretto, A. Keksis, M. Lunardon, A. Makeev, N. Marie, E. Martin, Z. Majka, A. Martinez-Davalos, A. Menchaca-Rocha, G. Nebbia, G. Prete, V. Rizzi, A. Ruangma, D. V. Shetty, G. Souliotis, P. Staszel, M. Veselsky, G. Viesti, E. M. Winchester, S. J. Yennello, W. Zipper, A. Ono, Phys. Rev. C **72**, 024603 (2005).

[49] J. Wang, T. Keutgen, R. Wada, K. Hagel, Y. G. Ma, M. Murray, L. Qin, P. Smith, J. B. Natowitz, R. Alfaro, J. Cibor, A. Botvina, M. Cinausero, Y. El Masri, D. Fabris, A. Keksis, S. Kowalski, M. Lunardon, A. Makeev, N. Marie, E. Martin, Z. Majka, A. Martinez-Davalos, A. Menchaca-Rocha, G. Nebbia, S. Moretto, G. Prete, V. Rizzi, A. Ruangma, D. V. Shetty, G. Souliotis, P. Staszel, M. Veselsky, G. Viesti, E. M. Winchester, S. J. Yennello, W. Zipper, A. Ono, Phys. Rev. C **71**, 054608 (2005).

[50] J. Wang, T. Keutgen, R. Wada, K. Hagel, S. Kowalski, T. Materna, L. Qin, Z. Chen, J. B. Natowitz, Y. G. Ma, M. Murray, A. Keksis, E. Martin, A. Ruangma, D. V. Shetty, G. Souliotis, M. Veselsky, E. M. Winchester, S. J. Yennello, D. Fabris, M. Lunardon, S. Moretto, G. Nebbia, S. Pesente, V. Rizzi, G. Viesti, M. Cinausero, G. Prete, J. Cibor, W. Zipper, Z. Majka, P. Staszel, Y. El Masri, R. Alfarro, A. Martinez-Davalos, A. Menchaca-Rocha, A. Ono, Phys. Rev. C **75**, 014604 (2007).

[51] L. P. Csernai and J. I. Kapusta, Phys. Rep. **131**, 223 (1986).

[52] A. Z. Mekjian, Phys. Rev. C **17**, 1051 (1978); Phys. Rev. Lett. **38**, 640 (1977); Phys. Lett. **B89**, 177 (1980).

[53] J. Cibor *et al.*, in *Isospin Physics in Heavy-Ion Collisions at Intermediate Energies*, edited by Bao-An Li and W. Udo Schroeder, (NOVA Science Publishers, Inc., New York, 2001).

[54] J. Cibor, R. Wada, K. Hagel, M. Lunardon, N. Marie, R. Alfaro, W. Q. Shen, B. Xiao, Y. Zhao, J. Li, B. A. Li, M. Murray, J. B. Natowitz, Z. Majka and P. Staszel, Phys. Lett. **B473**, 29 (2000).

[55] R. P. Schmitt, L. Cooke, G. Derrig, D. Fabris, B. Hurst, J.B. Natowitz, G. Nebbia, D. O'Kelly, B. Srivastava , B. Turmel, D. Utley, H. Utsonomiya and R. Wada, Nucl. Inst. and Meth. **A354**, 487 (1995).

[56] R. Lacey, N. N. Ajitanand and J. M. Alexander, Phys. Rev. C **37**, 2561 (1988).

[57] R. Lacey, N. N. Ajitanand and J. M. Alexander, Phys. Lett. **B191**, 253 (1987).

[58] M. Cinausero, G. Prete, D. Fabris, G, Nebbia, G. Viesti, G. X. Dai, K. Hagel, J. Li, Y. Lou, J. B. Natowitz, D. Utley, R. Wada, N. Gelli, F. Lucarelli and M.

Colonna, Phys. Lett. **B383**, 372 (1996).

[59] H. Shen et al., Nucl. Phys. **A637**, 435 (1998); Prog. Theor. Phys. **100**, 1013 (1998).

[60] J. M. Lattimer and F. D. Swesty, Nucl. Phys. **A535**, 331 (2001).

[61] M. Beyer, S. A. Sofianos, C. Kuhrts, G. Roepke, P. Schuck, Phys. Lett. **B488**, 247 (2000).

[62] M. Beyer, S. Strauss, P. Schuck, S. A. Sofianos, Eur. Phys. J. **A22**, 261 (2004).

[63] NIMROD Webpage, http://cyclotron.tamu.edu/nimrod.htm, Cyclotron Institute, 2000.

[64] T. Keutgen, Private Communication.

[65] E. Bell, N/Z Equilibration, Ph.D dissertation, Texas A&M University, College Station, 2005.

[66] The Stopping and Range of Ions Webpage, http://www.srim.org, J. F. Ziegler *et al.*, 2000.

[67] ROOT webpage, http://root.cern.ch, Rene Brun and Fons Rademakers, 2008.

[68] S. Albergo, S. Costa, E. Costanzo, and A. Rubbino, Nuovo Cimento **A89**, 1 (1985).

[69] C. M. Famiano *et al.*, Phys. Rev. Lett. **97**, 057601 (2006).

[70] M. Beyer, W. Schadow, C. Kurhts and G. Roepke Phys. Rev. C **60**, 034004 (1999).

[71] P. Schuck, M. Beyer, G. Roepke, W. Schadow, and A. Schell, Few-Body Suppl.**12** (2000) 50-59.

[72] H. H. Wolter, J. Rizzo, M. Colonna, M. Di Toro, V. Greco, V. Baran, M. Zielinska-Pfabe, arXiv:0712.2187 (2007).

[73] J. Decharge and D. Gogny, Phys. Rev. C **21**, 1568 (1980).

[74] L-W Chen, C. M. Ko, B-A Li, Phys. Rev. C **72**, 064309 (2005).

[75] B-A Li, L-W Chen, C. M. Ko, Phys. Rep. **464**, 113 (2008).

[76] A. Sedrakian, H. Muther and P. Schuck, Nucl. Phys. **A766**, 97 (2006).

[77] P. Demo and Z. Kozisek J. Phys G. Nucl. Part. Phys. **23**, 971 (1997).

APPENDIX A

SPECTRA OF d, t, ^{3}He, AND ^{4}He AFTER SECOND NORMALIZATION

The typical light particle spectra of third ring from system ^{64}Zn+^{112}Sn.

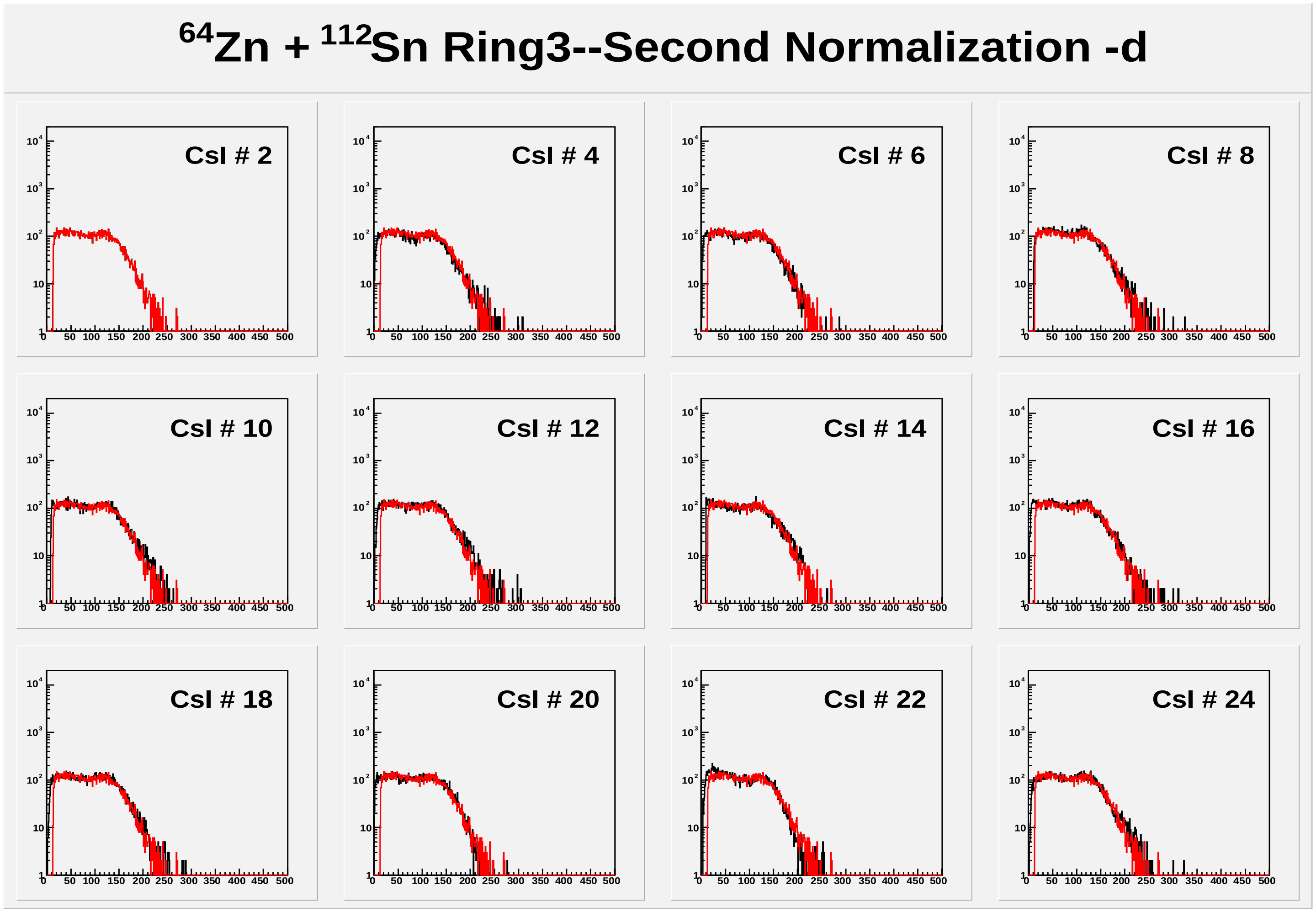

Fig. 64. X axis is energy in MeV. Y axis is the counts in log scale.

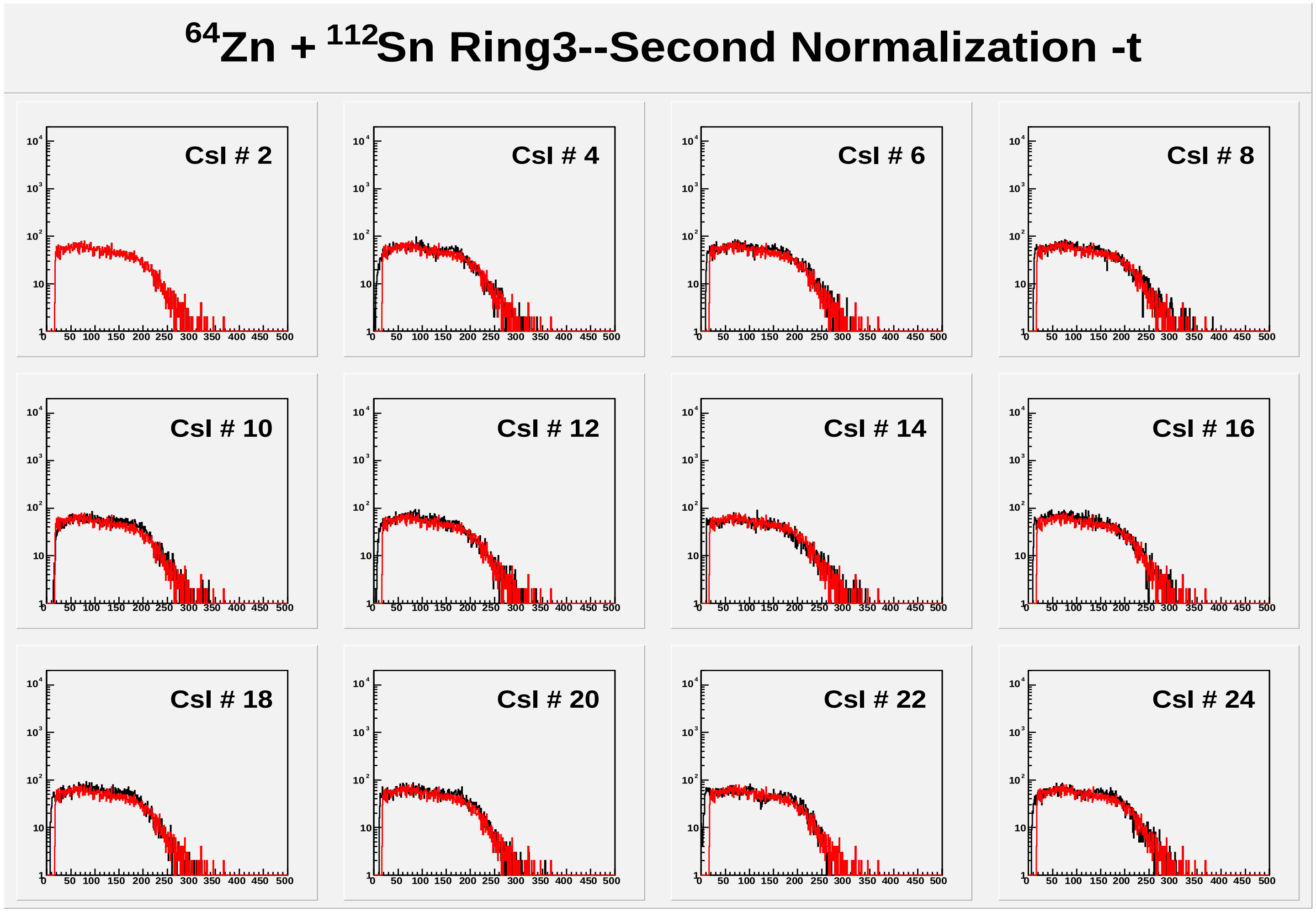

Fig. 65. X axis is energy in MeV. Y axis is the counts in log scale.

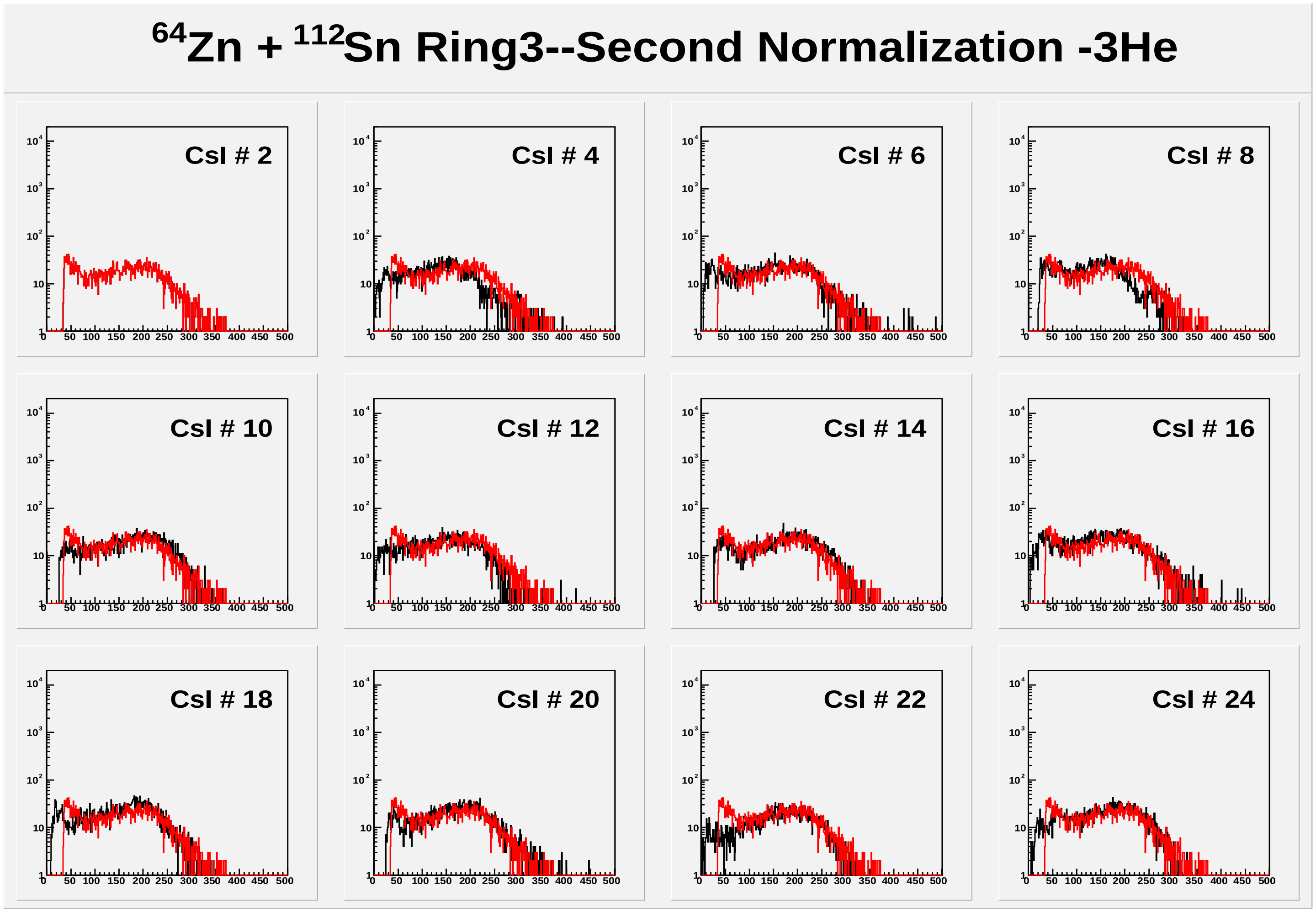

Fig. 66. X axis is energy in MeV. Y axis is the counts in log scale.

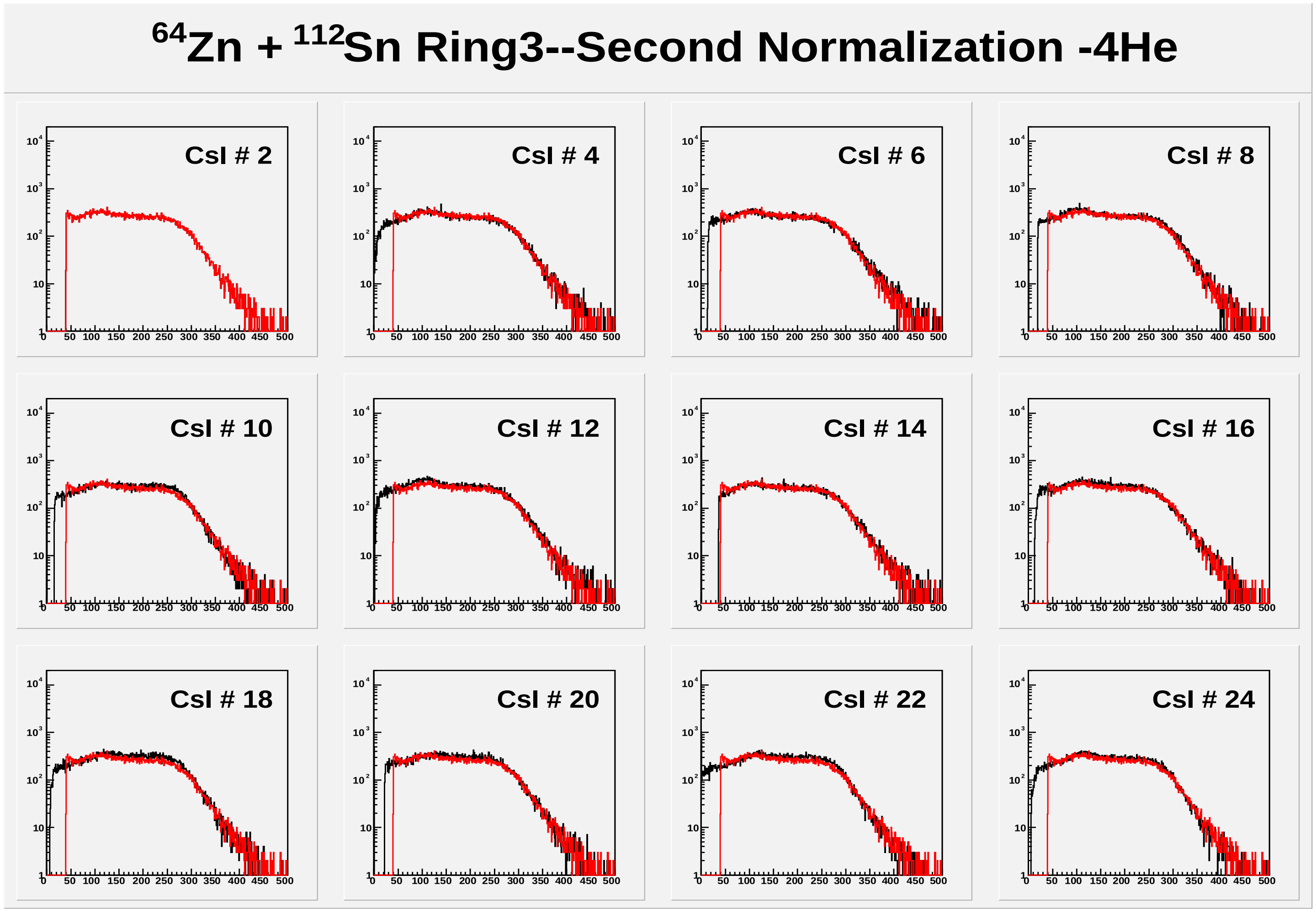

Fig. 67. X axis is energy in MeV. Y axis is the counts in log scale.

APPENDIX B

ANGULAR DISTRIBUTION SPECTRA IN BIN4

The differential angular distributions of the particle multiplicity are listed.

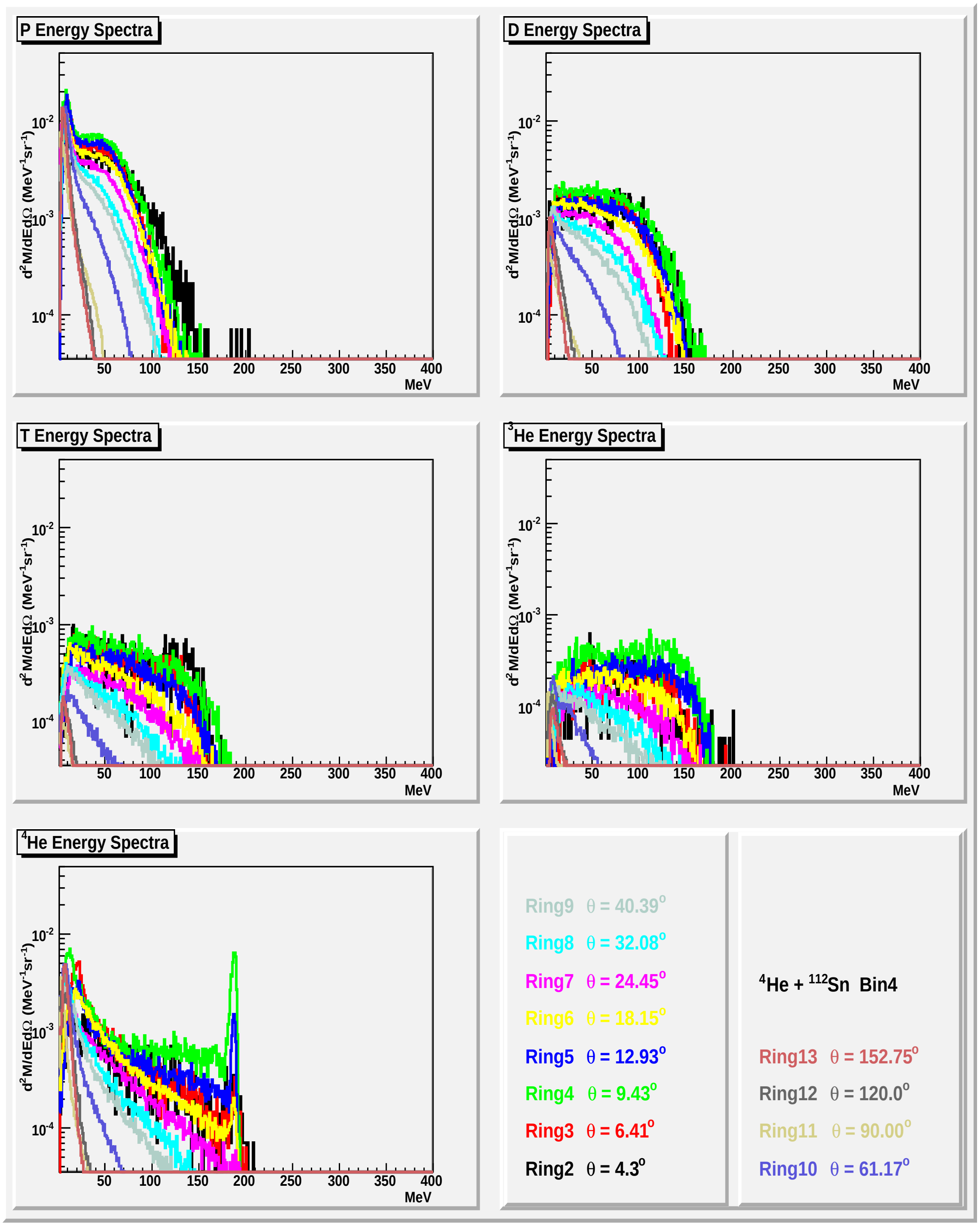

Fig. 68. X axis is energy in MeV. Y axis is the multiplicity distribution

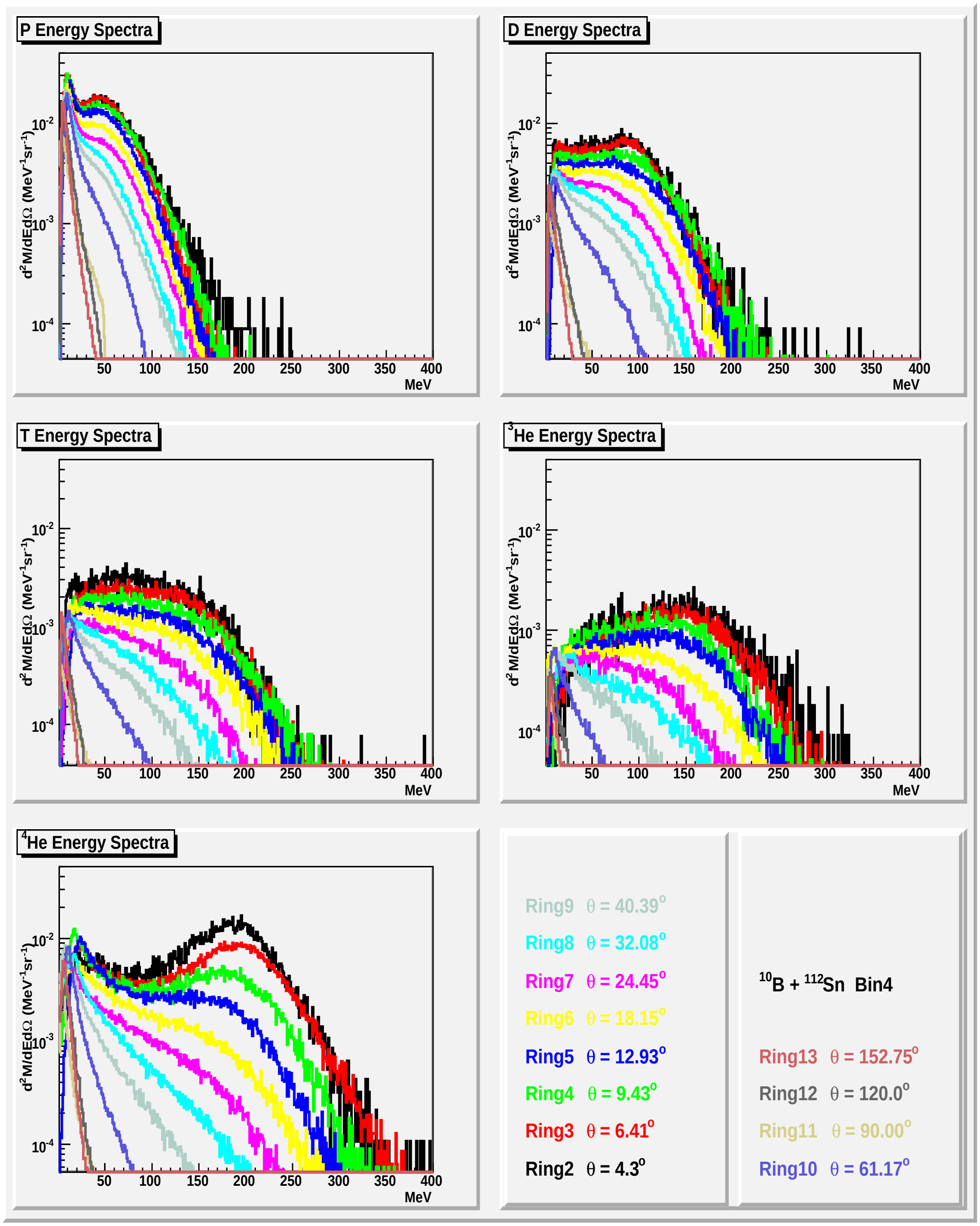

Fig. 69. X axis is energy in MeV. Y axis is the multiplicity distribution

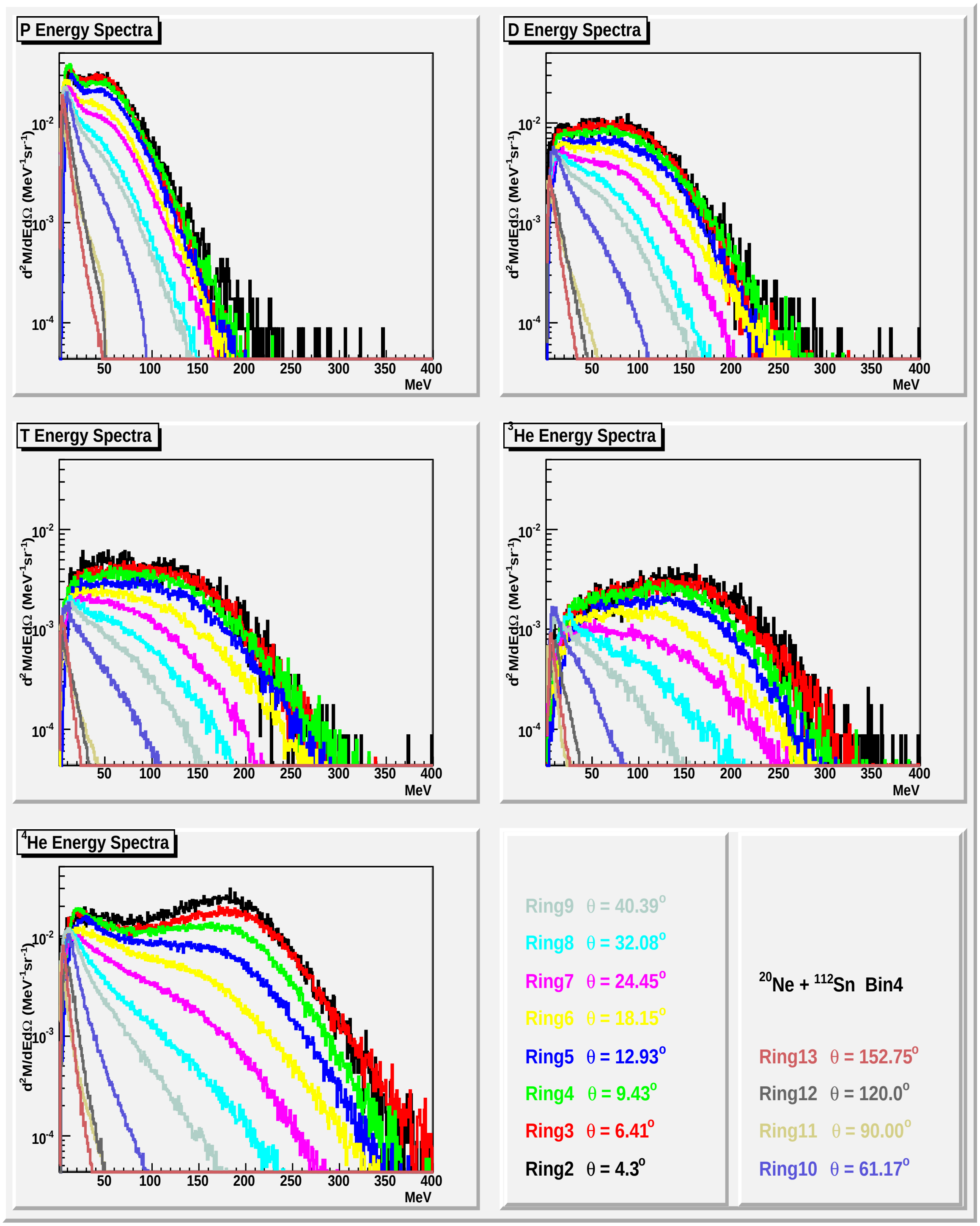

Fig. 70. X axis is energy in MeV. Y axis is the multiplicity distribution

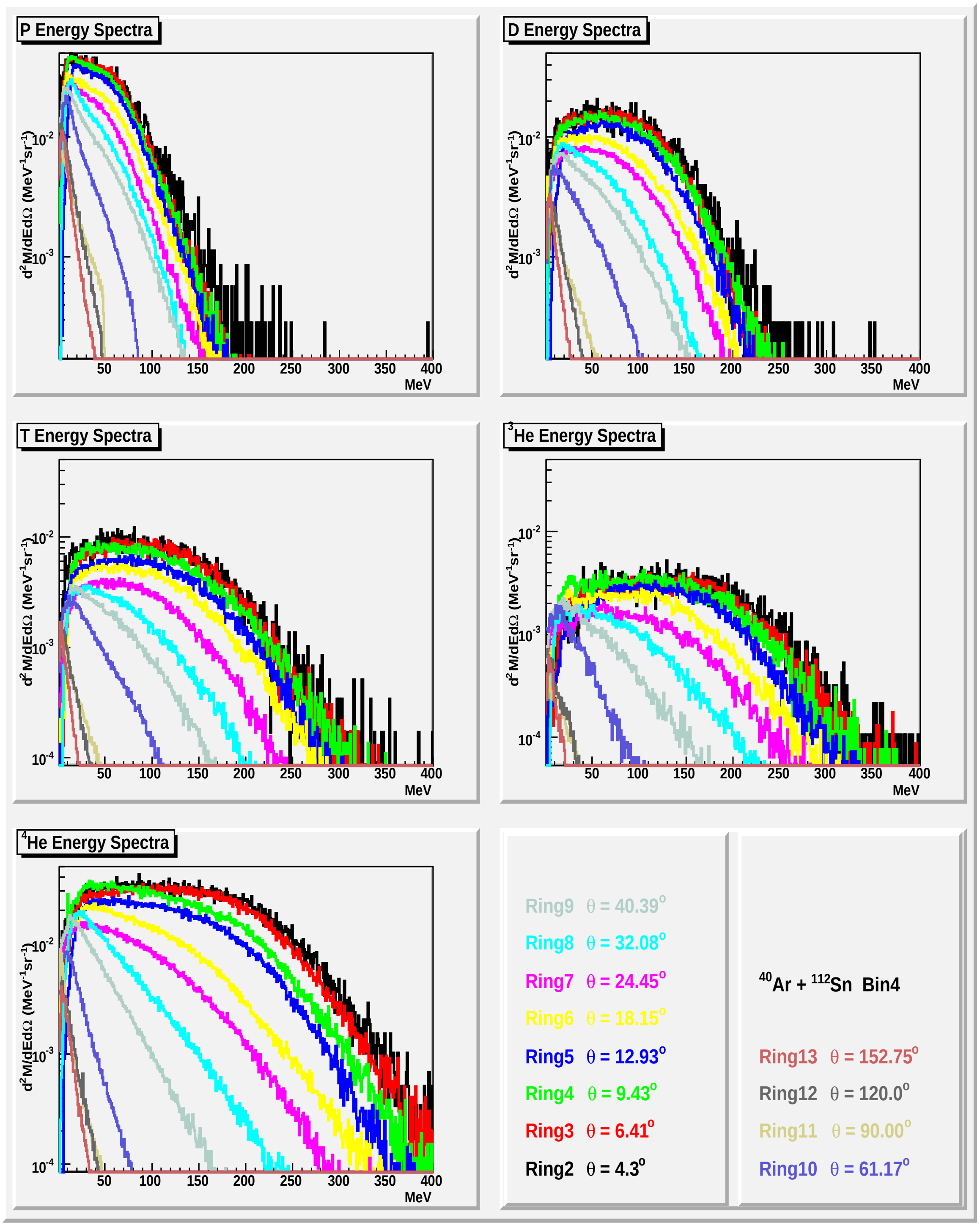

Fig. 71. X axis is energy in MeV. Y axis is the multiplicity distribution

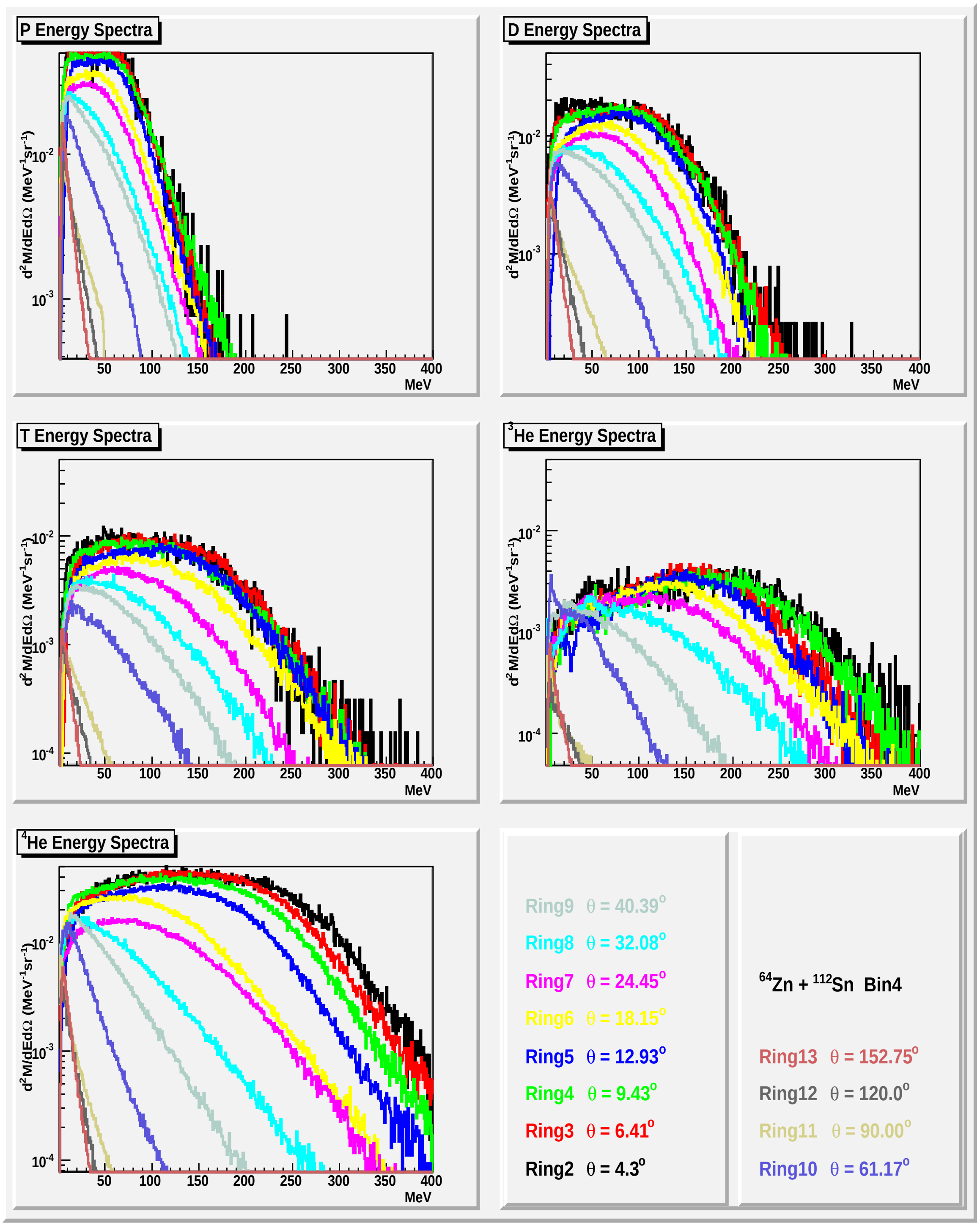

Fig. 72. X axis is energy in MeV. Y axis is the multiplicity distribution

APPENDIX C

ANGULAR DISTRIBUTION SPECTRA IN BIN3

The differential angular distributions of the particle multiplicity are listed.

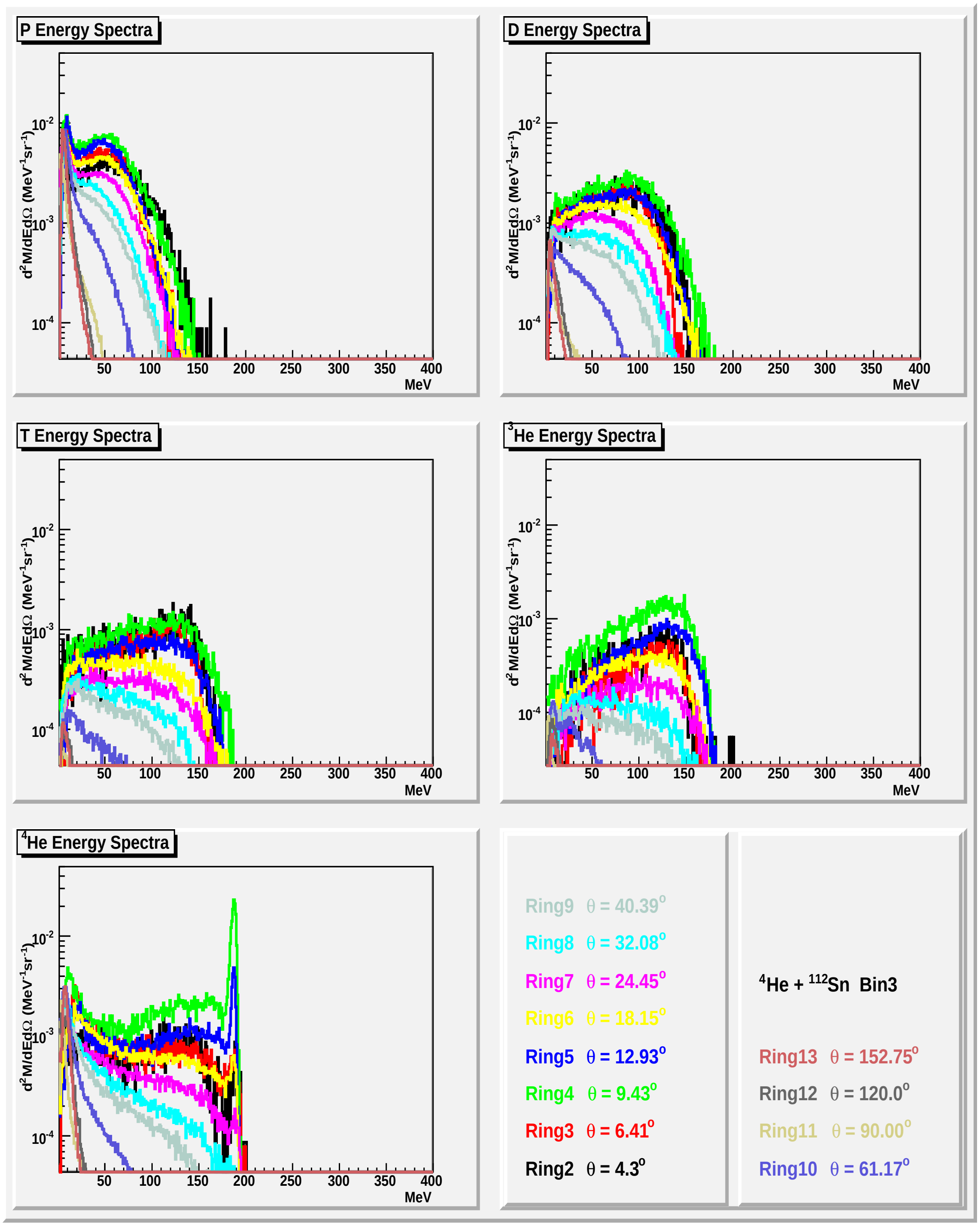

Fig. 73. X axis is energy in MeV. Y axis is the multiplicity distribution

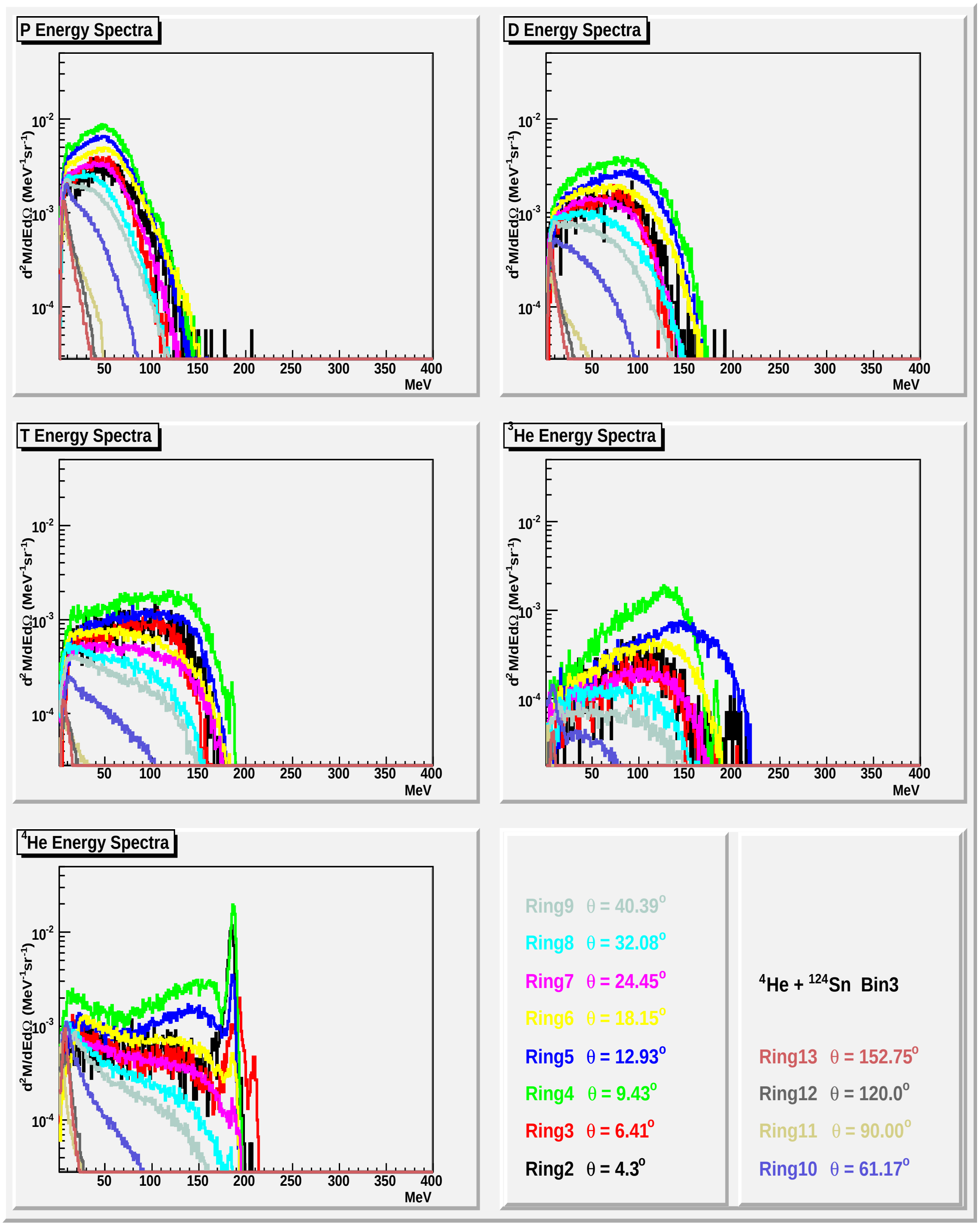

Fig. 74. X axis is energy in MeV. Y axis is the multiplicity distribution

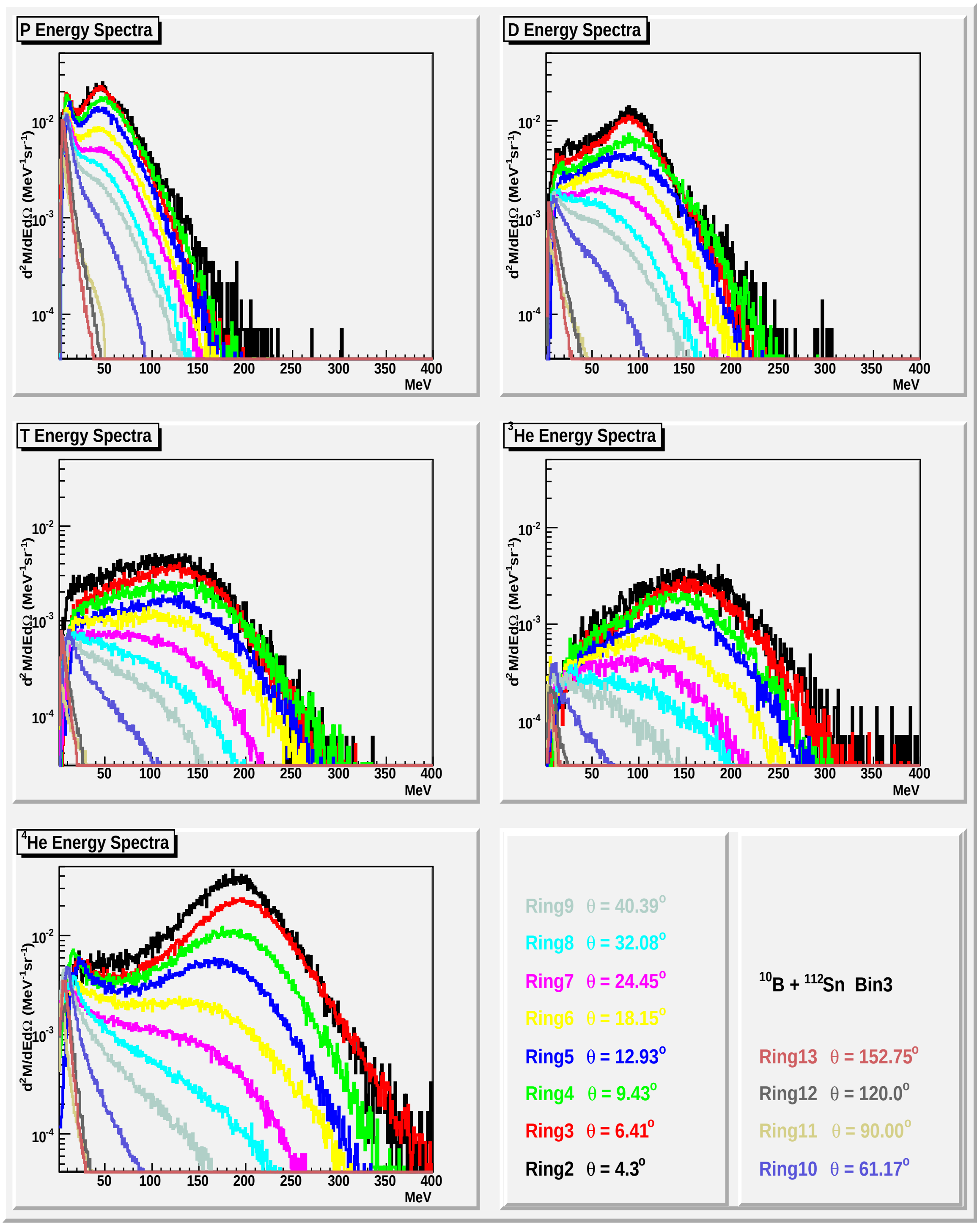

Fig. 75. X axis is energy in MeV. Y axis is the multiplicity distribution

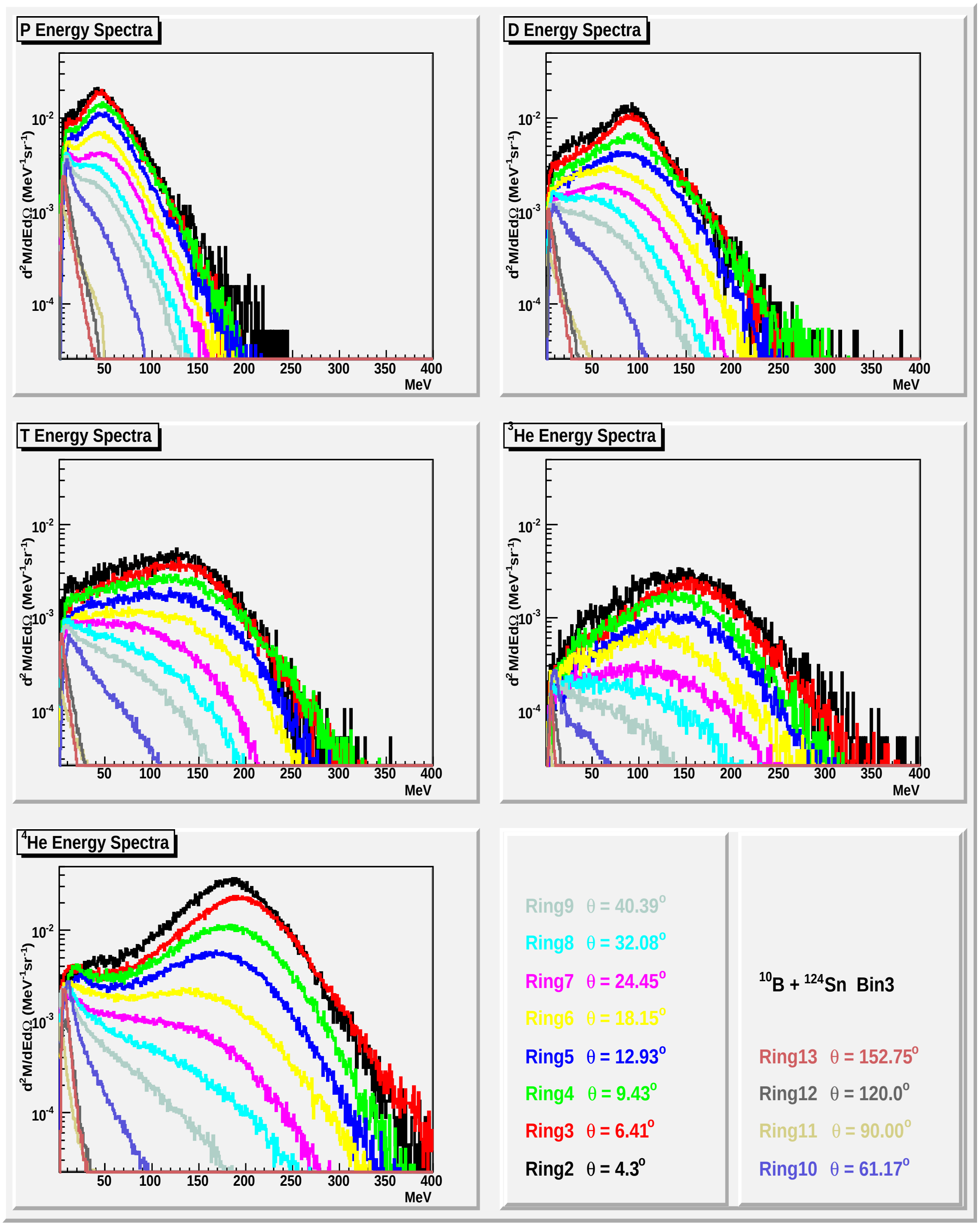

Fig. 76. X axis is energy in MeV. Y axis is the multiplicity distribution

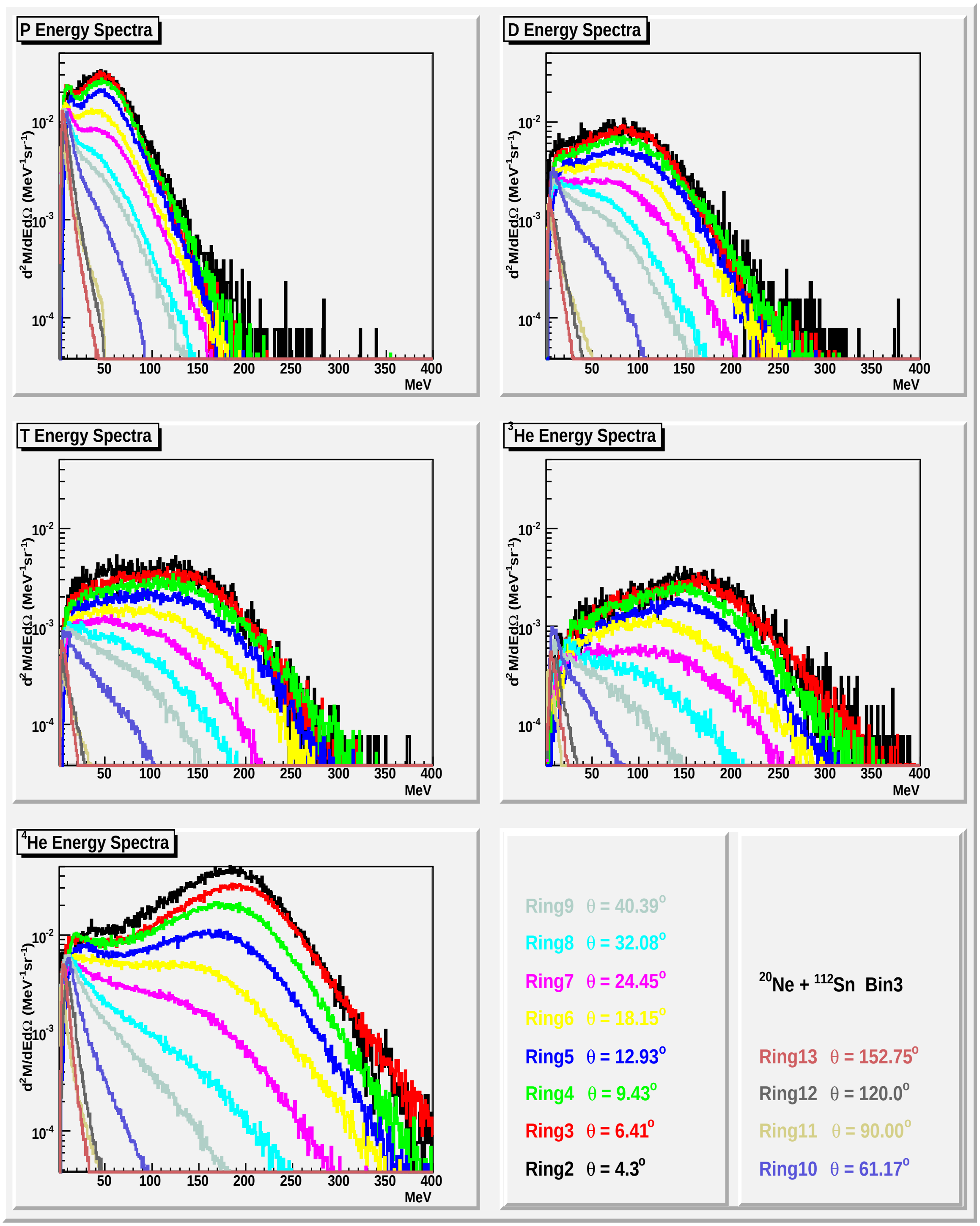

Fig. 77. X axis is energy in MeV. Y axis is the multiplicity distribution

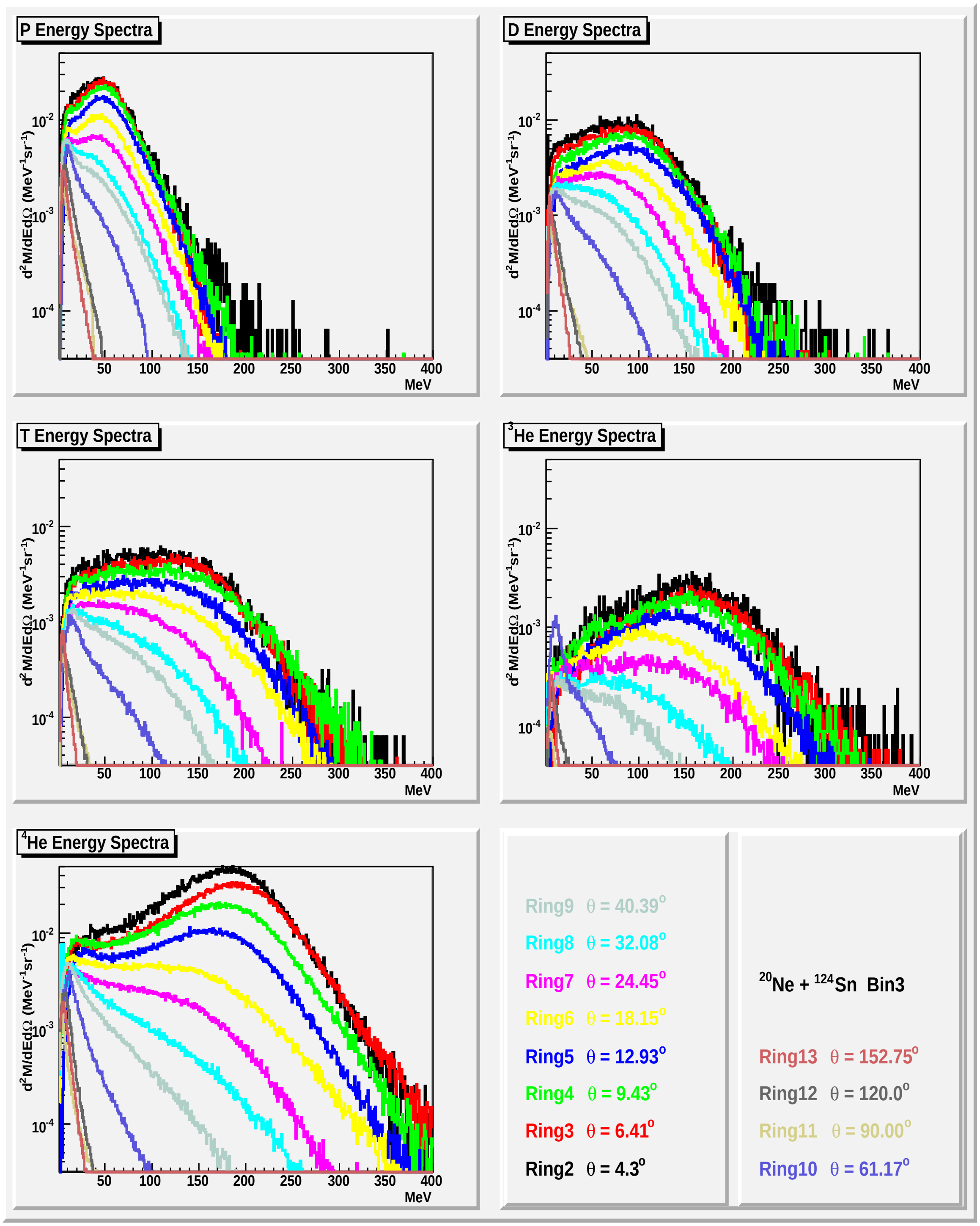

Fig. 78. X axis is energy in MeV. Y axis is the multiplicity distribution

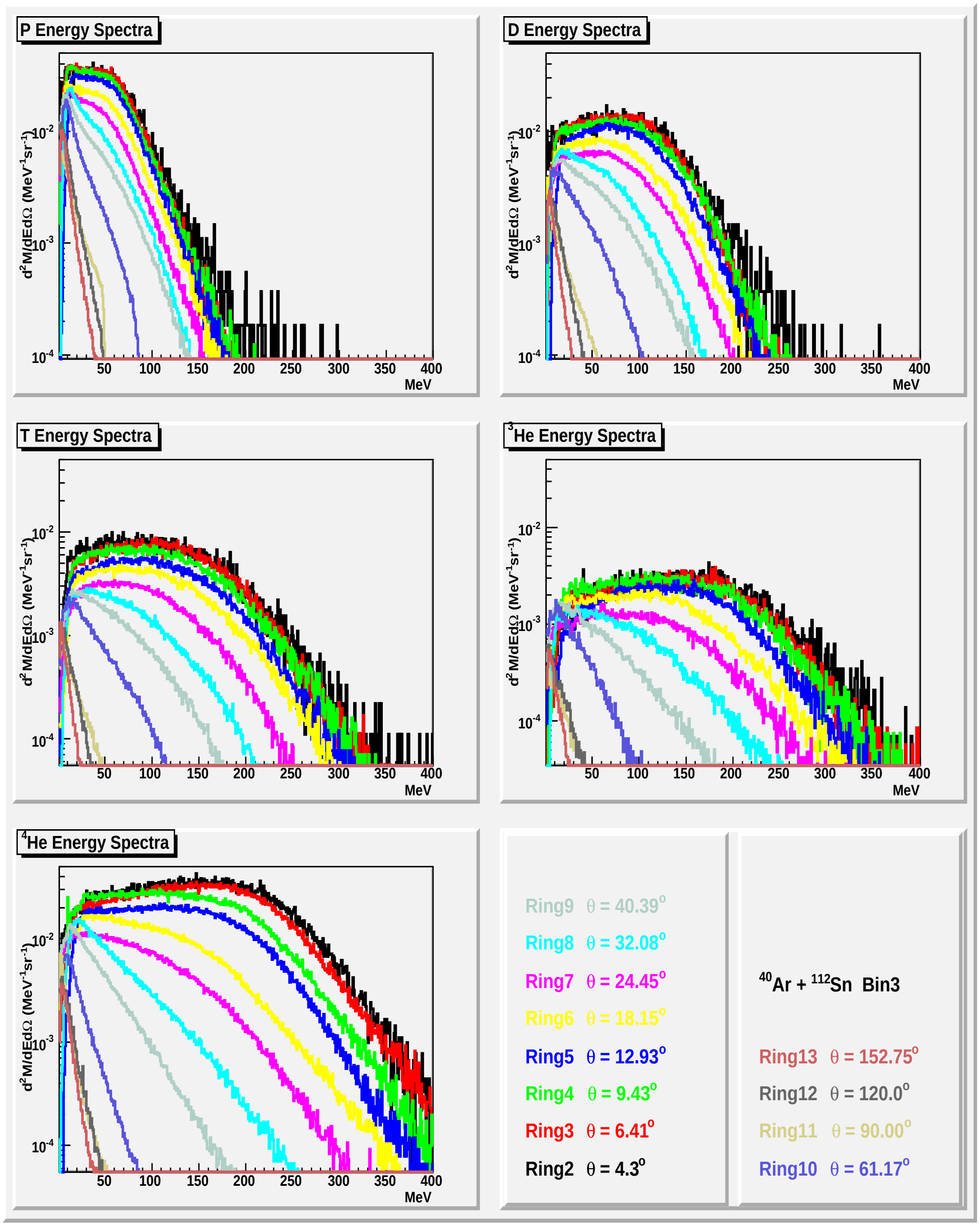

Fig. 79. X axis is energy in MeV. Y axis is the multiplicity distribution

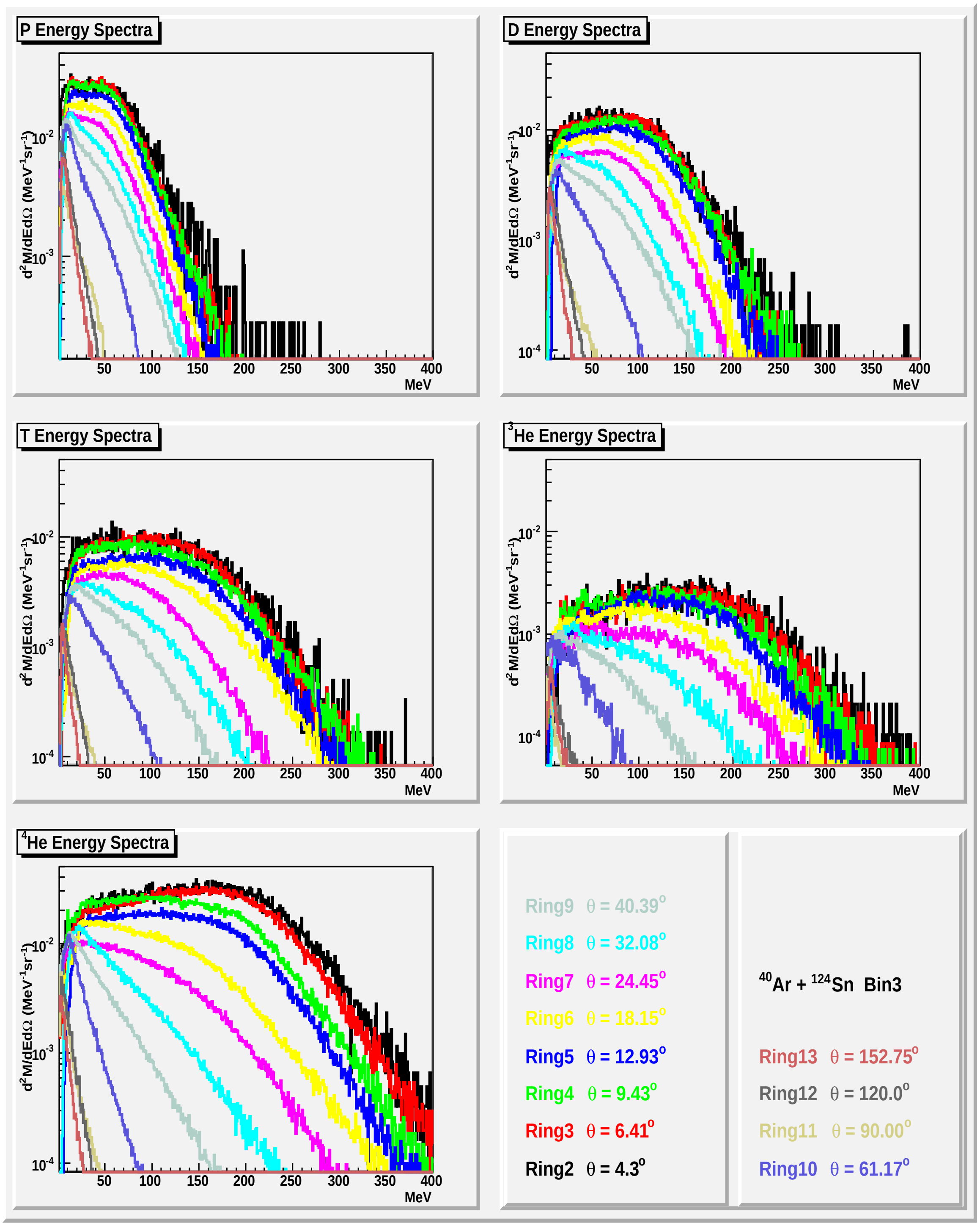

Fig. 80. X axis is energy in MeV. Y axis is the multiplicity distribution

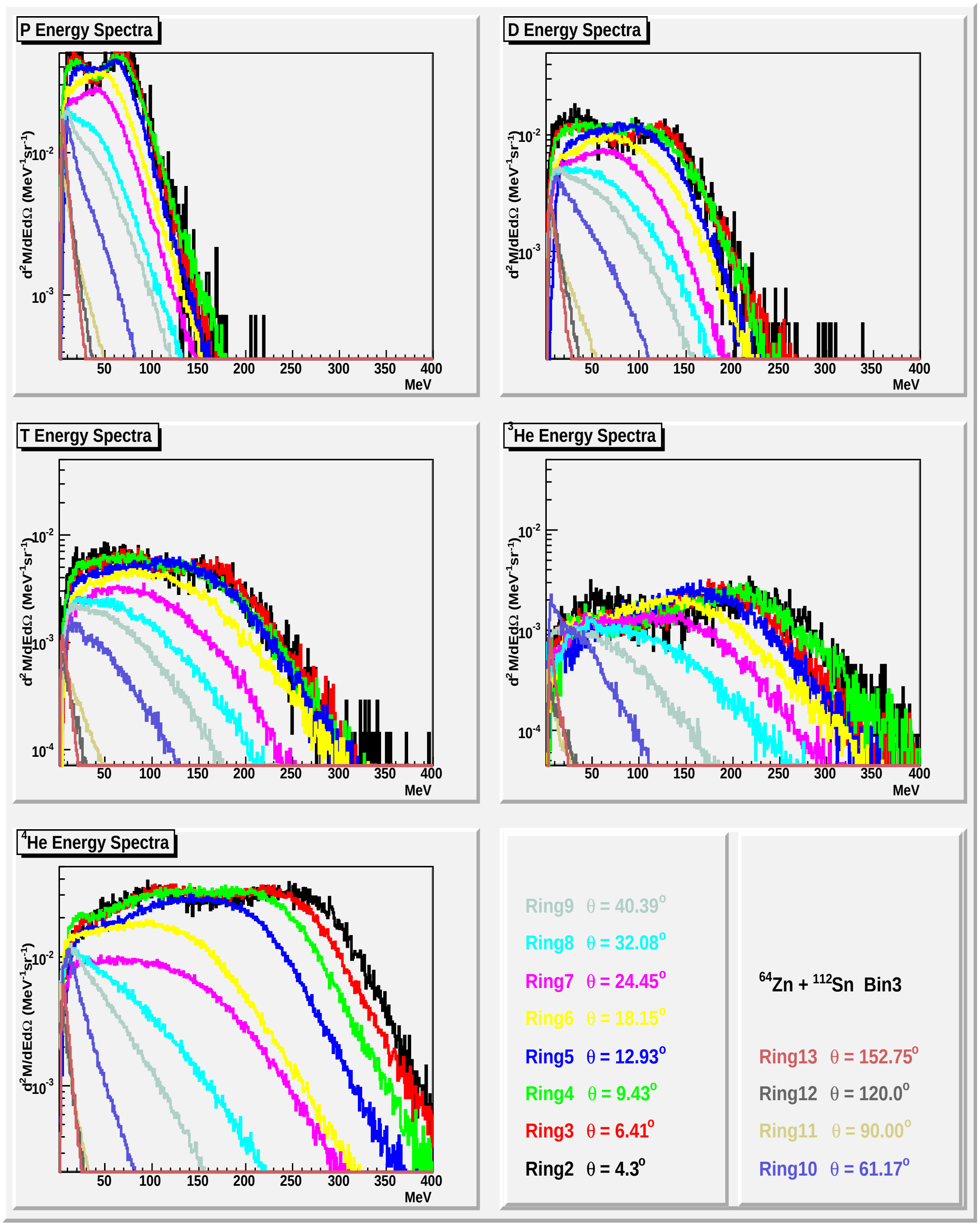

Fig. 81. X axis is energy in MeV. Y axis is the multiplicity distribution

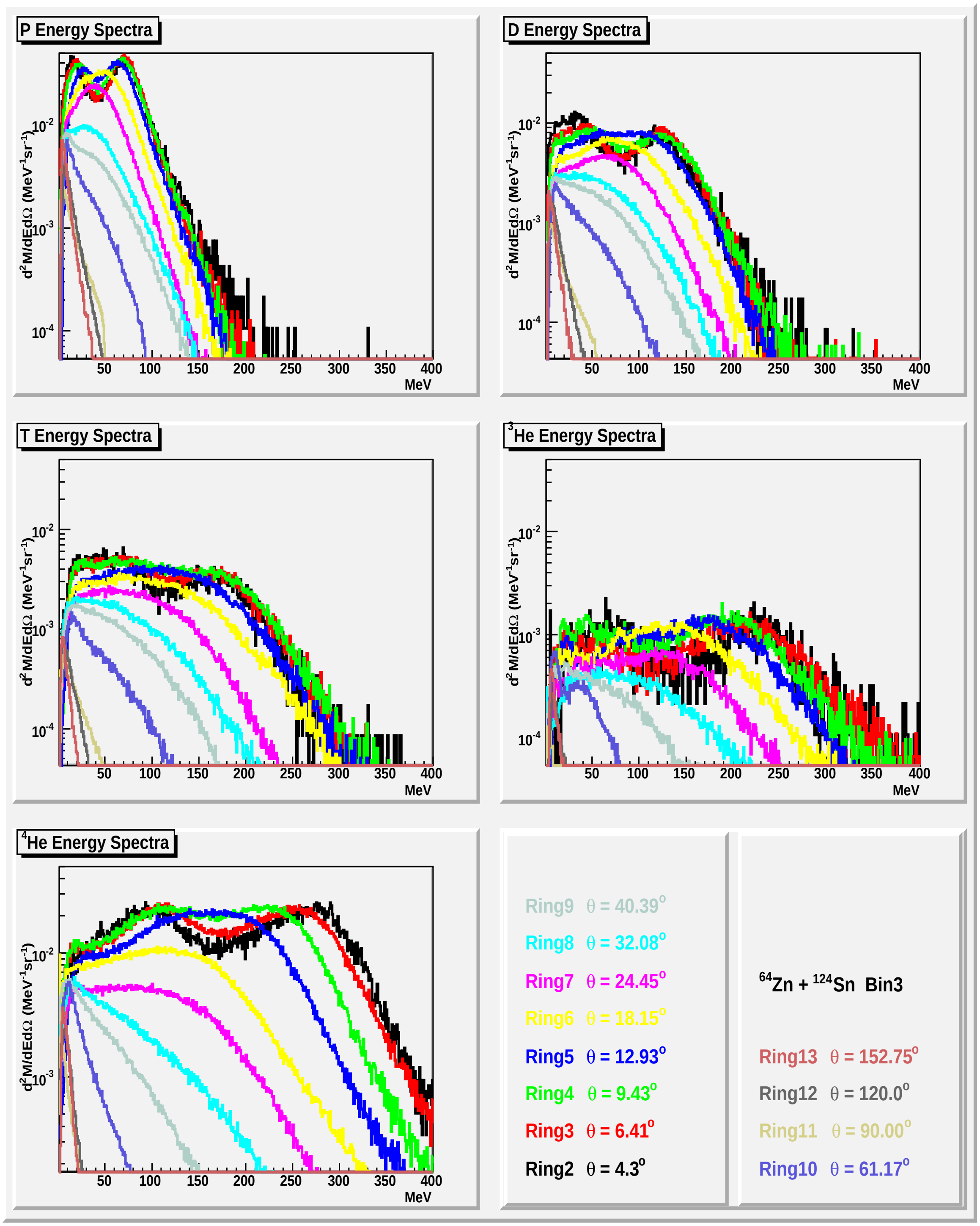

Fig. 82. X axis is energy in MeV. Y axis is the multiplicity distribution

APPENDIX D

ANGULAR DISTRIBUTION SPECTRA IN BIN2

The differential angular distributions of the particle multiplicity are listed.

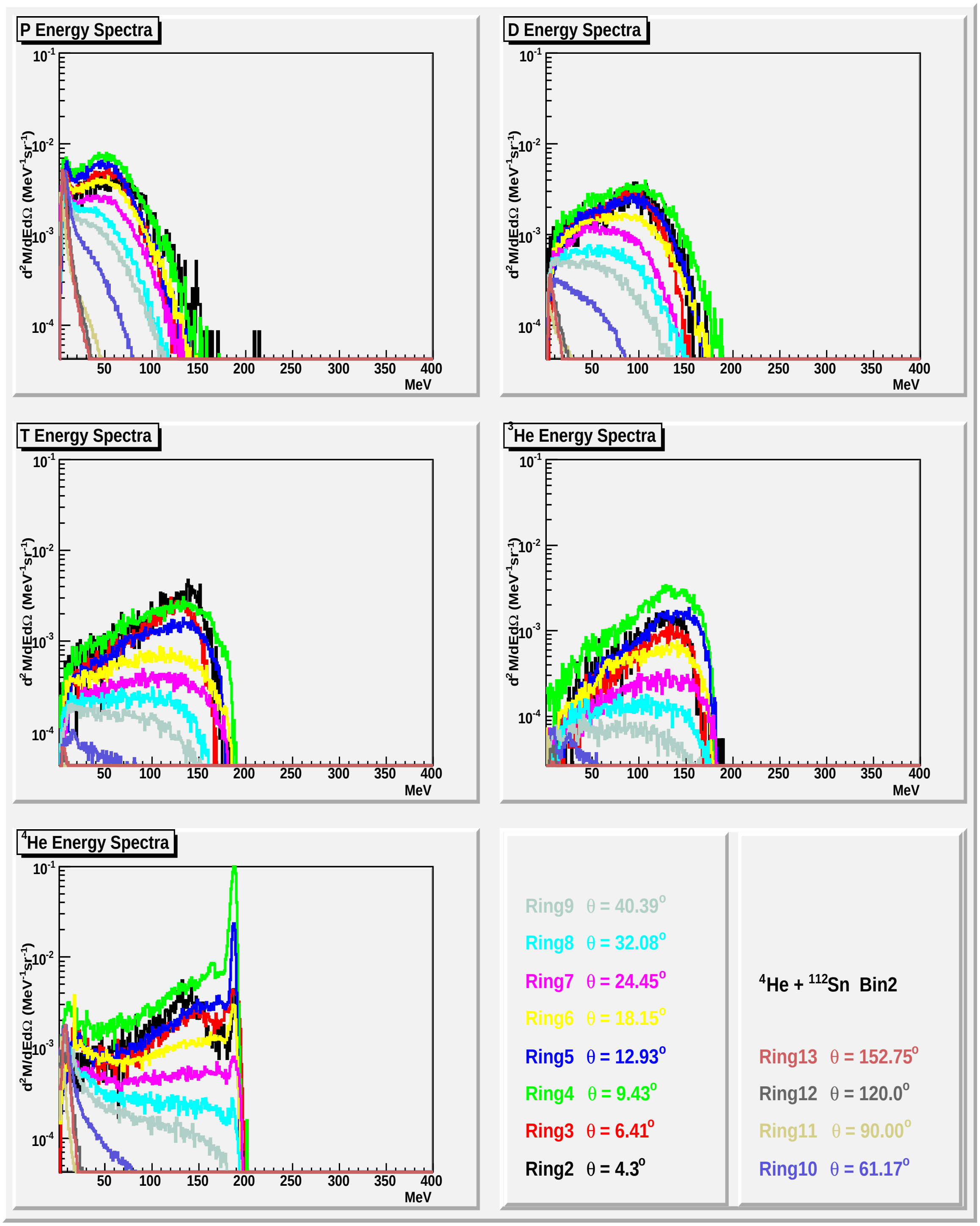

Fig. 83. X axis is energy in MeV. Y axis is the multiplicity distribution

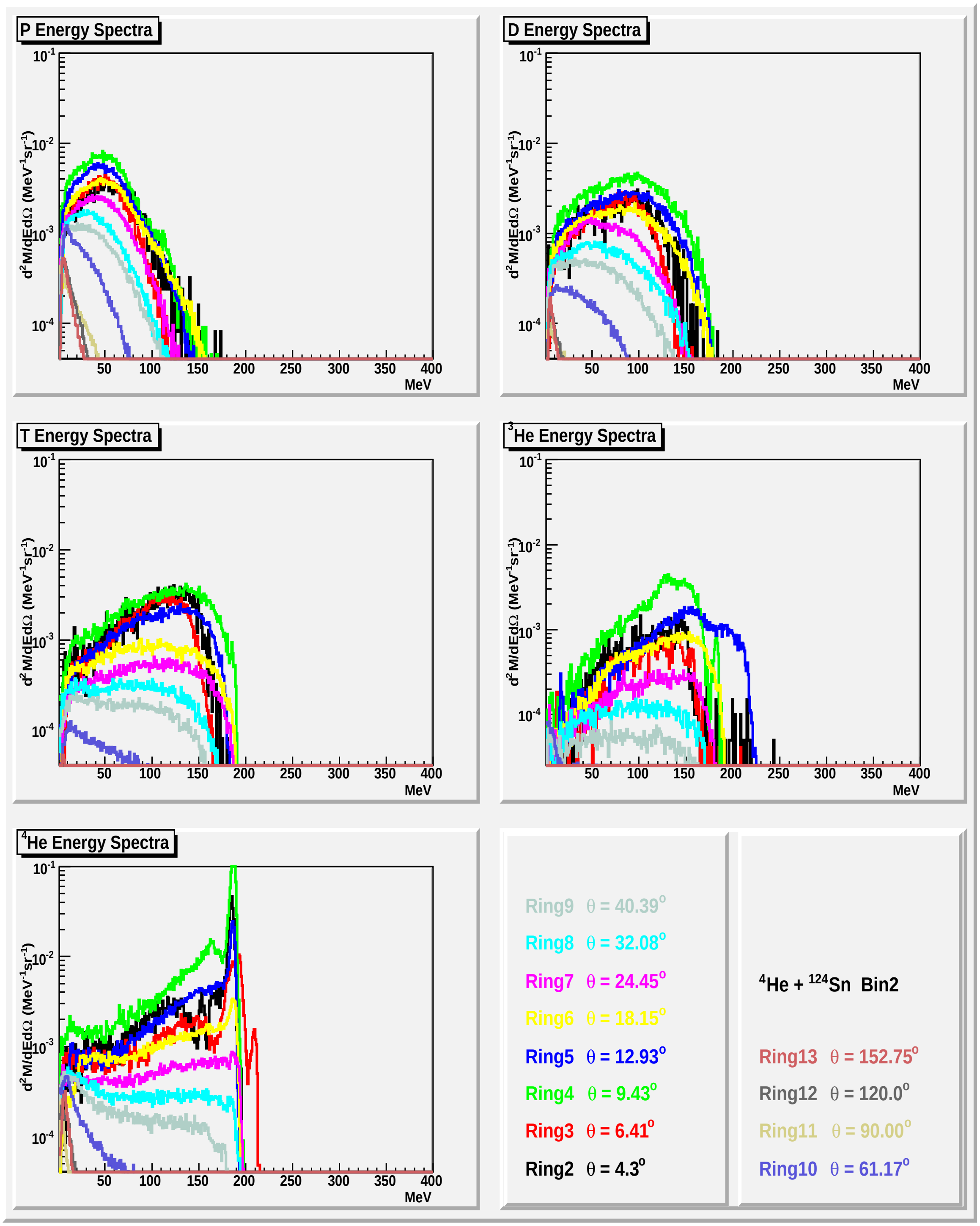

Fig. 84. X axis is energy in MeV. Y axis is the multiplicity distribution

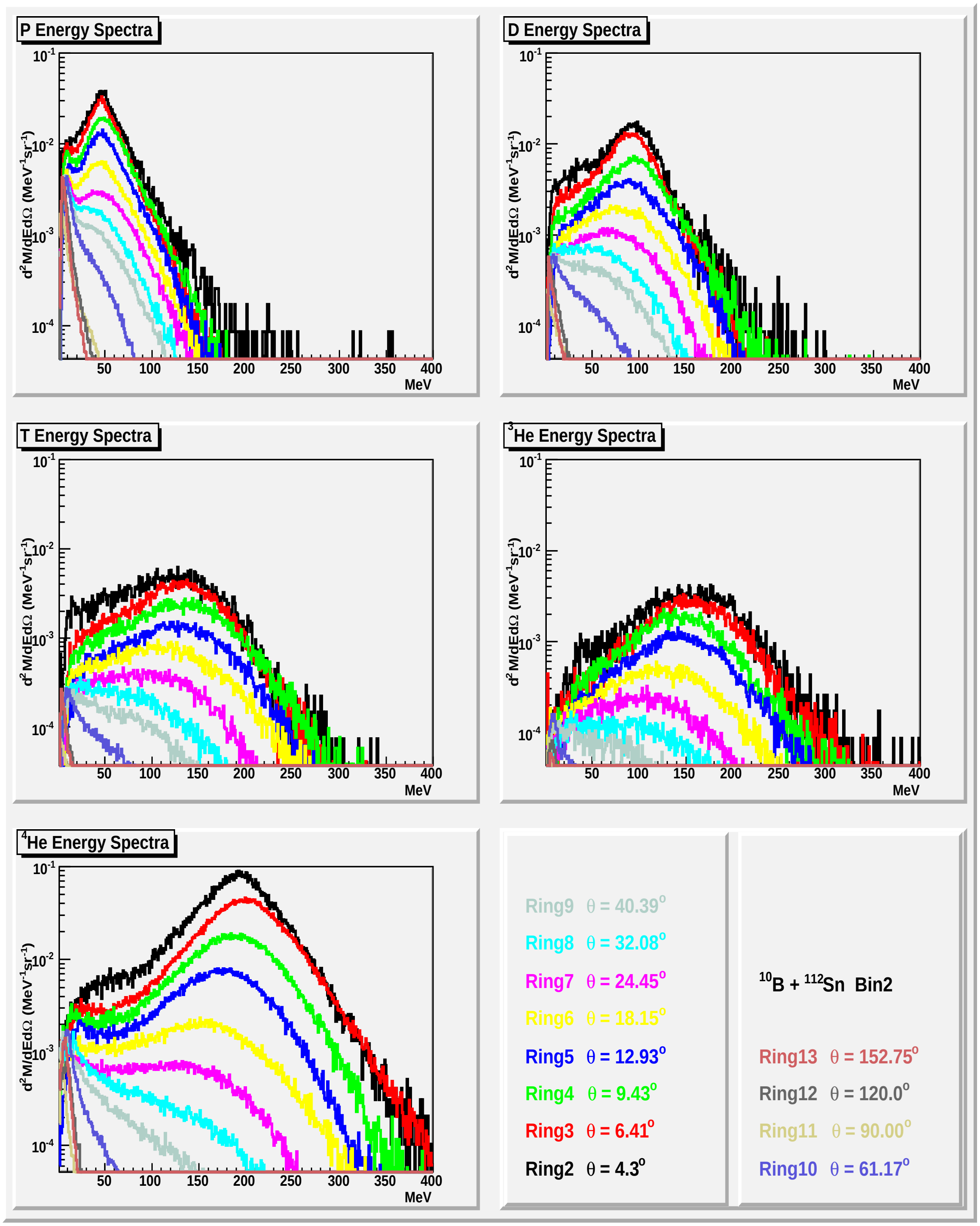

Fig. 85. X axis is energy in MeV. Y axis is the multiplicity distribution

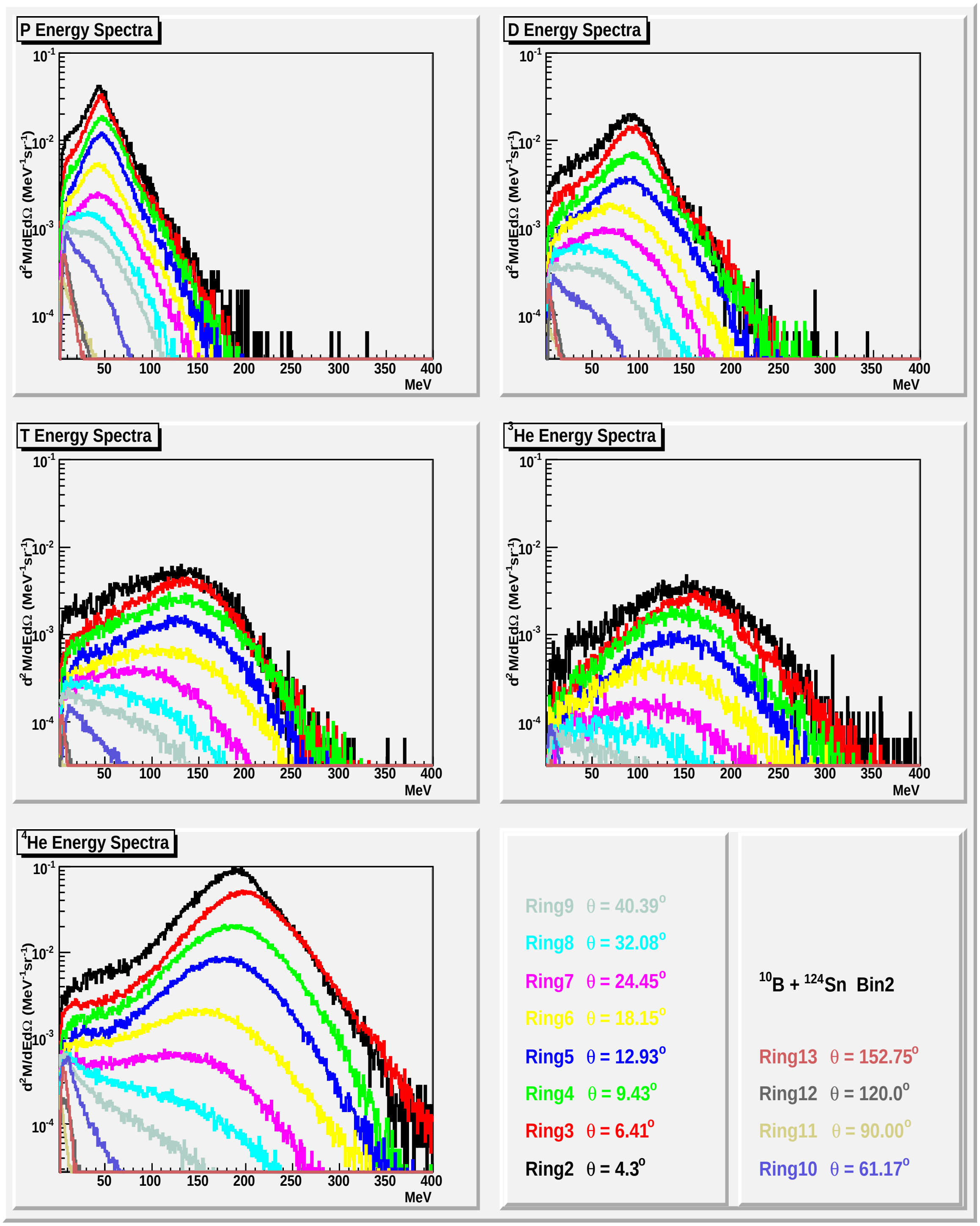

Fig. 86. X axis is energy in MeV. Y axis is the multiplicity distribution

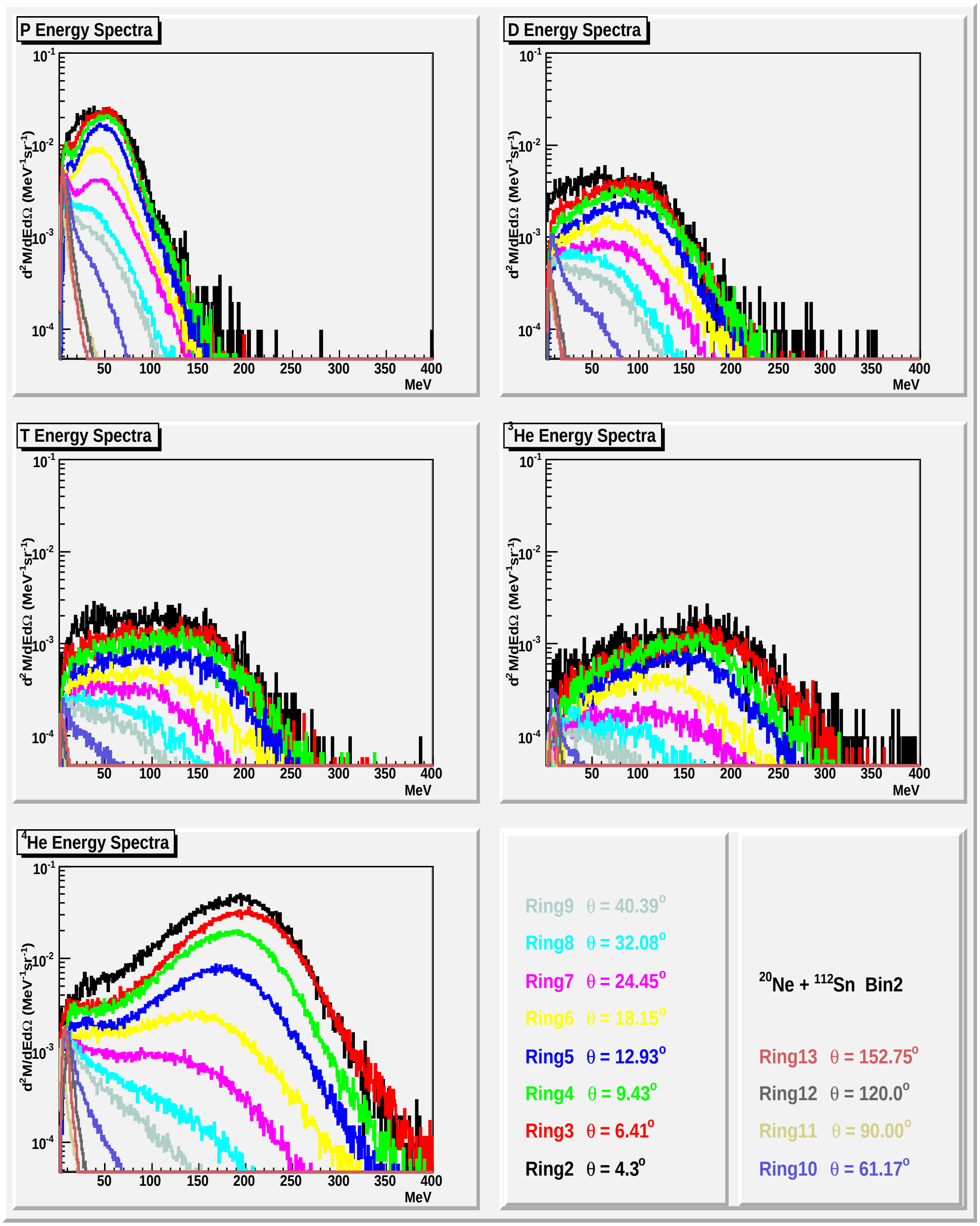

Fig. 87. X axis is energy in MeV. Y axis is the multiplicity distribution

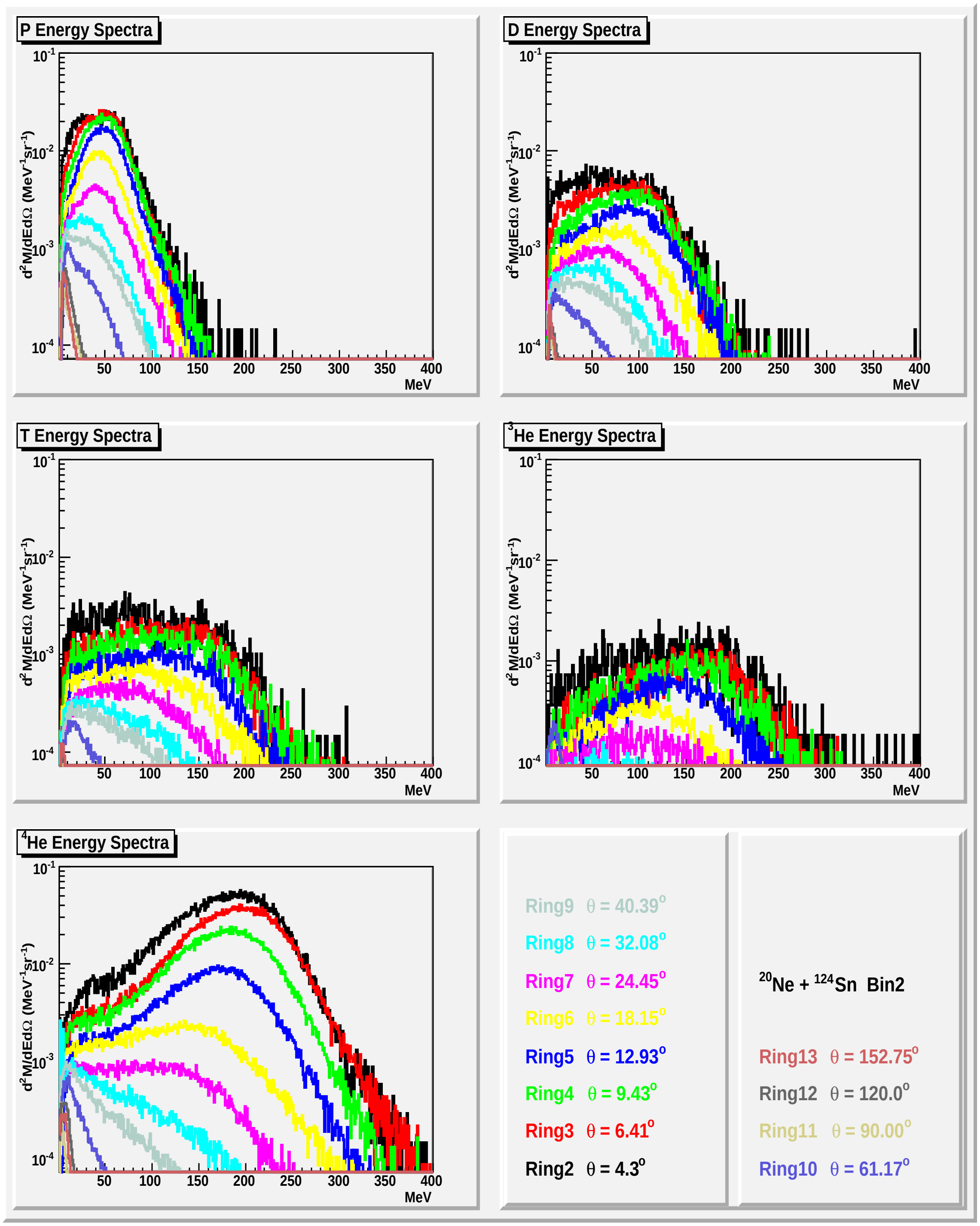

Fig. 88. X axis is energy in MeV. Y axis is the multiplicity distribution

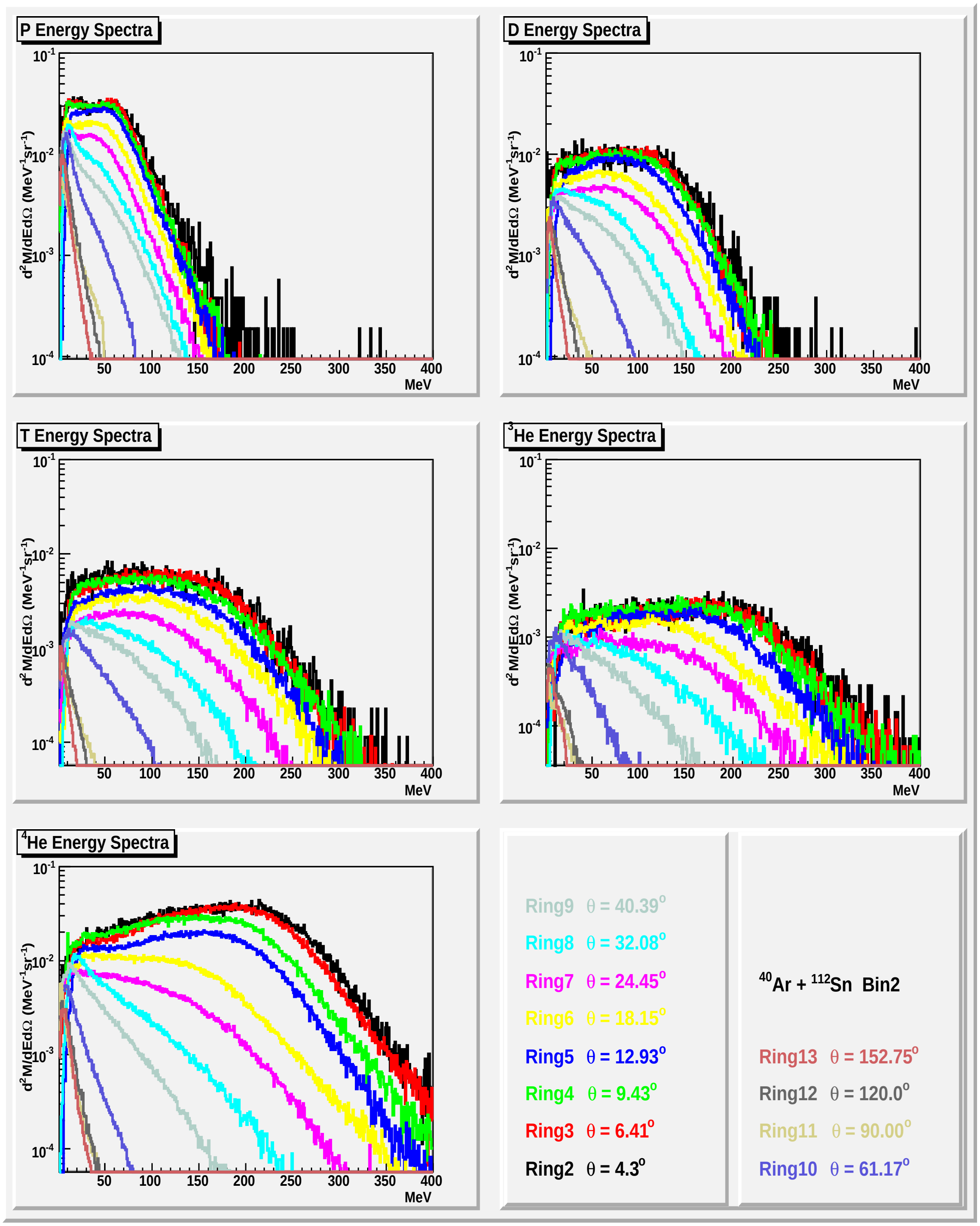

Fig. 89. X axis is energy in MeV. Y axis is the multiplicity distribution

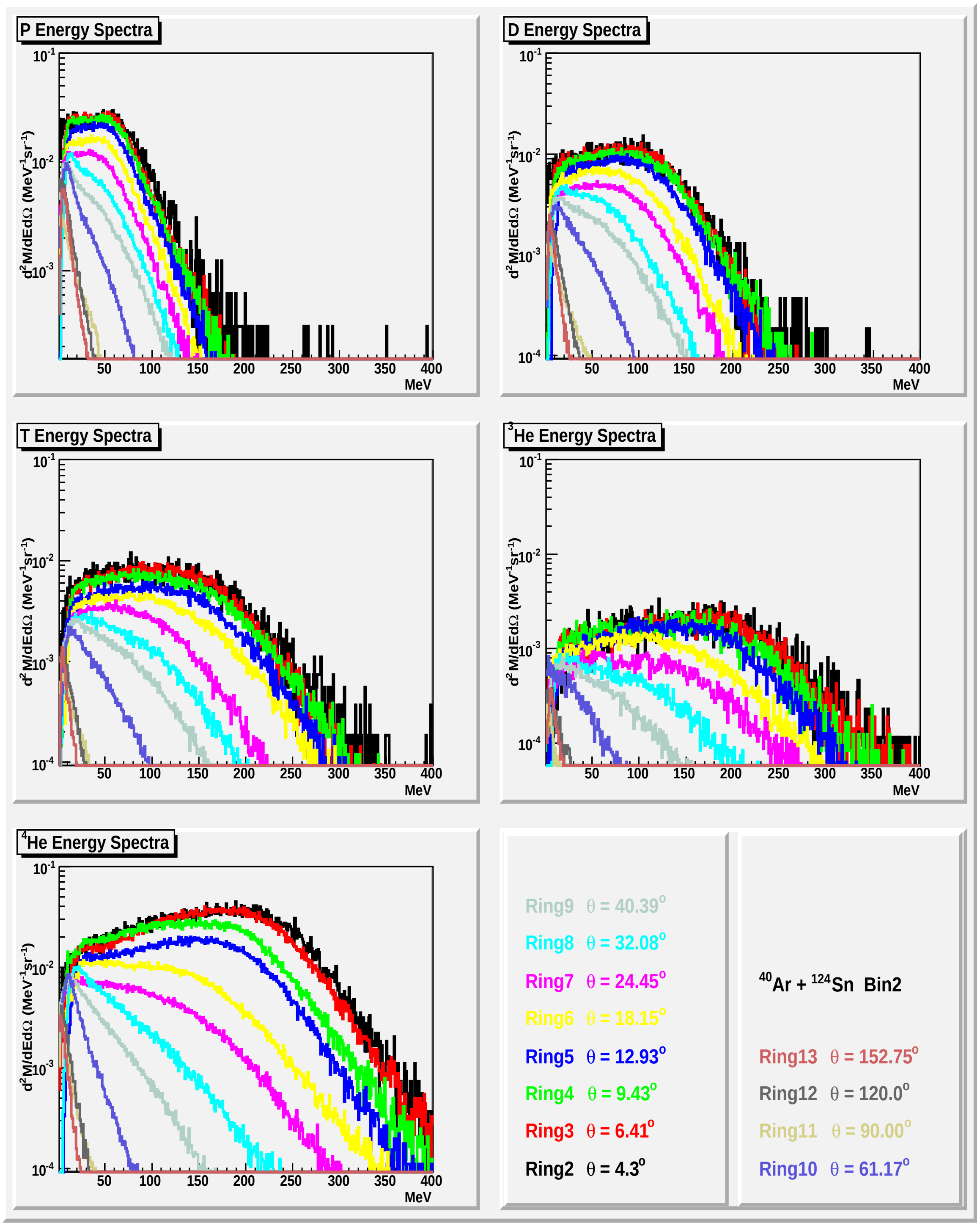

Fig. 90. X axis is energy in MeV. Y axis is the multiplicity distribution

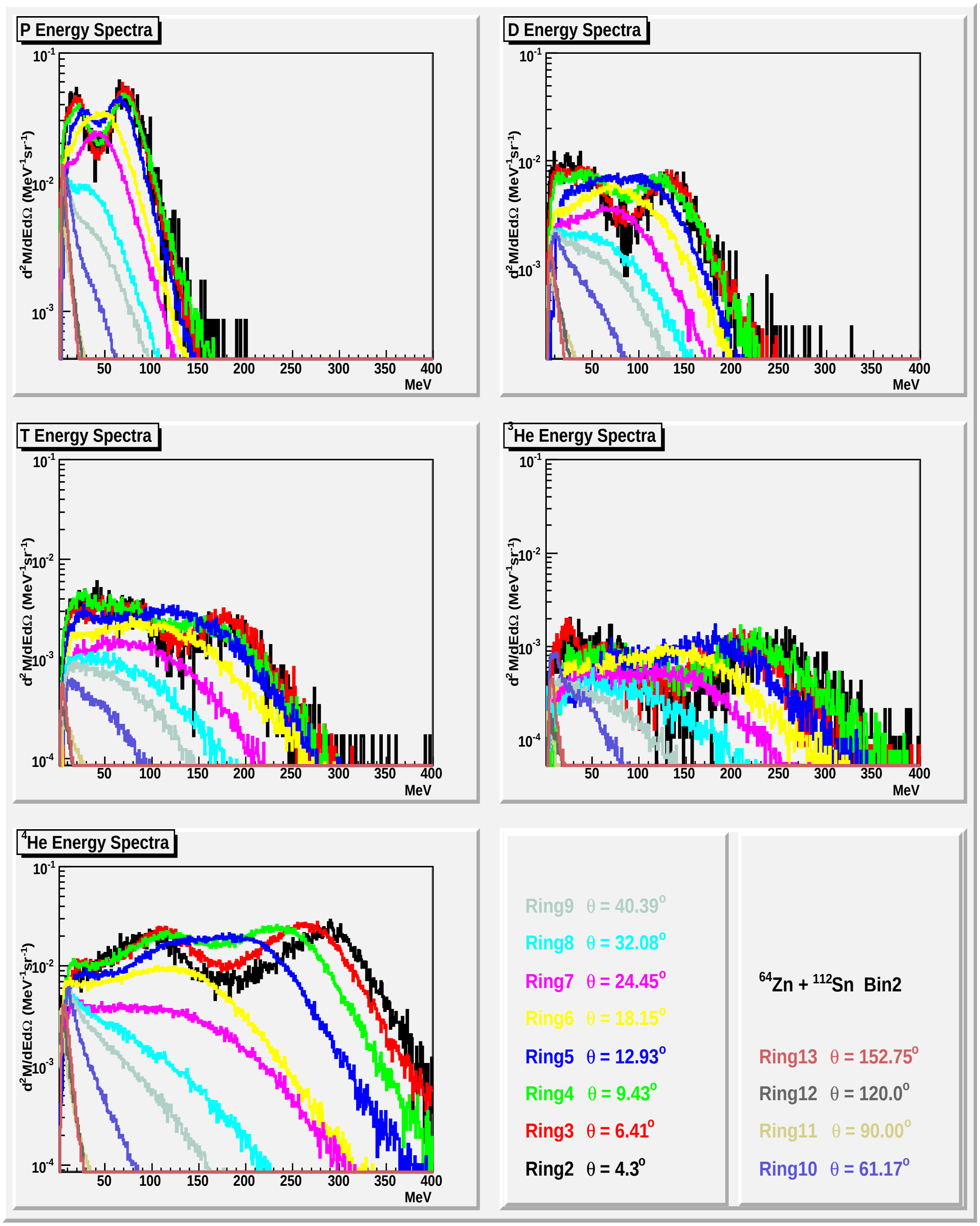

Fig. 91. X axis is energy in MeV. Y axis is the multiplicity distribution

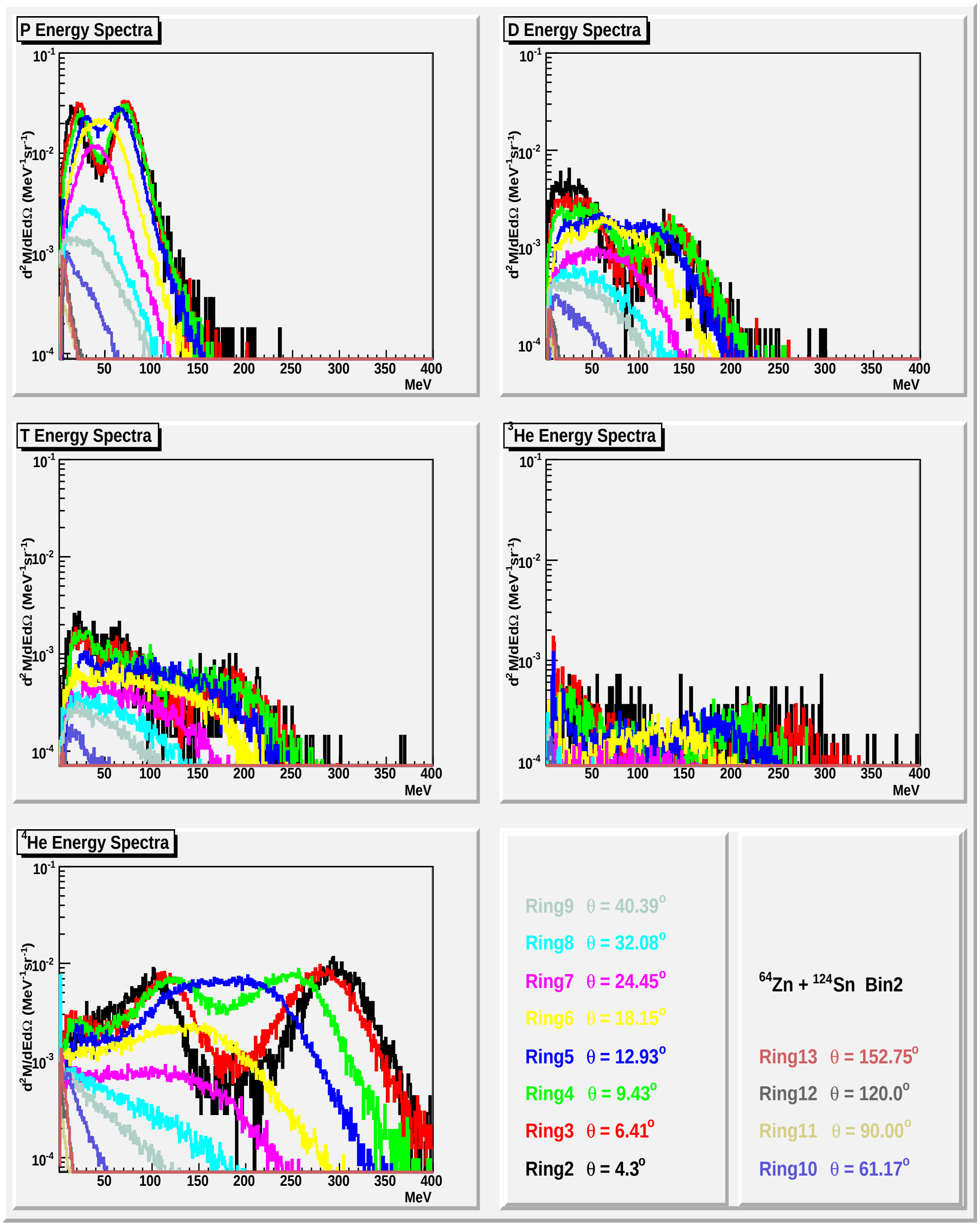

Fig. 92. X axis is energy in MeV. Y axis is the multiplicity distribution

APPENDIX E

ANGULAR DISTRIBUTION SPECTRA IN BIN1

The differential angular distributions of the particle multiplicity are listed.

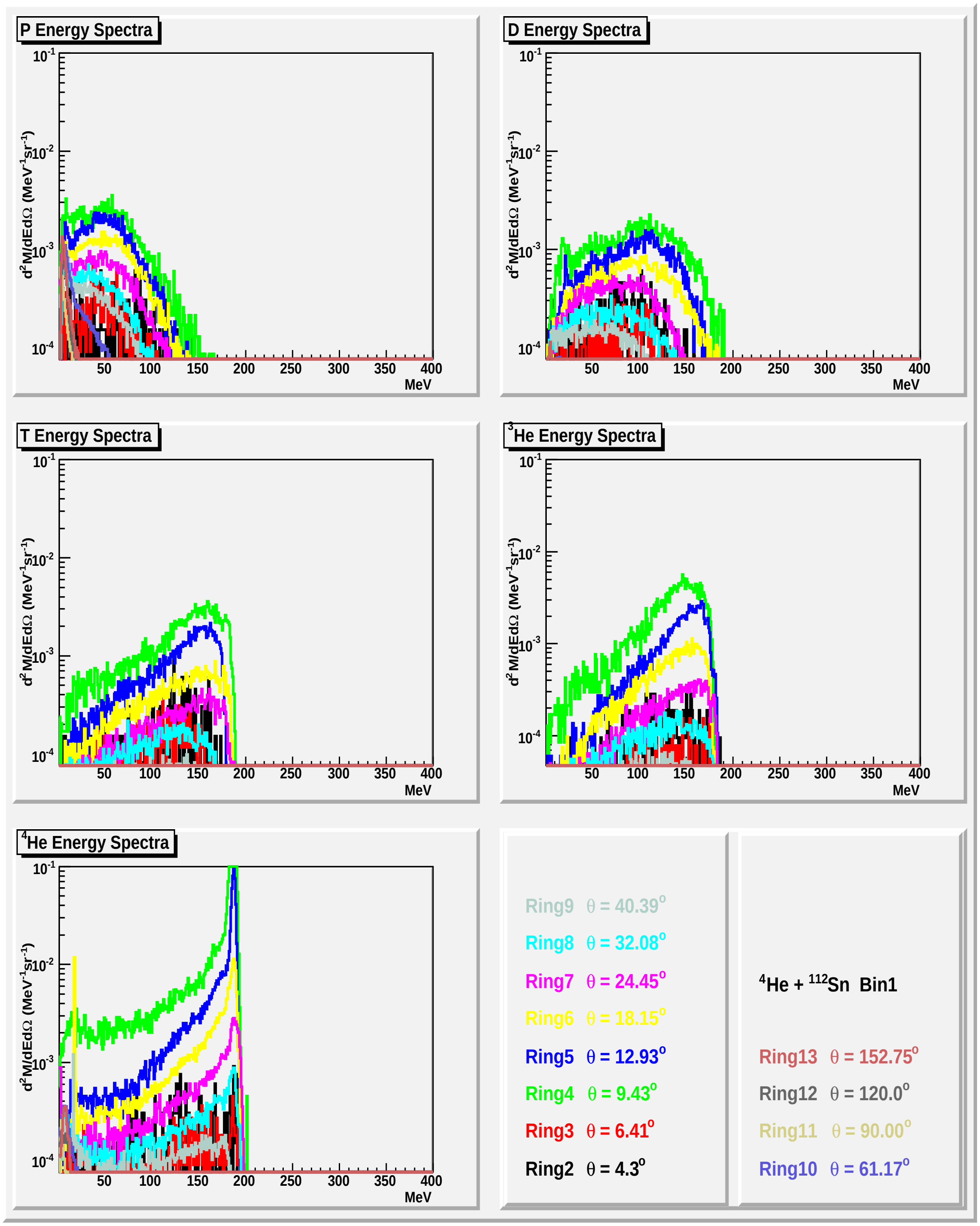

Fig. 93. X axis is energy in MeV. Y axis is the multiplicity distribution

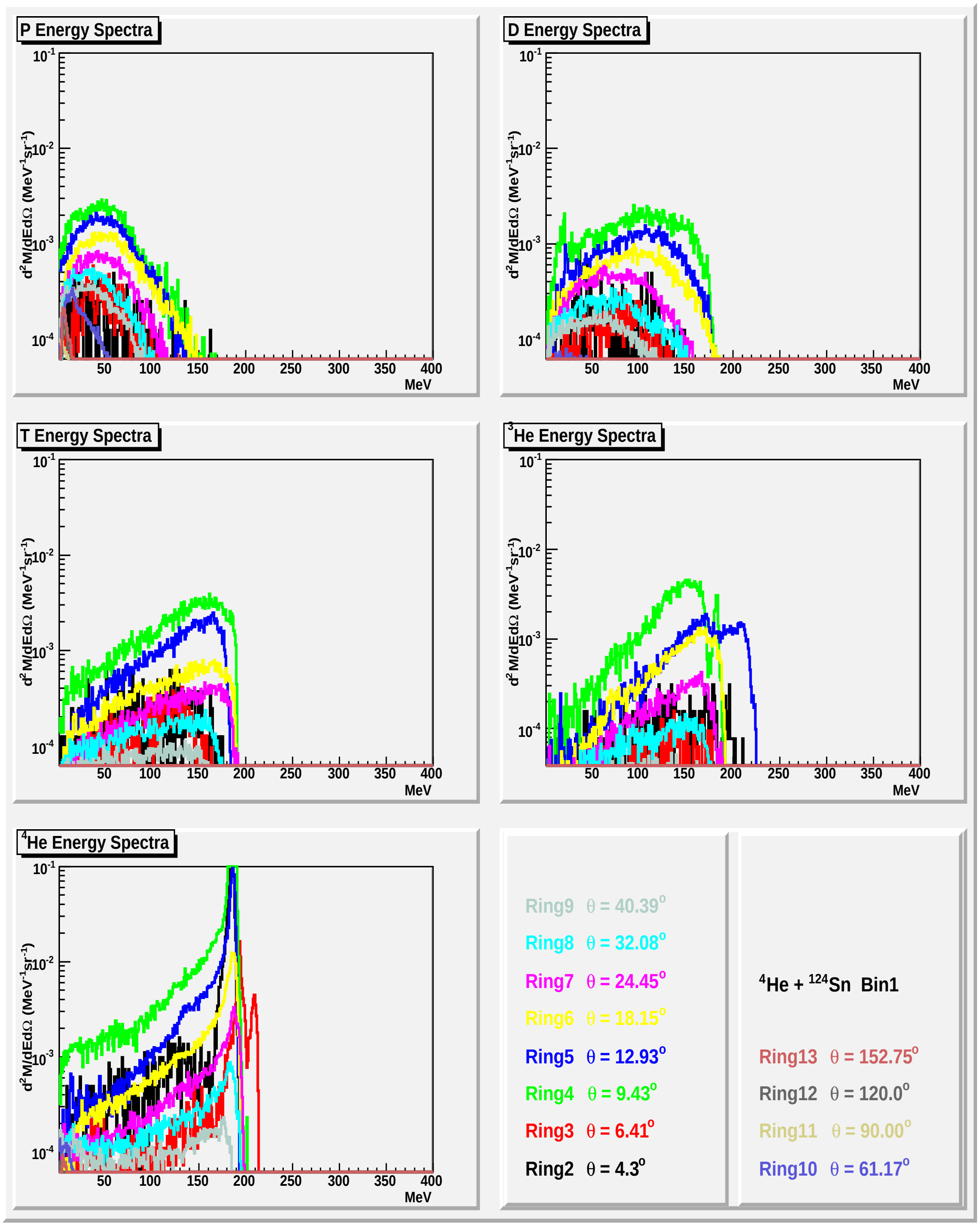

Fig. 94. X axis is energy in MeV. Y axis is the multiplicity distribution

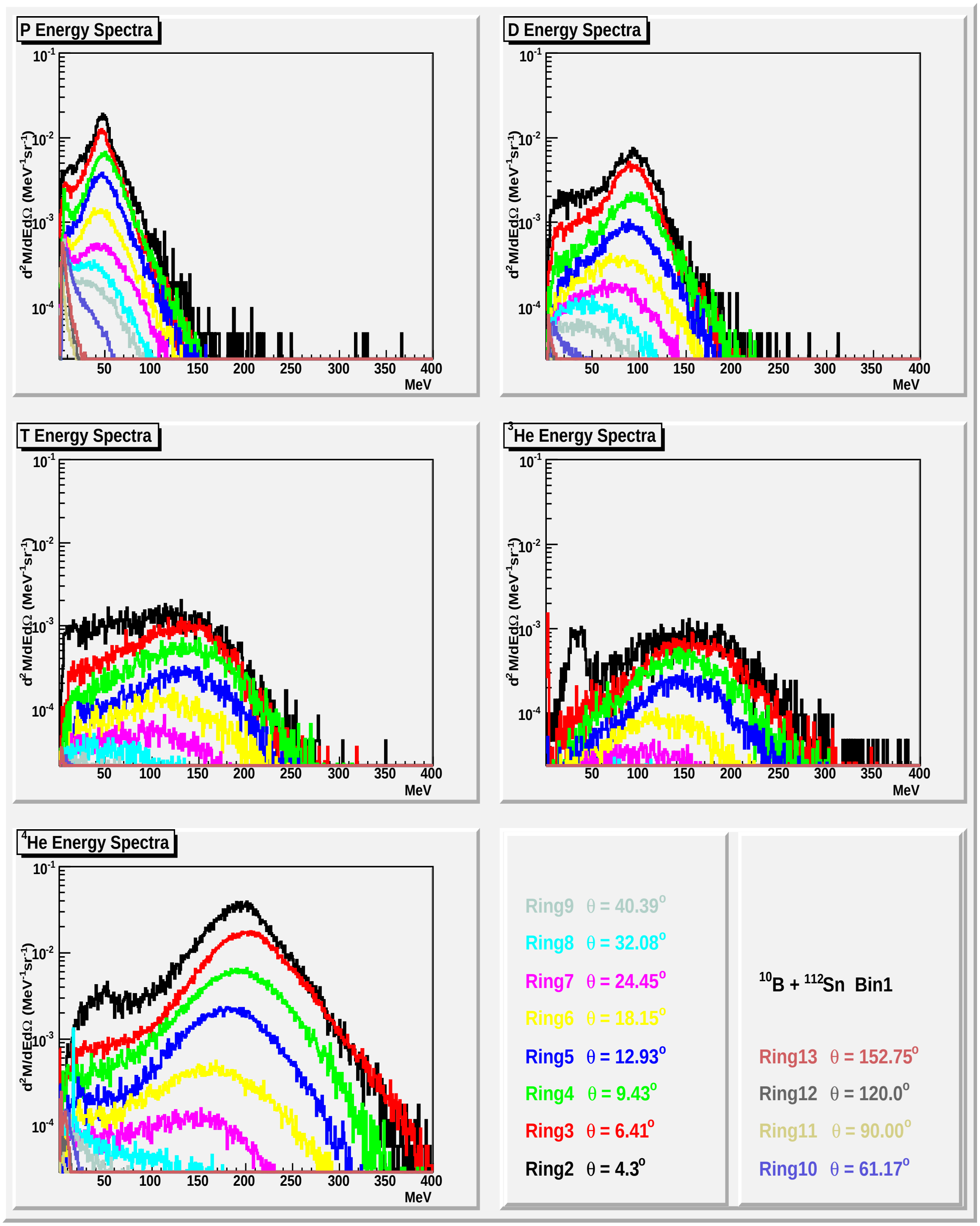

Fig. 95. X axis is energy in MeV. Y axis is the multiplicity distribution

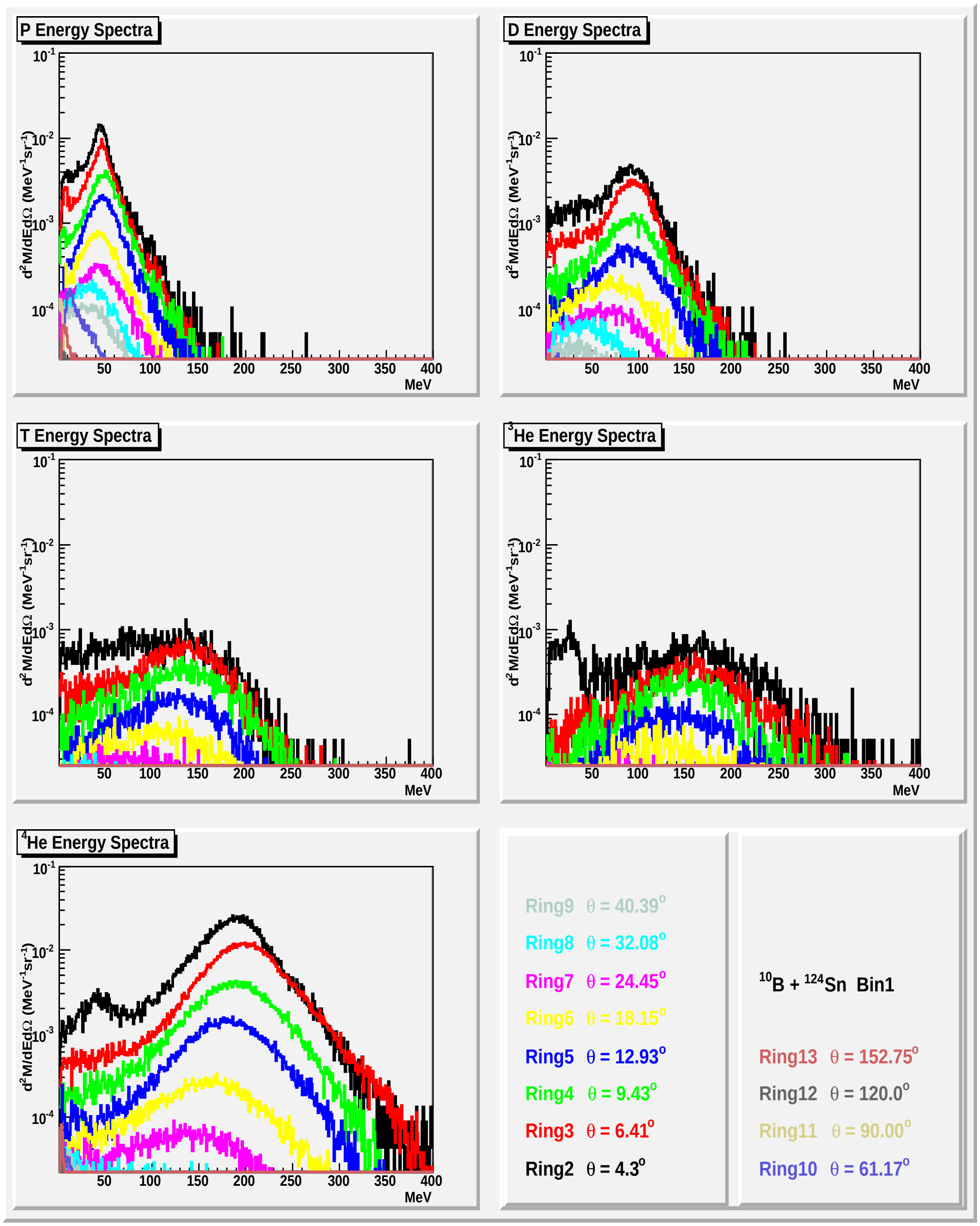

Fig. 96. X axis is energy in MeV. Y axis is the multiplicity distribution

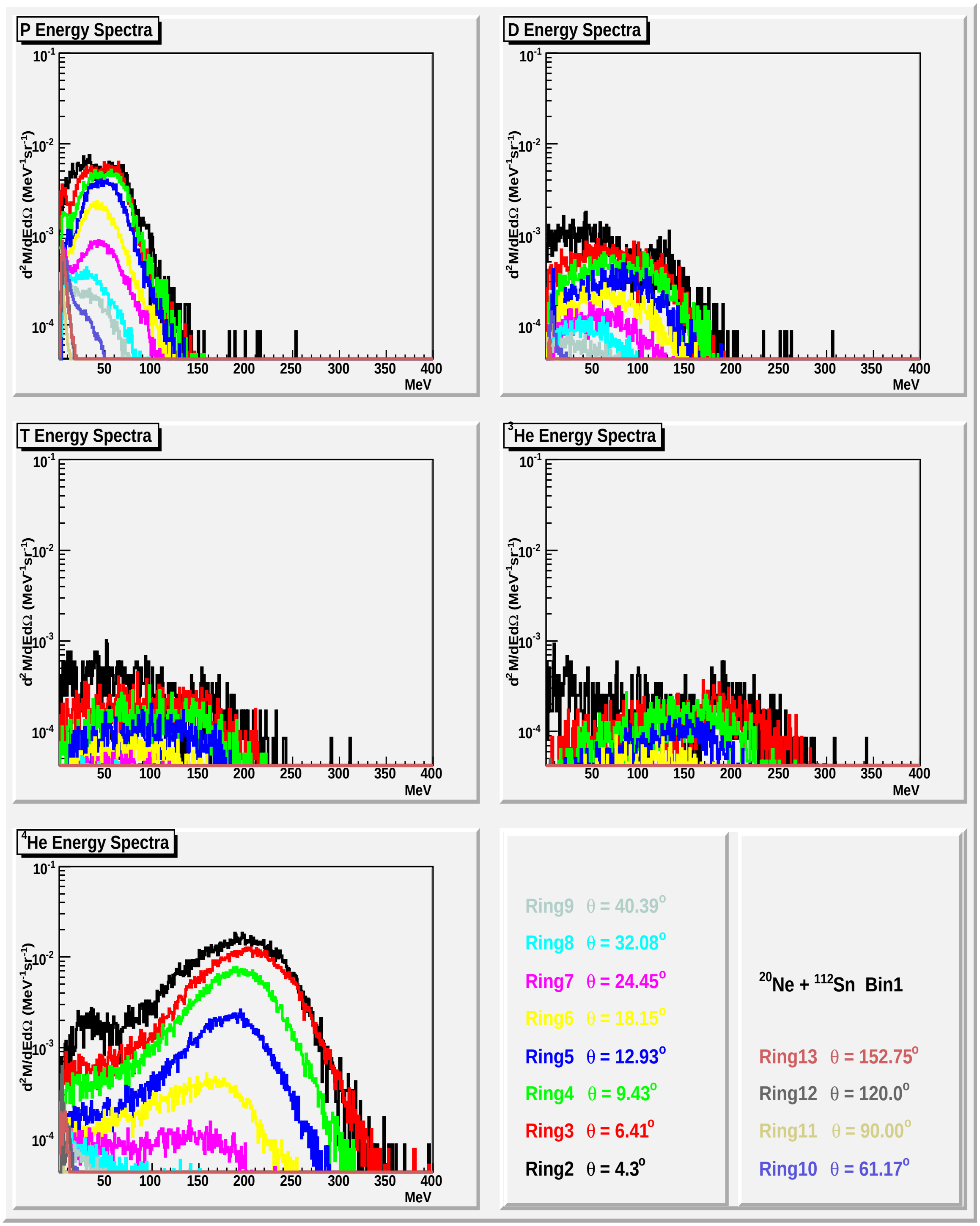

Fig. 97. X axis is energy in MeV. Y axis is the multiplicity distribution

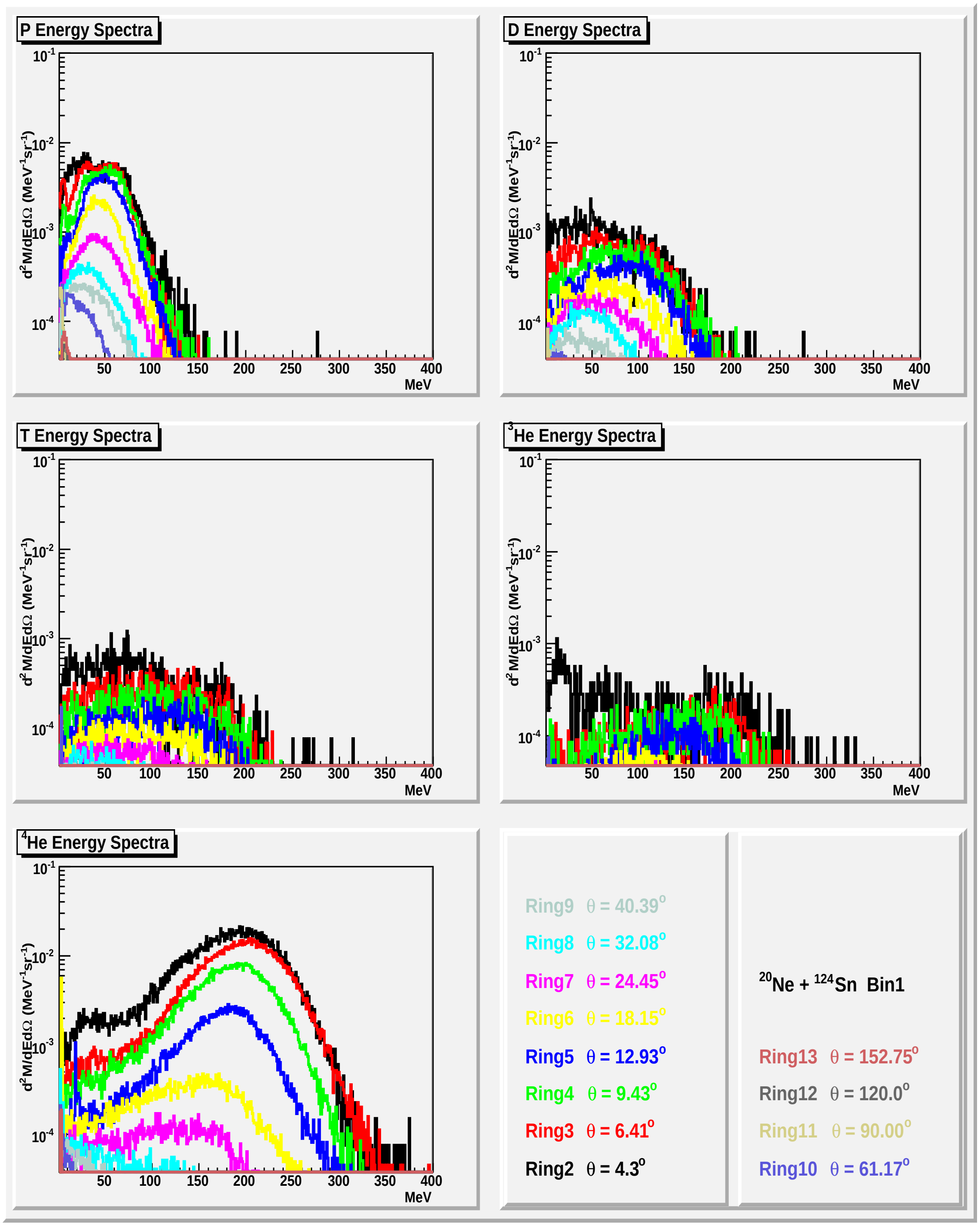

Fig. 98. X axis is energy in MeV. Y axis is the multiplicity distribution

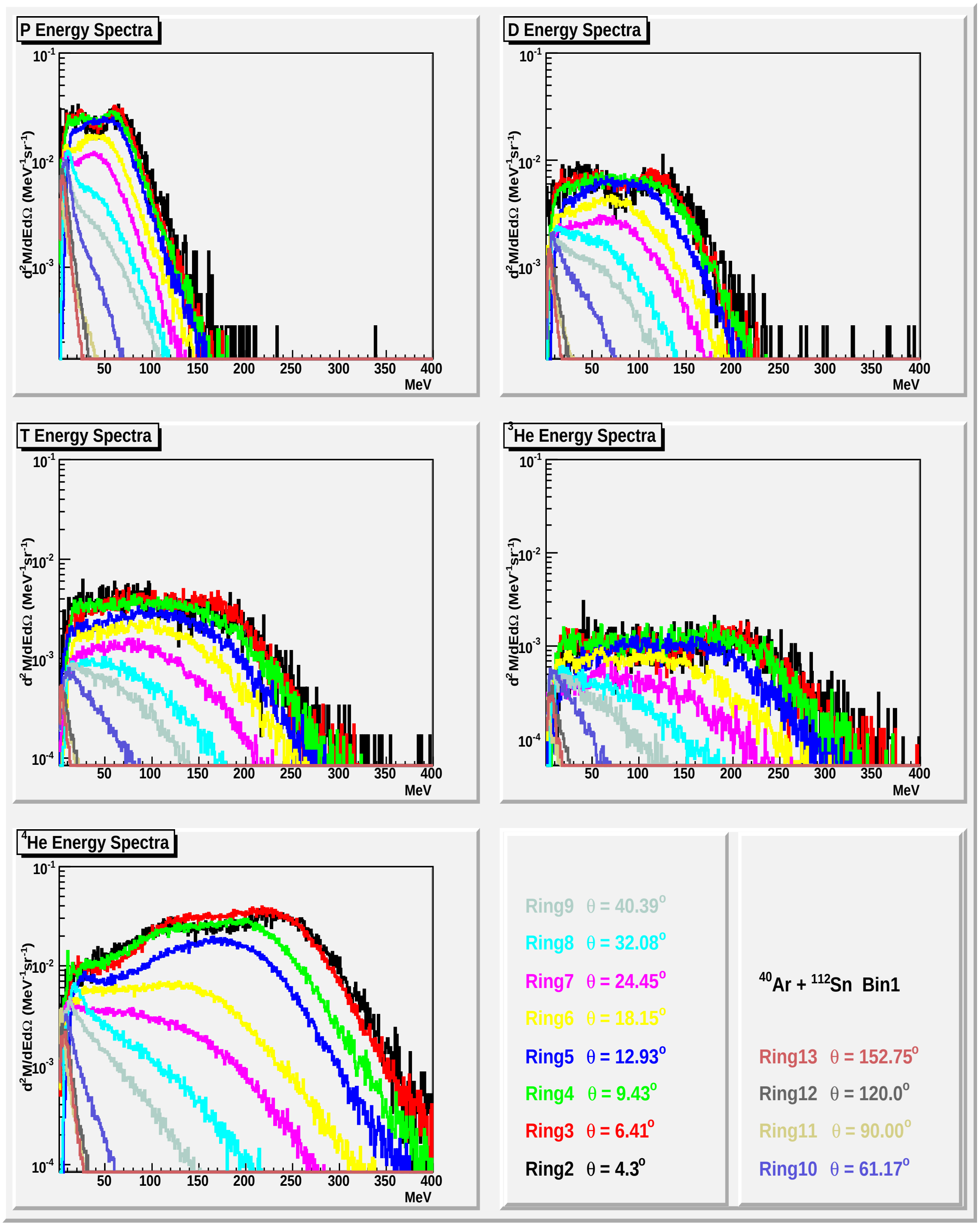

Fig. 99. X axis is energy in MeV. Y axis is the multiplicity distribution

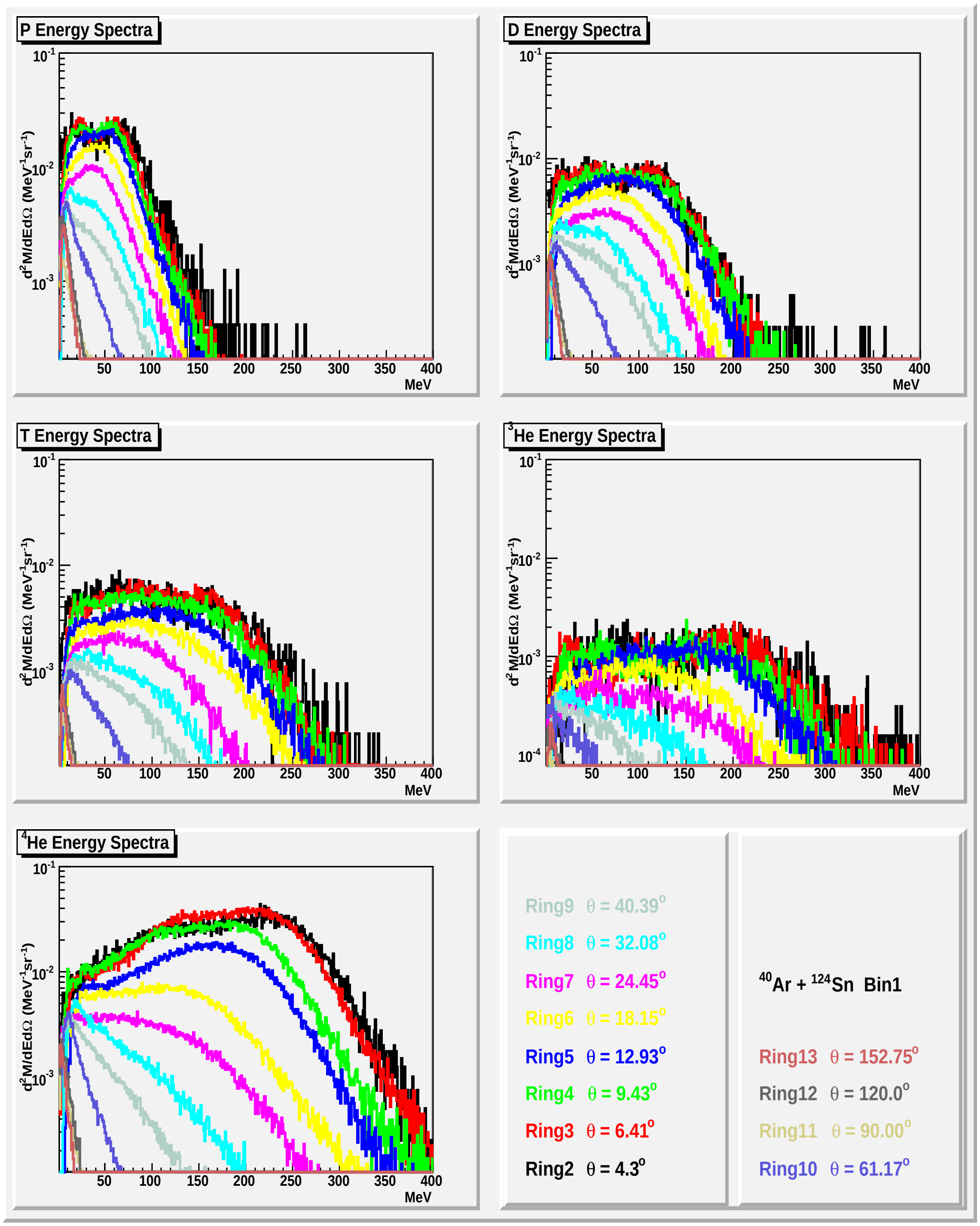

Fig. 100. X axis is energy in MeV. Y axis is the multiplicity distribution

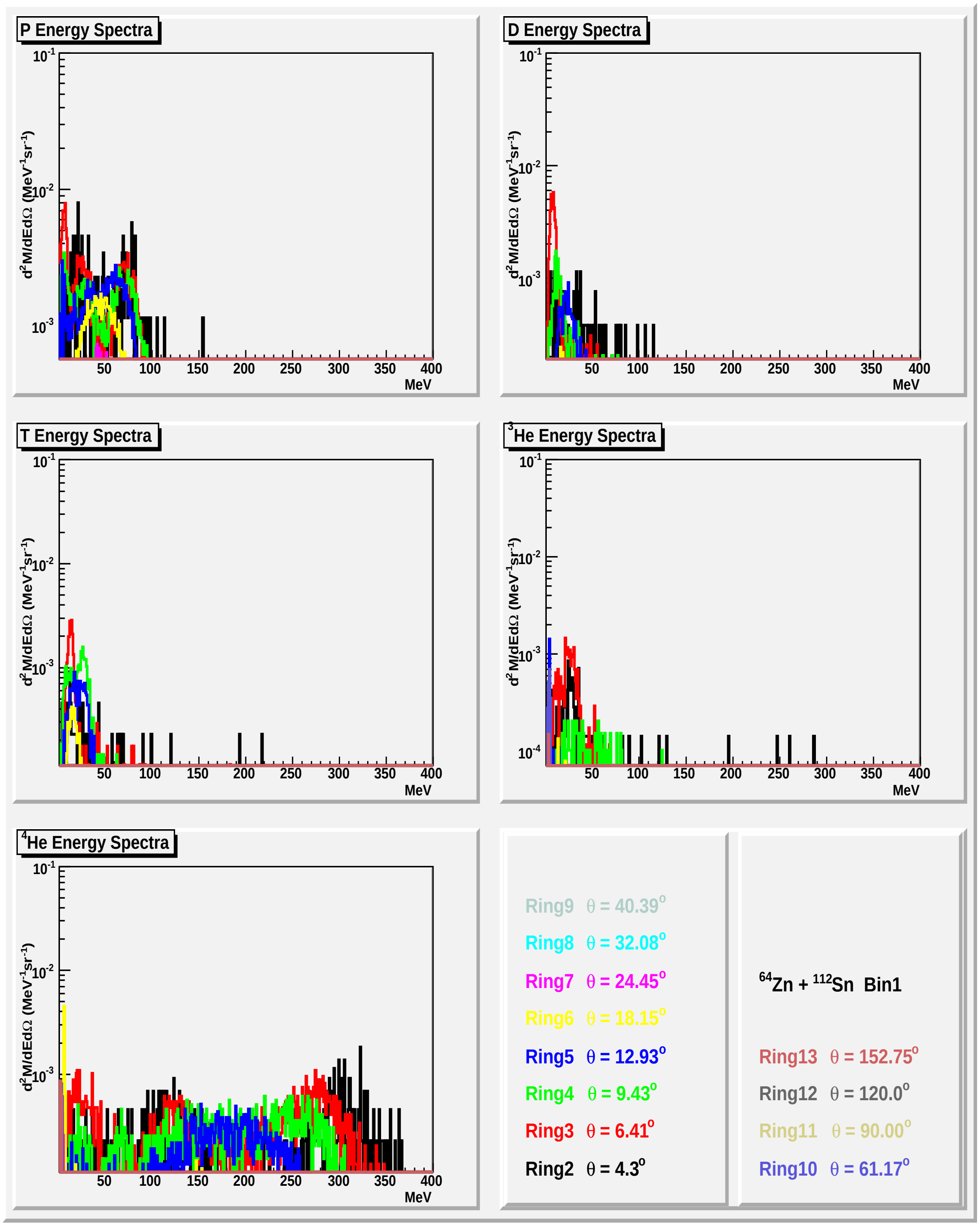

Fig. 101. X axis is energy in MeV. Y axis is the multiplicity distribution

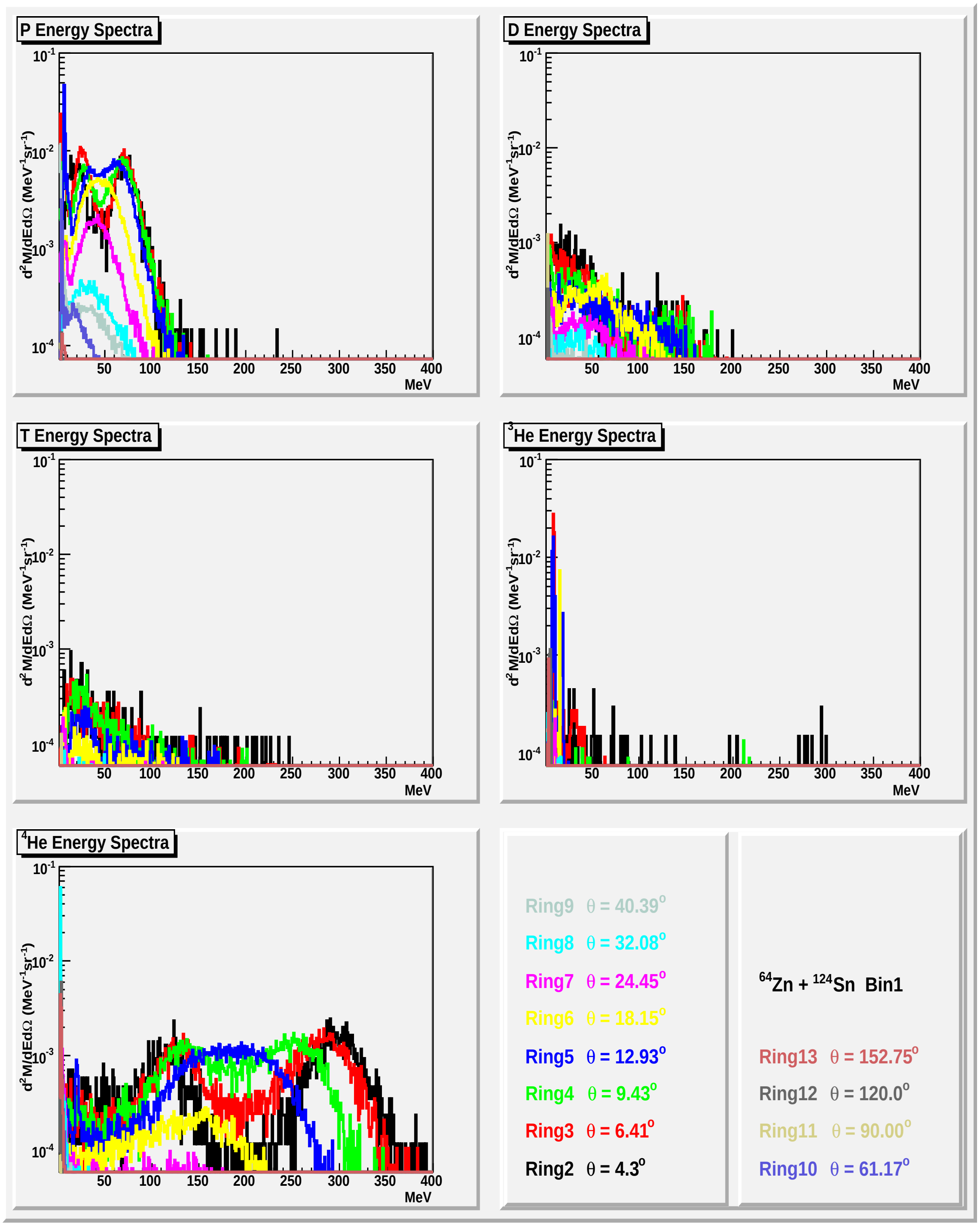

Fig. 102. X axis is energy in MeV. Y axis is the multiplicity distribution

APPENDIX F

THREE SOURCE FITTING SPECTRA FROM PROJECTILE ^{4}He

This appendix lists all of three source fitting spectra of systems ^{4}He + ^{112}Sn and ^{4}He + ^{124}Sn in which the parameters Multiplicity, Temperature , Coulomb Barrier and Source Velocities are indicated.

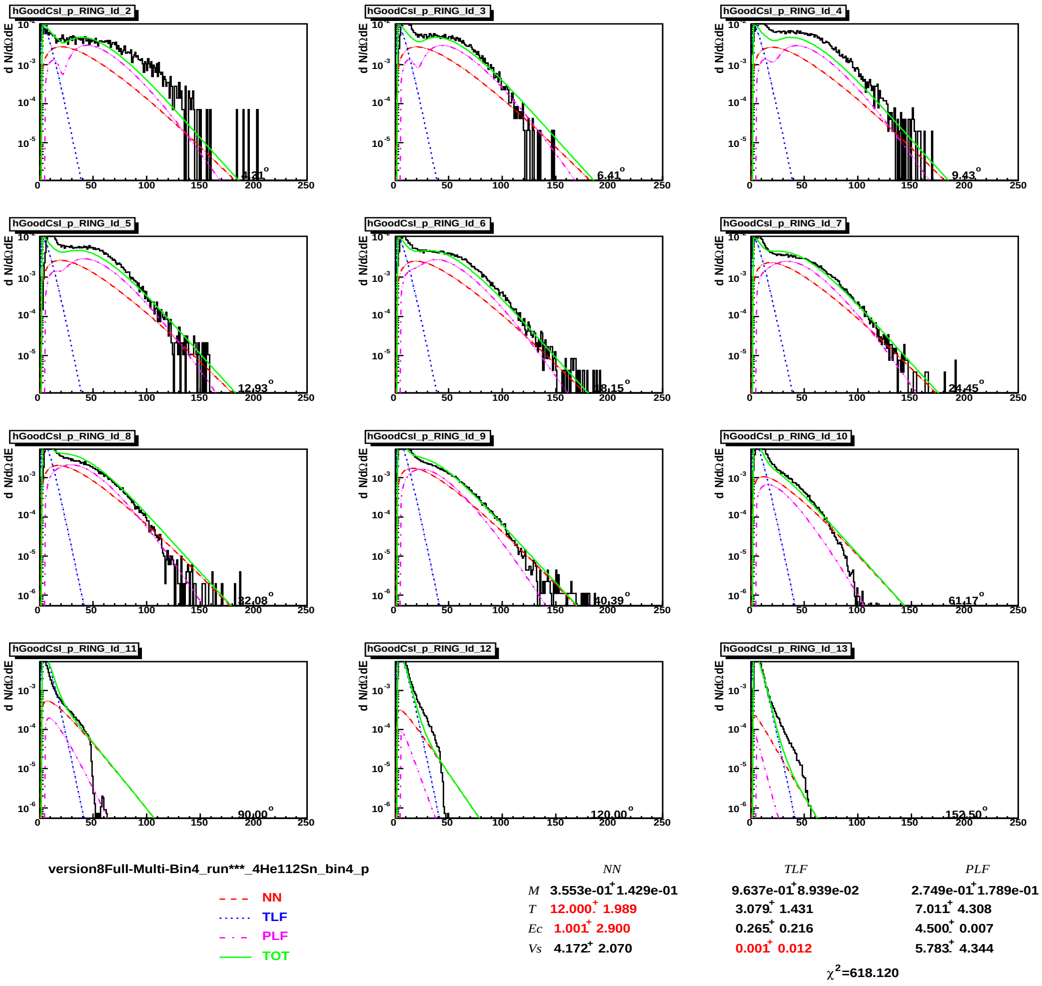

	NN	*TLF*	*PLF*
M	3.553e-01 $\pm$ 1.429e-01	9.637e-01 $\pm$ 8.939e-02	2.749e-01 $\pm$ 1.789e-01
T	12.000 $\pm$ 1.989	3.079 $\pm$ 1.431	7.011 $\pm$ 4.308
Ec	1.001 $\pm$ 2.900	0.265 $\pm$ 0.216	4.500 $\pm$ 0.007
Vs	4.172 $\pm$ 2.070	0.001 $\pm$ 0.012	5.783 $\pm$ 4.344

χ^2=618.120

Fig. 103. X axis is energy in MeV. Y axis is multiplicity distribution

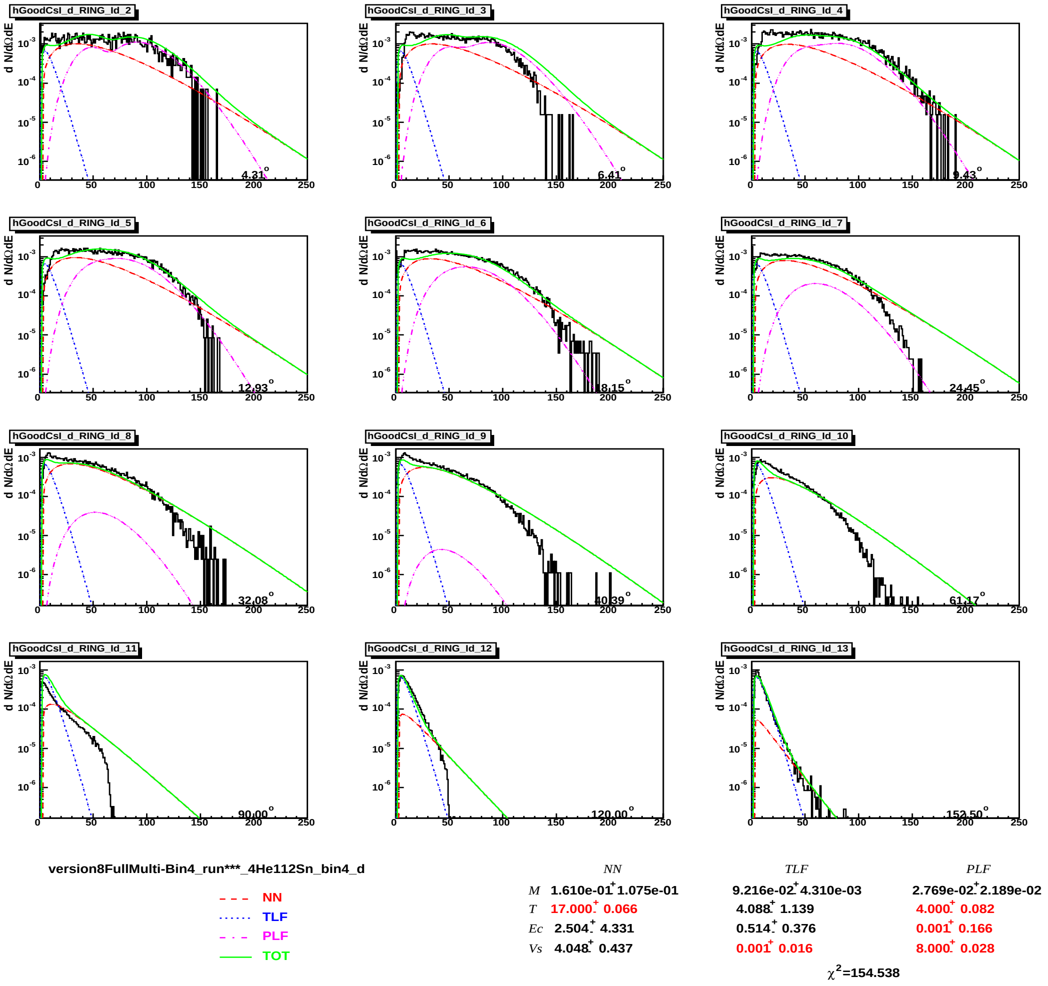

	NN	*TLF*	*PLF*
M	1.610e-01 ± 1.075e-01	9.216e-02 ± 4.310e-03	2.769e-02 ± 2.189e-02
T	17.000 ± 0.066	4.088 ± 1.139	4.000 ± 0.082
Ec	2.504 ± 4.331	0.514 ± 0.376	0.001 ± 0.166
Vs	4.048 ± 0.437	0.001 ± 0.016	8.000 ± 0.028

χ^2=154.538

Fig. 104. X axis is energy in MeV. Y axis is multiplicity distribution

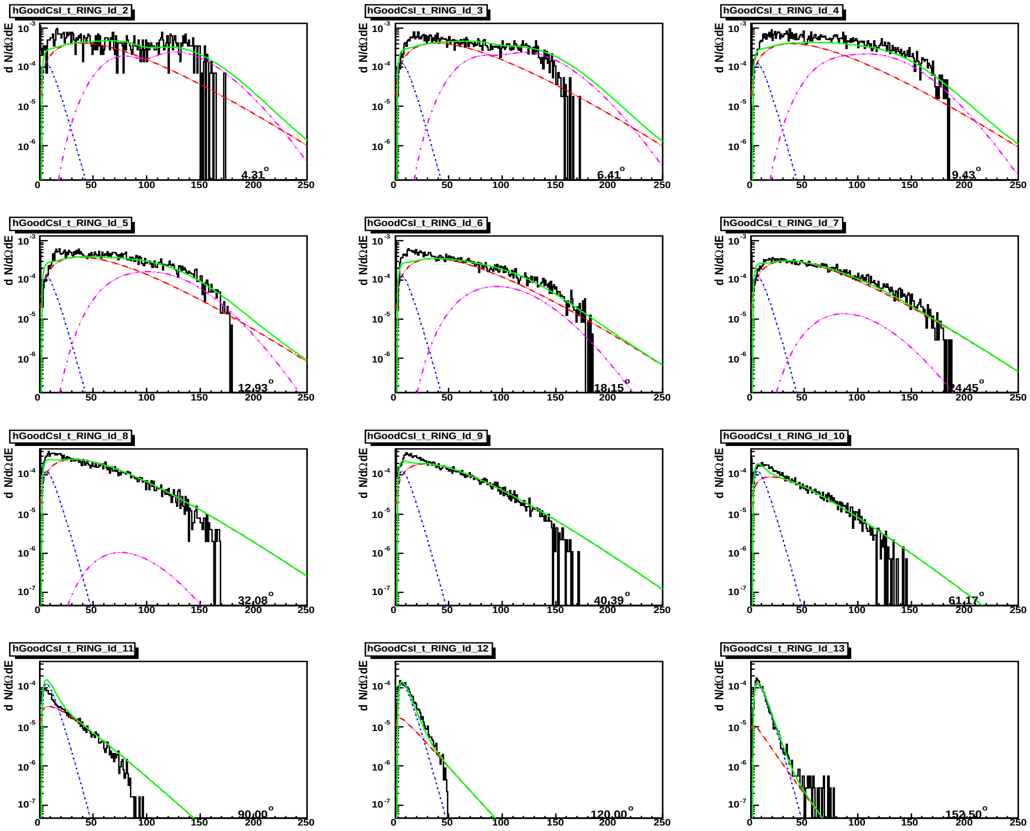

version8FullMulti-Bin4_run*_4He112Sn_bin4_t**

- - - NN
······ TLF
- · - PLF
—— TOT

	NN	*TLF*	*PLF*
M	5.891e-02 $\pm$ 9.422e-03	1.729e-02 $\pm$ 2.127e-03	5.131e-03 $\pm$ 5.130e-03
T	17.000 $\pm$ 3.747	3.996 $\pm$ 0.393	4.003 $\pm$ 0.010
Ec	0.003 $\pm$ 0.004	2.159 $\pm$ 0.309	0.001 $\pm$ 6.684
Vs	3.898 $\pm$ 0.381	0.001 $\pm$ 0.302	8.000 $\pm$ 1.857

χ^2=14.999

Fig. 105. X axis is energy in MeV. Y axis is multiplicity distribution

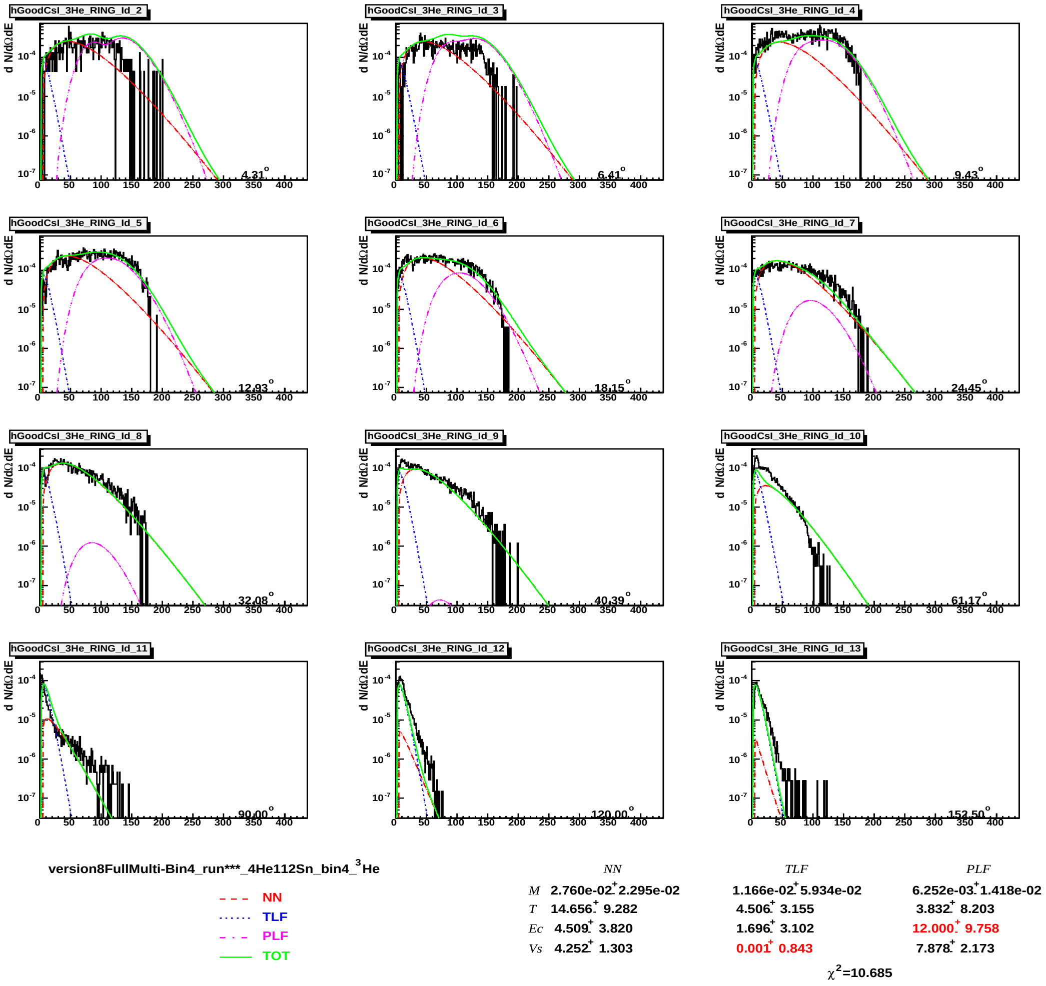

	NN	*TLF*	*PLF*
M	2.760e-02 $\pm$ 2.295e-02	1.166e-02 $\pm$ 5.934e-02	6.252e-03 $\pm$ 1.418e-02
T	14.656 $\pm$ 9.282	4.506 $\pm$ 3.155	3.832 $\pm$ 8.203
Ec	4.509 $\pm$ 3.820	1.696 $\pm$ 3.102	12.000 $\pm$ 9.758
Vs	4.252 $\pm$ 1.303	0.001 $\pm$ 0.843	7.878 $\pm$ 2.173

χ^2=10.685

Fig. 106. X axis is energy in MeV. Y axis is multiplicity distribution

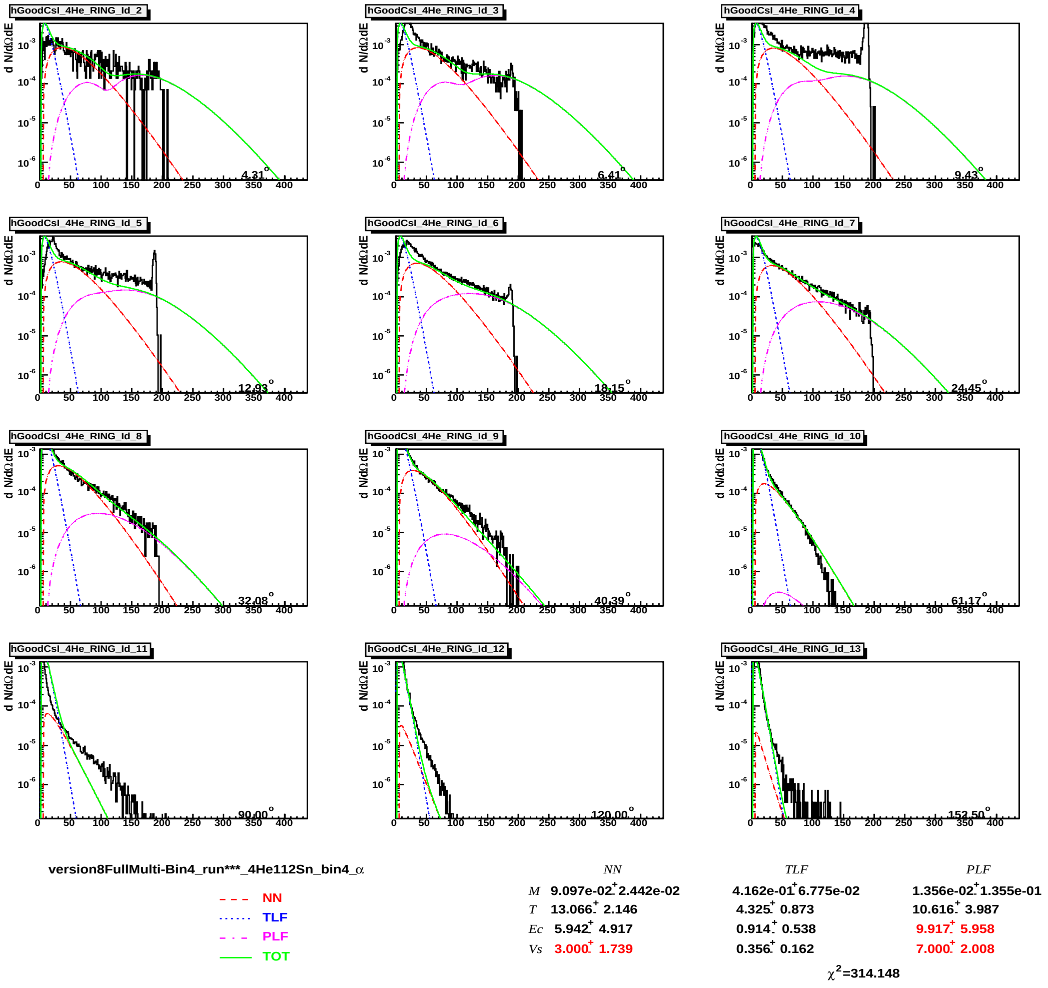

	NN	*TLF*	*PLF*
M	9.097e-02 $\pm$ 2.442e-02	4.162e-01 $\pm$ 6.775e-02	1.356e-02 $\pm$ 1.355e-01
T	13.066 $\pm$ 2.146	4.325 $\pm$ 0.873	10.616 $\pm$ 3.987
Ec	5.942 $\pm$ 4.917	0.914 $\pm$ 0.538	9.917 $\pm$ 5.958
Vs	3.000 $\pm$ 1.739	0.356 $\pm$ 0.162	7.000 $\pm$ 2.008

χ^2=314.148

Fig. 107. X axis is energy in MeV. Y axis is multiplicity distribution

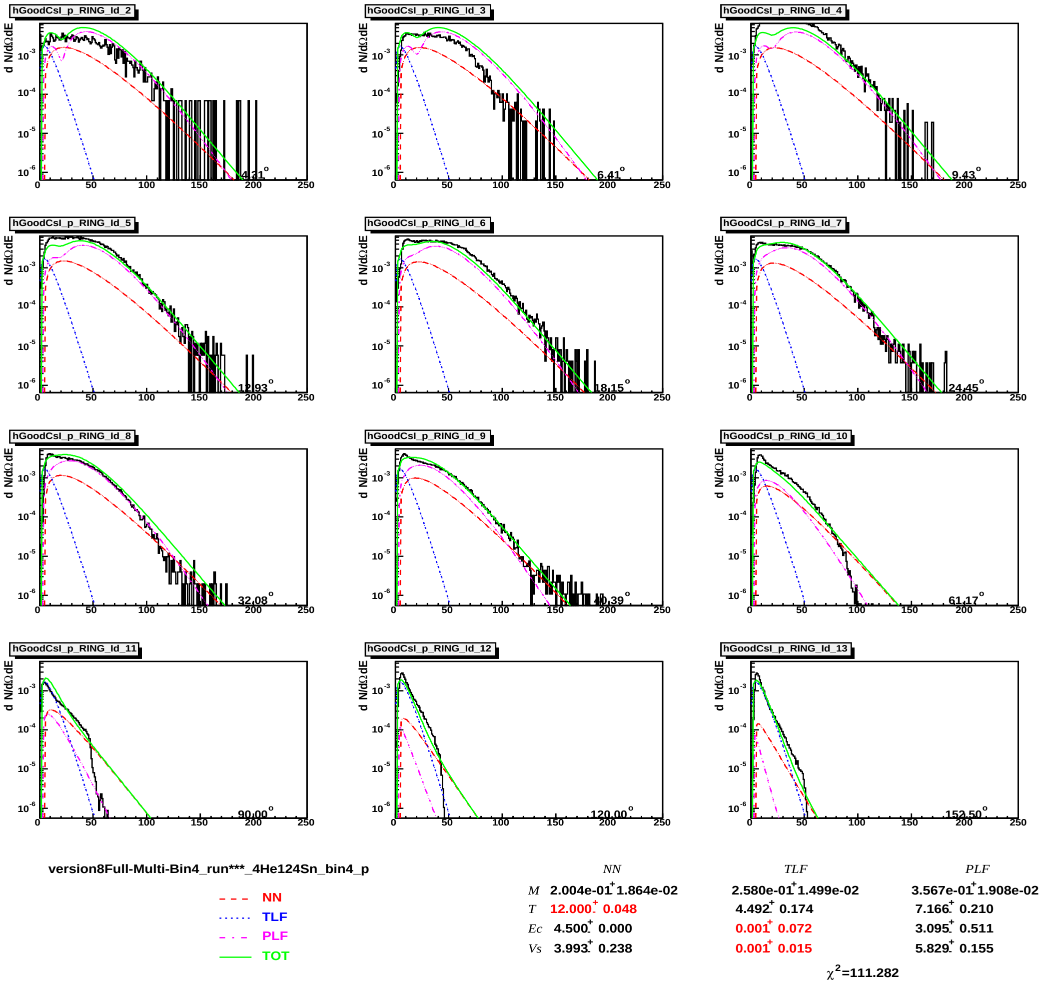

	NN	TLF	PLF
M	2.004e-01 ± 1.864e-02	2.580e-01 ± 1.499e-02	3.567e-01 ± 1.908e-02
T	12.000 ± 0.048	4.492 ± 0.174	7.166 ± 0.210
Ec	4.500 ± 0.000	0.001 ± 0.072	3.095 ± 0.511
Vs	3.993 ± 0.238	0.001 ± 0.015	5.829 ± 0.155

χ^2=111.282

Fig. 108. X axis is energy in MeV. Y axis is multiplicity distribution

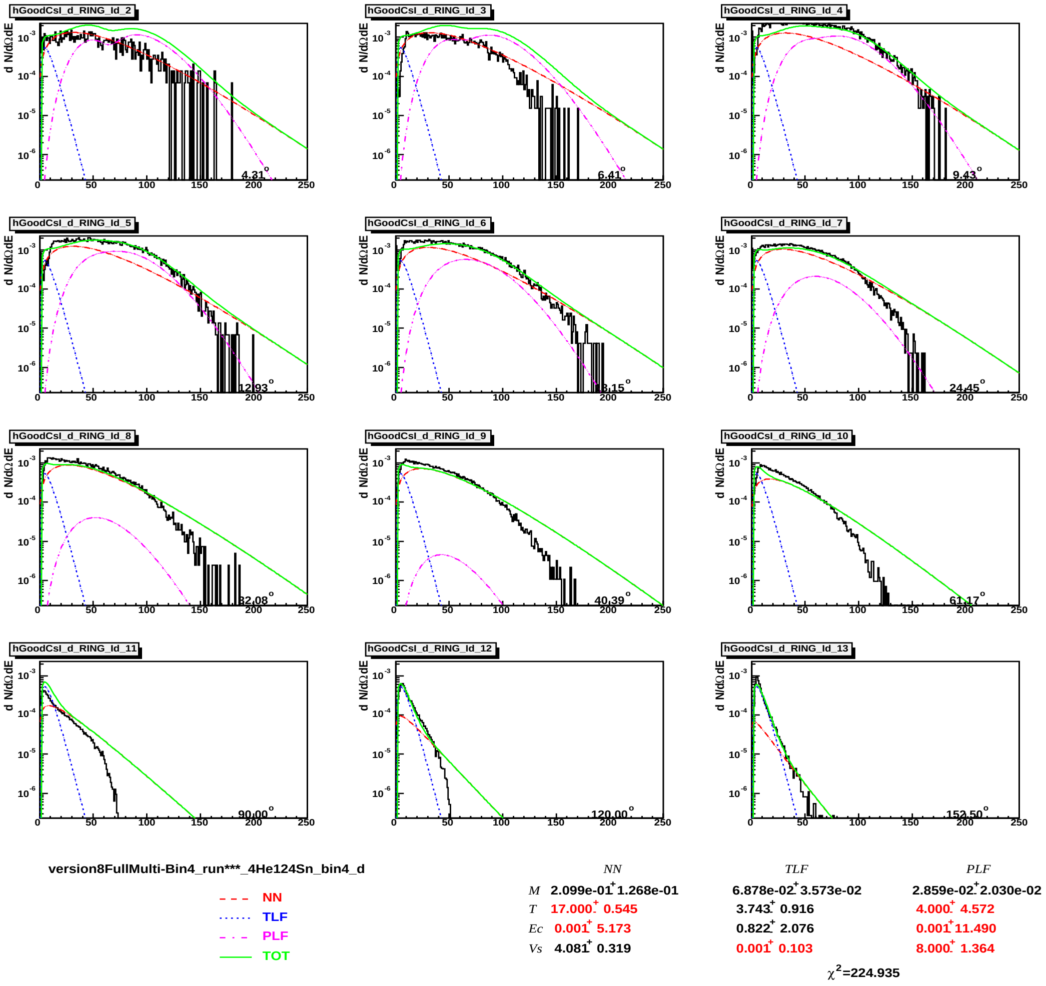

	NN	*TLF*	*PLF*
M	2.099e-01 $\pm$ 1.268e-01	6.878e-02 $\pm$ 3.573e-02	2.859e-02 $\pm$ 2.030e-02
T	17.000 $\pm$ 0.545	3.743 $\pm$ 0.916	4.000 $\pm$ 4.572
Ec	0.001 $\pm$ 5.173	0.822 $\pm$ 2.076	0.001 $\pm$ 11.490
Vs	4.081 $\pm$ 0.319	0.001 $\pm$ 0.103	8.000 $\pm$ 1.364

χ^2=224.935

Fig. 109. X axis is energy in MeV. Y axis is multiplicity distribution

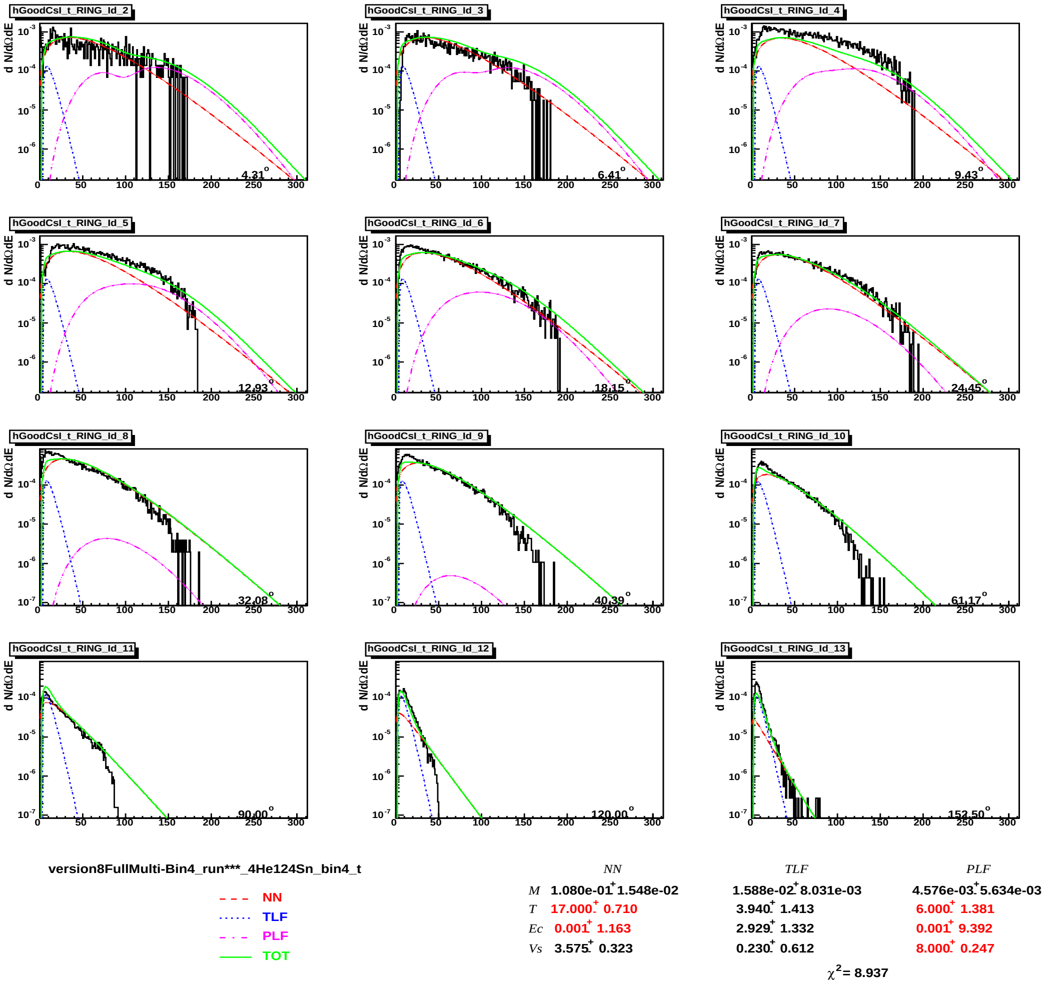

	NN	TLF	PLF
M	1.080e-01 ± 1.548e-02	1.588e-02 ± 8.031e-03	4.576e-03 ± 5.634e-03
T	17.000 ± 0.710	3.940 ± 1.413	6.000 ± 1.381
Ec	0.001 ± 1.163	2.929 ± 1.332	0.001 ± 9.392
Vs	3.575 ± 0.323	0.230 ± 0.612	8.000 ± 0.247

$\chi^2 = 8.937$

Fig. 110. X axis is energy in MeV. Y axis is multiplicity distribution

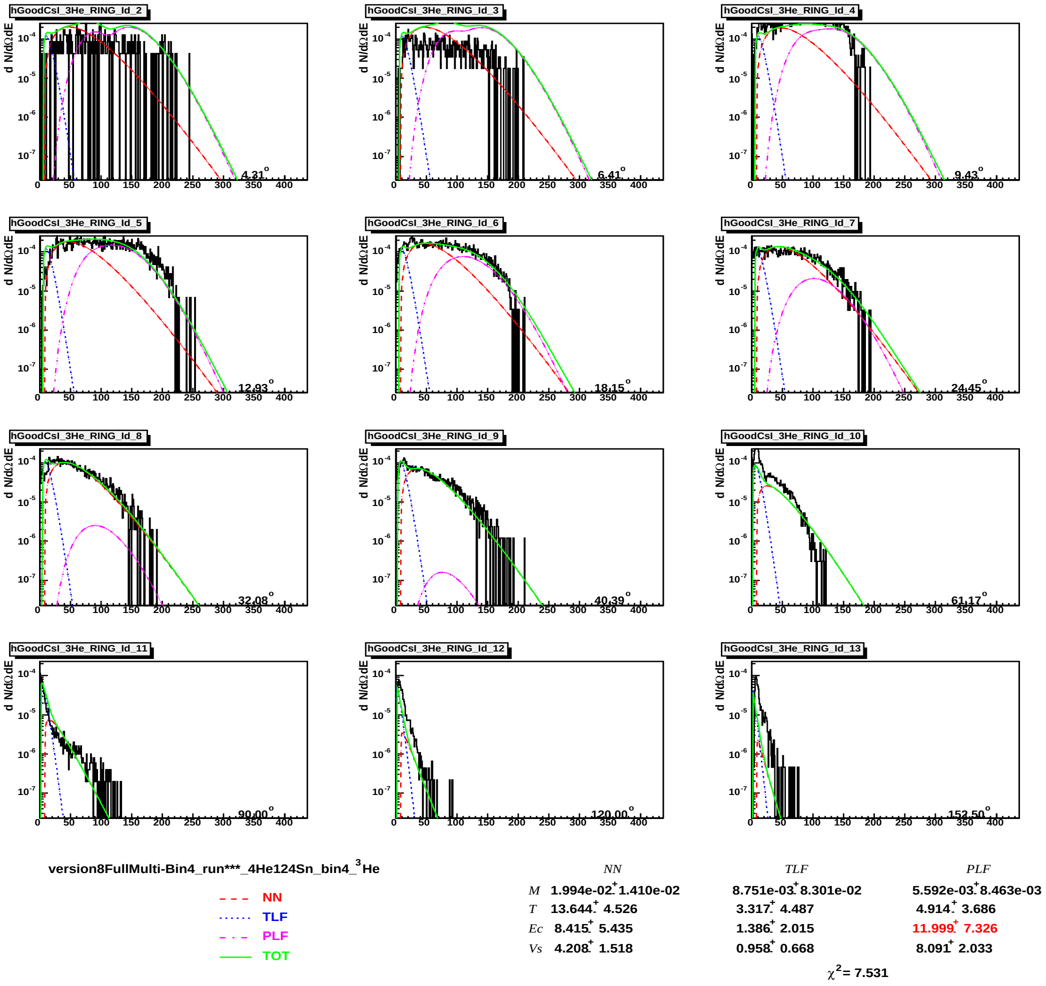

	NN	*TLF*	*PLF*
M	1.994e-02 $\pm$ 1.410e-02	8.751e-03 $\pm$ 8.301e-02	5.592e-03 $\pm$ 8.463e-03
T	13.644 $\pm$ 4.526	3.317 $\pm$ 4.487	4.914 $\pm$ 3.686
Ec	8.415 $\pm$ 5.435	1.386 $\pm$ 2.015	11.999 $\pm$ 7.326
Vs	4.208 $\pm$ 1.518	0.958 $\pm$ 0.668	8.091 $\pm$ 2.033

χ^2= 7.531

Fig. 111. X axis is energy in MeV. Y axis is multiplicity distribution

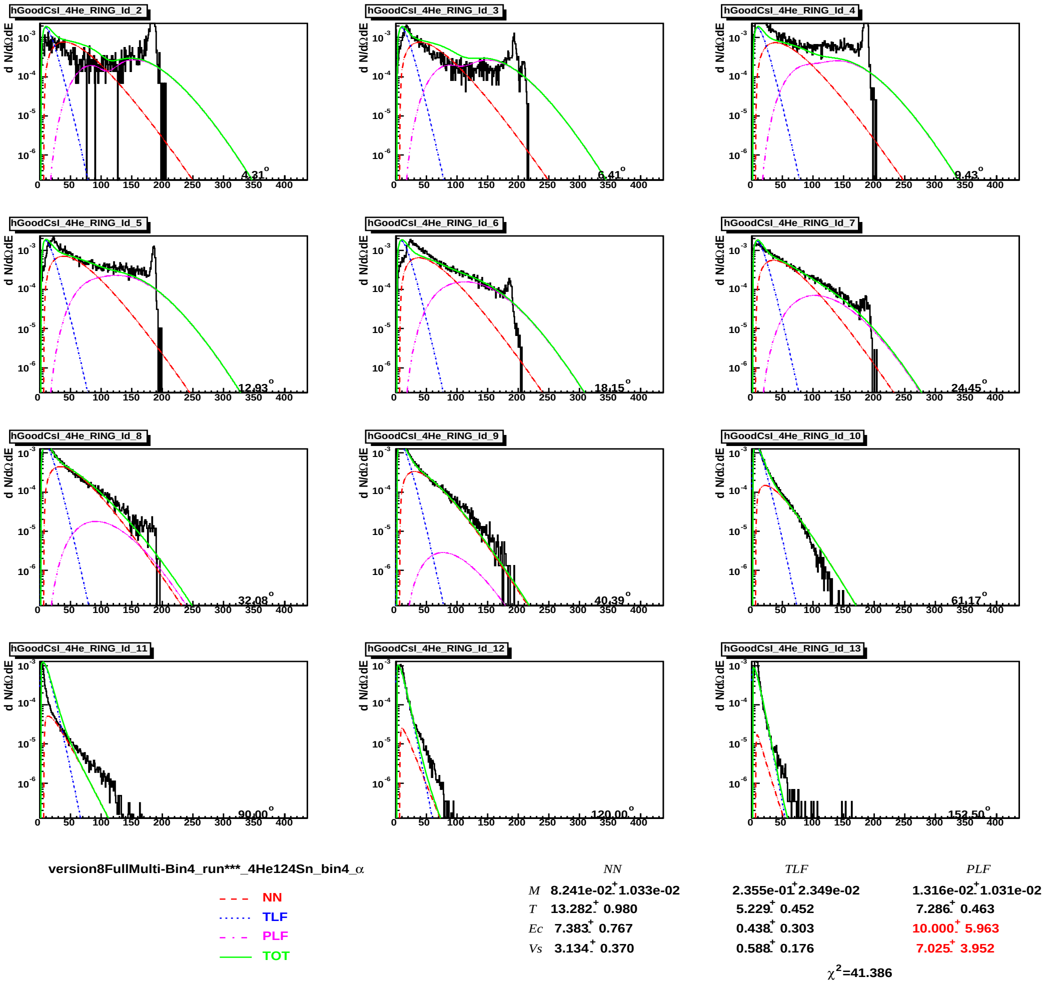

	NN	*TLF*	*PLF*
M	8.241e-02 ± 1.033e-02	2.355e-01 ± 2.349e-02	1.316e-02 ± 1.031e-02
T	13.282 ± 0.980	5.229 ± 0.452	7.286 ± 0.463
Ec	7.383 ± 0.767	0.438 ± 0.303	10.000 ± 5.963
Vs	3.134 ± 0.370	0.588 ± 0.176	7.025 ± 3.952

χ^2=41.386

Fig. 112. X axis is energy in MeV. Y axis is multiplicity distribution

APPENDIX G

THREE SOURCE FITTING SPECTRA FROM PROJECTILE ^{10}B

This appendix lists all of three source fitting spectra of systems ^{10}B+^{112}Sn and ^{10}B+^{124}Sn in which the parameters Multiplicity, Temperature , Coulomb Barrier and Source Velocities are indicated.

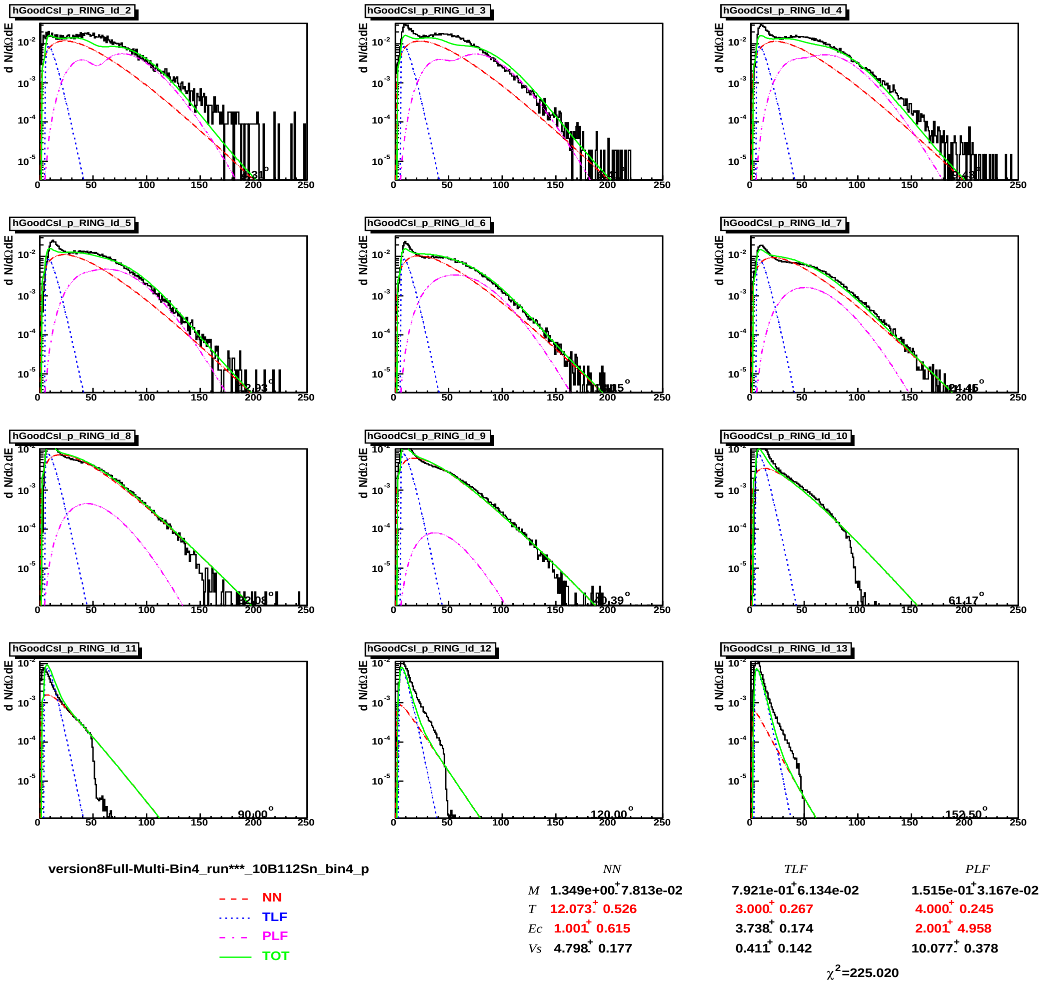

	NN	TLF	PLF
M	1.349e+00 ± 7.813e-02	7.921e-01 ± 6.134e-02	1.515e-01 ± 3.167e-02
T	12.073 ± 0.526	3.000 ± 0.267	4.000 ± 0.245
Ec	1.001 ± 0.615	3.738 ± 0.174	2.001 ± 4.958
Vs	4.798 ± 0.177	0.411 ± 0.142	10.077 ± 0.378

χ^2=225.020

Fig. 113. X axis is energy in MeV. Y axis is multiplicity distribution

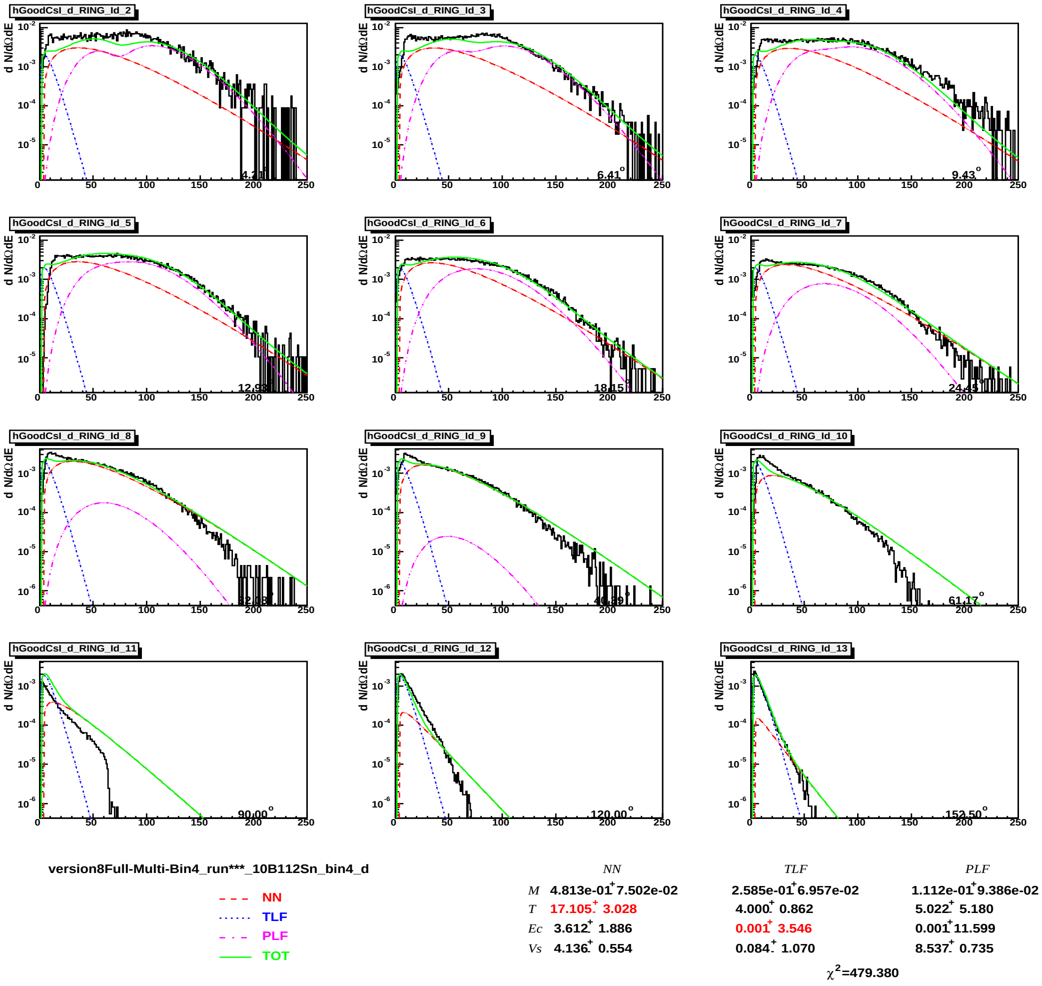

	NN	TLF	PLF
M	4.813e-01 ± 7.502e-02	2.585e-01 ± 6.957e-02	1.112e-01 ± 9.386e-02
T	17.105 ± 3.028	4.000 ± 0.862	5.022 ± 5.180
Ec	3.612 ± 1.886	0.001 ± 3.546	0.001 ± 11.599
Vs	4.136 ± 0.554	0.084 ± 1.070	8.537 ± 0.735

χ^2=479.380

Fig. 114. X axis is energy in MeV. Y axis is multiplicity distribution

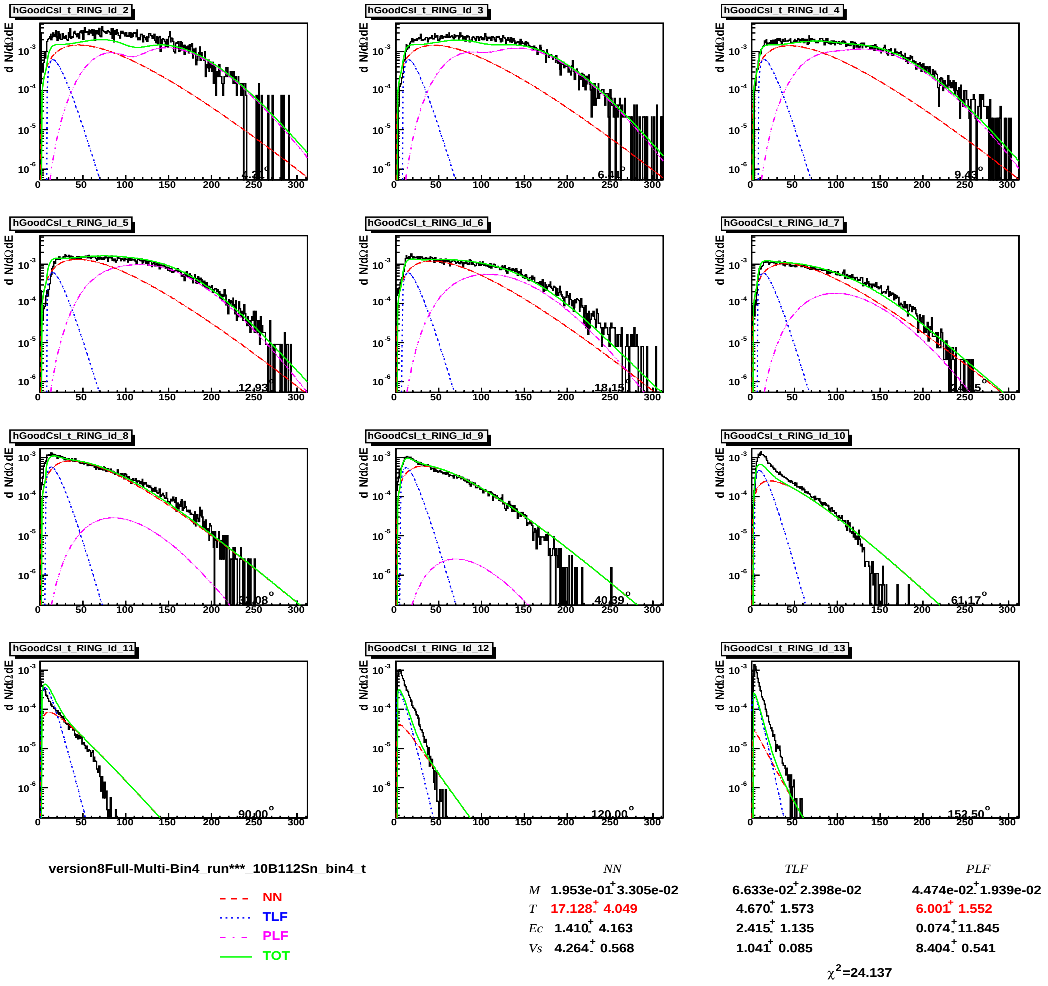

	NN	*TLF*	*PLF*
M	1.953e-01 ± 3.305e-02	6.633e-02 ± 2.398e-02	4.474e-02 ± 1.939e-02
T	17.128 ± 4.049	4.670 ± 1.573	6.001 ± 1.552
Ec	1.410 ± 4.163	2.415 ± 1.135	0.074 ± 11.845
Vs	4.264 ± 0.568	1.041 ± 0.085	8.404 ± 0.541

χ^2=24.137

Fig. 115. X axis is energy in MeV. Y axis is multiplicity distribution

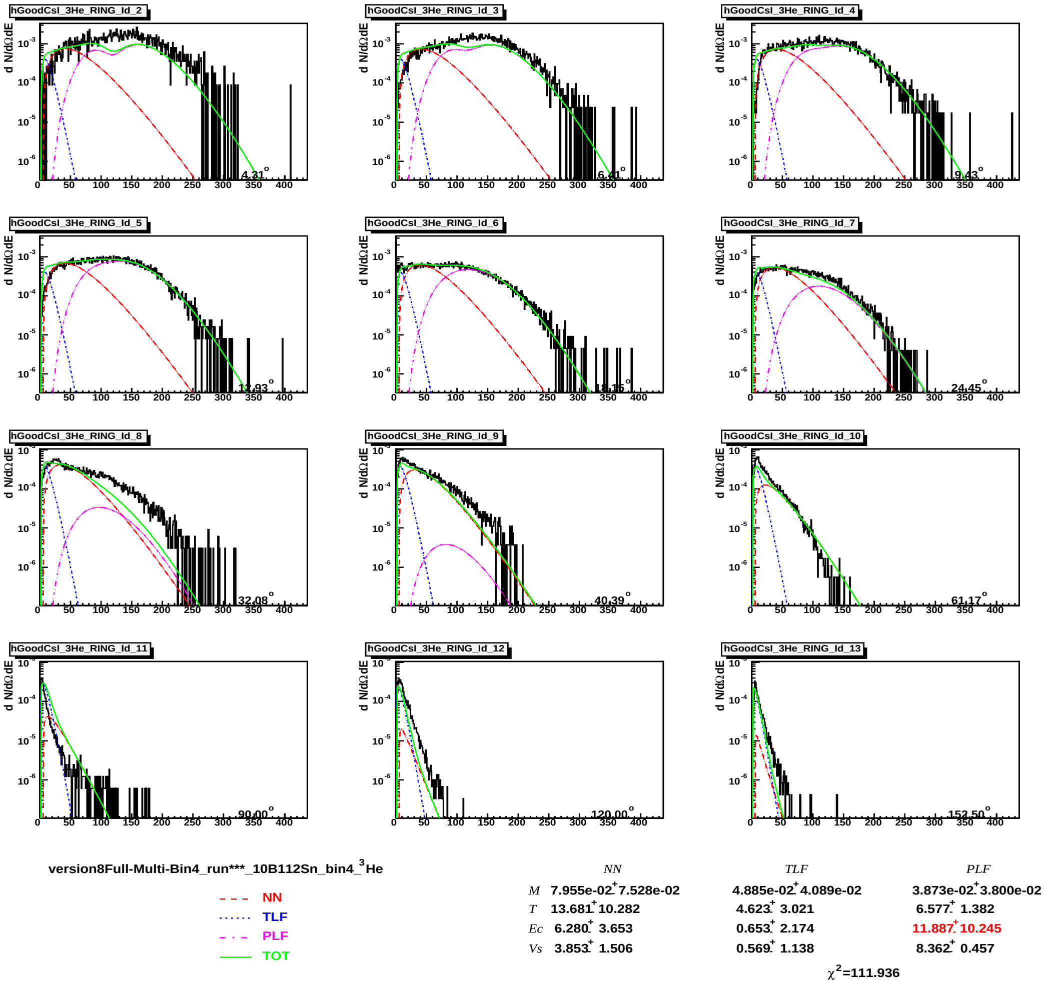

	NN	*TLF*	*PLF*
M	7.955e-02 $\pm$ 7.528e-02	4.885e-02 $\pm$ 4.089e-02	3.873e-02 $\pm$ 3.800e-02
T	13.681 $\pm$ 10.282	4.623 $\pm$ 3.021	6.577 $\pm$ 1.382
Ec	6.280 $\pm$ 3.653	0.653 $\pm$ 2.174	11.887 $\pm$ 10.245
Vs	3.853 $\pm$ 1.506	0.569 $\pm$ 1.138	8.362 $\pm$ 0.457

χ^2=111.936

Fig. 116. X axis is energy in MeV. Y axis is multiplicity distribution

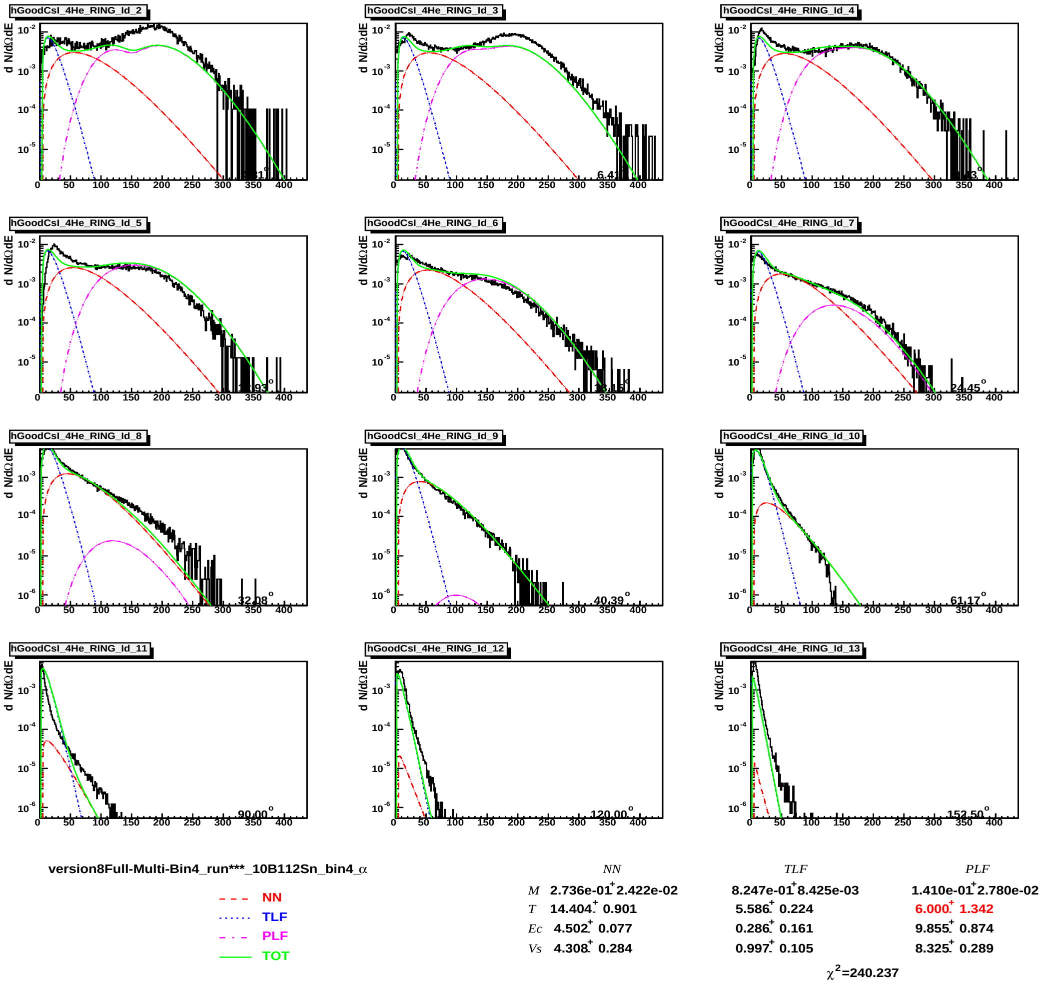

	NN	*TLF*	*PLF*
M	2.736e-01 ± 2.422e-02	8.247e-01 ± 8.425e-03	1.410e-01 ± 2.780e-02
T	14.404 ± 0.901	5.586 ± 0.224	6.000 ± 1.342
Ec	4.502 ± 0.077	0.286 ± 0.161	9.855 ± 0.874
Vs	4.308 ± 0.284	0.997 ± 0.105	8.325 ± 0.289

χ^2=240.237

Fig. 117. X axis is energy in MeV. Y axis is multiplicity distribution

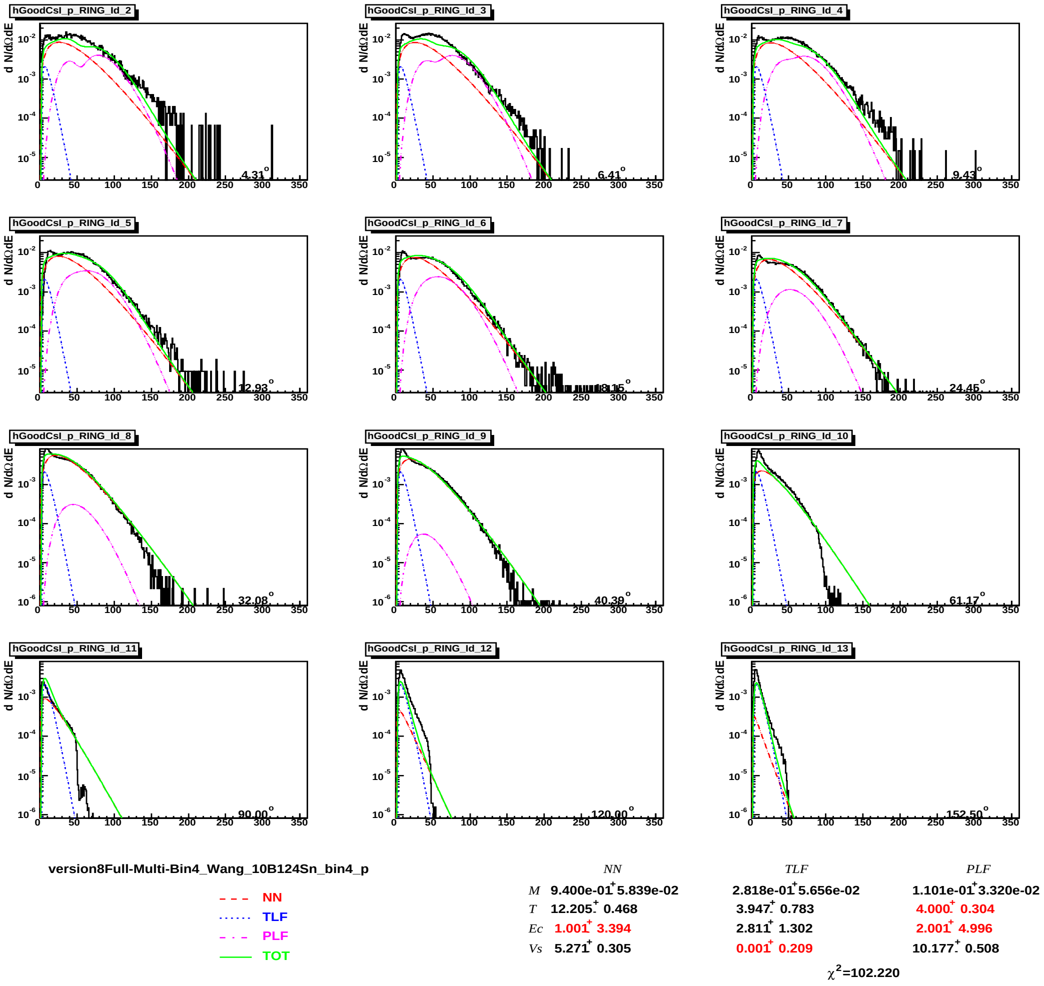

Fig. 118. X axis is energy in MeV. Y axis is multiplicity distribution

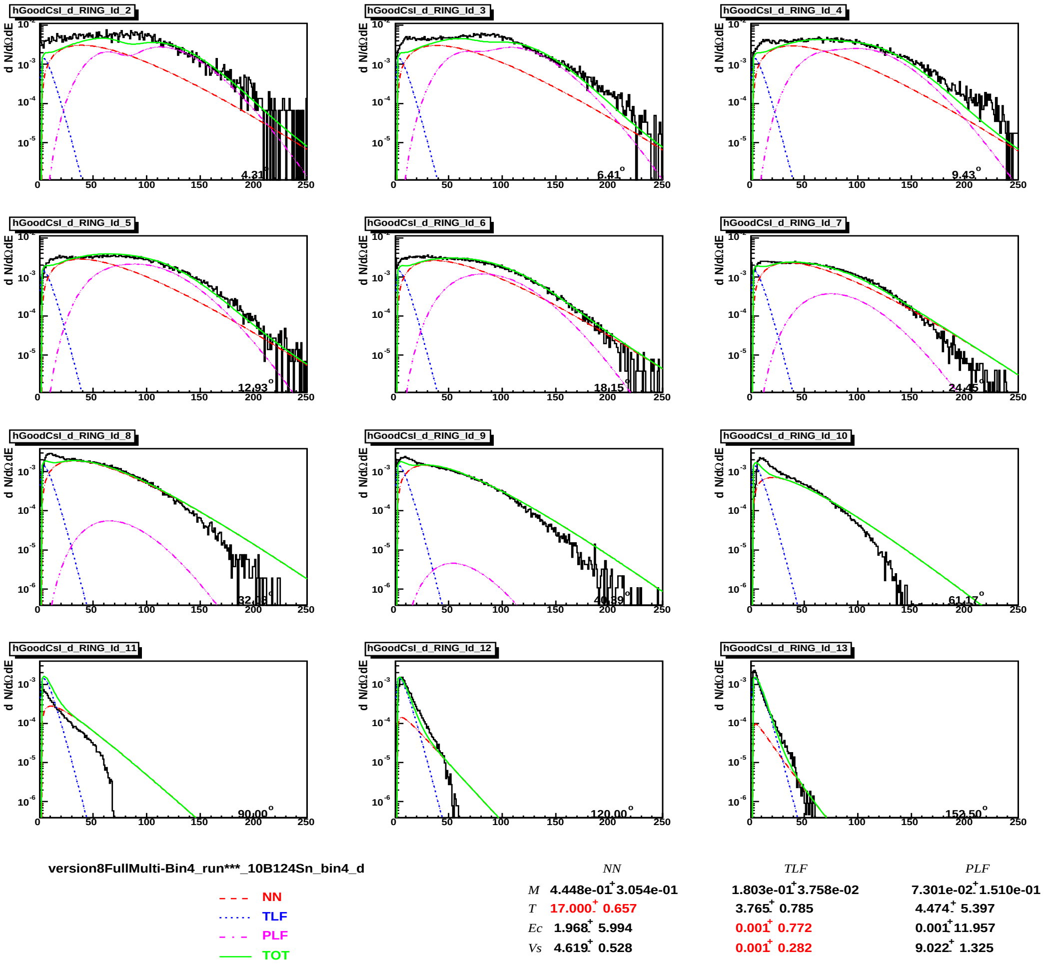

	NN	TLF	PLF
M	4.448e-01 ± 3.054e-01	1.803e-01 ± 3.758e-02	7.301e-02 ± 1.510e-01
T	17.000 ± 0.657	3.765 ± 0.785	4.474 ± 5.397
Ec	1.968 ± 5.994	0.001 ± 0.772	0.001 ± 11.957
Vs	4.619 ± 0.528	0.001 ± 0.282	9.022 ± 1.325

χ^2=372.161

Fig. 119. X axis is energy in MeV. Y axis is multiplicity distribution

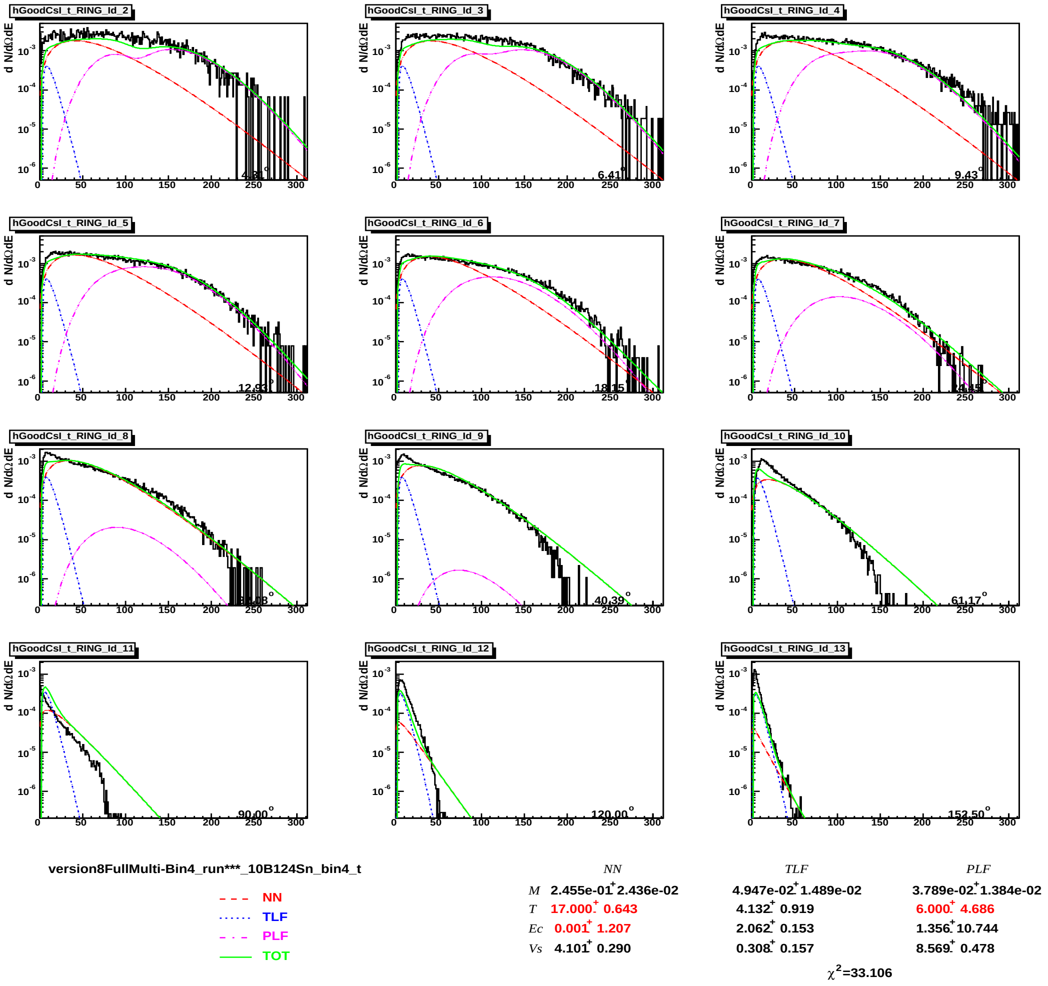

	NN	TLF	PLF
M	2.455e-01 ± 2.436e-02	4.947e-02 ± 1.489e-02	3.789e-02 ± 1.384e-02
T	17.000 ± 0.643	4.132 ± 0.919	6.000 ± 4.686
Ec	0.001 ± 1.207	2.062 ± 0.153	1.356 ± 10.744
Vs	4.101 ± 0.290	0.308 ± 0.157	8.569 ± 0.478

χ^2=33.106

Fig. 120. X axis is energy in MeV. Y axis is multiplicity distribution

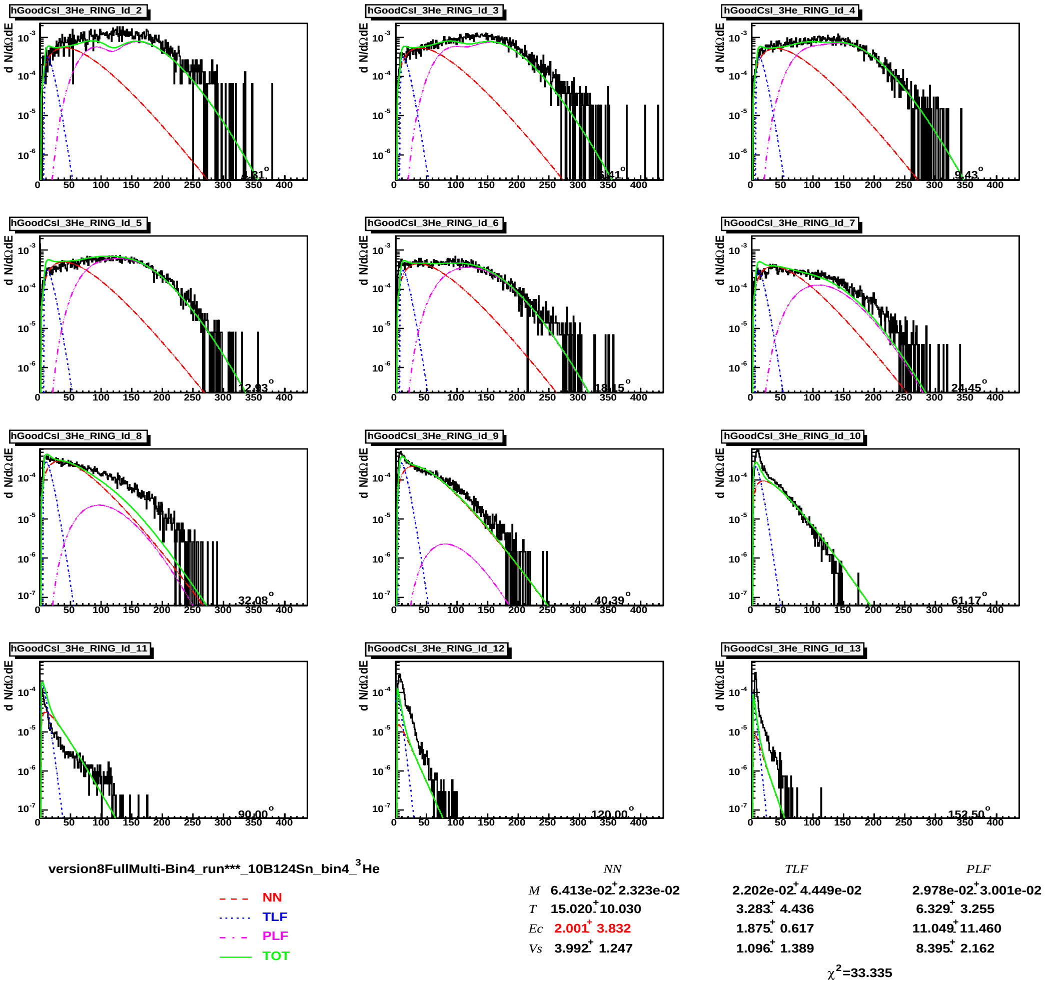

Fig. 121. X axis is energy in MeV. Y axis is multiplicity distribution

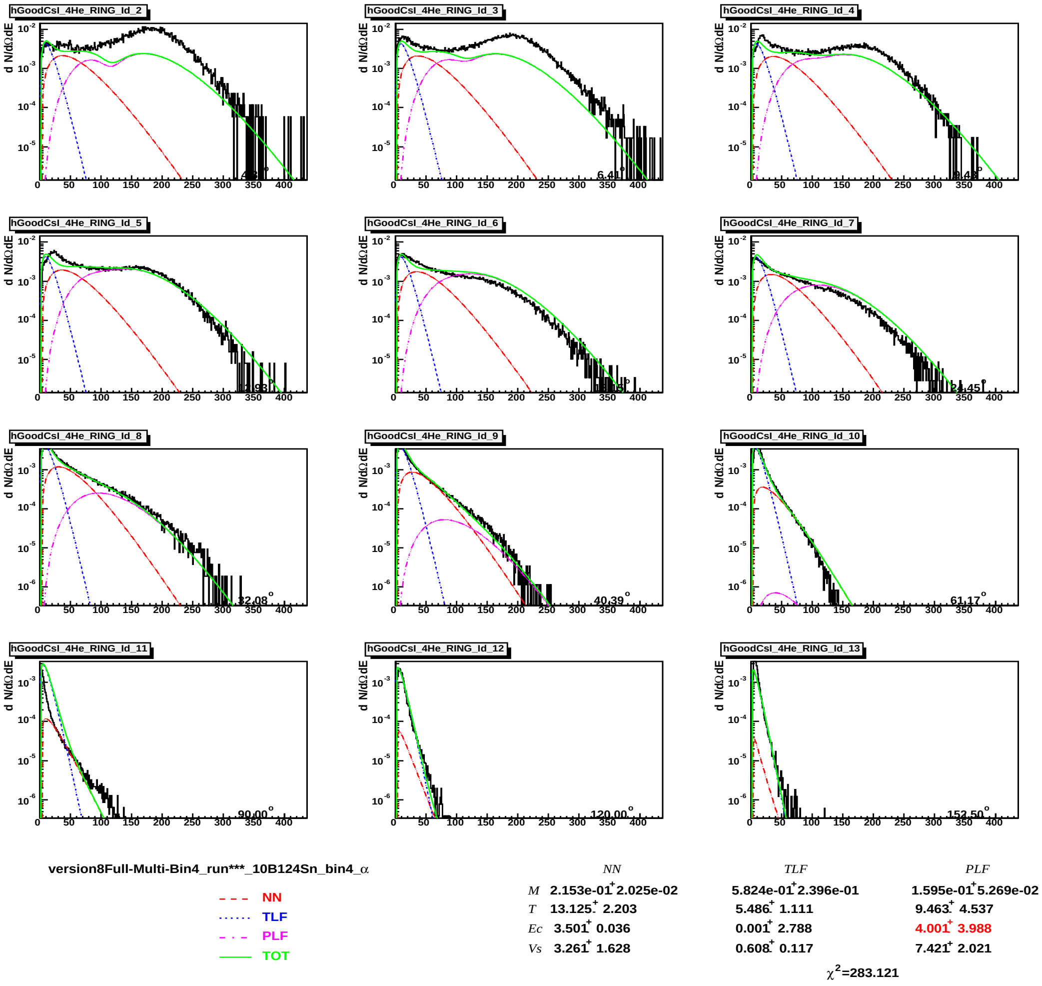

	NN	TLF	PLF
M	2.153e-01 ± 2.025e-02	5.824e-01 ± 2.396e-01	1.595e-01 ± 5.269e-02
T	13.125 ± 2.203	5.486 ± 1.111	9.463 ± 4.537
Ec	3.501 ± 0.036	0.001 ± 2.788	4.001 ± 3.988
Vs	3.261 ± 1.628	0.608 ± 0.117	7.421 ± 2.021

χ^2=283.121

Fig. 122. X axis is energy in MeV. Y axis is multiplicity distribution

APPENDIX H

THREE SOURCE FITTING SPECTRA FROM PROJECTILE ^{20}Ne

This appendix lists all of three source fitting spectra of systems ^{20}Ne+^{112}Sn and ^{20}Ne+^{124}Sn in which the parameters Multiplicity, Temperature , Coulomb Barrier and Source Velocities are indicated.

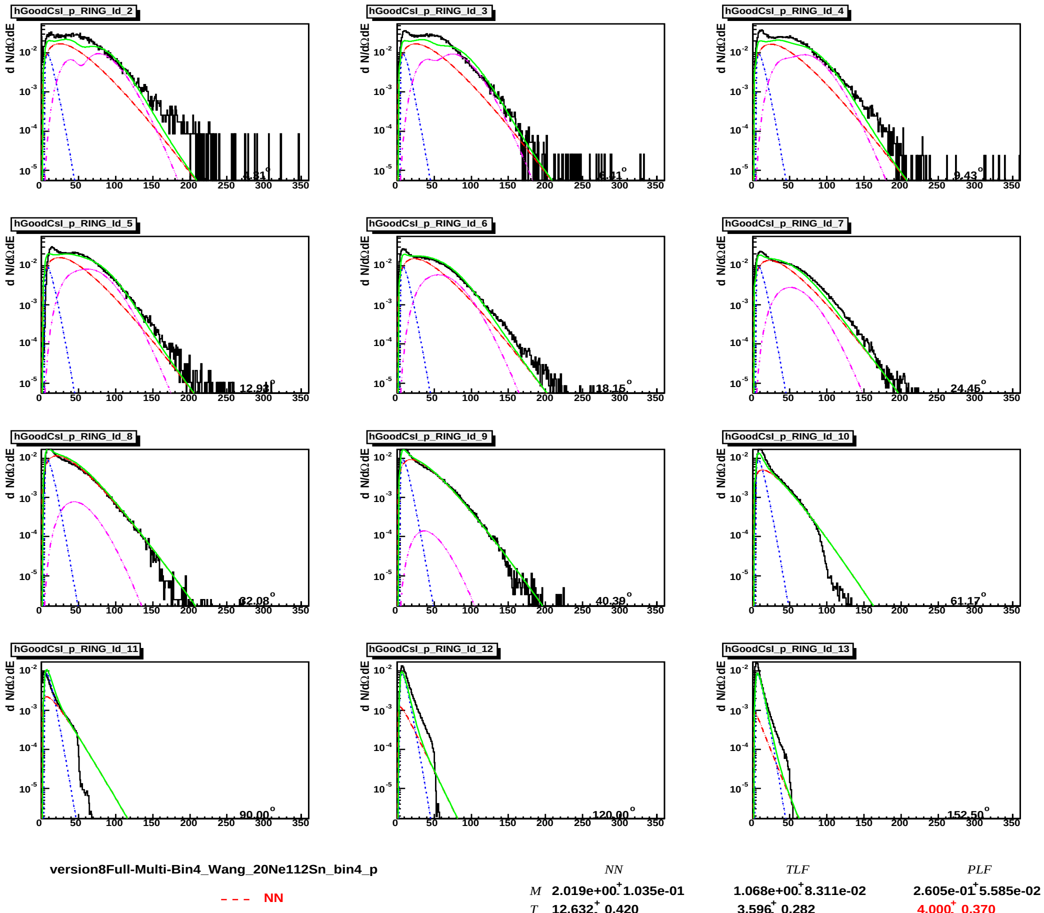

	NN	TLF	PLF
M	2.019e+00 ± 1.035e-01	1.068e+00 ± 8.311e-02	2.605e-01 ± 5.585e-02
T	12.632 ± 0.420	3.596 ± 0.282	4.000 ± 0.370
Ec	1.001 ± 2.782	3.652 ± 0.276	2.001 ± 3.842
Vs	5.000 ± 0.250	0.280 ± 0.108	10.076 ± 0.394

χ^2=231.045

Fig. 123. X axis is energy in MeV. Y axis is multiplicity distribution

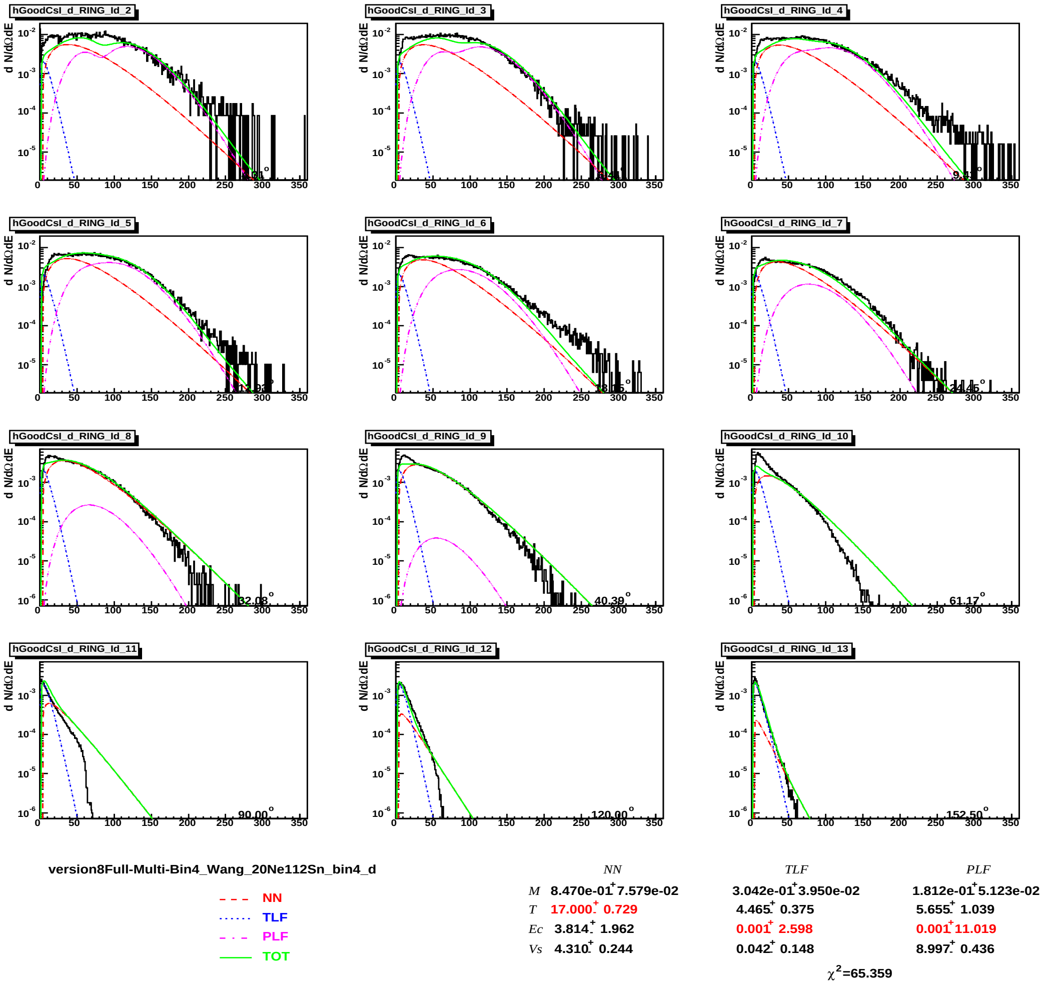

	NN	*TLF*	*PLF*
M	8.470e-01 ± 7.579e-02	3.042e-01 ± 3.950e-02	1.812e-01 ± 5.123e-02
T	17.000 ± 0.729	4.465 ± 0.375	5.655 ± 1.039
Ec	3.814 ± 1.962	0.001 ± 2.598	0.001 ± 11.019
Vs	4.310 ± 0.244	0.042 ± 0.148	8.997 ± 0.436

χ^2=65.359

Fig. 124. X axis is energy in MeV. Y axis is multiplicity distribution

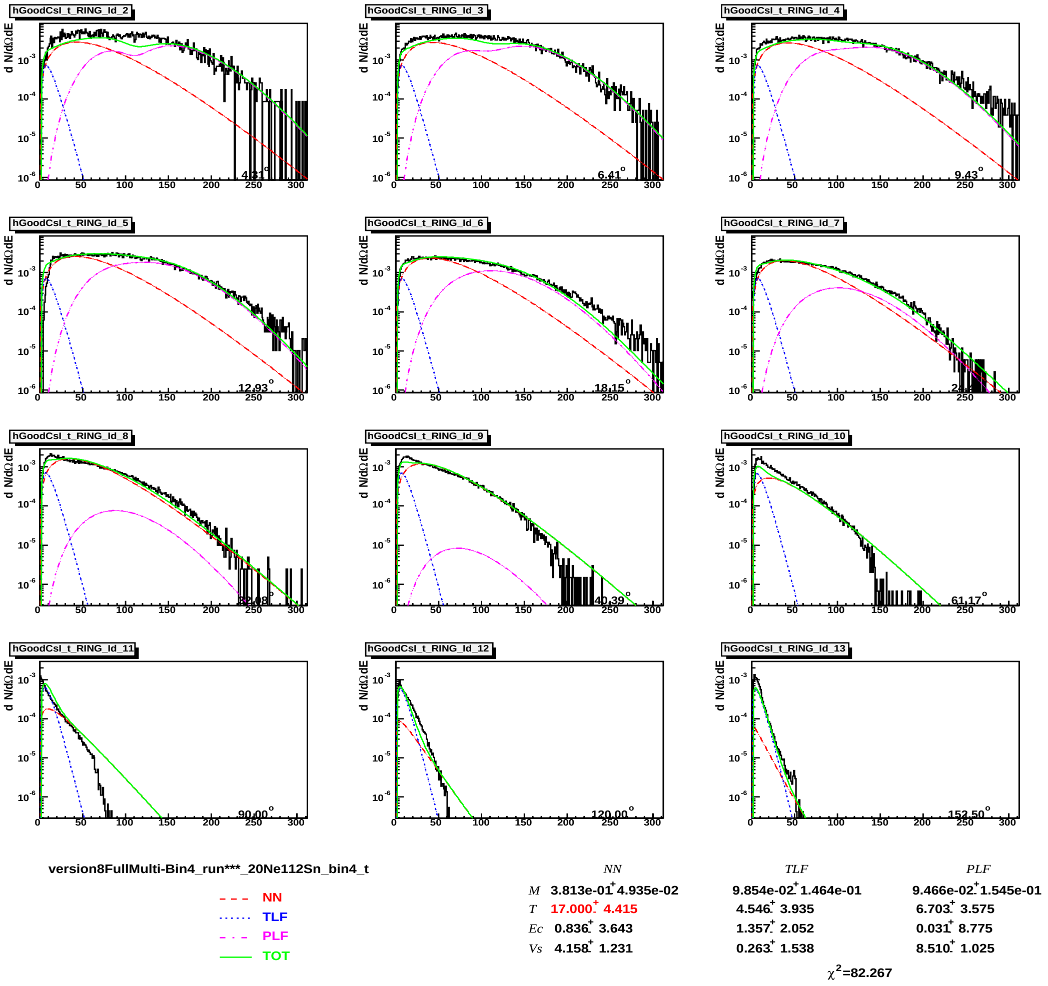

	NN	*TLF*	*PLF*
M	3.813e-01 ± 4.935e-02	9.854e-02 ± 1.464e-01	9.466e-02 ± 1.545e-01
T	17.000 ± 4.415	4.546 ± 3.935	6.703 ± 3.575
Ec	0.836 ± 3.643	1.357 ± 2.052	0.031 ± 8.775
Vs	4.158 ± 1.231	0.263 ± 1.538	8.510 ± 1.025

χ^2=82.267

Fig. 125. X axis is energy in MeV. Y axis is multiplicity distribution

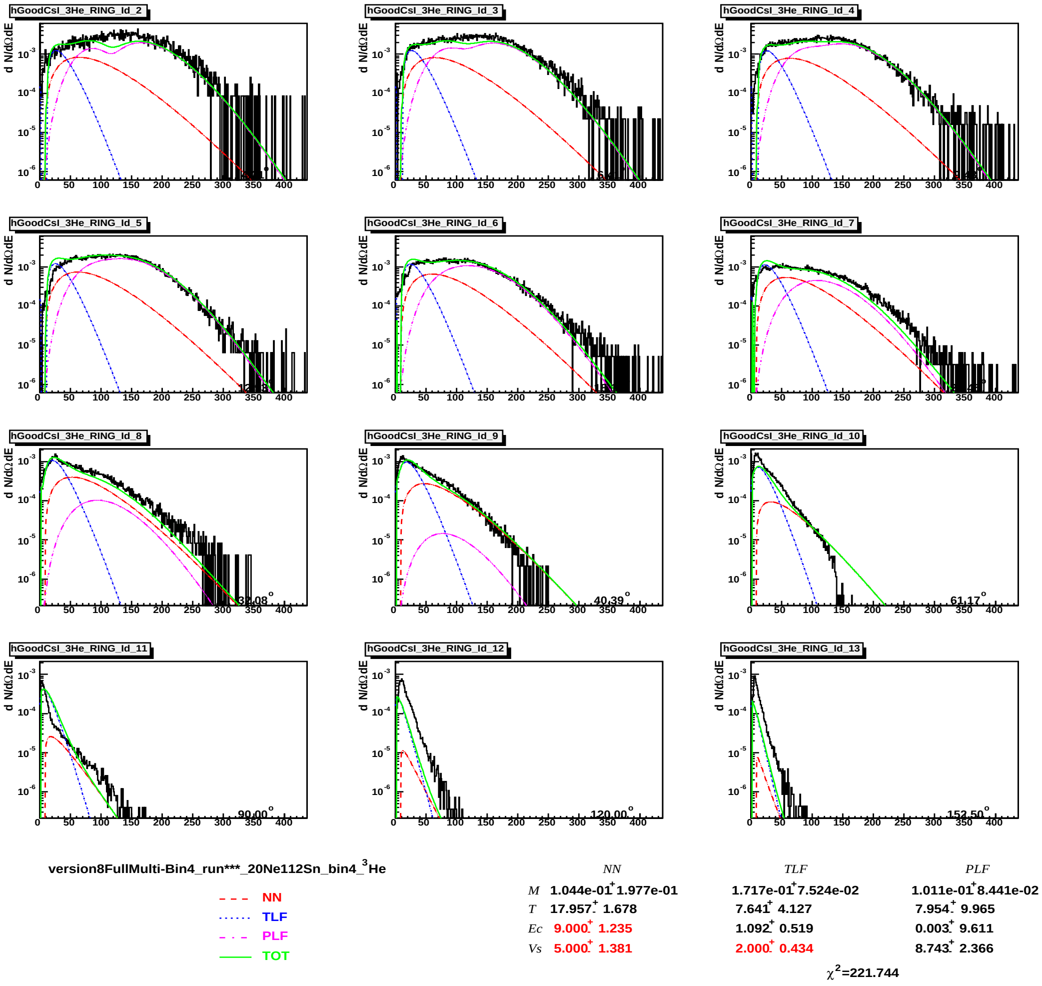

	NN	*TLF*	*PLF*
M	1.044e-01 $\pm$ 1.977e-01	1.717e-01 $\pm$ 7.524e-02	1.011e-01 $\pm$ 8.441e-02
T	17.957 $\pm$ 1.678	7.641 $\pm$ 4.127	7.954 $\pm$ 9.965
Ec	9.000 $\pm$ 1.235	1.092 $\pm$ 0.519	0.003 $\pm$ 9.611
Vs	5.000 $\pm$ 1.381	2.000 $\pm$ 0.434	8.743 $\pm$ 2.366

χ^2=221.744

Fig. 126. X axis is energy in MeV. Y axis is multiplicity distribution

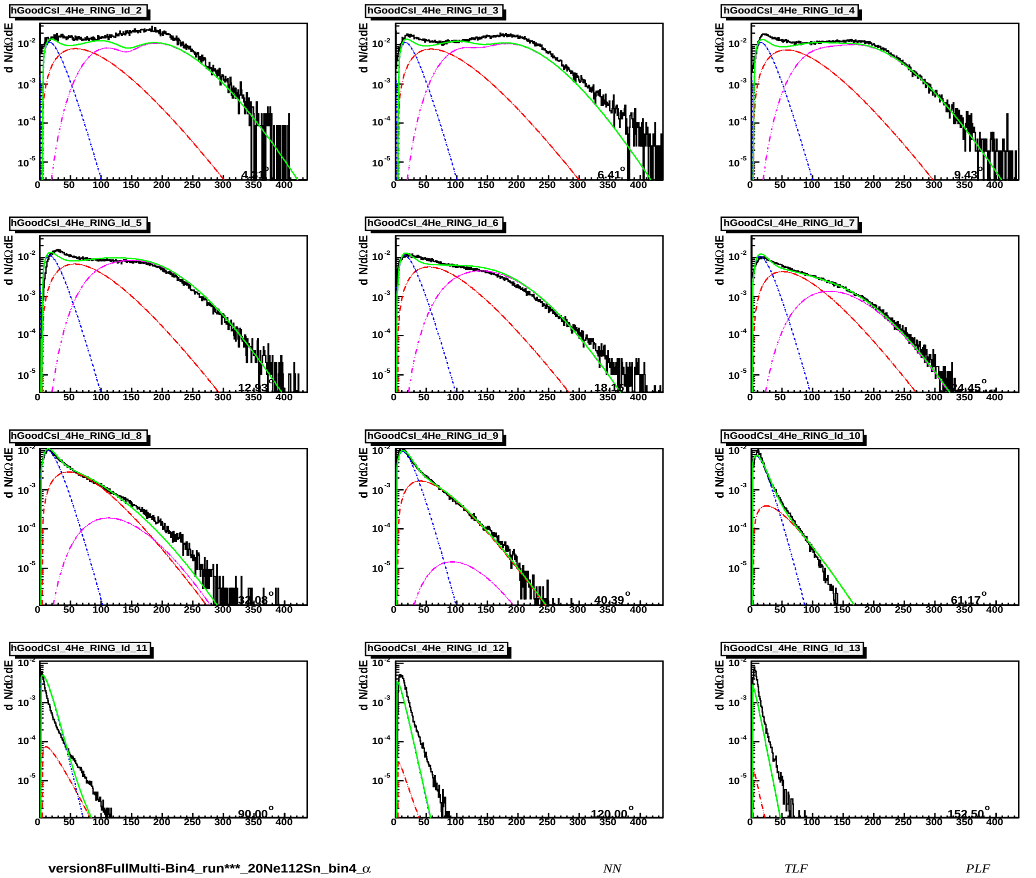

	NN	*TLF*	*PLF*
M	6.306e-01 ± 4.619e-02	1.375e+00 ± 7.949e-02	4.595e-01 ± 7.559e-02
T	13.347 ± 0.637	6.089 ± 0.263	7.210 ± 1.049
Ec	3.501 ± 0.213	0.182 ± 0.072	4.001 ± 4.501
Vs	4.544 ± 0.394	1.248 ± 0.087	8.212 ± 0.322

χ^2=290.202

Fig. 127. X axis is energy in MeV. Y axis is multiplicity distribution

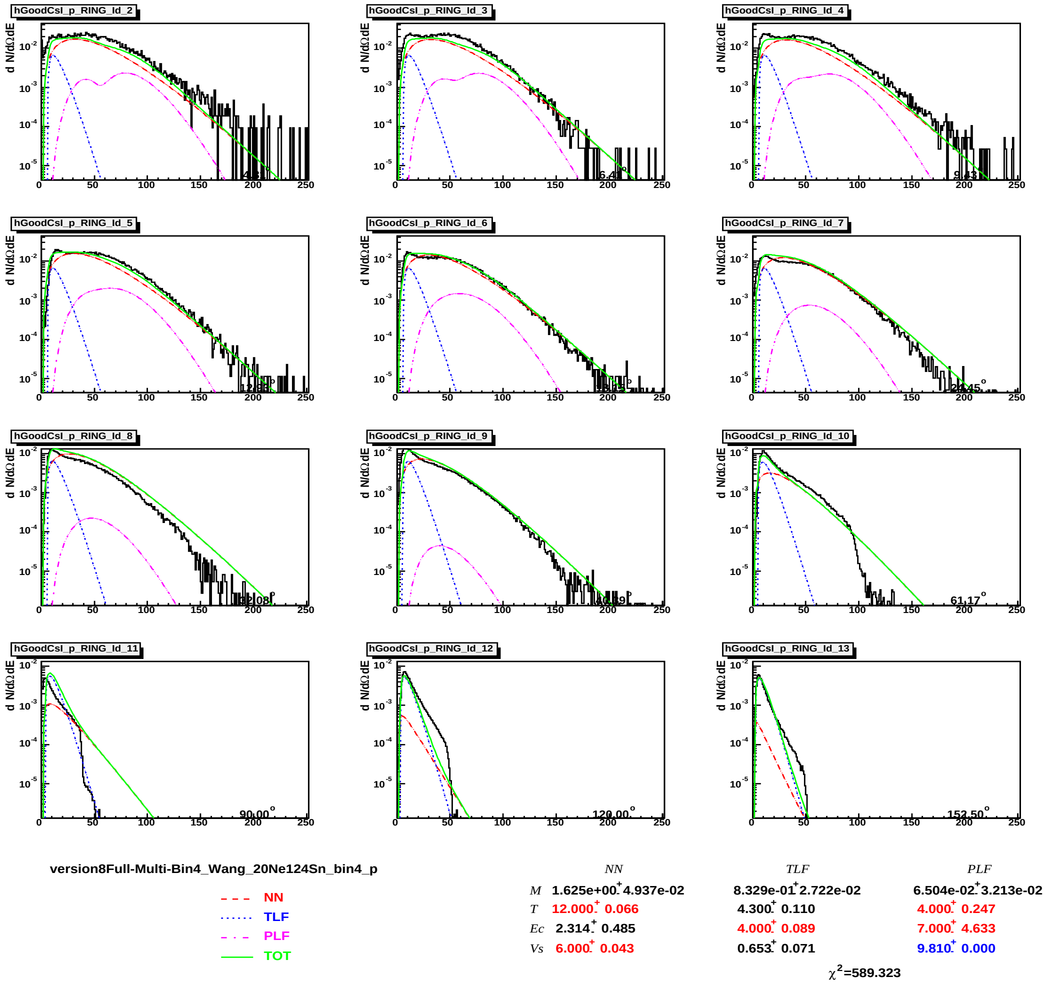

Fig. 128. X axis is energy in MeV. Y axis is multiplicity distribution

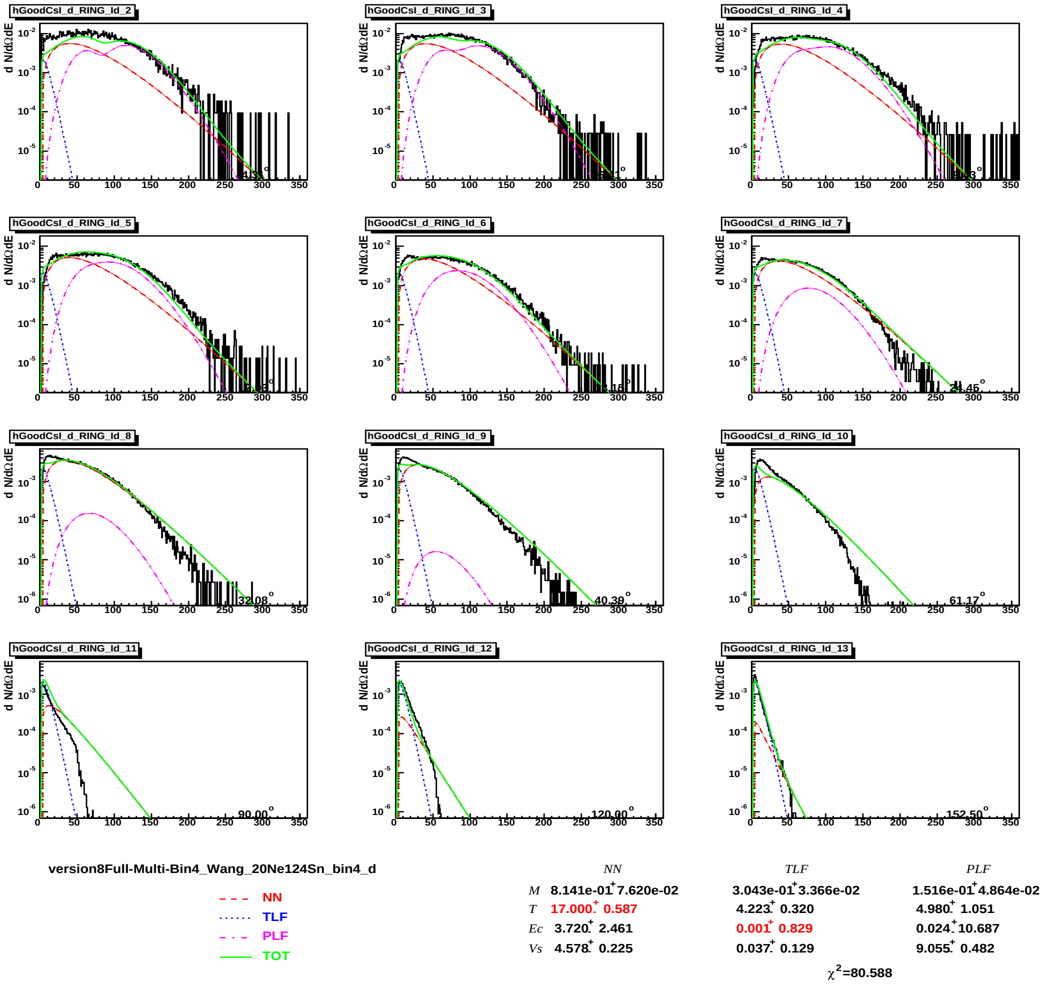

	NN	*TLF*	*PLF*
M	8.141e-01 ± 7.620e-02	3.043e-01 ± 3.366e-02	1.516e-01 ± 4.864e-02
T	17.000 ± 0.587	4.223 ± 0.320	4.980 ± 1.051
Ec	3.720 ± 2.461	0.001 ± 0.829	0.024 ± 10.687
Vs	4.578 ± 0.225	0.037 ± 0.129	9.055 ± 0.482

χ^2=80.588

Fig. 129. X axis is energy in MeV. Y axis is multiplicity distribution

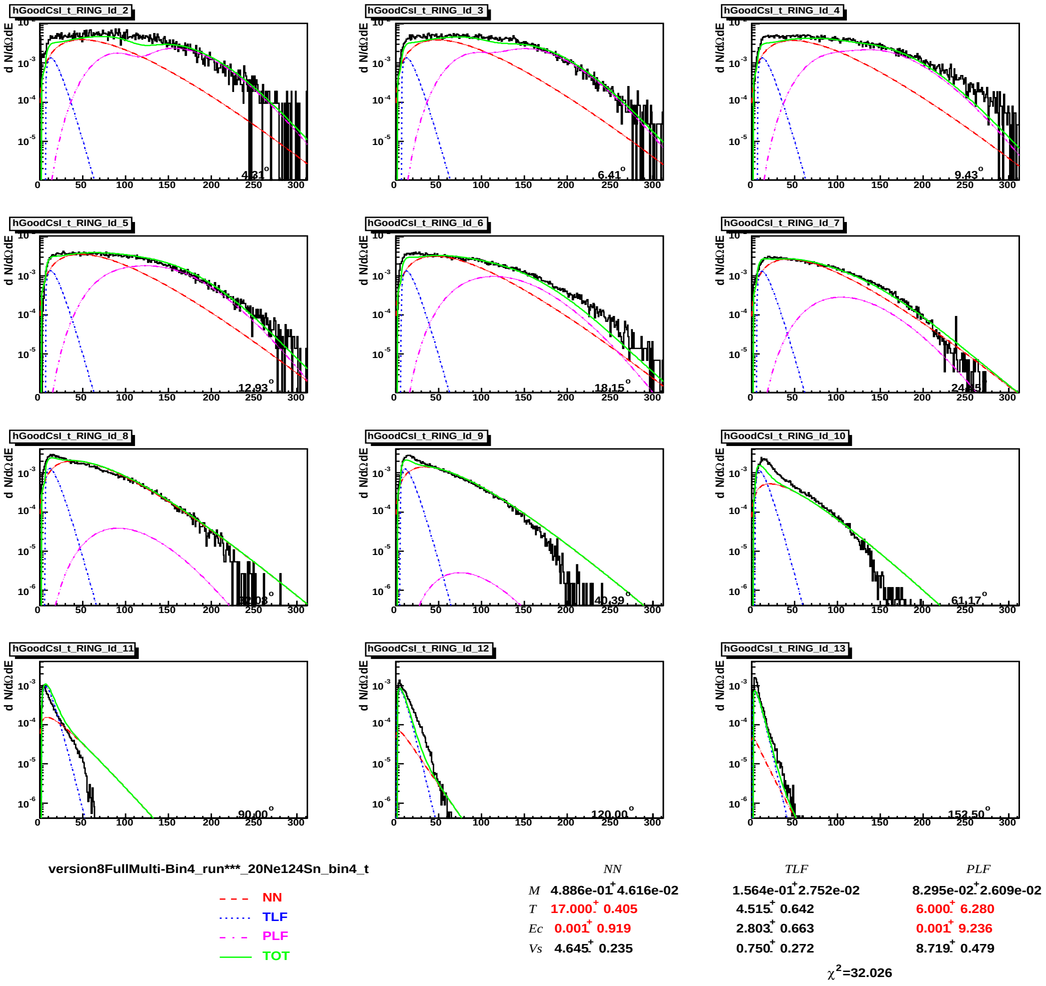

	NN	*TLF*	*PLF*
M	4.886e-01 ± 4.616e-02	1.564e-01 ± 2.752e-02	8.295e-02 ± 2.609e-02
T	17.000 ± 0.405	4.515 ± 0.642	6.000 ± 6.280
Ec	0.001 ± 0.919	2.803 ± 0.663	0.001 ± 9.236
Vs	4.645 ± 0.235	0.750 ± 0.272	8.719 ± 0.479

χ^2=32.026

Fig. 130. X axis is energy in MeV. Y axis is multiplicity distribution

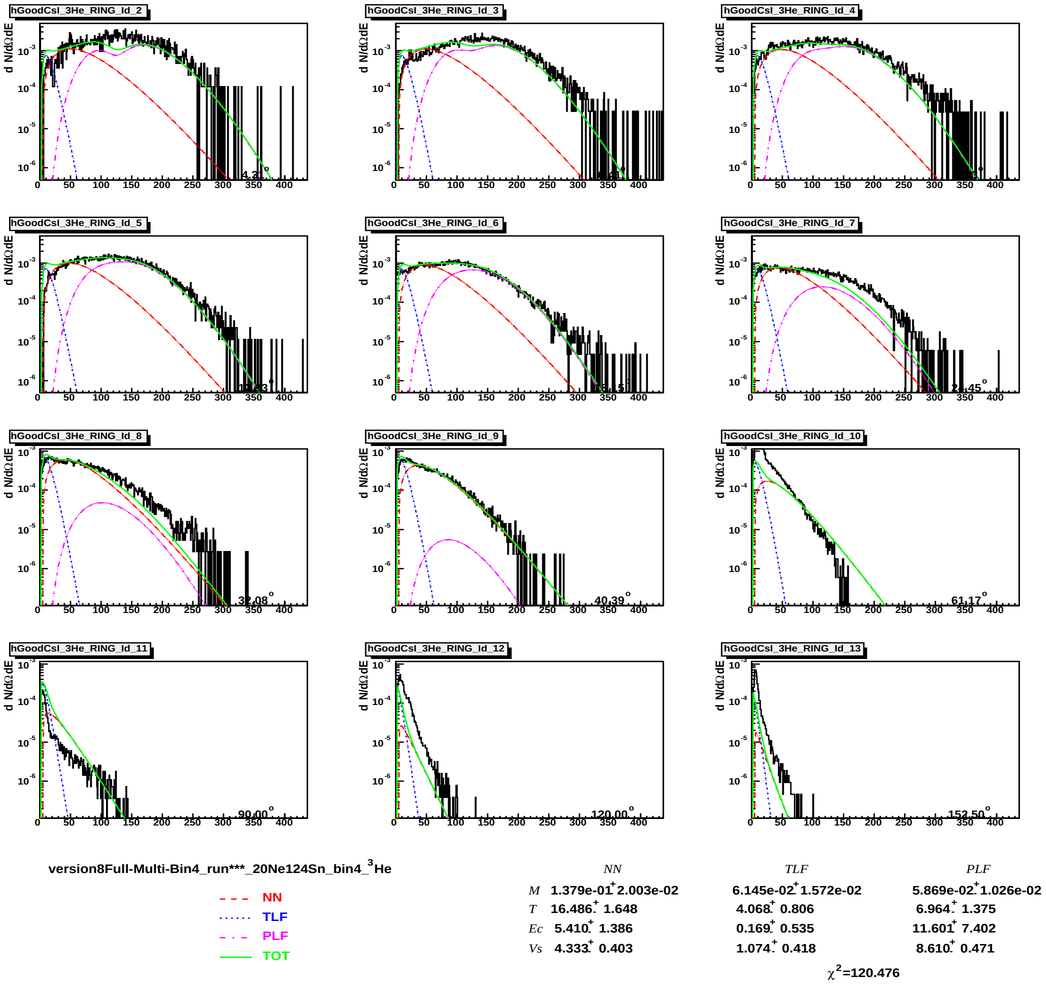

Fig. 131. X axis is energy in MeV. Y axis is multiplicity distribution

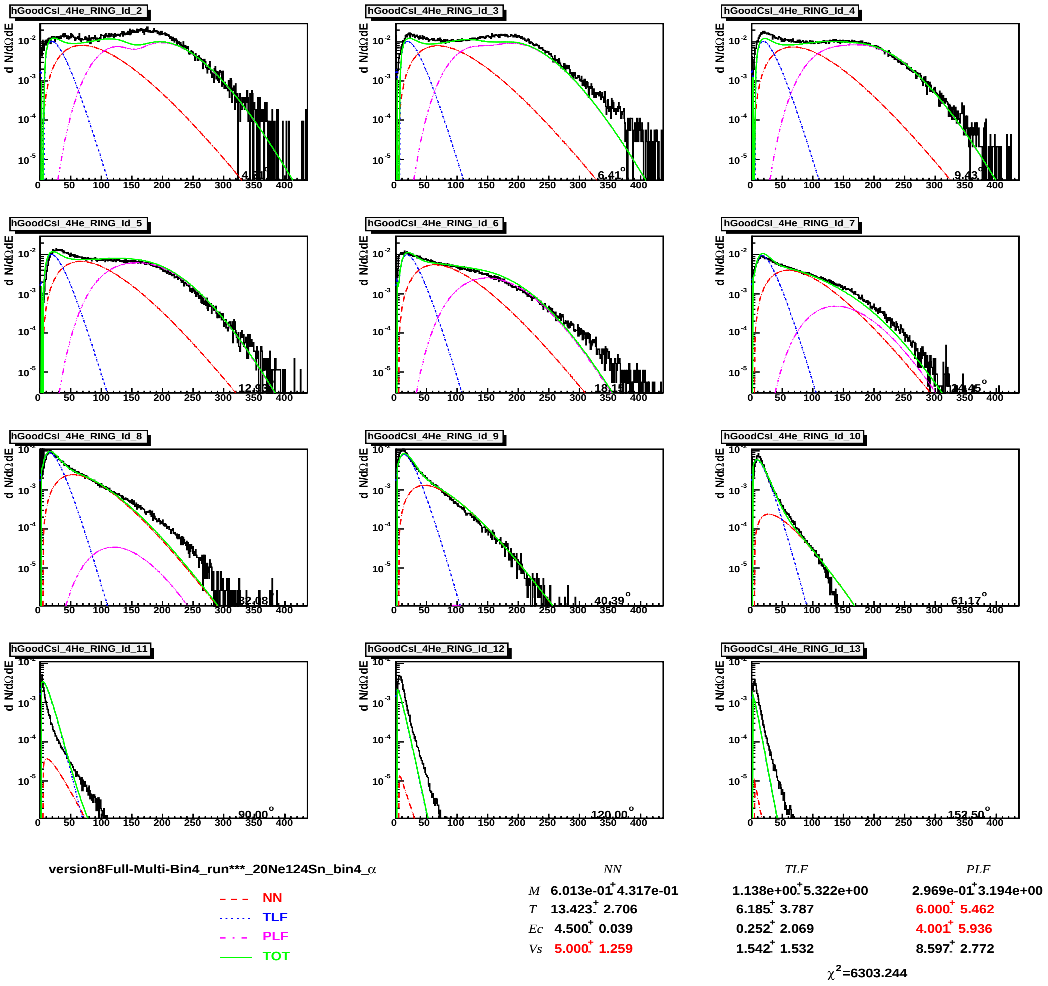

	NN	*TLF*	*PLF*
M	6.013e-01 $\pm$ 4.317e-01	1.138e+00 $\pm$ 5.322e+00	2.969e-01 $\pm$ 3.194e+00
T	13.423 $\pm$ 2.706	6.185 $\pm$ 3.787	6.000 $\pm$ 5.462
Ec	4.500 $\pm$ 0.039	0.252 $\pm$ 2.069	4.001 $\pm$ 5.936
Vs	5.000 $\pm$ 1.259	1.542 $\pm$ 1.532	8.597 $\pm$ 2.772

χ^2=6303.244

Fig. 132. X axis is energy in MeV. Y axis is multiplicity distribution

APPENDIX I

THREE SOURCE FITTING SPECTRA FROM PROJECTILE ^{40}Ar

This appendix lists all of three source fitting spectra of systems ^{40}Ar+^{124}Sn in which the parameters Multiplicity, Temperature , Coulomb Barrier and Source Velocities are indicated.

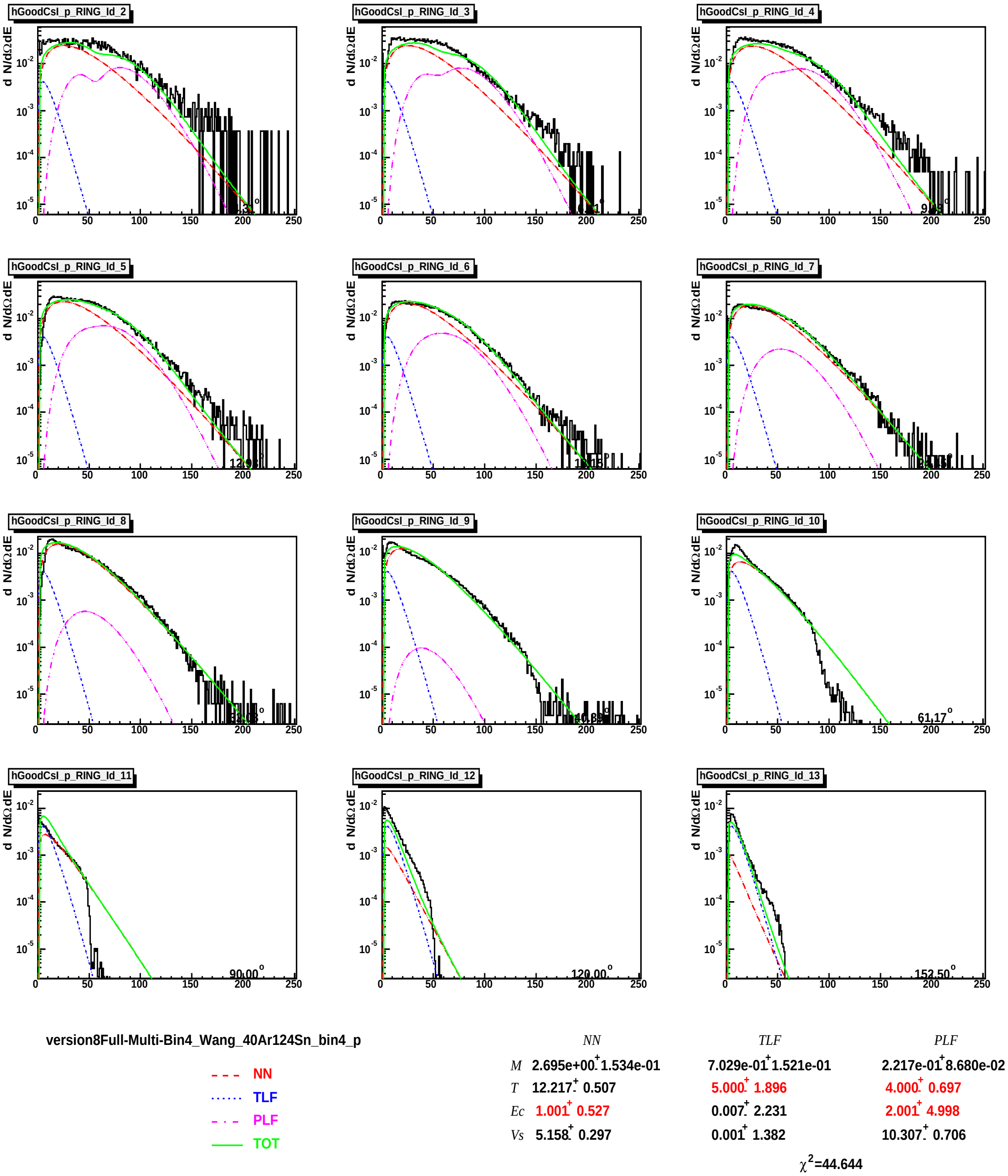

	NN	TLF	PLF
M	2.695e+00 ± 1.534e-01	7.029e-01 ± 1.521e-01	2.217e-01 ± 8.680e-02
T	12.217 ± 0.507	5.000 ± 1.896	4.000 ± 0.697
Ec	1.001 ± 0.527	0.007 ± 2.231	2.001 ± 4.998
Vs	5.158 ± 0.297	0.001 ± 1.382	10.307 ± 0.706

χ^2=44.644

Fig. 133. X axis is energy in MeV. Y axis is multiplicity distribution

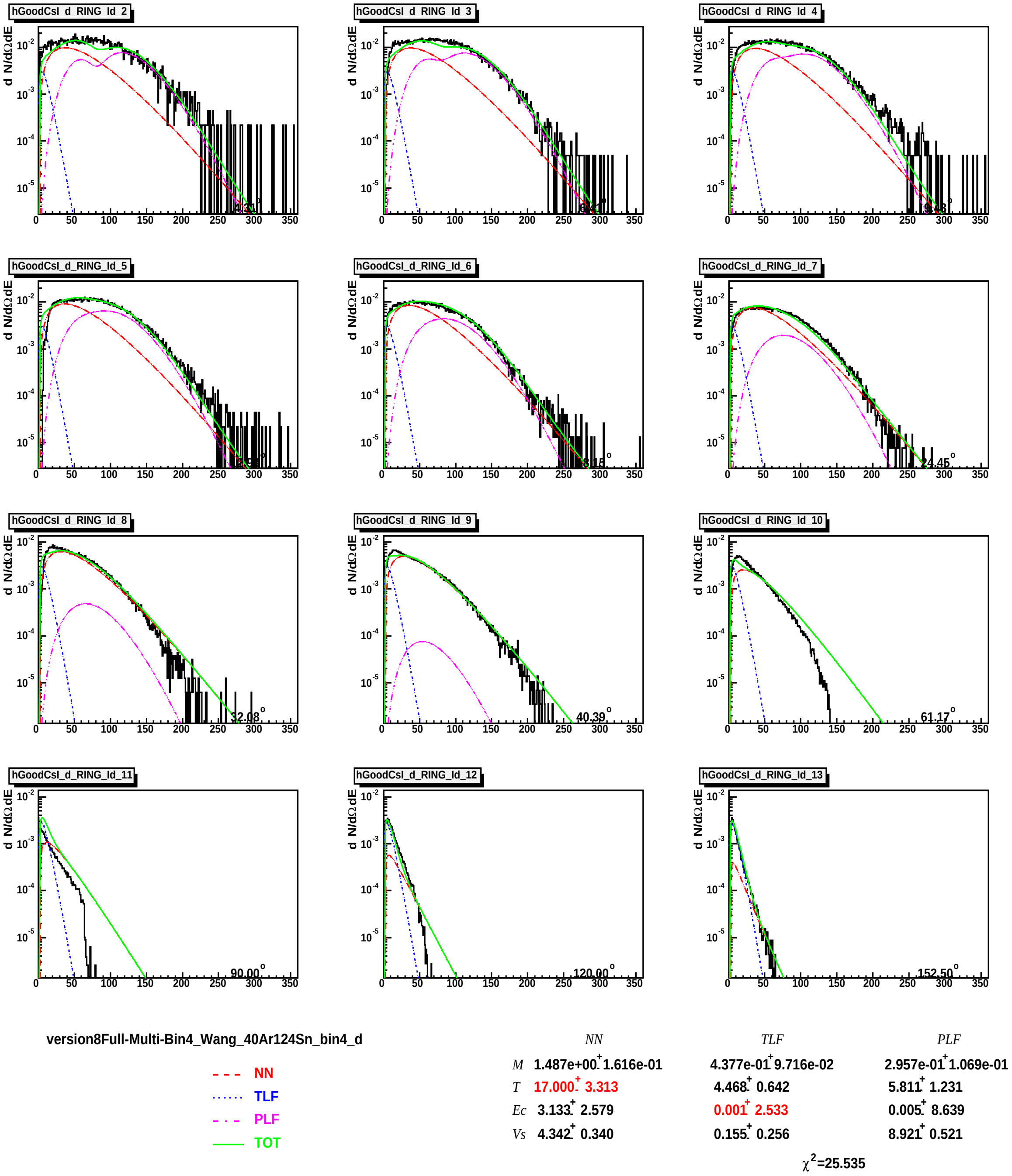

	NN	TLF	PLF
M	1.487e+00 ± 1.616e-01	4.377e-01 ± 9.716e-02	2.957e-01 ± 1.069e-01
T	17.000 ± 3.313	4.468 ± 0.642	5.811 ± 1.231
Ec	3.133 ± 2.579	0.001 ± 2.533	0.005 ± 8.639
Vs	4.342 ± 0.340	0.155 ± 0.256	8.921 ± 0.521

χ^2=25.535

Fig. 134. X axis is energy in MeV. Y axis is multiplicity distribution

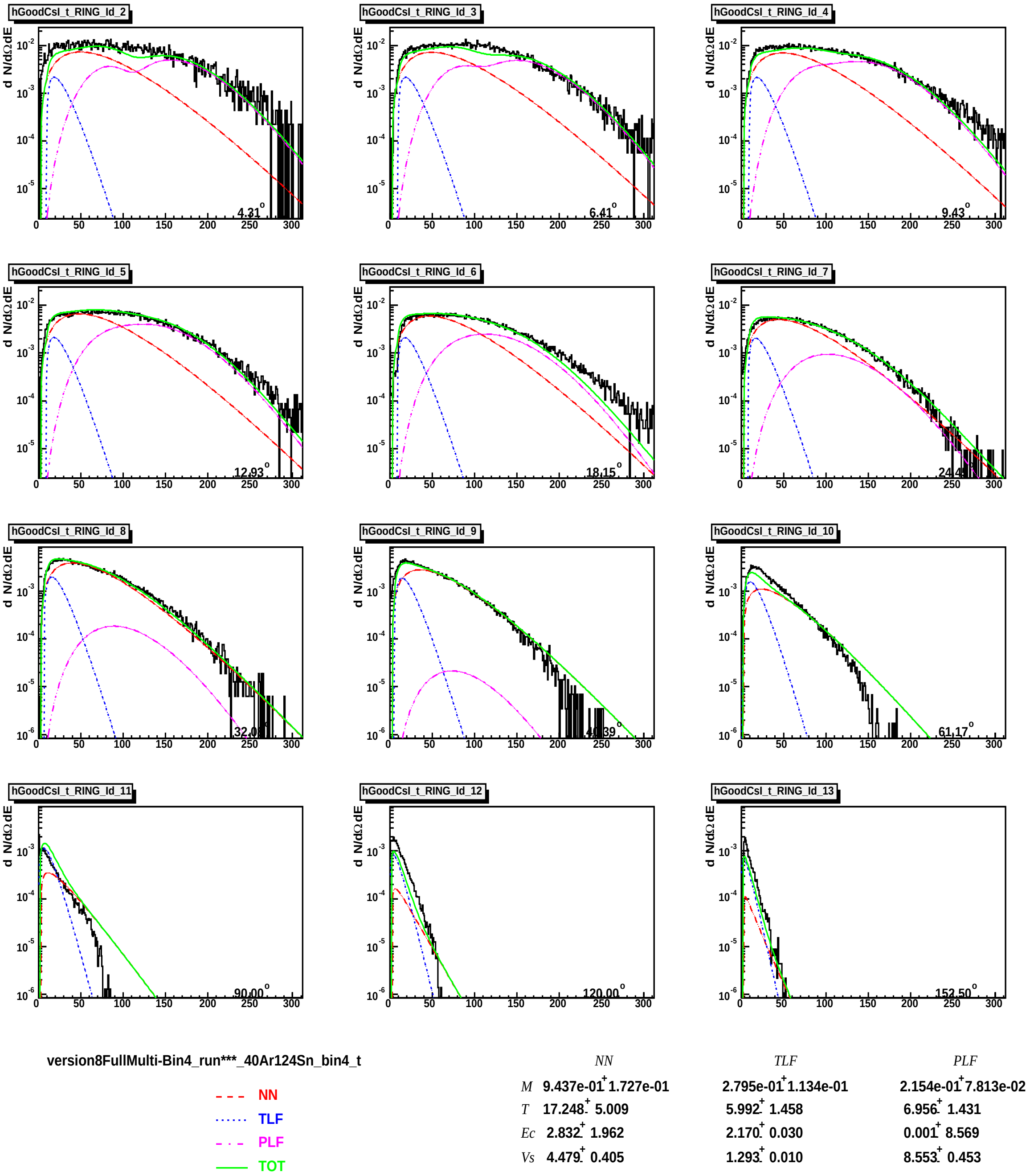

	NN	*TLF*	*PLF*
M	9.437e-01 ± 1.727e-01	2.795e-01 ± 1.134e-01	2.154e-01 ± 7.813e-02
T	17.248 ± 5.009	5.992 ± 1.458	6.956 ± 1.431
Ec	2.832 ± 1.962	2.170 ± 0.030	0.001 ± 8.569
Vs	4.479 ± 0.405	1.293 ± 0.010	8.553 ± 0.453

χ^2=14.439

Fig. 135. X axis is energy in MeV. Y axis is multiplicity distribution

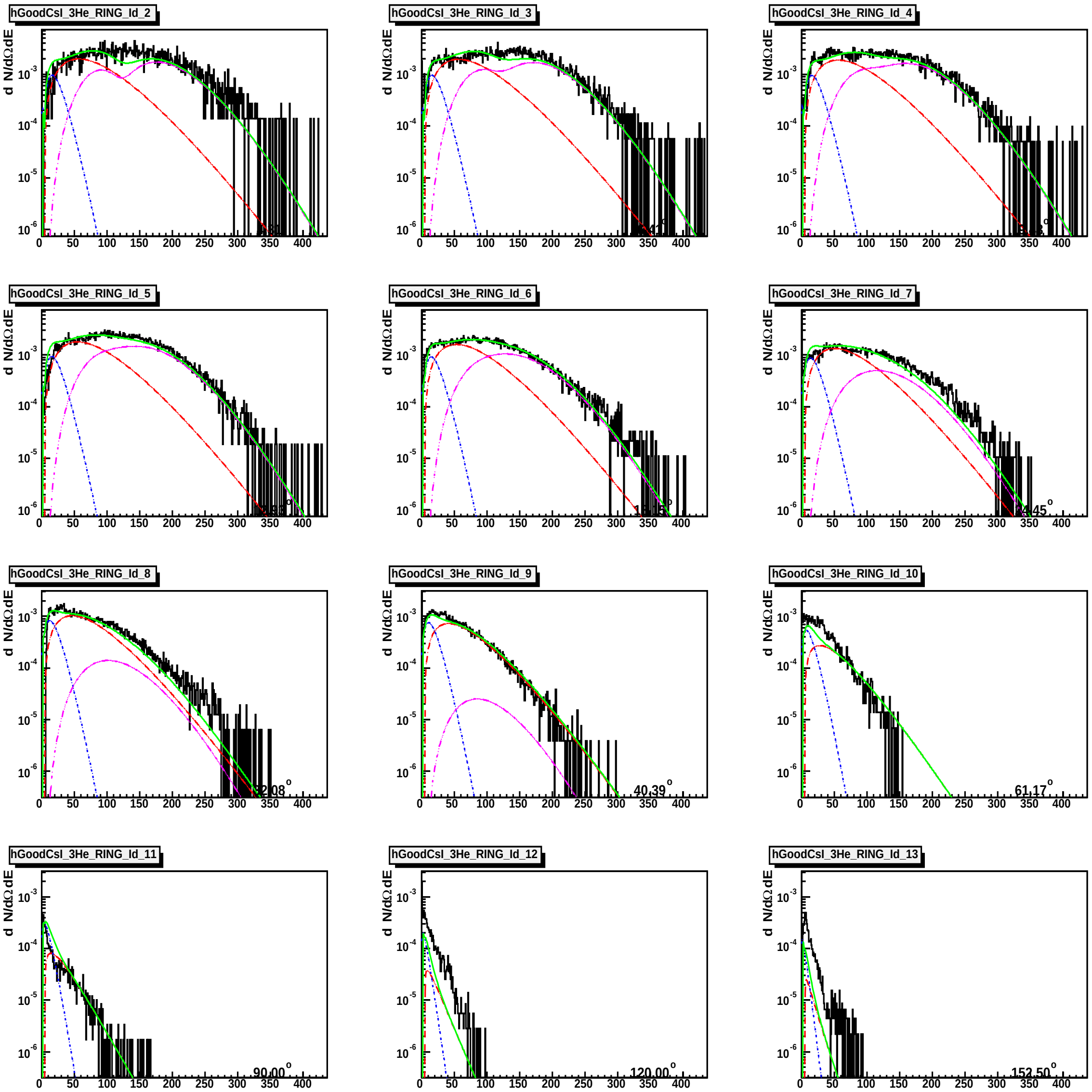

version8FullMulti-Bin4_run***_40Ar124Sn_bin4_^{3}He

- - - NN
······ TLF
-·-· PLF
—— TOT

	NN	TLF	PLF
M	2.640e-01 ± 6.388e-02	8.944e-02 ± 4.652e-02	1.058e-01 ± 7.211e-02
T	18.125 ± 18.995	5.237 ± 3.197	8.951 ± 10.835
Ec	5.348 ± 4.415	0.001 ± 3.063	7.225 ± 7.534
Vs	4.751 ± 1.684	1.631 ± 0.632	8.716 ± 2.217

χ^2=86.531

Fig. 136. X axis is energy in MeV. Y axis is multiplicity distribution

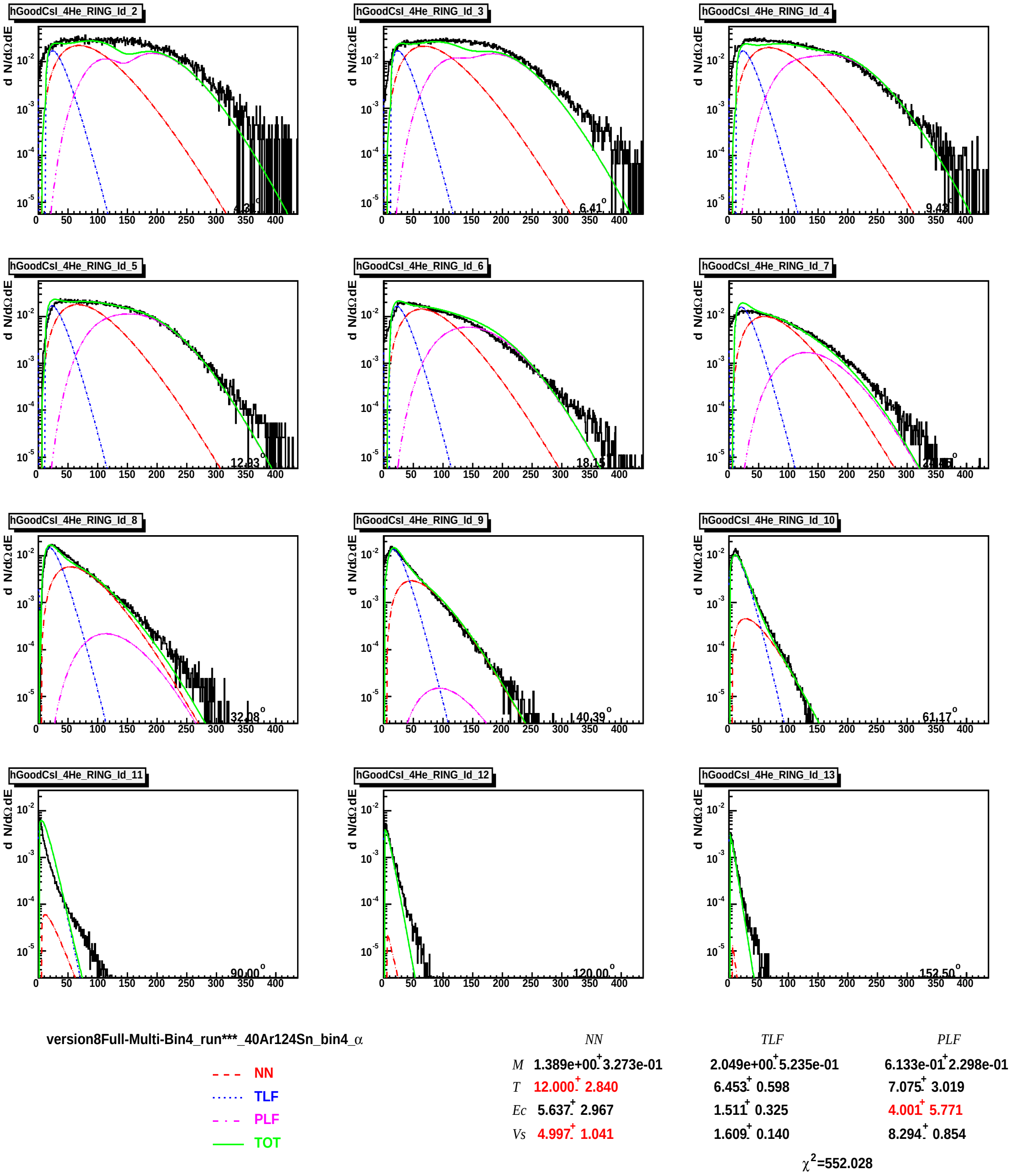

Fig. 137. X axis is energy in MeV. Y axis is multiplicity distribution

APPENDIX J

THREE SOURCE FITTING SPECTRA FROM PROJECTILE ^{64}Zn

This appendix lists all of three source fitting spectra of systems ^{64}Zn+^{112}Sn and ^{64}Zn+^{124}Sn in which the parameters Multiplicity, Temperature , Coulomb Barrier and Source Velocities are indicated.

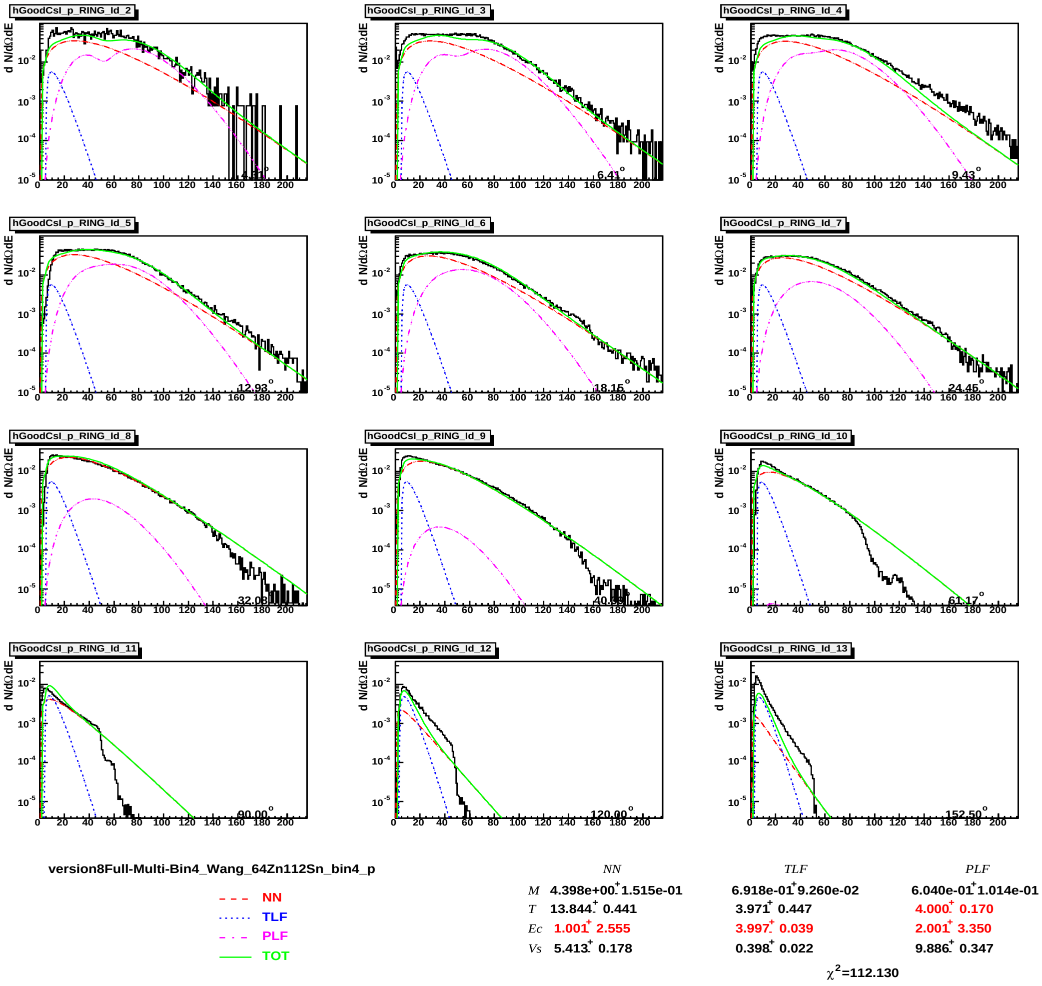

	NN	TLF	PLF
M	4.398e+00 ± 1.515e-01	6.918e-01 ± 9.260e-02	6.040e-01 ± 1.014e-01
T	13.844 ± 0.441	3.971 ± 0.447	4.000 ± 0.170
Ec	1.001 ± 2.555	3.997 ± 0.039	2.001 ± 3.350
Vs	5.413 ± 0.178	0.398 ± 0.022	9.886 ± 0.347

χ^2=112.130

Fig. 138. X axis is energy in MeV. Y axis is multiplicity distribution

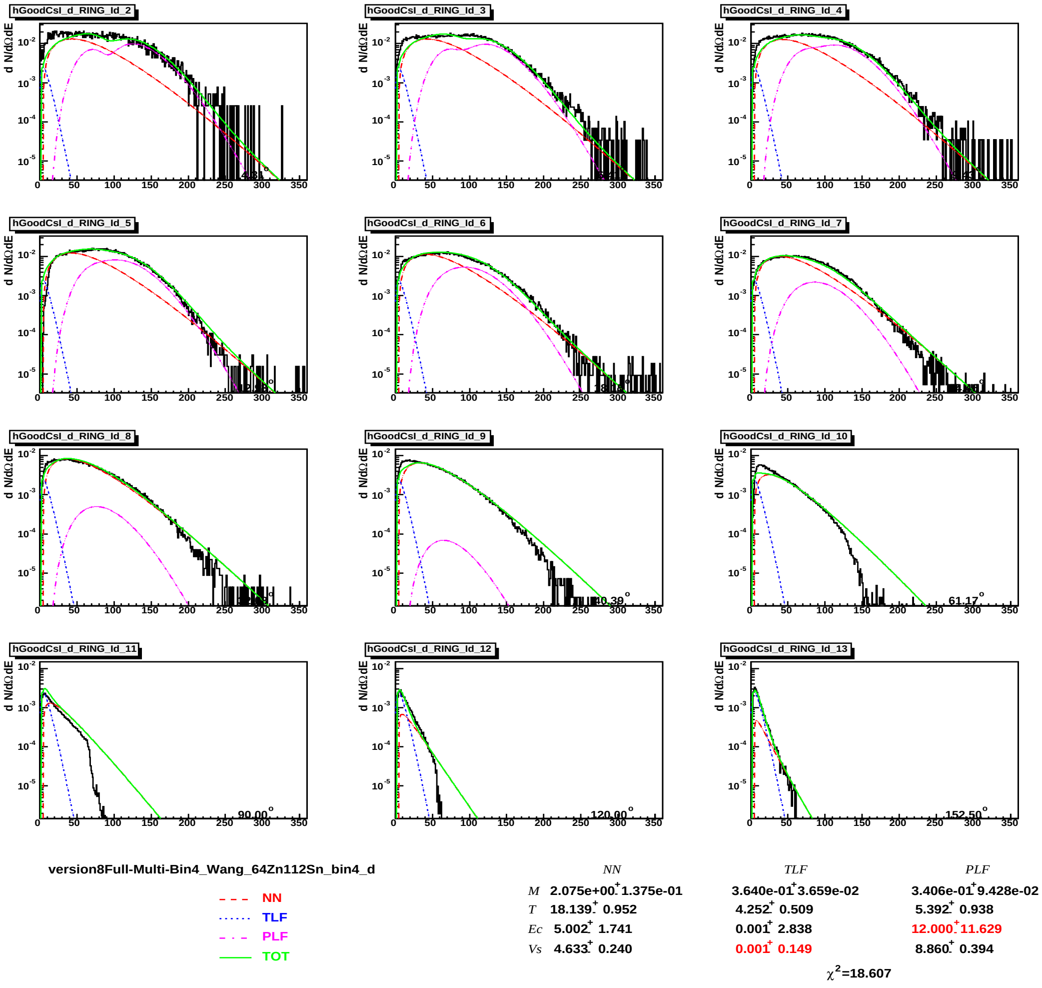

	NN	TLF	PLF
M	2.075e+00 $\pm$ 1.375e-01	3.640e-01 $\pm$ 3.659e-02	3.406e-01 $\pm$ 9.428e-02
T	18.139 $\pm$ 0.952	4.252 $\pm$ 0.509	5.392 $\pm$ 0.938
Ec	5.002 $\pm$ 1.741	0.001 $\pm$ 2.838	12.000 $\pm$ 11.629
Vs	4.633 $\pm$ 0.240	0.001 $\pm$ 0.149	8.860 $\pm$ 0.394

χ^2=18.607

Fig. 139. X axis is energy in MeV. Y axis is multiplicity distribution

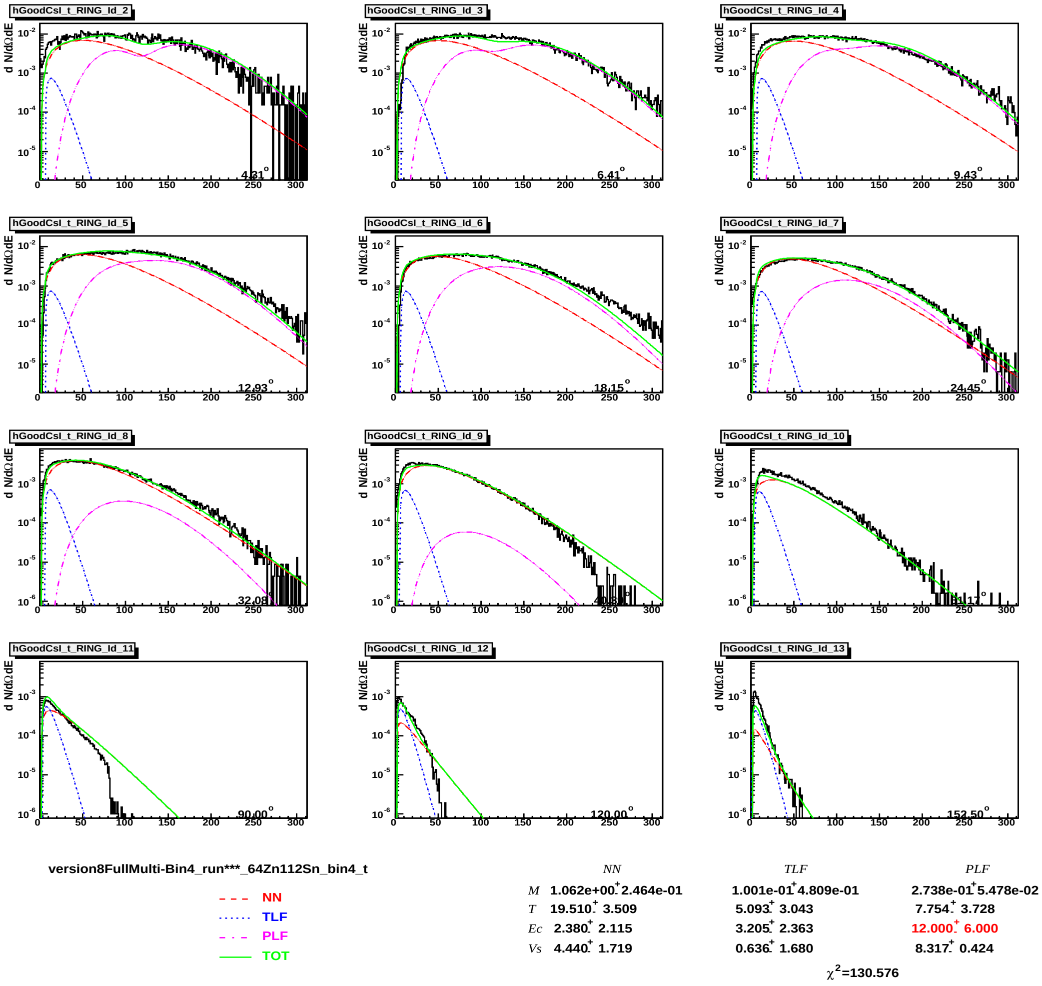

	NN	*TLF*	*PLF*
M	1.062e+00 $^{+}_{-}$ 2.464e-01	1.001e-01 $^{+}_{-}$ 4.809e-01	2.738e-01 $^{+}_{-}$ 5.478e-02
T	19.510 $^{+}_{-}$ 3.509	5.093 $^{+}_{-}$ 3.043	7.754 $^{+}_{-}$ 3.728
Ec	2.380 $^{+}_{-}$ 2.115	3.205 $^{+}_{-}$ 2.363	12.000 $^{+}_{-}$ 6.000
Vs	4.440 $^{+}_{-}$ 1.719	0.636 $^{+}_{-}$ 1.680	8.317 $^{+}_{-}$ 0.424

χ^2=130.576

Fig. 140. X axis is energy in MeV. Y axis is multiplicity distribution

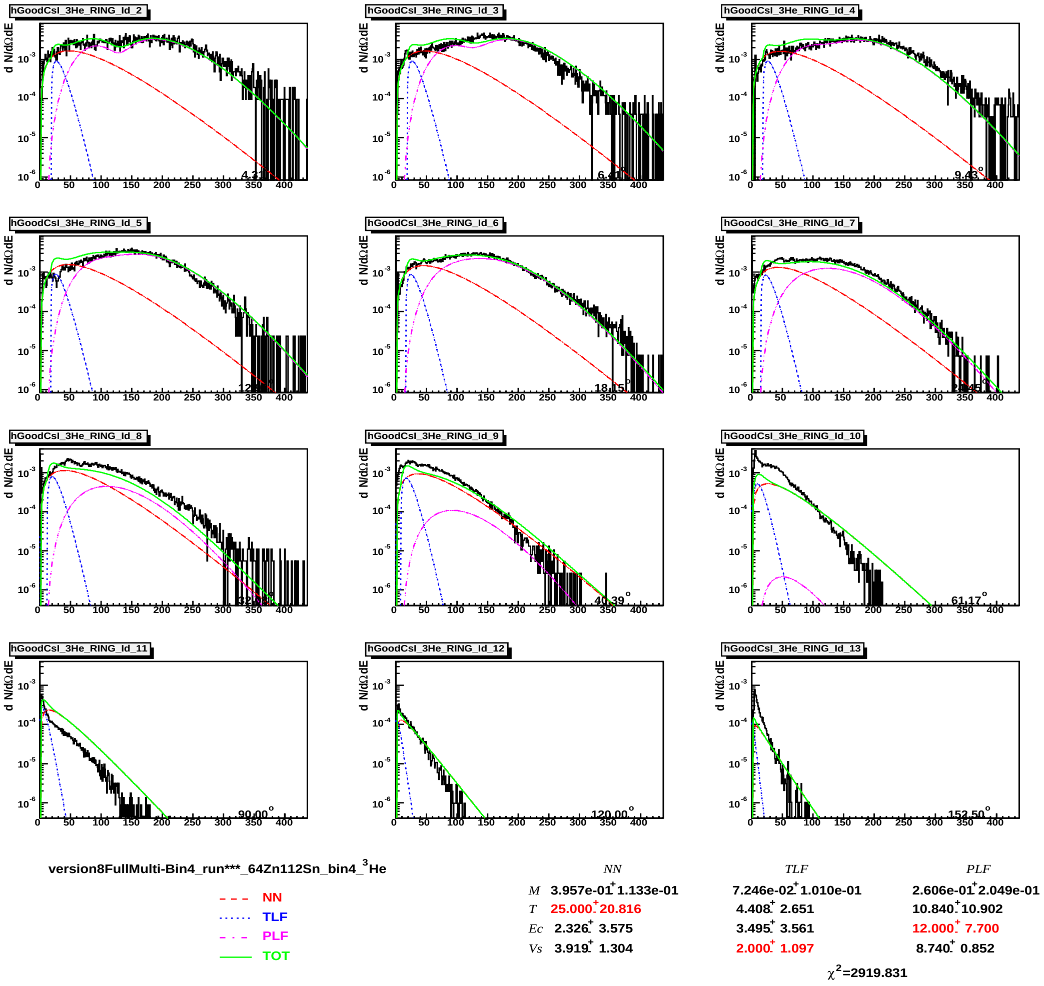

	NN	*TLF*	*PLF*
M	3.957e-01 ± 1.133e-01	7.246e-02 ± 1.010e-01	2.606e-01 ± 2.049e-01
T	25.000 ± 20.816	4.408 ± 2.651	10.840 ± 10.902
Ec	2.326 ± 3.575	3.495 ± 3.561	12.000 ± 7.700
Vs	3.919 ± 1.304	2.000 ± 1.097	8.740 ± 0.852

χ^2=2919.831

Fig. 141. X axis is energy in MeV. Y axis is multiplicity distribution

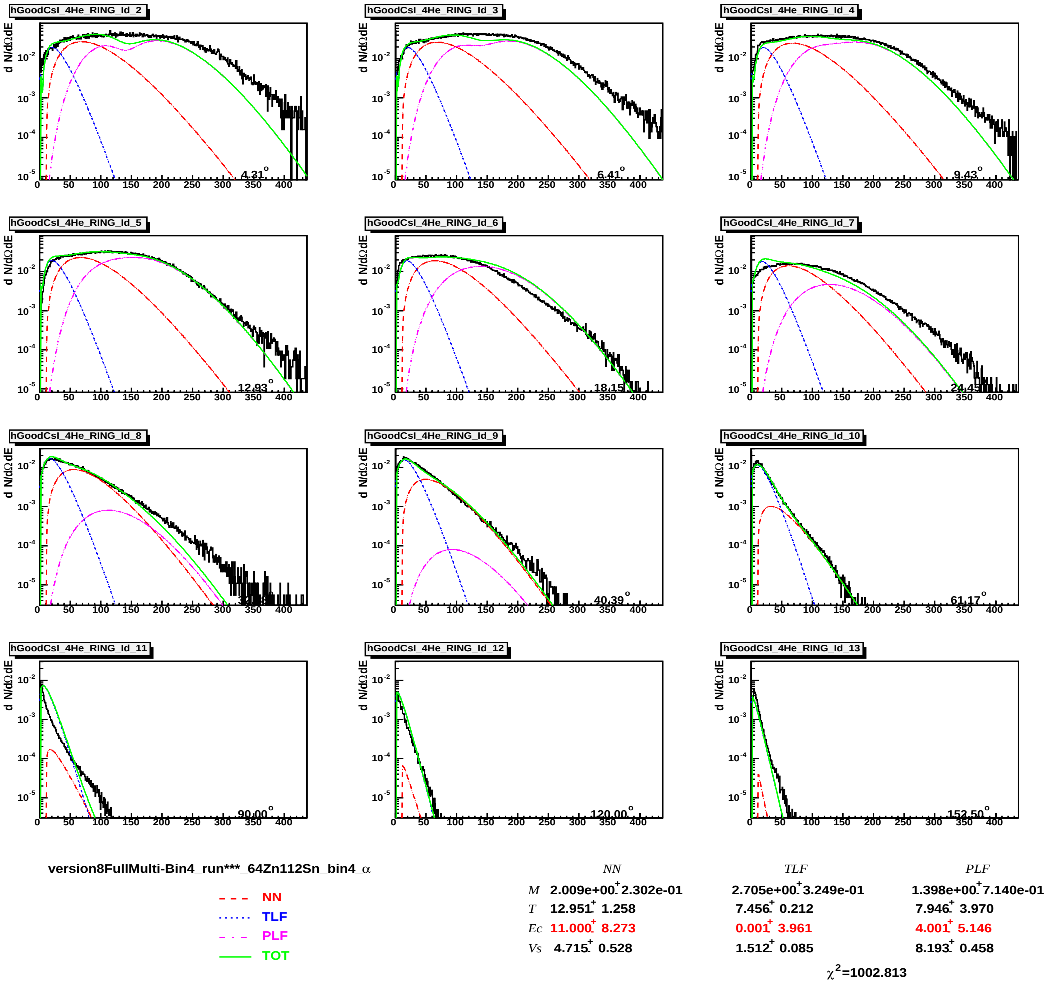

	NN	*TLF*	*PLF*
M	2.009e+00 ± 2.302e-01	2.705e+00 ± 3.249e-01	1.398e+00 ± 7.140e-01
T	12.951 ± 1.258	7.456 ± 0.212	7.946 ± 3.970
Ec	11.000 ± 8.273	0.001 ± 3.961	4.001 ± 5.146
Vs	4.715 ± 0.528	1.512 ± 0.085	8.193 ± 0.458

χ^2=1002.813

Fig. 142. X axis is energy in MeV. Y axis is multiplicity distribution

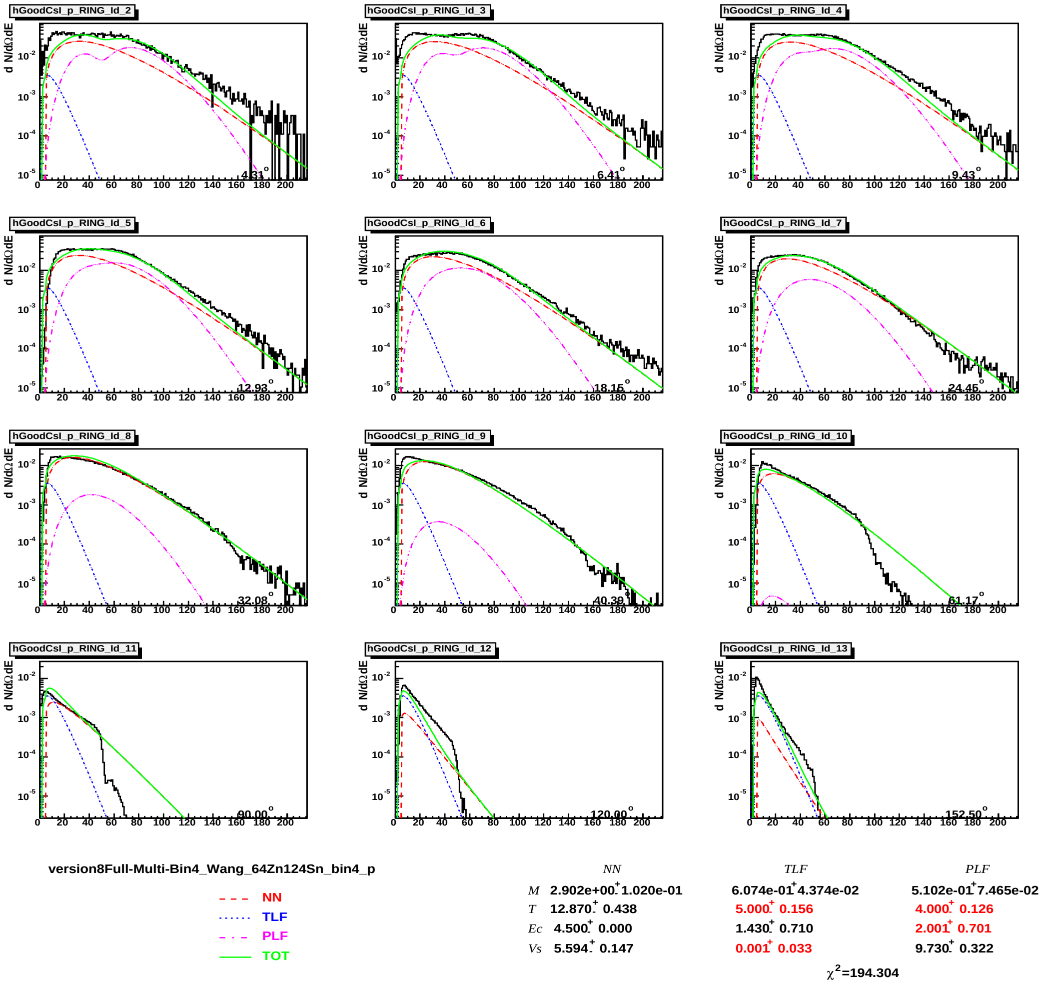

	NN	TLF	PLF
M	2.902e+00 ± 1.020e-01	6.074e-01 ± 4.374e-02	5.102e-01 ± 7.465e-02
T	12.870 ± 0.438	5.000 ± 0.156	4.000 ± 0.126
Ec	4.500 ± 0.000	1.430 ± 0.710	2.001 ± 0.701
Vs	5.594 ± 0.147	0.001 ± 0.033	9.730 ± 0.322

χ^2=194.304

Fig. 143. X axis is energy in MeV. Y axis is multiplicity distribution

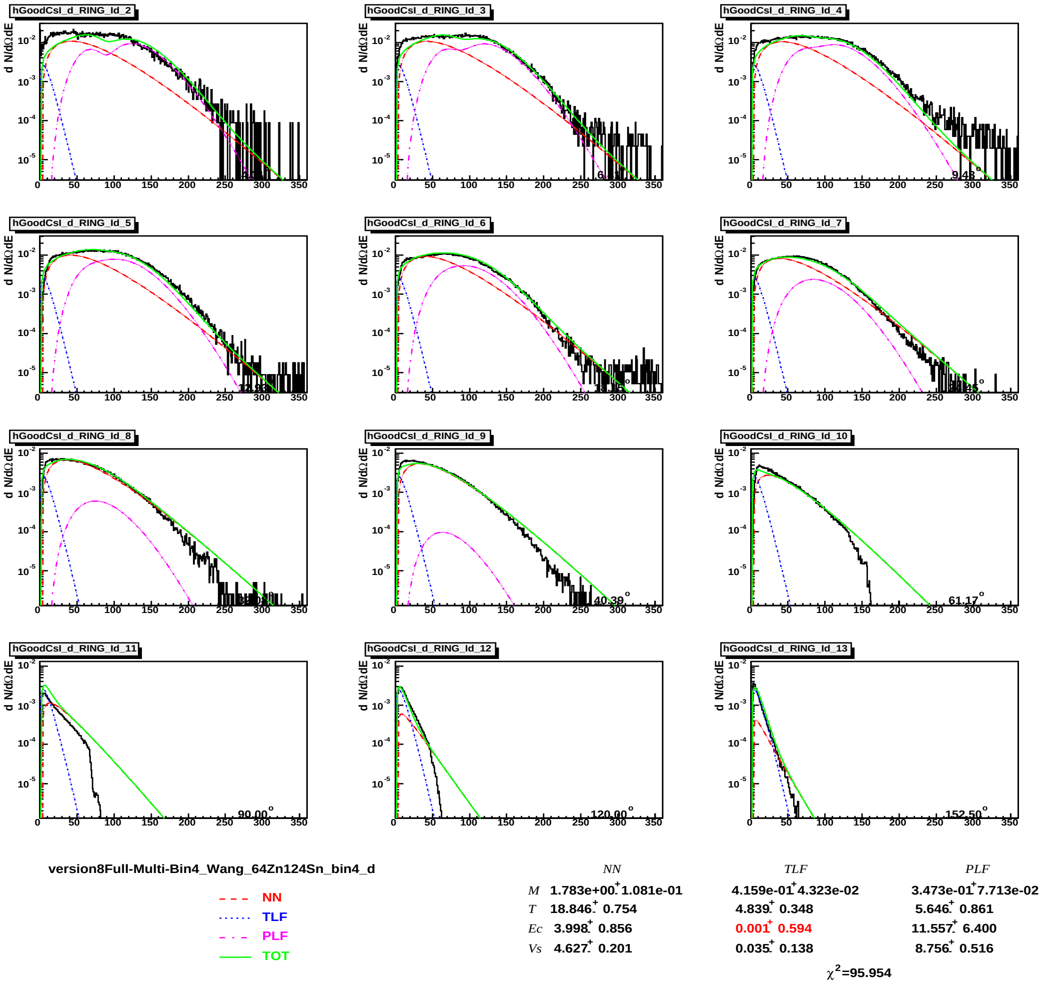

	NN	*TLF*	*PLF*
M	1.783e+00 ± 1.081e-01	4.159e-01 ± 4.323e-02	3.473e-01 ± 7.713e-02
T	18.846 ± 0.754	4.839 ± 0.348	5.646 ± 0.861
Ec	3.998 ± 0.856	0.001 ± 0.594	11.557 ± 6.400
Vs	4.627 ± 0.201	0.035 ± 0.138	8.756 ± 0.516

χ^2=95.954

Fig. 144. X axis is energy in MeV. Y axis is multiplicity distribution

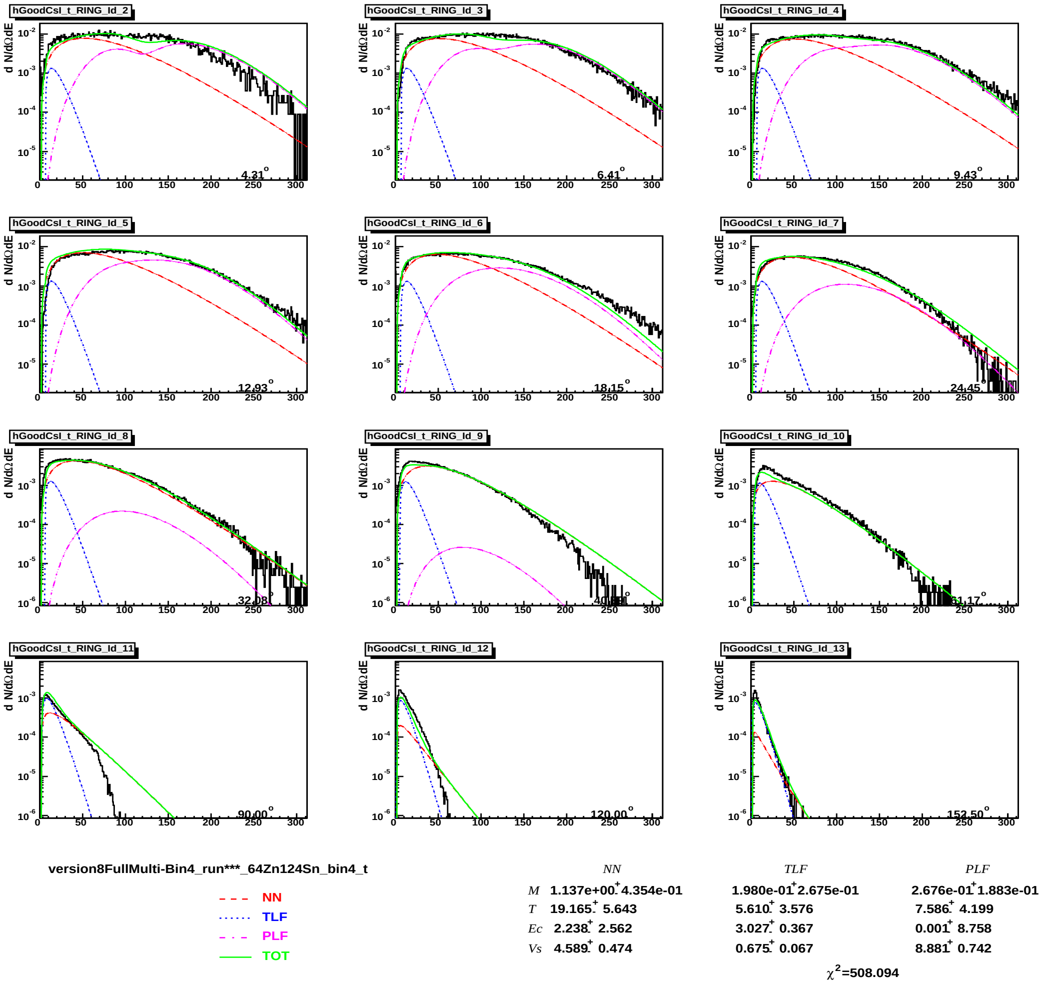

	NN	*TLF*	*PLF*
M	1.137e+00 ± 4.354e-01	1.980e-01 ± 2.675e-01	2.676e-01 ± 1.883e-01
T	19.165 ± 5.643	5.610 ± 3.576	7.586 ± 4.199
Ec	2.238 ± 2.562	3.027 ± 0.367	0.001 ± 8.758
Vs	4.589 ± 0.474	0.675 ± 0.067	8.881 ± 0.742

χ^2=508.094

Fig. 145. X axis is energy in MeV. Y axis is multiplicity distribution

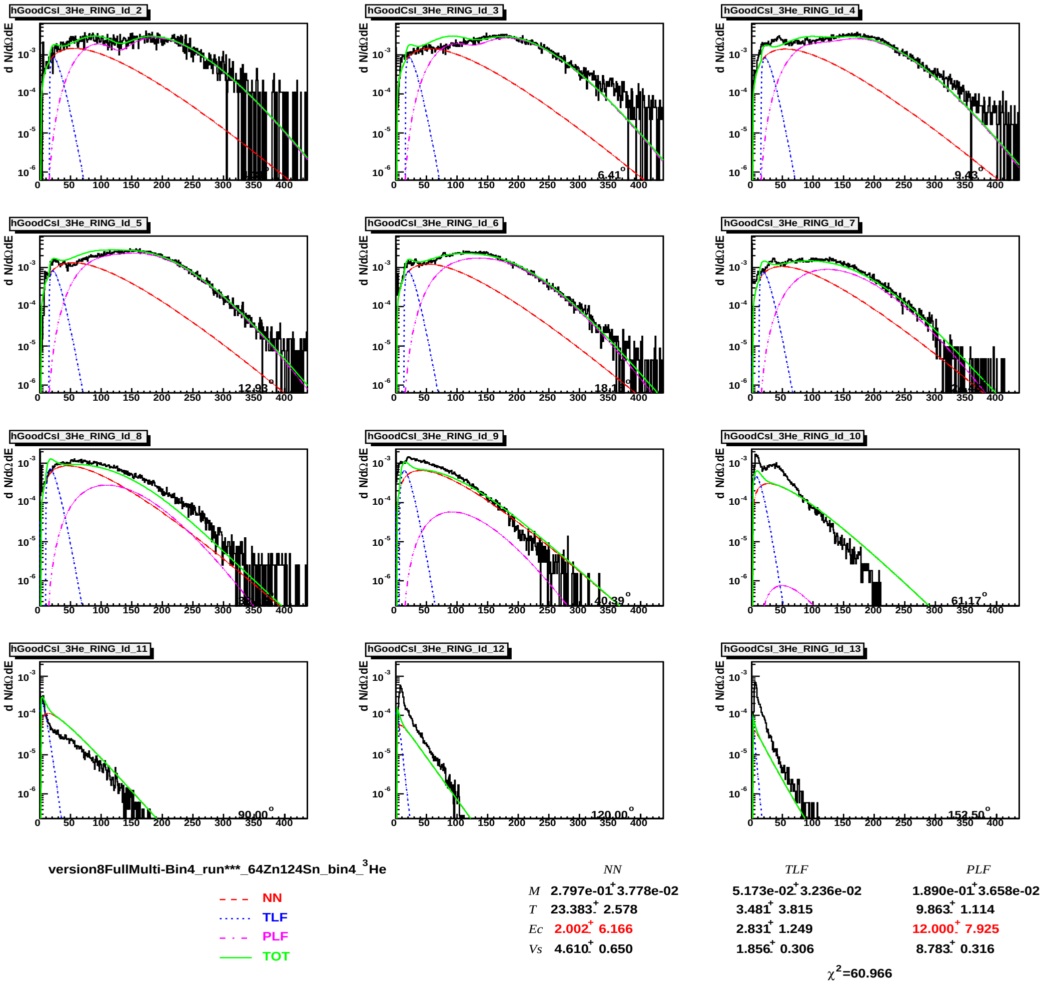

Fig. 146. X axis is energy in MeV. Y axis is multiplicity distribution

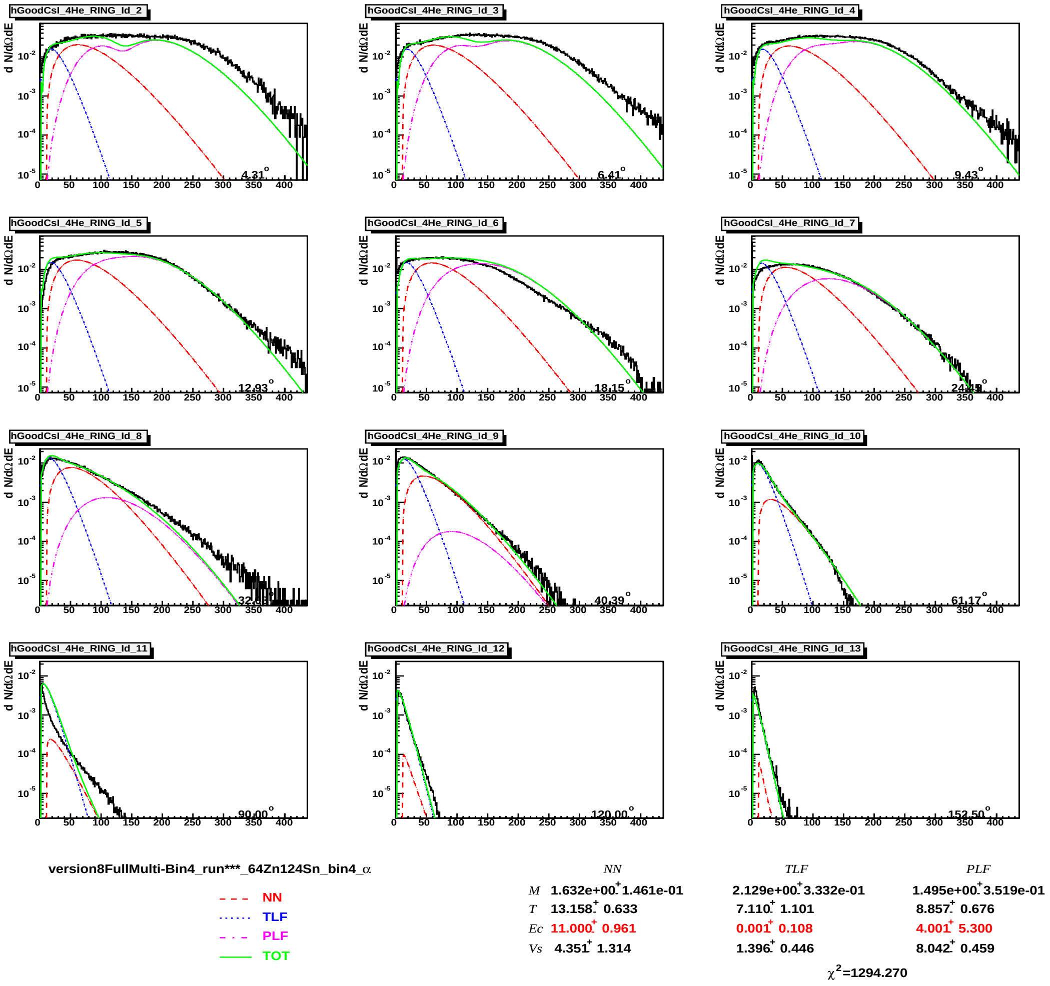

Fig. 147. X axis is energy in MeV. Y axis is multiplicity distribution

APPENDIX K

REACTION TOMOGRAPHY OF THE MOST VIOLENT COLLISION EVENTS

Surface velocity plots of light particles from different reaction systems.

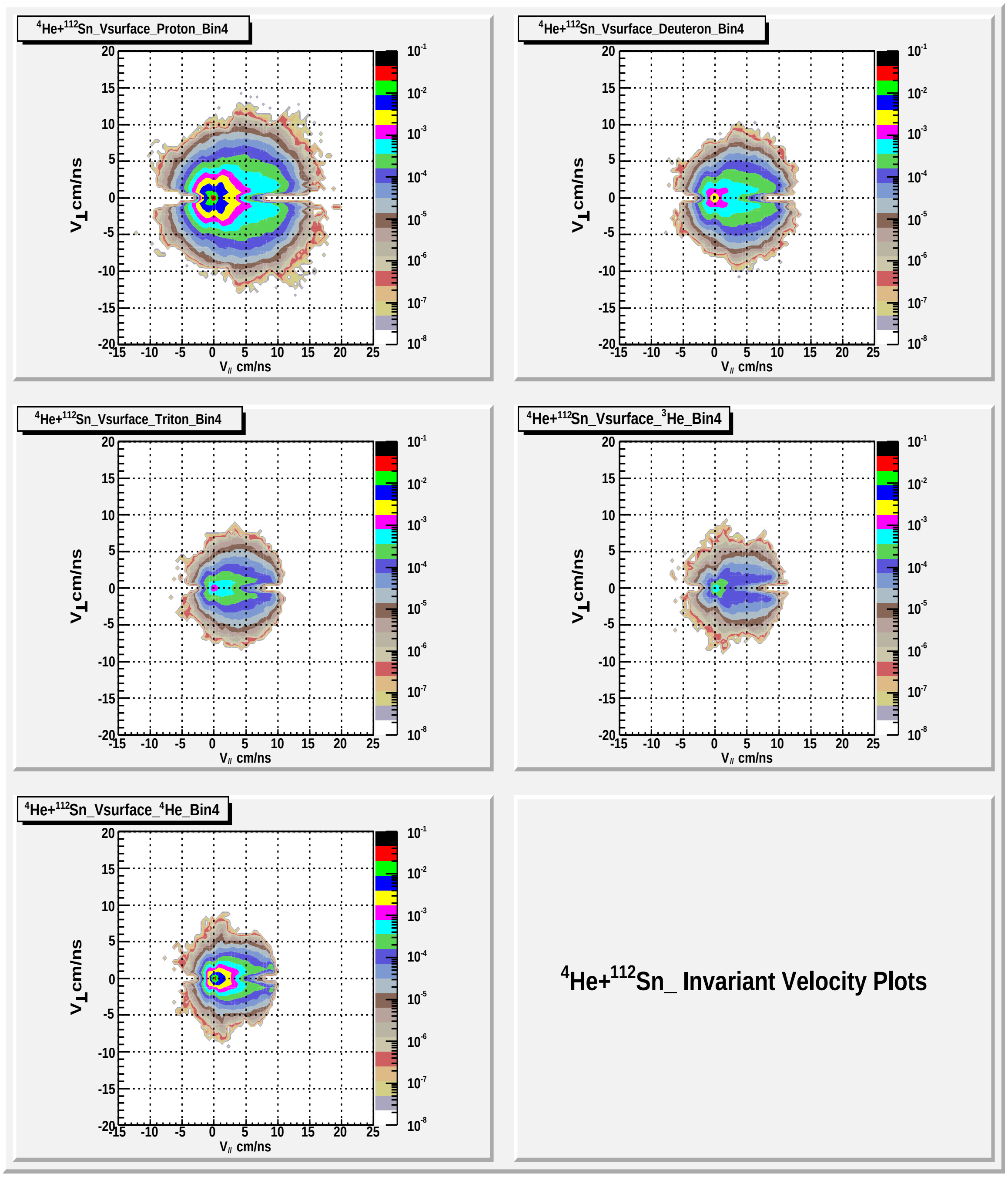

Fig. 148. Particle Surface Velocity Plot of ^{4}He+ ^{112}Sn

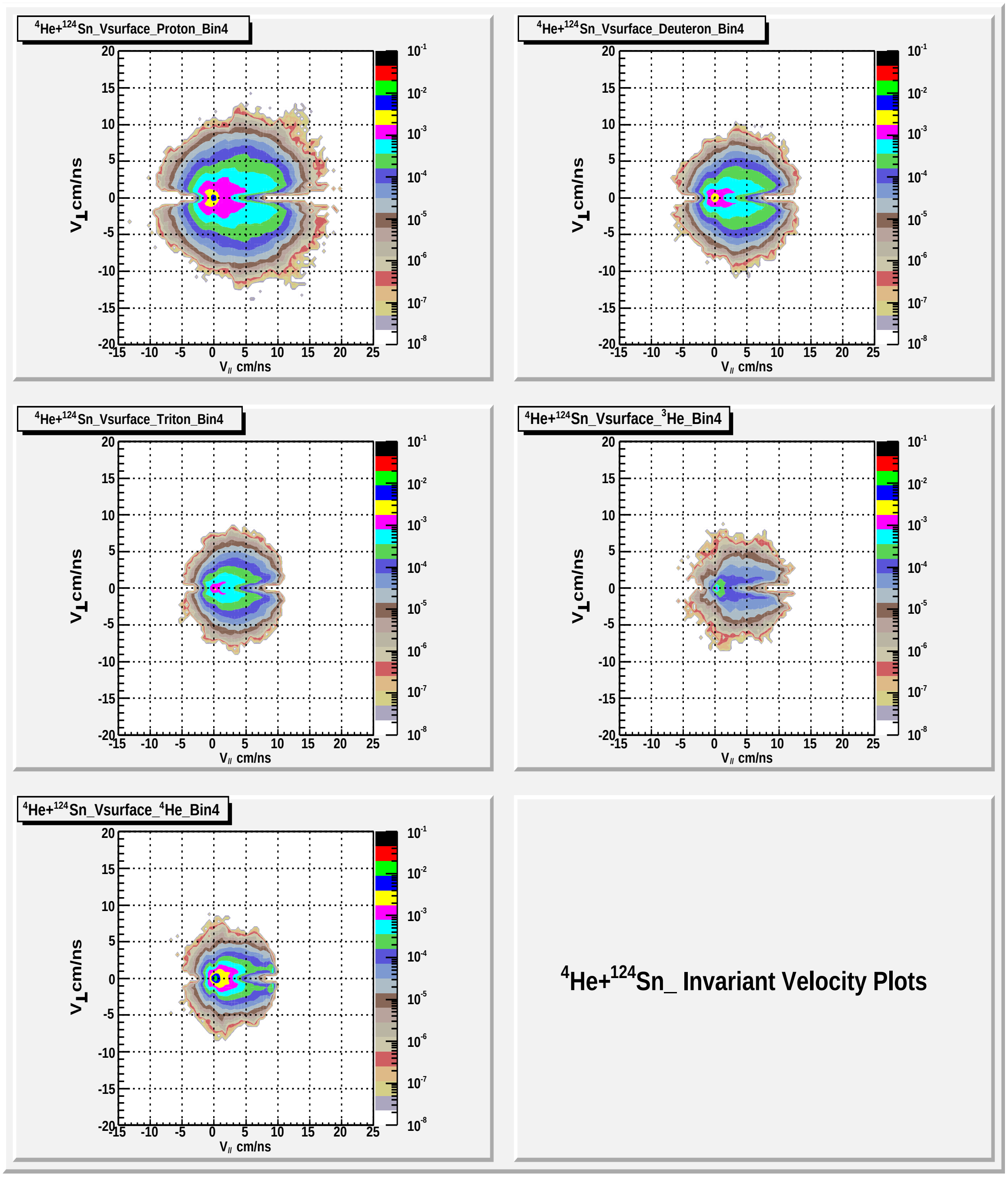

Fig. 149. Particle Surface Velocity Plot of ^{4}He+ ^{124}Sn

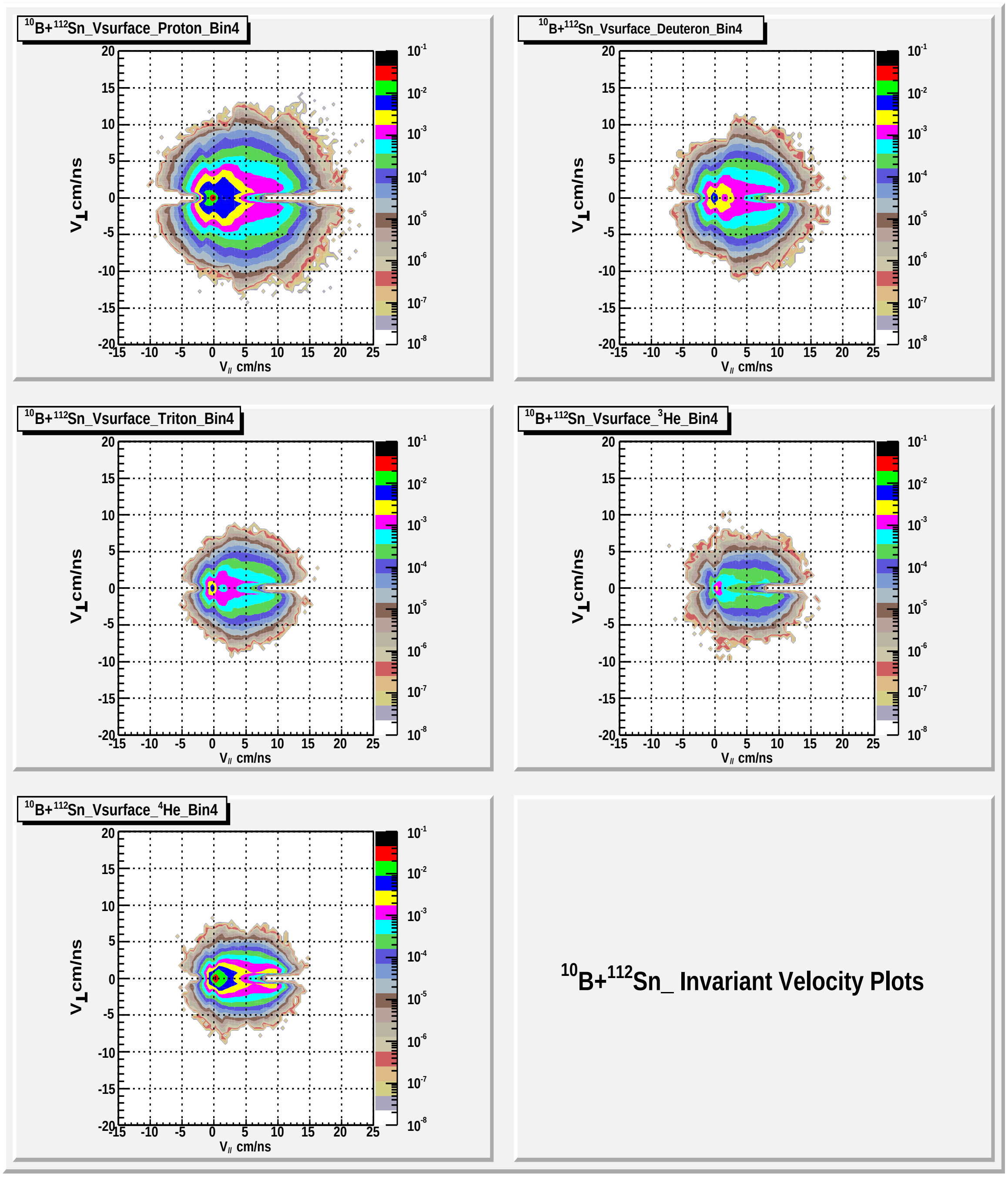

Fig. 150. Particle Surface Velocity Plot of ^{10}B+ ^{112}Sn

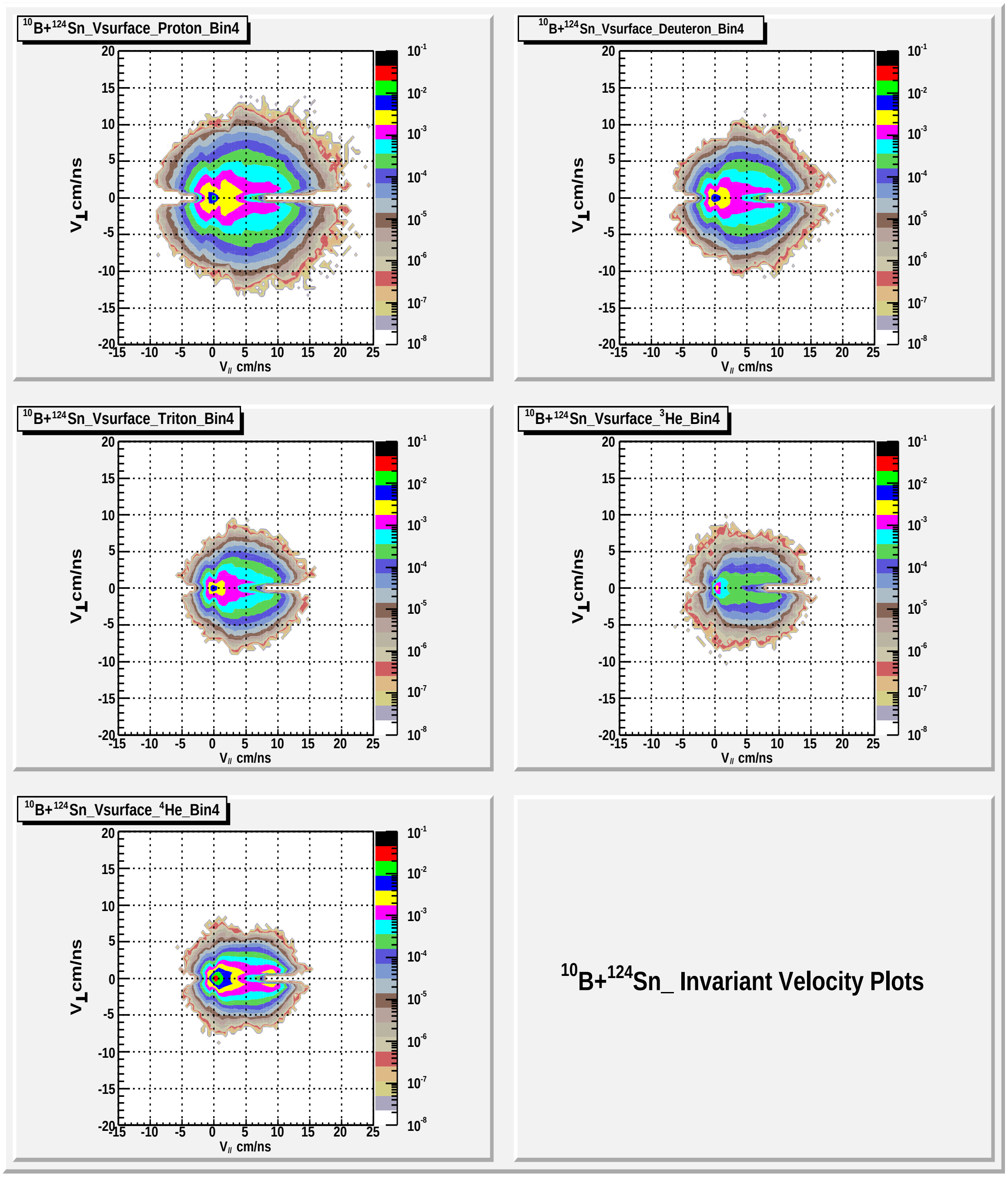

Fig. 151. Particle Surface Velocity Plot of ^{10}B+ ^{124}Sn

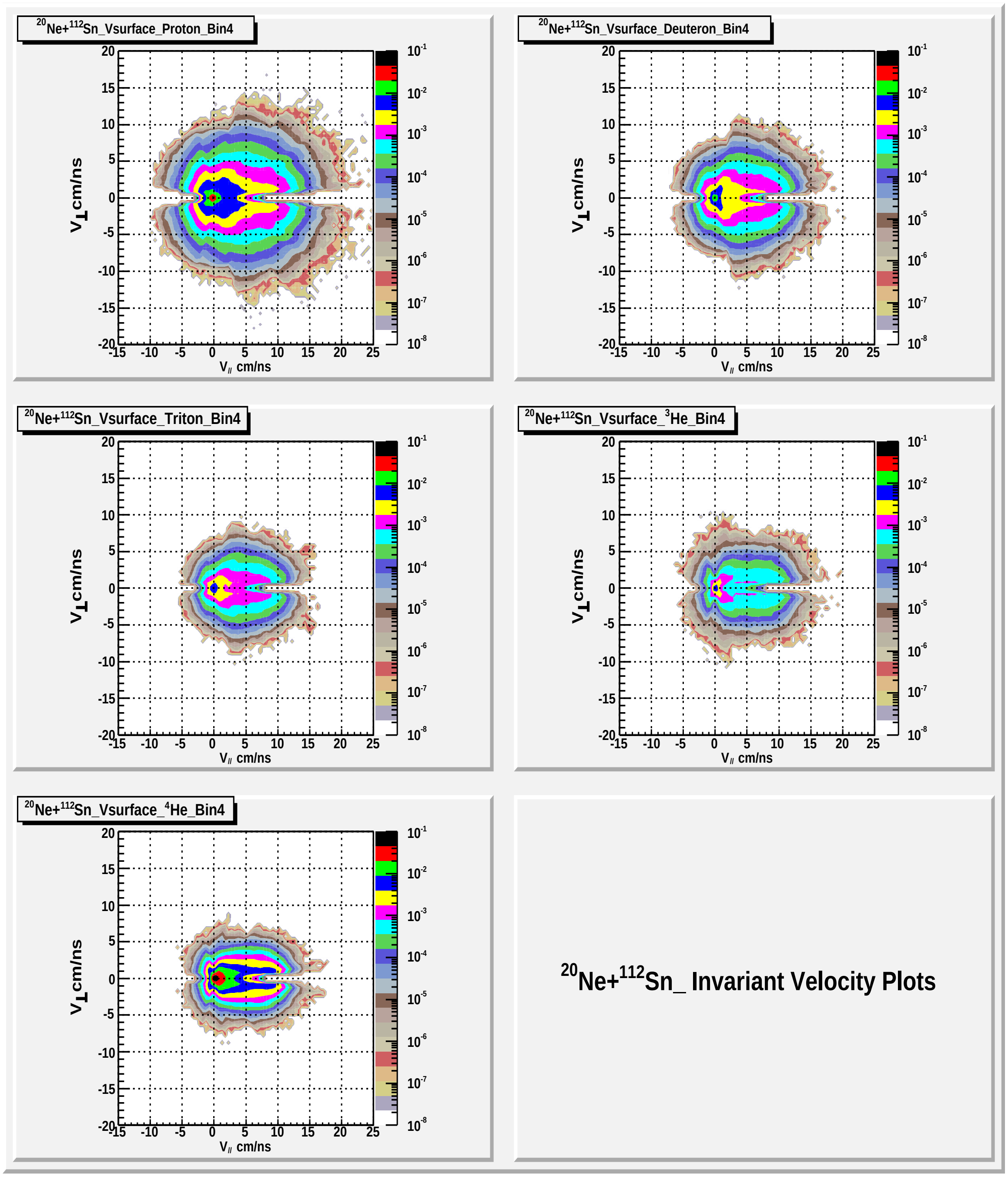

Fig. 152. Particle Surface Velocity Plot of ^{20}Ne+ ^{112}Sn

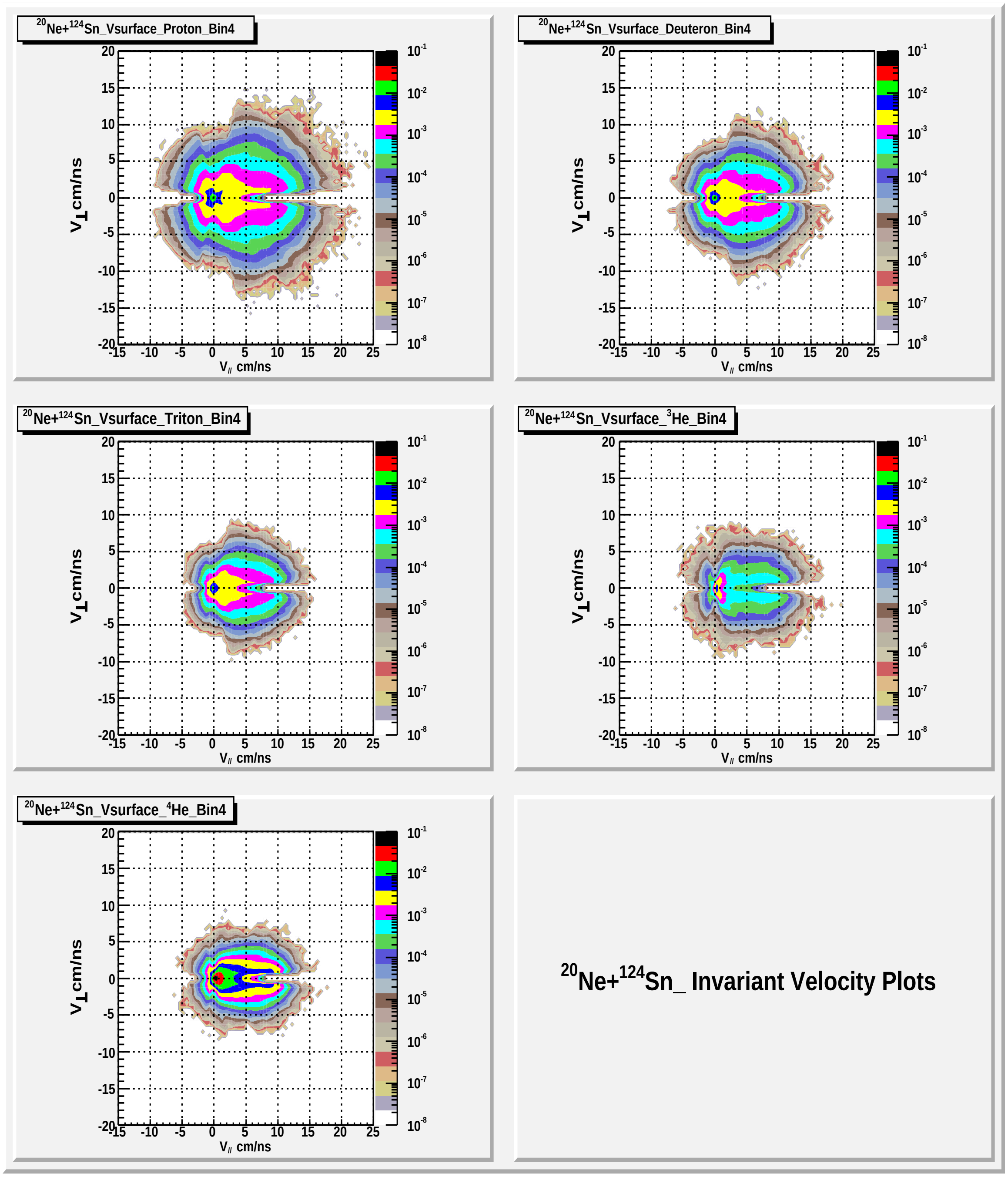

Fig. 153. Particle Surface Velocity Plot of ^{20}Ne+ ^{124}Sn

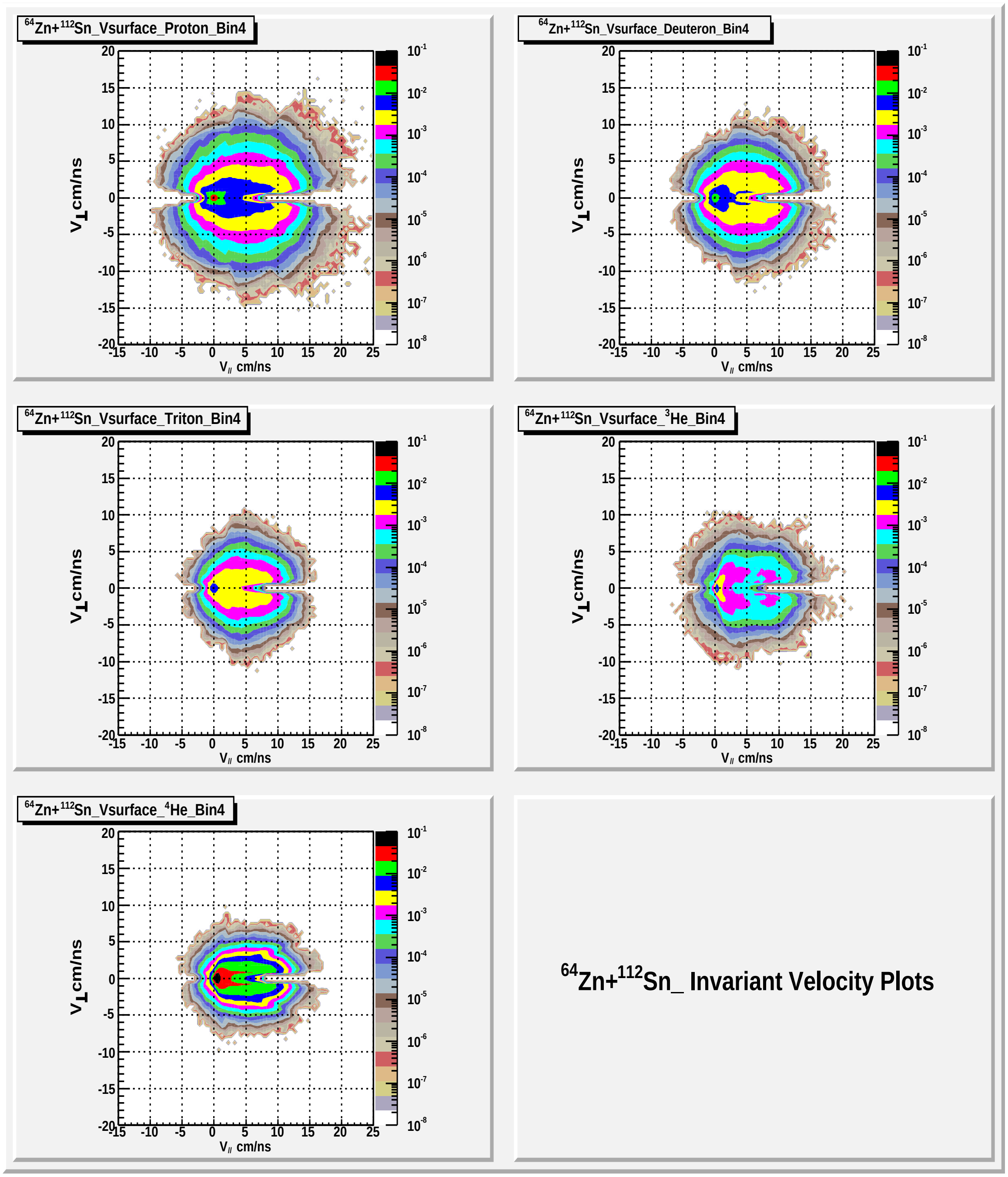

Fig. 154. Particle Surface Velocity Plot of ^{64}Zn+ ^{112}Sn

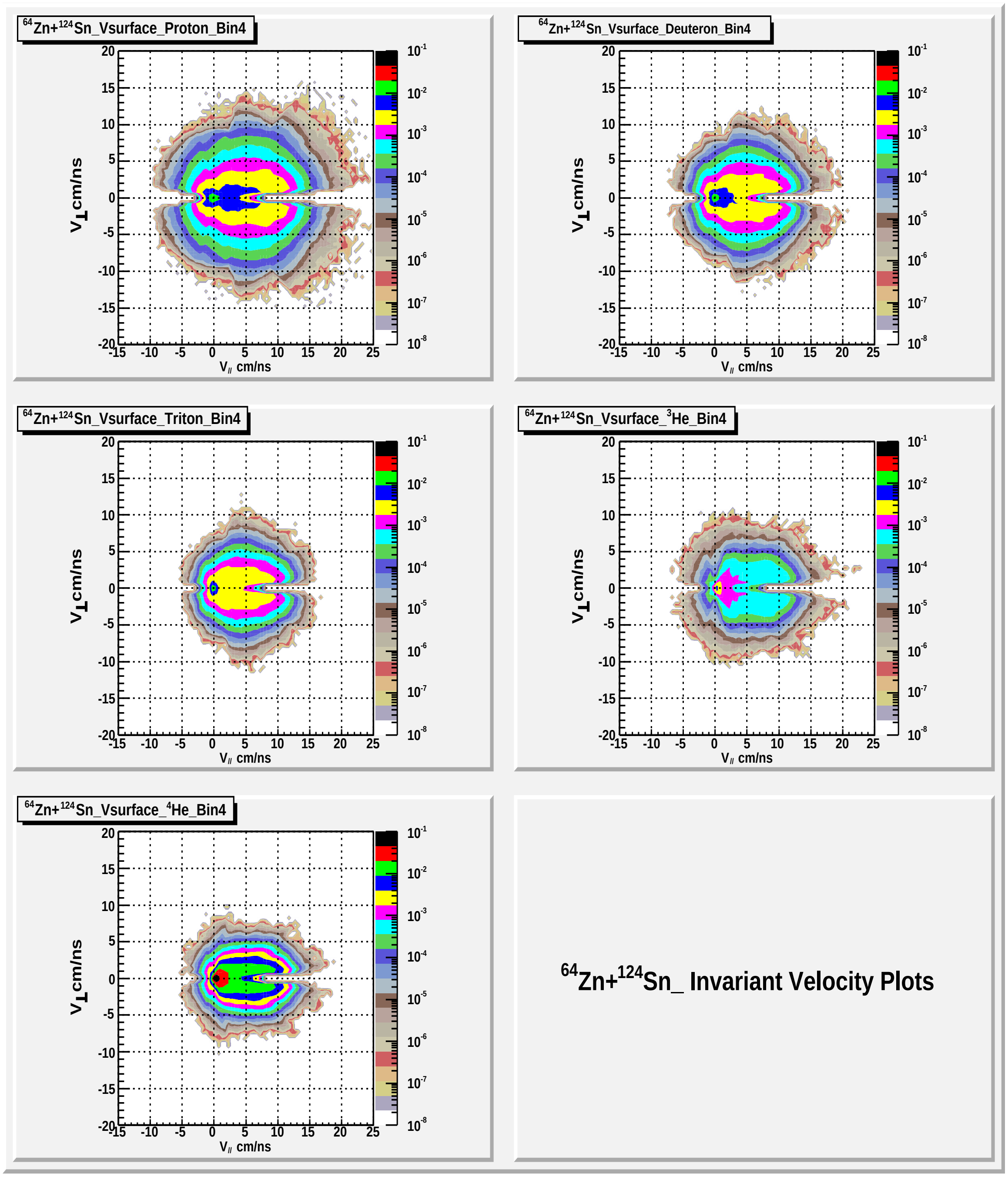

Fig. 155. Particle Surface Velocity Plot of ^{64}Zn+ ^{124}Sn

APPENDIX L

ISOSCALING PARAMETER ALPHA

This appendix list some of typical isoscaling parameters at parallel velocity from 4.75 cm/ns to 5.75 cm/ms range.

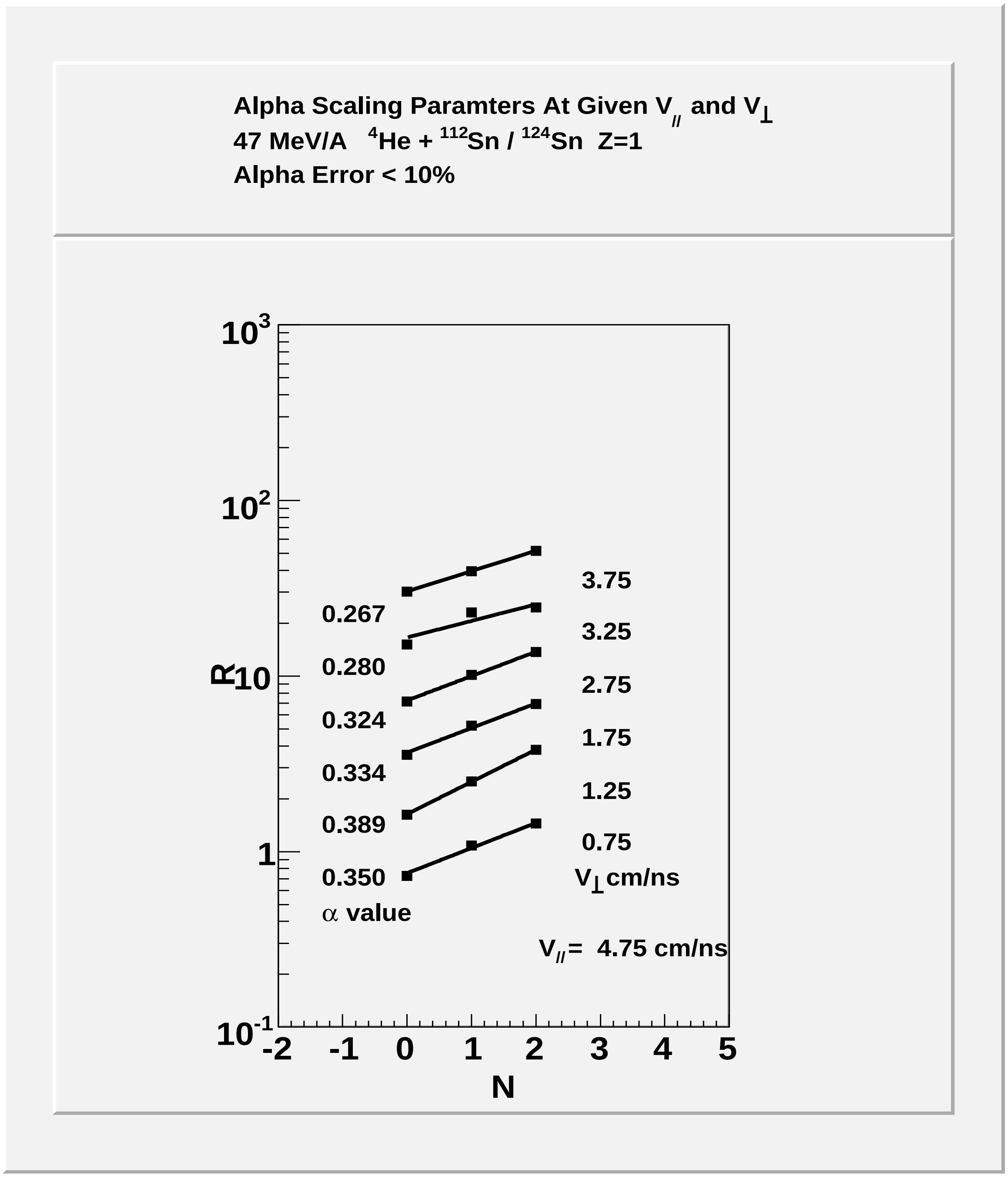

Fig. 156. Scaling parameter Alpha at parallel velocity 4.75 cm/ns and different perpendicular velocities

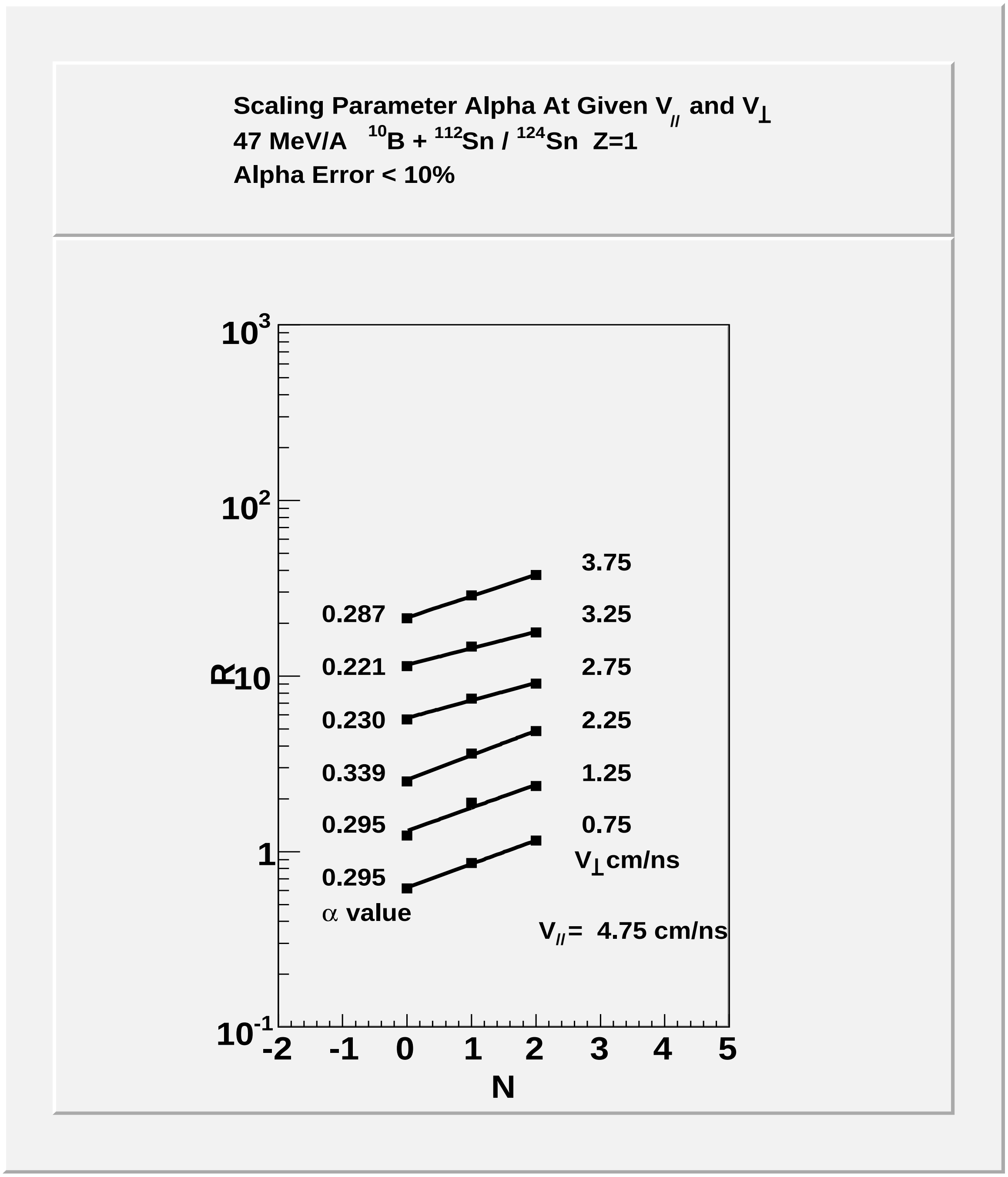

Fig. 157. Scaling parameter Alpha at parallel velocity 4.75 cm/ns and different perpendicular velocities

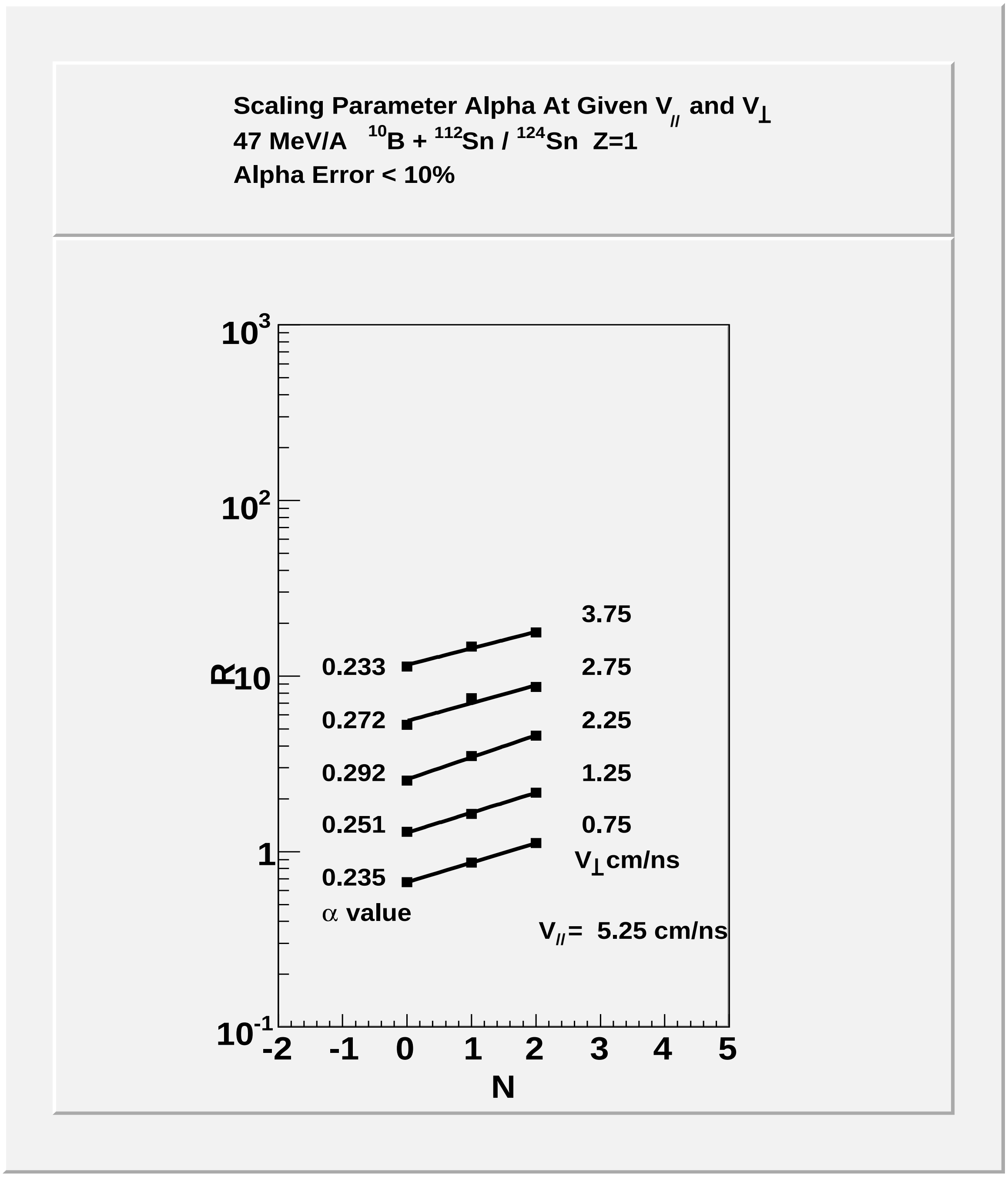

Fig. 158. Scaling parameter Alpha at parallel velocity 5.25 cm/ns and different perpendicular velocities

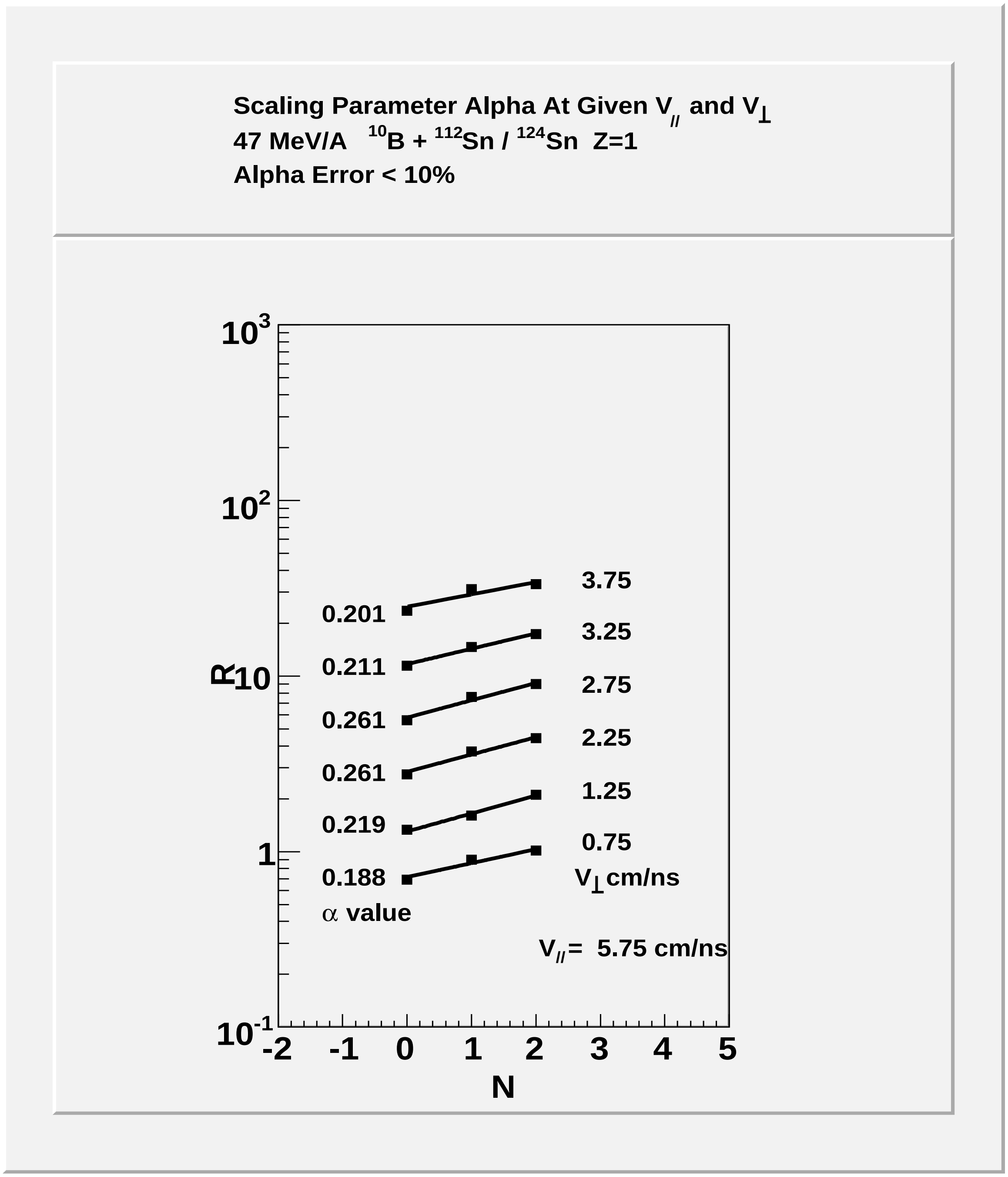

Fig. 159. Scaling parameter Alpha at parallel velocity 5.75 cm/ns and different perpendicular velocities

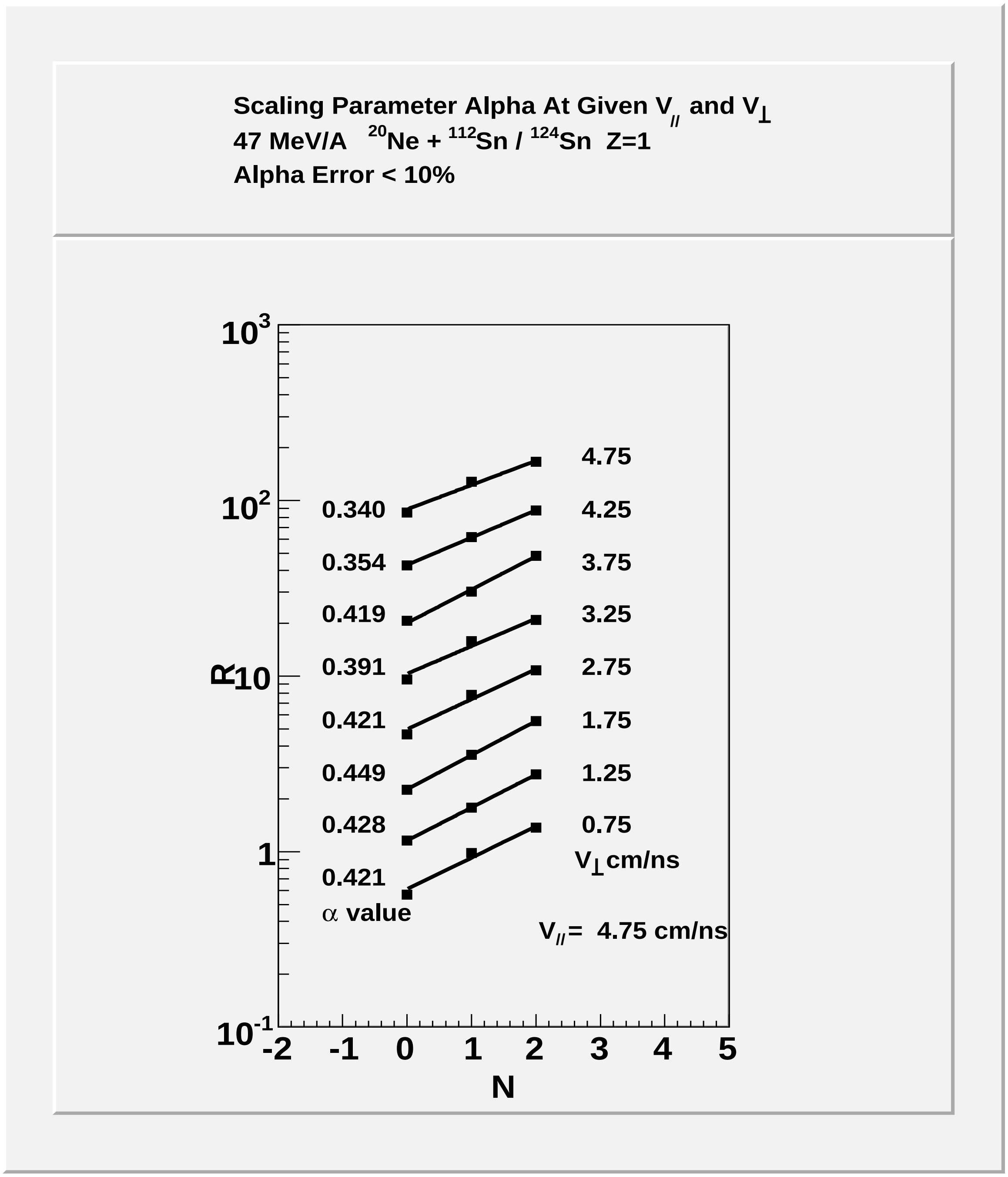

Fig. 160. Scaling parameter Alpha at parallel velocity 4.75 cm/ns and different perpendicular velocities

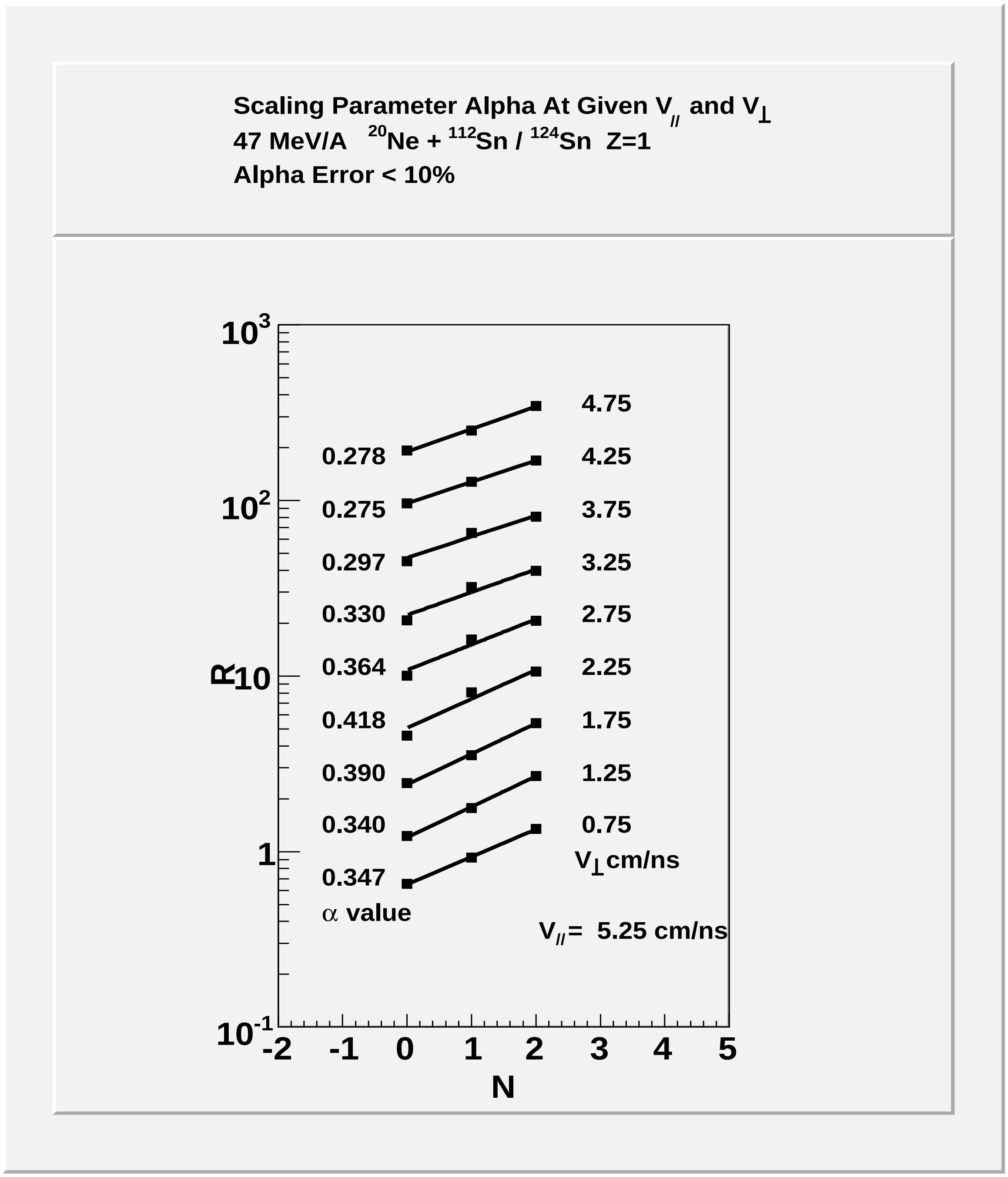

Fig. 161. Scaling parameter Alpha at parallel velocity 5.25 cm/ns and different perpendicular velocities

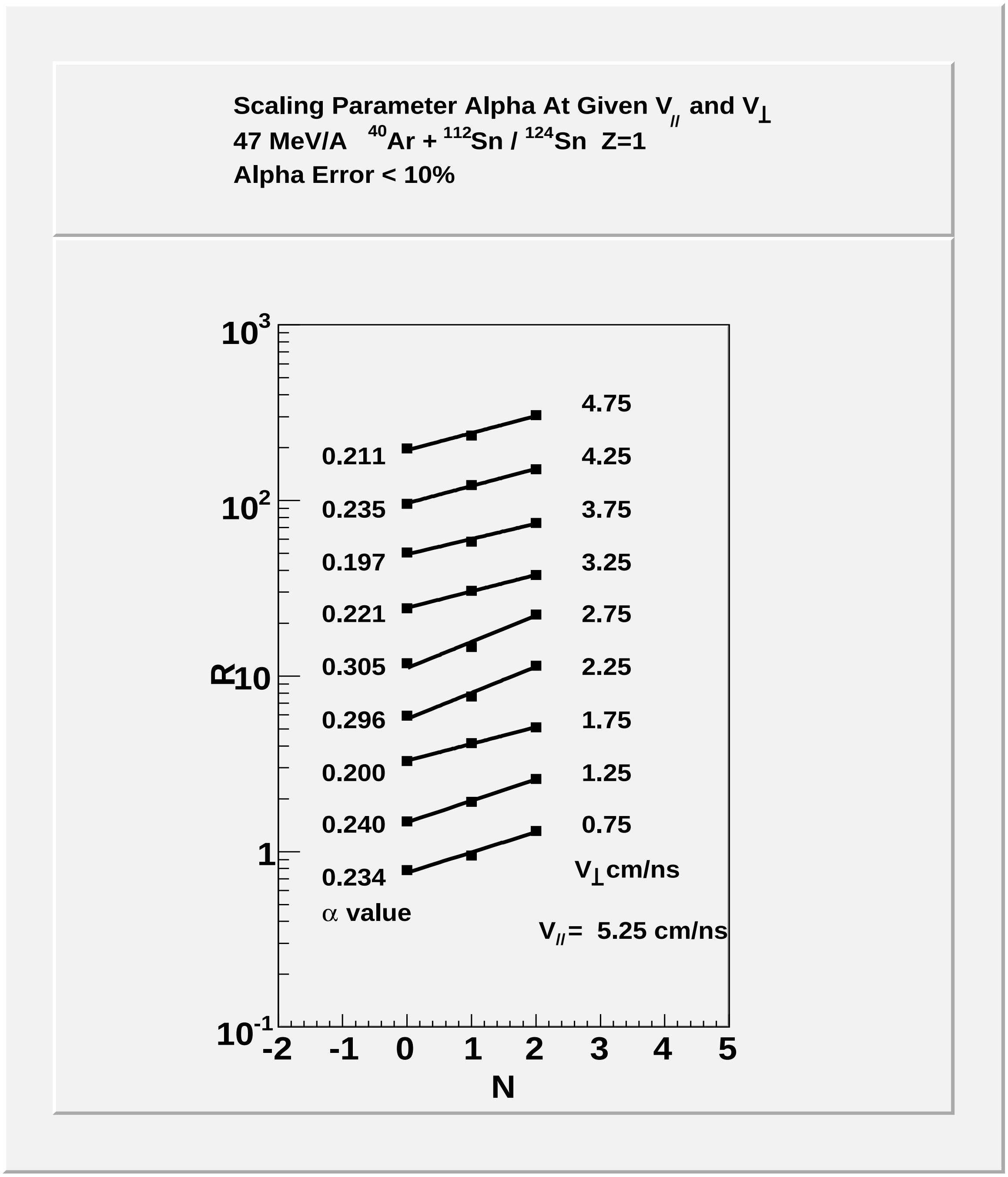

Fig. 162. Scaling parameter Alpha at parallel velocity 5.25 cm/ns and different perpendicular velocities

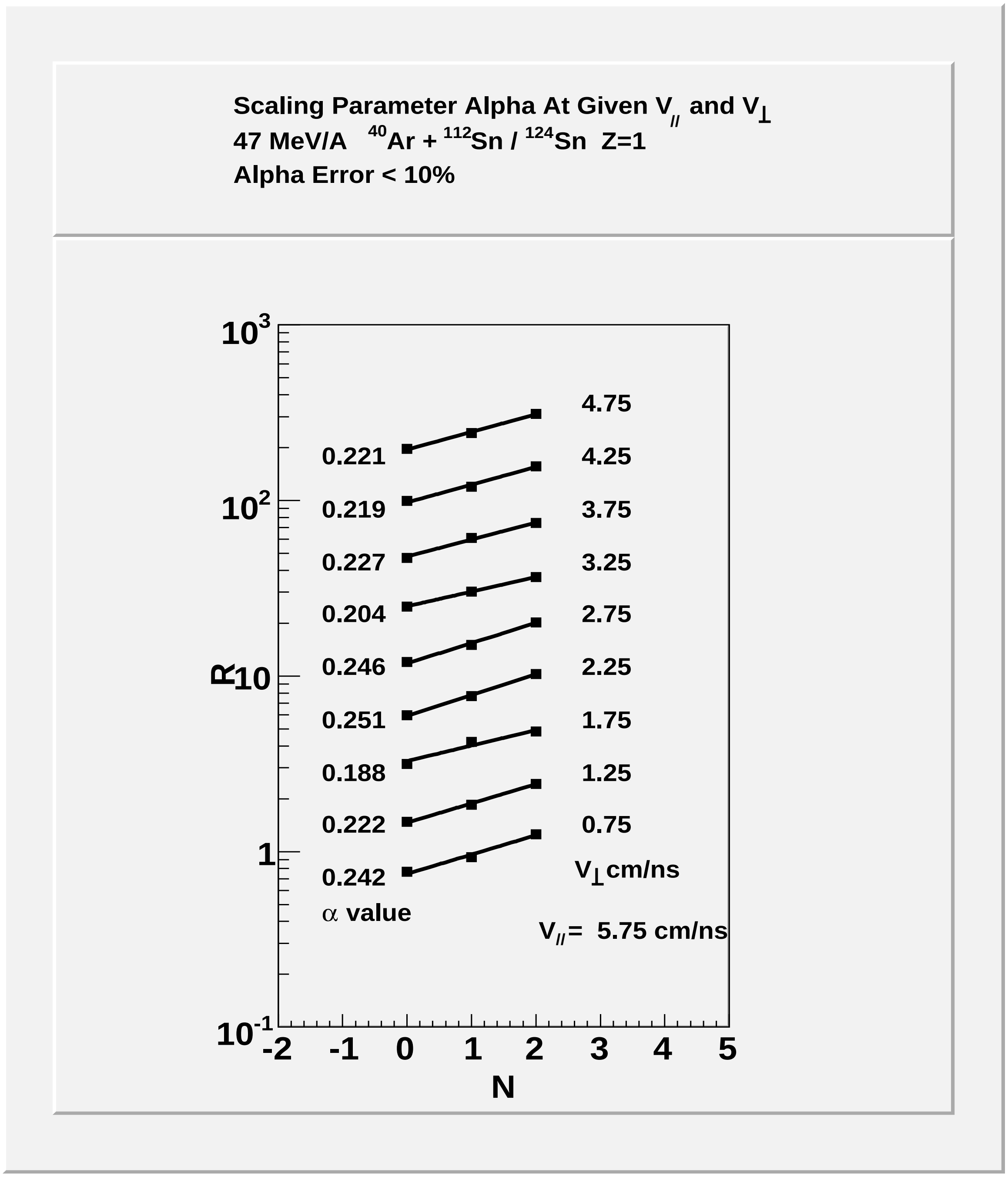

Fig. 163. Scaling parameter Alpha at parallel velocity 5.75 cm/ns and different perpendicular velocities

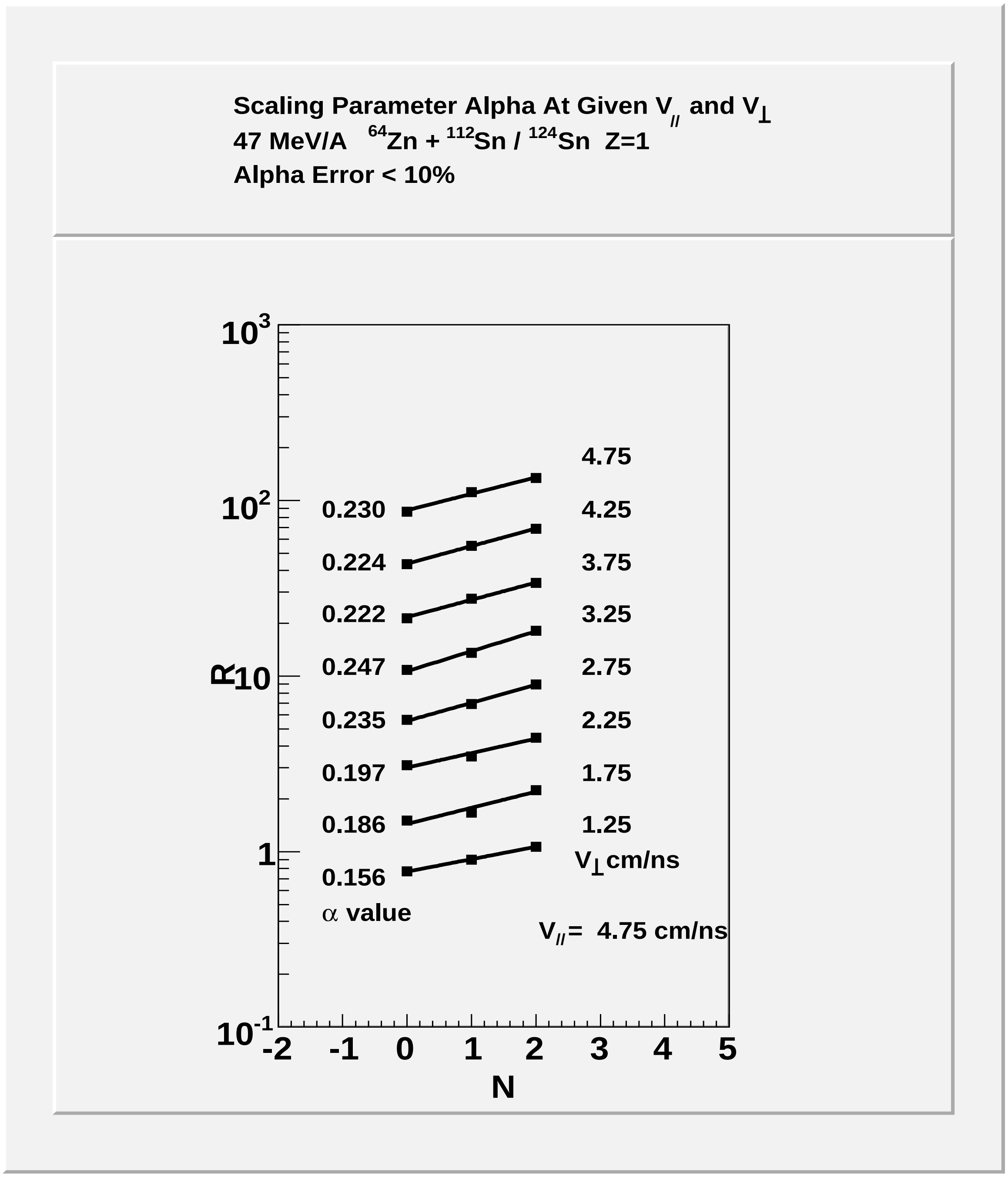

Fig. 164. Scaling parameter Alpha at parallel velocity 4.75 cm/ns and different perpendicular velocities

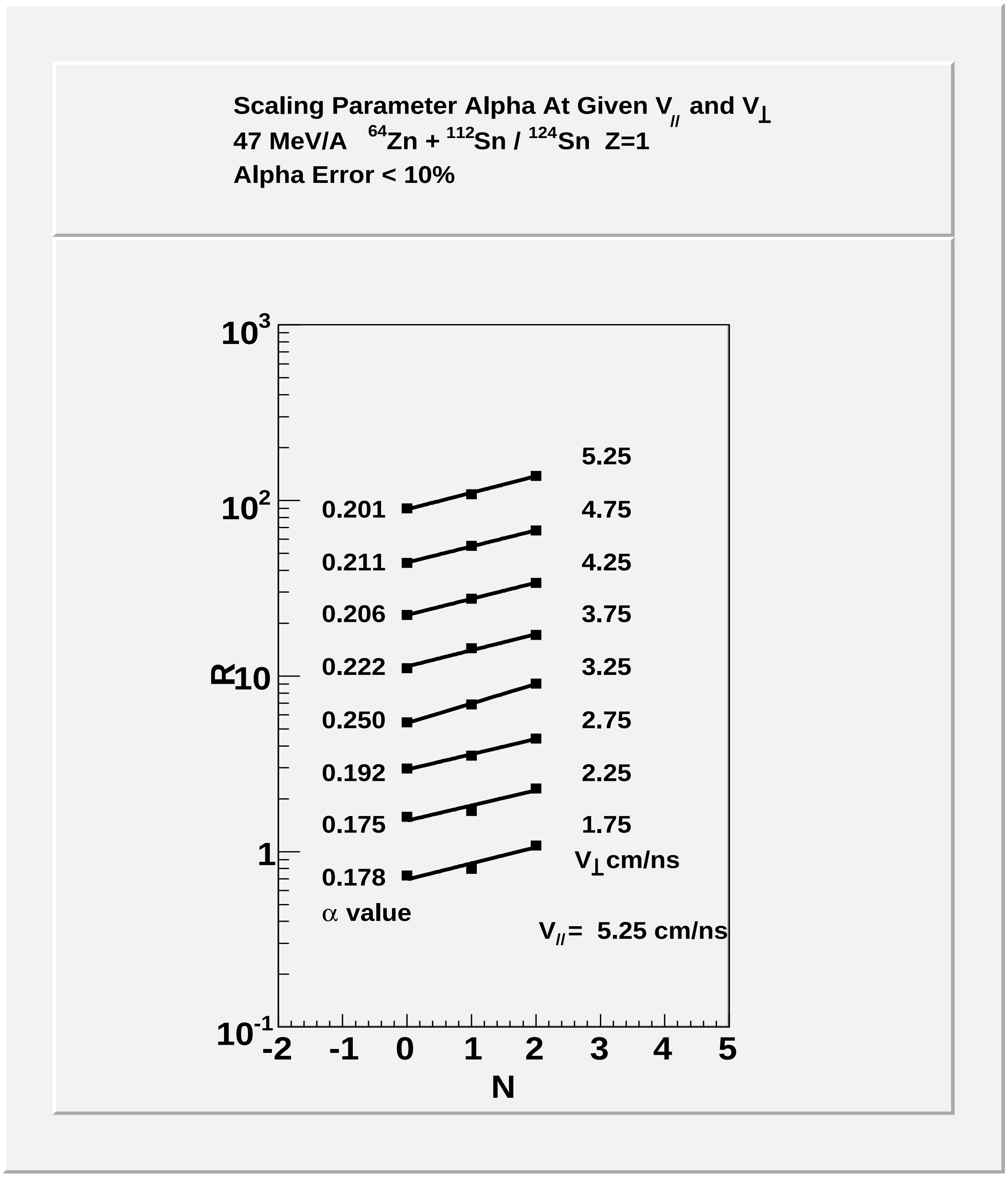

Fig. 165. Scaling parameter Alpha at parallel velocity 5.25 cm/ns and different perpendicular velocities

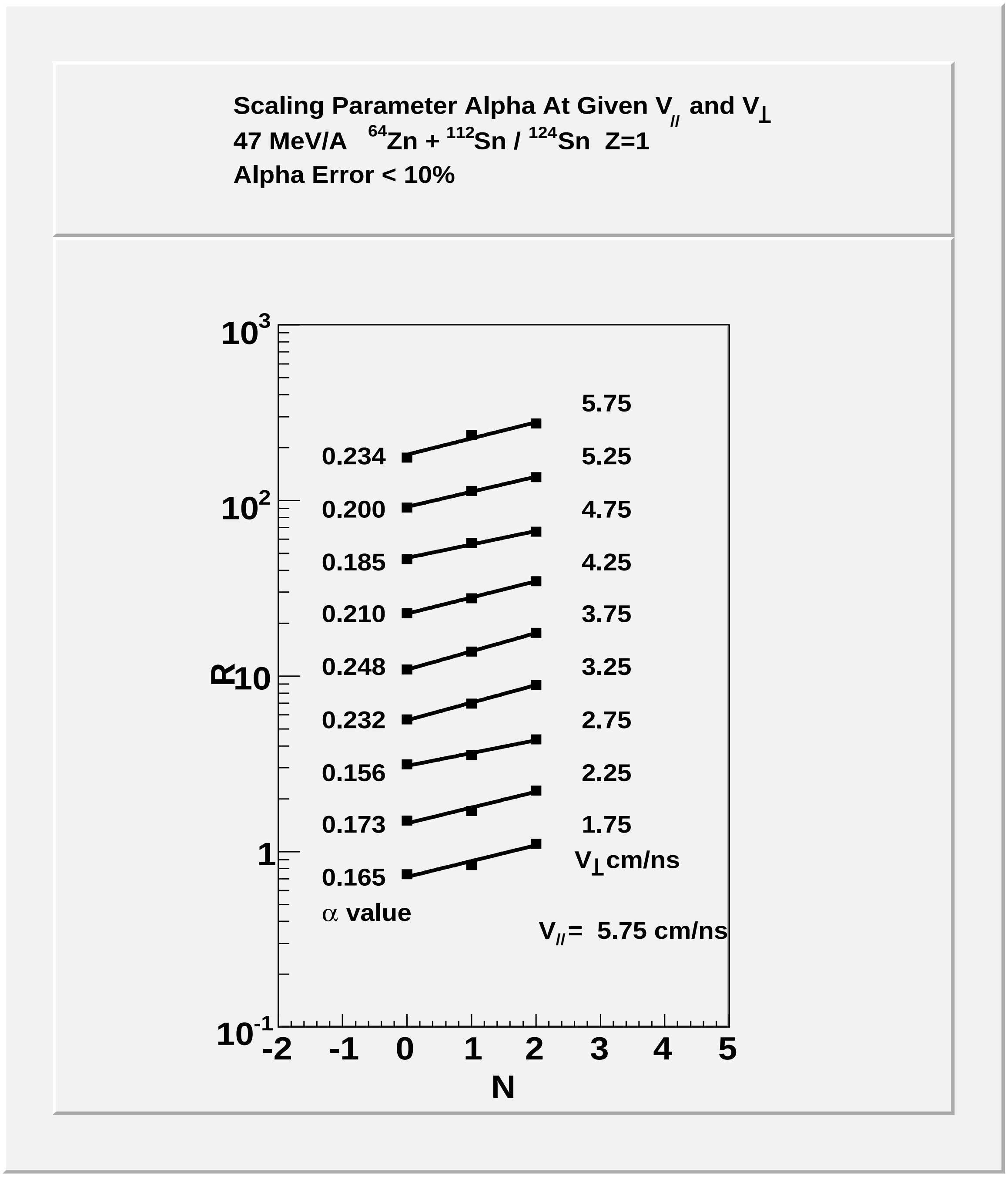

Fig. 166. Scaling parameter Alpha at parallel velocity 5.75 cm/ns and different perpendicular velocities

VITA

Lijun Qin was born and raised in Shuyang, Jiangsu Province, P.R. China. He earned a B.S. in physics from Xi'An Jiaotong University, China in 1995. He received his M.S. degree in nuclear physics from the Institute of Modern Physics, the Chinese Academy of Sciences in July 1998. He received his Ph.D. in physics from Texas A&M University in December 2008. Lijun Qin may be reached at Lijunqin2005@gmail.com or through Li Zhang at the Department of Soil and Crop Sciences, Texas A&M University, College Station,TX, 77843-2474.

The typist for this dissertation was Lijun Qin.